

NEUTRON SCATTERING FROM LOW-DIMENSIONAL
QUANTUM MAGNETS

A thesis submitted for
the degree of Doctor of Philosophy

by

Elisa Maria da Silva Wheeler

Somerville College

Clarendon Laboratory
Oxford University Physics Department



Michaelmas 2007

Neutron Scattering from Low-Dimensional Quantum Magnets

Elisa Wheeler, Somerville College

Thesis for the Degree of Doctor of Philosophy, Michaelmas Term, 2007

Neutron scattering measurements were used to investigate the magnetic and crystal structure and magnetic excitations of three compounds characterized as low-dimensional quantum magnets. The materials are frustrated systems with low spin quantum number. The first was a powder sample of AgNiO_2 . The Ni ions form a triangular lattice antiferromagnet in which, according to the published crystal structure, both the orbital order and magnetic couplings are frustrated. However, it is shown here that there was a small distortion of the crystal structure at 365 K, which is proposed to result from charge disproportionation and this relieves the orbital frustration. The magnetic structure was investigated and, below 20 K, the triangular lattice of electron-rich Ni sites was observed to order into antiferromagnetic stripes. Investigations of the magnetic excitations showed that the main dispersions were within the triangular plane, indicating a strong two-dimensionality. The dispersion was larger along the stripes than between the stripes of collinear spins. The second material investigated was CoNb_2O_6 , a quasi Ising-like ferromagnet. It was studied with a magnetic field applied transverse to the Ising direction. The magnetic field introduced quantum fluctuations which drove a phase transition at a field comparable to the main exchange interaction. The phase diagram of the magnetic order was mapped out and a transition from an ordered phase to a paramagnetic phase was identified at high field. This low-temperature high-field phase transition was further investigated by inelastic neutron scattering measurements to observe the change in the energy gap and magnetic excitation spectrum on either side of the transition. The spectrum had two components in the ordered phase and had sharp magnon modes in the paramagnetic phase. The third material was the spin-half layered antiferromagnet CuSb_2O_6 . It has a square lattice of Cu^{2+} ions in which the main interaction is across only one diagonal of the square. The magnetic structure was studied by neutron scattering with a field applied along the direction of the zero-field ordered moment. A spin-flop was observed at low field and there was evidence for a high-field transition. The magnetic excitation spectrum was unusual in that it had an intense resonance at 13 meV at the magnetic Brillouin zone boundary.

Acknowledgements

I would like to thank my supervisors, Andrew Boothroyd, Radu Coldea and Mechthild Enderle, for all of their help and the fruitful discussions during the work on this thesis. I have also received a lot of help from Ewa Wawrzyńska for which I am very grateful.

I have had the opportunity to carry out my experiments at a variety of institutions and have had excellent support. The scientists who have helped during the experiments are Laurent Chapon, Bijorn Fak, Beatrice Grenier, Jens Hoffmann, Klaus Habicht, Richard Ibberson, Mark Johnson, Wilfried Kockelmann, Marek Koza, Paolo Radeilli, Kirrily Rule, Emanuelle Suard and Jon Taylor.

In Oxford I've appreciated the tea time chats, help and advice of those in the department, particularly Roger Cowley, Prabhakaran Dharmalingam, Russell Ewings, Lucy Heleme, Tom Huberman, Andrew James, Rhiannon Jones, Dave Keen, Heather Lewtas and Chiron Mukerjee.

I am also grateful to the support I have received from ILL and the welcome I received from the TAS group. The times I have spent in Grenoble have been made all the more enjoyable by the warm welcome and encouragement I received from Mechthild. I have profited greatly from coffee time discussions with many of the thesis students particularly Elizabeth Blackburn, Alexander Grunwald, Beate Bruning, Lola Ruiz Martín, Mark Lever and Martin Kempa.

I would like especially to thank Katy Wood who provided me with a nice place to stay in Grenoble and was such an understanding friend throughout my thesis. Also Katy Taheri who has always been a great friend throughout my time in Oxford and endeavoured to understand my work and offer support.

Finally, I would like to thank my family. Their help, love and patience has been invaluable. I am extremely grateful to my parents' continual advice and support throughout all my studies.

Contents

1	Introduction to Low-Dimensional Quantum Magnetism	1
1.1	Introduction	1
1.2	Magnetic Ordering and Excitations	2
1.3	Quantum Magnetism	9
1.3.1	Quantum Phase Transitions	10
1.3.2	One-Dimensional Magnetism	10
1.3.3	Frustration	13
1.3.4	Two-Dimensional Magnetism	15
1.4	Quantum Magnets Studied in this Thesis	17
2	Experimental Techniques	18
2.1	Introduction	18
2.2	The Neutron Scattering Cross-Section	19
2.3	Neutron Scattering Experiments	24
2.3.1	The Neutron Diffractometer	26
2.3.2	The Neutron Time-of-Flight Spectrometer	27
2.3.3	The Neutron Triple-Axis Spectrometer	28
2.4	Susceptibility and Heat Capacity	30
3	Investigation of the Frustrated Triangular Antiferromagnet AgNiO_2	33
3.1	Introduction	34
3.2	Structural and Magnetic Properties of AgNiO_2	35
3.2.1	Experimental Details	36
3.2.2	Measurements and Results	37
3.2.3	Discussion	47
3.3	Magnetic Excitations of AgNiO_2	51

3.3.1	Experimental Details	53
3.3.2	Measurements and Results	53
3.3.3	Analysis	57
3.4	Conclusions on AgNiO_2	72
4	Quantum Phase Transition in the Quasi One-Dimensional Ising Ferromagnet	
	CoNb_2O_6 in a Transverse Field	74
4.1	Introduction	75
4.2	Phase Diagram of CoNb_2O_6 in a Transverse Magnetic Field	78
4.2.1	Experimental Details	81
4.2.2	Measurements and Results	87
4.2.3	Analysis	92
4.3	Magnetic Excitations of CoNb_2O_6 in an Applied Magnetic Field Transverse to its Ising Axis	96
4.3.1	Experimental Details	98
4.3.2	Measurements and Results	100
4.3.3	Analysis	107
4.4	Conclusions on CoNb_2O_6	119
5	Neutron Scattering Study of the Layered Spin-Half Antiferromagnet CuSb_2O_6	120
5.1	Introduction	121
5.2	Low-Temperature Magnetic Structure of CuSb_2O_6	124
5.2.1	Experimental Details	124
5.2.2	Results	126
5.2.3	Discussion	131
5.3	Inelastic Neutron Scattering Study of the Excitation Spectrum of CuSb_2O_6 at Zero Field	133
5.3.1	Introduction	133
5.3.2	Experimental Details	134
5.3.3	Measurements and Results	135
5.3.4	Analysis	146
5.4	Conclusions on CuSb_2O_6	156
6	Conclusions and Perspectives	158

A	Low-Temperature and High-Temperature Structure Factors from Powder-Diffraction Measurements on AgNiO_2	162
B	Linear Spin-wave Theory for Stacked Triangular Layers with Stripe Order in AgNiO_2	166
C	Measured Magnetic Bragg Intensities in the Single-Crystal Diffraction Measurements on CoNb_2O_6	169
D	Linear Spin-Wave Calculations of the Magnon Dispersion Relations of the Ising Chains in CoNb_2O_6	171
E	Integrated Magnetic Bragg Intensities for the Single-Crystal Diffraction Measurements on CuSb_2O_6	174
F	Linear Spin-Wave Calculations of the Magnon Dispersion Relations of Heisenberg Spins in a Square Lattice in CuSb_2O_6	176
	Bibliography	178

Chapter 1

Introduction to Low-Dimensional Quantum Magnetism

1.1 Introduction

The compounds investigated within this work are spin systems chosen to explore the effect of quantum fluctuations. All of the materials have properties of low spin models that exemplify the basic concepts in quantum magnetism, especially the role of fluctuations.

- The one-dimensional Ising chain in a transverse field is a paradigm system of a quantum phase transition. In this system a phase transition is tuned by a magnetic field which introduces quantum fluctuations.
- The triangular lattice antiferromagnet with uniaxial anisotropy is a highly frustrated system. The couplings of the spins in the lattice cannot be satisfied simultaneously because of the geometry of the lattice.
- The square lattice antiferromagnet with a dominant antiferromagnetic next-nearest-neighbour exchange is a frustrated system due to the arrangement of the couplings within the lattice.

This chapter explains the origins of localized moments in magnets and the possible coupling mechanisms between them. The mean-field approach is briefly discussed together with an outline of the spin-wave approximation. The concepts of low-dimensional low-spin systems and frustration are discussed with reference to the types of systems covered in this thesis.

1.2 Magnetic Ordering and Excitations

The simplest models of magnetic systems are semi-classical descriptions which neglect quantum fluctuations. They are successful for three-dimensional systems where the spin quantum number is large. The semi-classical description is outlined here and the effect of quantum fluctuations is described in the following section.

The magnetic moment of an ion is due to electrons which are in unfilled electronic shells. The spin s_i and orbital angular momentum l_i of these electrons add to give a total spin and total orbital angular momentum. The spherical symmetry of an electronic shell implies that these vector sums are zero for filled shells of electrons. According to Hund's rules, the ground state of the free ion is that which maximizes the total spin, S and total orbital angular momentum, L , and thereby minimizes the Coulomb repulsion between electrons. The spin-orbit interaction couples the spin and orbital angular momentum to give a total angular momentum, $\mathbf{J} = \mathbf{L} + \mathbf{S} = \sum_i \mathbf{l}_i + \mathbf{s}_i$. However, the magnetic ion in a compound is not a free ion but sits in the environment of the electric field created by the ions around it. Therefore, the ground state may differ from that given by Hund's rules. Given a state of total angular momentum J the effective magnetic moment is given by

$$\mu_{\text{eff}} = g_J \mu_B \sqrt{J(J+1)} \quad (1.1)$$

where g_J is the Landé g-value or g-factor and is calculated as

$$g_J = \frac{3}{2} + \frac{S(S+1) + L(L+1)}{2J(J+1)}.$$

In 3d ions it is often the case that the environment of the ion is such that the orbital angular momentum is effectively quenched and the ground state is an orbital singlet. In this case, the ground state can be described as a purely spin state. Also, the spin-orbit interaction can be included by allowing a small change from the $g = 2$ value, which is the case for an ideal $L = 0$ system.

In order to know the ground state of an ion in a particular compound it is necessary to know the particular electronic environment of the ion. The ground state can be probed by making measurements of excitations of the outer electrons from the ground state to higher energy levels. Crystal-field excitations are local excitations of the electrons in magnetic ions. Measurements of crystal-field excitations are generally made at low temperatures; these measurements look at excitations from the ground state to excited crystal-field levels. The excitations are flat dispersionless modes at constant energy. The energy of the crystal-field levels is due to the local electron environment of the ion. The environment causes splitting of degenerate energy levels of the free ion which can be measured directly by inelastic neutron scattering measurements.

The spins in the system couple via an exchange interaction which is dependent on the structure and composition of the crystal [1]. It is the exchange interaction that provides long-range order and dispersion of excitations in the system of spins. The forms of magnetic coupling may differ between materials. A weak coupling may occur due to the magnetic dipolar interaction. This is a weak interaction which cannot explain the interaction energies of approximately 10 meV which is the order of magnitude of the interactions observed in the experiments described in this thesis. A greater coupling arises from interactions such as direct exchange, super-exchange and indirect exchange.

The origin of the exchange interaction can be understood by considering the exchange

of two electrons [2]. In such a system the combined wavefunction of the two electrons, which are spin-half objects, is either a spin triplet, $S = 1$, or spin singlet state, $S = 0$. The symmetry of the spatial states of the combined electrons is necessarily different because the combined state must obey exchange symmetry. The exchange integral calculates the energy difference between the two states associated with the spin singlet, E_s , and spin triplet, E_t . The Hamiltonian can be written as:

$$\mathcal{H} = \frac{1}{4}(E_s + 3E_t) - (E_s - E_t)\mathbf{S}_1 \cdot \mathbf{S}_2 \quad (1.2)$$

where the exchange integral is:

$$J = E_s - E_t = \int \phi_1^*(\mathbf{x}_1)\phi_2^*(\mathbf{x}_2)\hat{\mathcal{H}}\phi_1(\mathbf{x}_2)\phi_2(\mathbf{x}_1)$$

The effective Hamiltonian can be simplified to:

$$\mathcal{H} = J\mathbf{S}_1 \cdot \mathbf{S}_2 \quad (1.3)$$

A series of spins may interact in this way. The effective interaction between a series of spins within a material may be anisotropic due to the effects of the crystal field. The ground state levels are mapped onto an effective spin system. The degeneracy of the ground state determines the effective spin. Therefore an effective spin Hamiltonian is formed from the lowest energy levels and the Heisenberg Hamiltonian becomes:

$$\mathcal{H} = \sum_{l,j} J_{lj}^x S_l^x S_j^x + J_{lj}^y S_l^y S_j^y + J_{lj}^z S_l^z S_j^z \quad (1.4)$$

where l, j refer to the interaction between the pair of magnetic ions l and j (i.e. each interaction is counted once). A positive J leads to the anti-alignment of spins, and a negative J leads to co-alignment of spins. The two different values of J are referred to as antiferromagnetic or ferromagnetic interactions, respectively.

The physical origin of the exchange may vary between different materials. The main exchange mechanisms are direct exchange, superexchange, double exchange and the RKKY interaction. Each will be outlined in turn next. The direct overlap of neighbouring magnetic orbitals is referred to as a direct exchange mechanism. It can lead to an exchange interaction between magnetic ions with extended electron orbitals arranged as neighbours on a lattice. Superexchange refers to exchange between magnetic ions through a non-magnetic ion. It describes exchange between magnetic ions which are not nearest neighbours, when considering all the ions in the unit cell. Superexchange is highly dependent on the overlap of the orbitals of the magnetic ions with the non-magnetic ion. It is therefore related to the angles of the bonds between the magnetic ion and the non-magnetic ion. The Goodenough-Kanamori rules [3, 4] outline, to some extent, whether interactions between ions are likely to be antiferromagnetic or ferromagnetic. Double exchange occurs between mixed valency states and comes about from electrons hopping between magnetic ions. Therefore, from Hund's rules, the alignment of spins in a particular polarization is favoured. The RKKY interaction is used to describe interactions in a metallic bond. In the RKKY interaction a local spin moment polarizes conduction electrons, which then move to polarize neighbouring local magnetic moments.

In classical magnets long-range order is typically seen below a characteristic temperature, T_c , where thermal fluctuations are reduced to the extent that the magnetic moments in the system are able to form a well defined structure. At this temperature the thermal fluctuations are small enough such that the magnetic interactions are strong enough to bring about long-range order of all the magnetic moments in the system. The different magnetic structures which can form are related to the type of lattice of magnetic moments and the sign and magnitude of the interactions between the moments. For example, in a ferromagnet, where the main interaction is ferromagnetic, there is an overall magnetization. Near the critical temperature the functional form of the magnetization can be described as

$$M(T) \propto (T_c - T)^\beta$$

and β is referred to as a critical exponent. For an antiferromagnet the magnetisation, $M(T)$, is that of the sublattice of co-aligned spins. Mean-field theory was an early method of understanding the magnetisation in a magnet and is often used to gain an initial understanding of a system. It assumes an effective field is acting on a magnetic moment and that it is due to the exchange interaction and the average field created by the surrounding moments. Therefore it is assumed that the magnetic moments all have the same mean value. In mean-field theory the behaviour of the magnetisation below the transition temperature is predicted to give an exponent $\beta = 1/2$ for any lattice dimension. This shows a failure of the mean-field approach in accounting for the differences observed in the behaviour of lattices of different dimensions.

The exchange interaction between moments leads to magnetic excitations dispersing through the material. For large spin systems in three dimensional lattices, magnetic excitations are successfully described by linear spin-wave theory [5]. In this method a $\Delta S = 1$ excitation from the ground state is spread coherently throughout the system. The spin deviation propagates through the system like a wave with a momentum and energy related through the dispersion relation. In the linear spin-wave calculation, lattices of spins aligned along the same ordering direction are considered as separate sublattices. The spin deviations are then calculated from this assumed ground state. Using the Holstein-Primakoff transformations, the spin operators in the Hamiltonian are expressed in terms of spin deviation operators [6]. The spin deviation operators obey the Bose commutation relations and create and annihilate the spin deviations. Terms higher than second order in these operators are not considered in linear spin-wave theory. Therefore the Heisenberg Hamiltonian in Eqn. 1.4, for the case of a simple ferromagnet, would become:

$$\mathcal{H} \approx \sum_{l_j} J_{l_j} S(S - a_l^\dagger a_l - a_j^\dagger a_j + a_l a_j^\dagger + a_l^\dagger a_j) \quad (1.5)$$

where the spin deviation operators are

$$\begin{aligned}
S_l^z &= S - a_l^\dagger a_l \\
S_l^+ &= S_l^x + iS_l^y \approx \sqrt{2S} a_l, \\
S_l^- &= S_l^x - iS_l^y \approx \sqrt{2S} a_l^\dagger.
\end{aligned} \tag{1.6}$$

The normal modes of the system can be calculated by taking the Fourier transform of the Hamiltonian and diagonalizing it using the Bogliubov transformations. In this way, descriptions of the excitations as a function of energy and momentum transfer are obtained. For example, the dispersion relation for the the Hamiltonian in Equation 1.5 as calculated within linear spin-wave theory is

$$\hbar\omega_{\mathbf{q}} = 2S(J(0) - J(\mathbf{q})).$$

For the case of an antiferromagnetic interaction in Eqn. 1.4, it is assumed that the spin structure can be divided into two interpenetrating lattices of spins. The spin deviation operators for the two sublattices a and b are defined as:

$$\begin{aligned}
S_l^{az} &= S - a_l^\dagger a_l & S_l^{bz} &= (S - b_l^\dagger b_l) \\
S_l^{a+} &= \sqrt{S/2} (a_l + a_l^\dagger), & S_l^{b+} &= \sqrt{S/2} (b_l^\dagger + b_l), \\
S_l^{a-} &= -i\sqrt{S/2} (a_l - a_l^\dagger), & S_l^{b-} &= \sqrt{S/2} (b_l^\dagger - b_l).
\end{aligned} \tag{1.7}$$

where the operators a_l^\dagger or b_l^\dagger creates a spin deviation on site l of sublattice a or b. The Hamiltonian is first expressed in terms of the spin deviation operators and then the Fourier transform of the Hamiltonian is taken such that the spin-wave variables are:

$$\begin{aligned}
a_{\mathbf{Q}} &= \frac{1}{\sqrt{N}} \sum_l e^{-i\mathbf{Q}\cdot\mathbf{r}_l} a_l & b_{\mathbf{Q}} &= \frac{1}{\sqrt{N}} \sum_l e^{+i\mathbf{Q}\cdot\mathbf{r}_l} b_l \\
a_{\mathbf{Q}}^\dagger &= \frac{1}{\sqrt{N}} \sum_l e^{+i\mathbf{Q}\cdot\mathbf{r}_l} a_l^\dagger, & b_{\mathbf{Q}}^\dagger &= \frac{1}{\sqrt{N}} \sum_l e^{-i\mathbf{Q}\cdot\mathbf{r}_l} b_l^\dagger.
\end{aligned} \tag{1.8}$$

where l runs over the N sites on sublattice a (or b). The linear spin wave calculation considers only bilinear terms in $a_{\mathbf{Q}}$ or $b_{\mathbf{Q}}$ and so the Hamiltonian becomes:

$$\mathcal{H} = \sum_{\mathbf{Q}} X^\dagger H X + E_0 \quad (1.9)$$

where E_0 is the zero point energy and $X^\dagger = (a_{\mathbf{Q}}^\dagger, b_{\mathbf{Q}}^\dagger, a_{\mathbf{Q}}, b_{\mathbf{Q}})$ and the matrix H is written as:

$$H = \frac{1}{2} \begin{pmatrix} 2JS & 0 & 0 & JS\gamma_{\mathbf{Q}} \\ 0 & 2JS & JS\gamma_{\mathbf{Q}} & 0 \\ 0 & JS\gamma_{\mathbf{Q}} & 2JS & 0 \\ JS\gamma_{\mathbf{Q}} & 0 & 0 & 2JS \end{pmatrix} \quad (1.10)$$

where $\gamma_{\mathbf{Q}} = 2(\cos(2\pi h) + \cos(2\pi k) + \cos(2\pi l))$ for a three dimensional antiferromagnet, $\mathbf{Q} = h\mathbf{a}^* + k\mathbf{b}^* + l\mathbf{c}^*$. In order to diagonalize H the Bogoliubov transformations are used to transform $a_{\mathbf{Q}}$ to $\alpha_{\mathbf{Q}}$ and $b_{\mathbf{Q}}$ to $\beta_{\mathbf{Q}}$. The Bogoliubov transformation is such that:

$$\begin{aligned} \alpha_{\mathbf{Q}} &= u_{\mathbf{Q}} a_{\mathbf{Q}} - v_{\mathbf{Q}} b_{\mathbf{Q}}^\dagger & \beta_{\mathbf{Q}} &= u_{\mathbf{Q}} b_{\mathbf{Q}} - v_{\mathbf{Q}} a_{\mathbf{Q}}^\dagger \\ \alpha_{\mathbf{Q}}^\dagger &= u_{\mathbf{Q}} a_{\mathbf{Q}}^\dagger - v_{\mathbf{Q}} b_{\mathbf{Q}} & \beta_{\mathbf{Q}}^\dagger &= u_{\mathbf{Q}} b_{\mathbf{Q}}^\dagger - v_{\mathbf{Q}} a_{\mathbf{Q}} \end{aligned} \quad (1.11)$$

where $u_{\mathbf{Q}}^2 + v_{\mathbf{Q}}^2 = 1$ to preserve the commutation relations. The commutation relations are:

$$[X, X^\dagger] = X(X^*)^T - (X^* X^T)^T = g = \begin{pmatrix} 1 & 0 & 0 & 0 \\ 0 & 1 & 0 & 0 \\ 0 & 0 & -1 & 0 \\ 0 & 0 & 0 & -1 \end{pmatrix}. \quad (1.12)$$

The transformations given in Eqn. 1.11 can be written as

$$X' = S X \quad (1.13)$$

and it was shown by White *et al.*[7] that the transformation matrix can be found by solving

the problem:

$$gHS = \mathcal{S}gH'. \quad (1.14)$$

The elements of the diagonal matrix gH' are the eigenvalues of the matrix gH . The columns of \mathcal{S} are the corresponding eigenvectors given the normalization condition $\mathcal{S}g\mathcal{S}' = g$. Therefore, by diagonalizing H using the Bogoliubov transformations, the dispersion for the antiferromagnet is:

$$\hbar\omega = 2JS\sqrt{1 - \gamma_{\mathbf{Q}}^2}. \quad (1.15)$$

Linear spin-wave theory is successful because it is possible to assume that, for large spin three-dimensional magnets, excitations are small spin deviations from a long-range ordered state. For large spin systems the spin deviation $\Delta S = 1$ is small in comparison to the spin, S , whereas for small spin states the approximation is no longer valid. Although spin-wave theory has been applied to low-dimensional spin systems with fewer than three dimensions, low-energy long-wavelength excitations destroy the magnetic ordering at finite temperature and the spin-wave approach is no longer valid.

1.3 Quantum Magnetism

Studies into quantum magnetism consider systems where the effects of quantum fluctuations must also be considered as well as thermal fluctuations. Low spin, low dimensionality and frustration all enhance quantum fluctuations. In this thesis three materials are studied which have all these attributes. In the following, the concept of the quantum phase transition is introduced. There is a brief outline of some of the novel ground states and excitations predicted to arise in one-dimensional and two-dimensional systems, where frustration is important.

1.3.1 Quantum Phase Transitions

The interest in quantum phase transitions in spin systems comes from a desire to understand the transition between novel quantum phases, such as spin liquids with fractional spin excitations [8]. A classical phase transition is driven by thermal fluctuations, the size of which can be varied by changing the temperature of the system. A quantum phase transition results from quantum fluctuations in an order parameter [8]. The quantum fluctuations are a result of the quantum uncertainty of the ground state. The quantum fluctuations can be increased by slightly varying a control parameter in the Hamiltonian of the system, such as an applied field, pressure, or a doping percentage of a chemical, so that a new ground state becomes preferable. A quantum critical point is the point at which the transition occurs at zero temperature. Although it is not possible to observe a system at $T = 0$, it is possible to reach temperatures where quantum fluctuations and not thermal fluctuations are dominant.

1.3.2 One-Dimensional Magnetism

A simple model in which the quantum phase transition can be understood is the one-dimensional Ising model in a transverse magnetic field. A quasi one-dimensional Ising ferromagnet in such a field arrangement is studied in Chapter 4. The one-dimensional Ising model is referred to as the Ising chain and its Hamiltonian is:

$$\mathcal{H} = J \sum_l S_l^z S_{l+1}^z, \quad (1.16)$$

where J is a negative parameter for a ferromagnetic Ising chain. An Ising chain is one in which the exchange interaction is anisotropic and dominant in one particular spin direction. The Hamiltonian for the one-dimensional Ising system is formed from Eqn. 1.4 taking $J^x = J^y = 0$. In a pure Ising system the ground state at zero temperature is two-fold degenerate and corresponds to the two possible ferromagnetic states of completely co-aligned spins. In a spin-half system an excitation to a spin-flipped state creates two domain walls separating regions of the chain with co-aligned spins as shown in Fig. 1.1 b). To understand

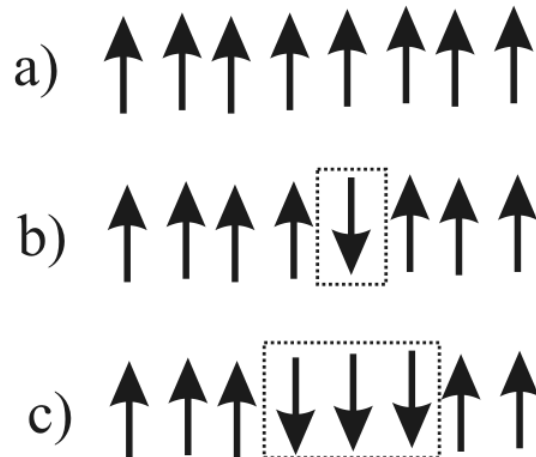


Figure 1.1: The Ising ferromagnetic chain. a) One of the two degenerate Néel ground states. b) a spin flip in the Ising magnet which creates two domain walls. c) The two domain walls separate along the chain creating a larger domain of flipped spins. Because there are two domain walls in both of the states b) and c) they have the same energy as at zero field.

the basic excitation of the system consider a state with many spin flips as in Fig. 1.1 c). In zero field, one region of many flipped spins is degenerate in energy with the single spin-flip state since, because the system is one-dimensional, two bonds are not satisfied in both cases. A sketch of such an excitation is shown in Fig. 1.1 b) and c). Therefore the basic excitations are domain walls which are deconfined spin-half particles and may be considered as a spin-wave decaying into two spin-half domain walls.

If a field is applied perpendicular to the ordering direction the Hamiltonian of the system is:

$$\mathcal{H} = -J \sum_l S_l^z S_{l+1}^z - \Gamma \sum_l S_l^x, \quad (1.17)$$

where J is a positive constant and is the magnitude of the ferromagnetic coupling, and Γ is a field applied transverse to the Ising direction. In a non-zero magnetic field, quantum fluctuations exist because the magnetisation, which is the order-parameter, does not commute with the Hamiltonian $[\mathcal{H}, S^z] \neq 0$ and the classical Néel ground state is no longer an eigenstate. The quantum fluctuations allow tunnelling between the two ferromagnetic states and these fluctuations increase with increasing field. The phase diagram for the Ising

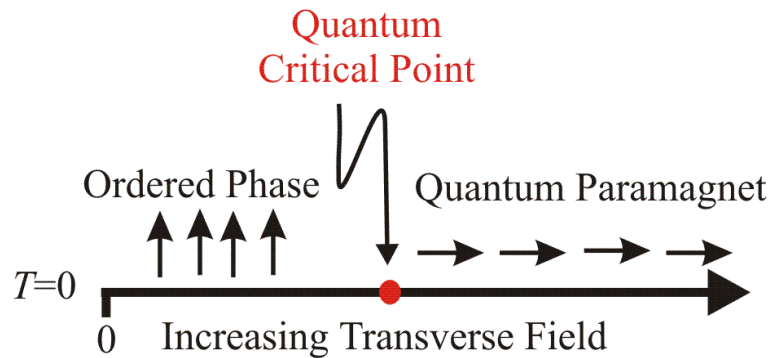


Figure 1.2: Phase diagram of the Ising chain at zero temperature in an increasing field transverse to the Ising direction. A quantum critical point separates the ordered phase and the quantum paramagnetic phase.

chain in a transverse field is given in Fig. 1.2. At zero temperature the Ising chain is ordered and the transverse field tunes an order-to-disorder quantum phase transition. Above a critical field the spontaneous magnetic long-range order is destroyed leading to a quantum paramagnetic state [9]. At zero temperature the critical field is a quantum critical point. At an infinitely large field, $\Gamma = \infty$, the spins are aligned along the field direction and the excitations, which are spin reversals from this direction, are bosonic states called magnons. The excitations below the phase transition, in the ordered phase, are close to domain walls which, in the Ising chain, are produced in pairs at a finite energy.

At a finite temperature thermal fluctuations are also involved in determining the state of the system. At high temperature the system is paramagnetic for all applied fields but there is a region where both the classical fluctuations and quantum fluctuations are relevant and much of the behaviour for the zero temperature regime, discussed above, is present.

Above $T = 0$, one-dimensional systems are not expected to order because of finite temperature long-wavelength thermal fluctuations. The Heisenberg model is a totally isotropic exchange and has continuous symmetry and is quite different to the very anisotropic Ising model which has discrete symmetry. In the case of spin-half Heisenberg chains with antiferromagnetic coupling, no order is expected even at zero temperature. The Néel ground

state for an antiferromagnet is not an eigenstate of the Hamiltonian. The spin-half Hamiltonian can be expanded into raising and lowering operators to demonstrate this:

$$\mathcal{H} = \sum_l J_l \mathbf{S}_l \cdot \mathbf{S}_{l+1} = \sum_l J_l (S_l^z S_{l+1}^z + \frac{1}{2}(S_l^+ S_{l+1}^- + S_l^- S_{l+1}^+)). \quad (1.18)$$

In this equation, J is the coupling constant between the spins, S 's are Pauli spin matrices and the raising and lowering operators are $S_l^+ = \frac{1}{2}(S_l^x + iS_l^y)$ and $S_l^- = \frac{1}{2}(S_l^x - iS_l^y)$. The effect of the operators $S_l^+ S_{l+1}^-$ and $S_l^- S_{l+1}^+$ on the Néel ground state is successively to flip the spins alternately up and down. By applying the Hamiltonian to one of the two classical Néel states the other state is formed and so it is not an eigenstate of the system. Again, the order parameter, which is the sublattice magnetisation, does not commute with the Hamiltonian. The ground state is in fact a spin singlet state and the excitations are again spin-half, which are created and destroyed in pairs, and are generally referred to as spinons. An experimental realization of a spin-half Heisenberg magnet is KCuF_3 in which two spinon scattering has been observed [10, 11]. The dispersion is gapless with a continuum of states across the Brillouin zone [10, 12].

Computational studies into the magnetic properties of the linear spin chains were initially carried out by Bonner and Fisher [13]. These computational results characterized the form of the exchange constants by comparing the numerical result with the data. Therefore they allowed the main exchange interactions within such systems to be approximately deduced.

1.3.3 Frustration

In addition to low-dimensionality, frustration in a material can enhance quantum fluctuations. Frustration is the inability of a system to satisfy all interactions simultaneously. One example of frustration is a square lattice of spin sites with antiferromagnetic diagonal exchanges. A square lattice of spins with nearest-neighbour coupling is not frustrated and the classical Néel states satisfy all the couplings in the system. Frustration is introduced by an

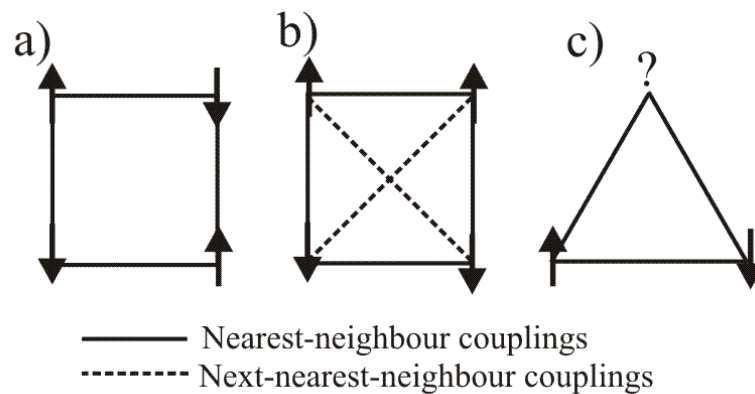


Figure 1.3: The two dimensional lattices considered are the square lattice, a) and b), and the triangular lattice c). The couplings on a square-lattice are frustrated when there is an antiferromagnetic next-nearest-neighbour interaction. The triangular lattice is a frustrated system when the nearest-neighbour interaction is antiferromagnetic.

antiferromagnetic next-nearest-neighbour interaction, as shown in Fig. 1.3. The system is frustrated, independent of the sign of the nearest-neighbour exchange. Geometric frustration is the name given to frustration resulting from the geometry of the lattice. Antiferromagnetic nearest-neighbour interactions on a triangular lattice are geometrically frustrated. Fig. 1.3 c) shows that all three bonds on the triangle cannot be satisfied simultaneously. Within a mean-field approximation a triangular lattice magnet is expected to have similar critical temperature to a simple cubic lattice because they have the same co-ordination number. Yet due to the low dimensionality and frustration they are not similar. The effect of adding frustration to low dimensional systems is often to lower the transition temperature to long-range order. In some cases the frustration removes the transition altogether.

Frustration may also occur in one-dimensional systems but the models considered here are two-dimensional lattices made up of squares of spins with next-nearest-neighbour antiferromagnetic exchange or triangles of spins with nearest-neighbour antiferromagnetic exchange. The physics of frustrated units discussed above is considered when extended to a lattice comprised of many of those units.

1.3.4 Two-Dimensional Magnetism

The Mermin-Wagner theorem [14] predicts no static long-range order at finite temperature in a two-dimensional Heisenberg antiferromagnet with short-range interactions. However, since most real systems have some small inter-layer couplings, long-range order is observed at low temperatures. In the spin-half square lattice model, as shown in Fig. 1.3, the spins sit on a square lattice coupled with nearest-neighbour antiferromagnetic interactions. In this system, quantum fluctuations have also been observed to reduce the ordered magnetic moment to 60% of the maximum value for a spin-half system. One material that has been extensively characterized is deuterated copper formate tetrahydrate, (CFTD) and is modelled as a two-dimensional square lattice of spin-half Cu^{2+} ions. Investigations have shown that renormalization of the exchange constants is necessary to describe the excitation spectrum in the mean-field spin-wave approach [15].

If next nearest-neighbour couplings are introduced into the square lattice the system can become frustrated and quantum fluctuations are increased. The Hamiltonian in such a case is:

$$\mathcal{H} = \sum_{lj} J_1 \mathbf{S}_l \cdot \mathbf{S}_j + \sum_{lk} J_2 \mathbf{S}_l \cdot \mathbf{S}_k,$$

where J_1 refers to the coupling between nearest-neighbour couplings and J_2 refers to next-nearest-neighbour couplings. The phase diagram has been predicted by Shannon *et al.* [16] for various J_1/J_2 ratios at finite temperature and is given in Fig. 1.4. The phase diagram is complex, with various unusual spin phases. When $J_2 > 0.5J_1$ quantum fluctuations are predicted to select a ground state of collinear spins arranged antiferromagnetically (CAF) by the ‘order by disorder’ mechanism and a spin liquid region is predicted close to where the $J_2 = \pm 0.5J_1$ which is marked in grey.

The second frustrated two-dimensional lattice considered here is the archetype of geometrical frustration which is the antiferromagnetic triangular lattice and has a macroscopic ground state degeneracy. The classical ground state of the antiferromagnetic triangular lattice of continuous spins, with a small next-nearest-neighbour coupling, has long-range

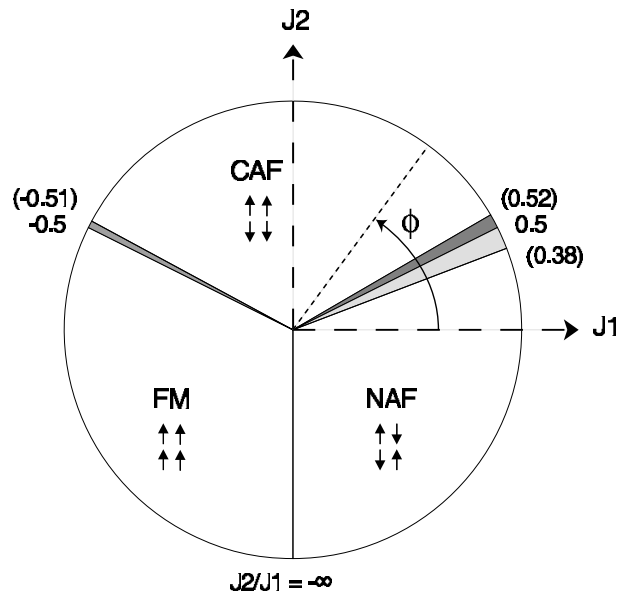


Figure 1.4: Phase diagram of the square-lattice spin-half system with nearest-neighbour(J_1) and next-nearest-neighbour(J_2) interactions. The grey region marks a spin-liquid state. CAF marks the collinear antiferromagnetic ordered state. FM marks a ferromagnetic state and NAF marks the Néel antiferromagnetic state. The angle ϕ indicates the ration of the couplings and $\tan \phi = J_2/J_1$ [16].

order when spins lie at 120° to each other. There are two degenerate states corresponding to the two different senses of rotation. In the 120° structure three sublattices are formed in a Néel type state and the frustration is partially released. Conversely, the antiferromagnetic Ising model on a two-dimensional triangular lattice does not order and has a large entropy at zero temperature [17, 18]. For a spin-half Heisenberg model, the effect of large quantum fluctuations and the geometrical frustration have been predicted to lead to a ‘resonating valance bond’ ground state which is similar to a spin liquid. Fazekas and Anderson[19, 1] proposed this unusual ground state, comprising of singlet spin pairing, which leads to short-range correlations and a continuum of highly dispersive excitations.

LiNiO_2 is proposed as a triangular lattice antiferromagnet and many studies of the material so far have found no long-range magnetic order. Such studies have been hindered by the inability to produce fully-stoichiometric samples because of Li and Ni substitution in the lattice.

1.4 Quantum Magnets Studied in this Thesis

In this thesis, samples are investigated which have magnetic ions that are arranged in well separated layers or chains. Those with dominant exchange interactions along one direction are one-dimensional magnets and those within a plane are two-dimensional magnets. In this work the materials studied are:

AgNiO₂ A system of Ni ions, forming layers in a triangular lattice, coupled with antiferromagnetic interactions. A study of the effects of both orbital and spin frustration in this system has led to a novel mechanism which released orbital frustration and an unusual magnetic structure. Inelastic scattering measurements revealed a band of excitations which could not be captured by linear spin-wave theory and demonstrated the need to consider the effects of quantum fluctuations.

CoNb₂O₆ A system of Co ions that form ferromagnetic Ising chains of effective spin-half sites arranged within a triangular lattice. The magnetic structure in an applied field transverse to the Ising direction was investigated. Inelastic scattering measurements were made in order to investigate the different excitations in the two phases and to look at the change in the energy gap to excitations. These technically very challenging experiments needed precise alignment of the sample and the applied magnetic field direction.

CuSb₂O₆ A system composed of planes of spin-half Cu²⁺ ions in a square lattice arrangement. This material closely resembles the structure of high temperature superconductors and as such is of interest in considering the physics of those systems. Although the system has been described as a one-dimensional antiferromagnetic Heisenberg chain, the interactions on the square lattice system of Cu²⁺ ions are frustrated. Therefore, it is possible it could be described better as a two dimensional system. The magnetic structure was investigated in an applied field parallel to the spin direction and inelastic scattering measurements gave an insight into an unusual excitation pattern.

Chapter 2

Experimental Techniques

2.1 Introduction

Neutron scattering is a technique well suited to the study of correlated electron systems. The de Broglie wavelength of thermal neutrons is comparable to the interatomic length scales of solid crystalline materials, and so thermal neutrons will be diffracted by a crystalline sample. Since the neutron carries a magnetic moment it is also sensitive to the magnetic field distribution in the sample. The energy of thermal neutrons is close to the energy of the excitations discussed in the previous chapter. Therefore neutron scattering will probe both the nuclear and magnetic structure and also the dynamics of a material. It is an established technique in studies of magnetic materials and a primary experimental method in the investigation of low-dimensional magnetic materials.

The properties and neutron-scattering cross-section for both nuclear and magnetic scattering will be briefly summarized next. There is an extensive theoretical literature, examples include books [20], lecture notes [21] and reviews [22]. The various types of neutron scattering techniques and instruments used in the experiments discussed later in this thesis will then be explained.

2.2 The Neutron Scattering Cross-Section

In a neutron scattering experiment incident neutrons, with wave vector \mathbf{k}_i , are scattered at an angle θ with a wave vector \mathbf{k}_f . If energy is transferred to the sample the neutron energy change is:

$$\begin{aligned}\hbar\omega &= E_i - E_f \\ &= \frac{\hbar^2 k_i^2}{2m} - \frac{\hbar^2 k_f^2}{2m} \\ &= \frac{\hbar^2 (k_i^2 - k_f^2)}{2m},\end{aligned}\tag{2.1}$$

where m is the mass of the neutron and $\hbar = h/2\pi$, h is Plank's constant. Momentum is also transferred to the sample and the neutron momentum change is $-\hbar\mathbf{Q}$. The *wave vector transfer*, \mathbf{Q} , illustrated in the the scattering triangle in Fig. 2.1 a), is calculated as

$$\mathbf{Q} = \mathbf{k}_i - \mathbf{k}_f \quad \text{and} \quad Q^2 = k_i^2 + k_f^2 - 2k_i k_f \cos(2\theta).$$

For elastic scattering, since $\hbar\omega = 0$, then $k_i = k_f$ and so Q is dependent on the scattering angle, θ , only. Fig. 2.1 a) shows the elastic scattering triangle for two different \mathbf{Q} vectors but for the same incident wave vector *length* k_i . For inelastic scattering, $\hbar\omega \neq 0$, and so $k_i \neq k_f$ and a range of Q values are achieved over a range of scattering angles.

The neutron is a spin-half particle with a magnetic moment of $\mu_n = -1.04\mu_B$ and it interacts with nuclei via the strong force and with magnetic fields via the electromagnetic interaction. The weak scattering which occurs can be well approximated by the first-order perturbation theory of the Born approximation, which assumes that incident and scattered neutron beams are plane waves. The quantity measured in an experiment is the flux of scattered neutrons within particular ranges of energy and solid angle. This then is the flux of neutrons, σ , with energy in the range $[E_f, E_f + dE_f]$ detected by a detector which subtends the solid angle range $[\Omega, \Omega + d\Omega]$. This quantity is referred to as the 'partial differential cross-section'. For a neutron scattered by a potential V , the partial differential

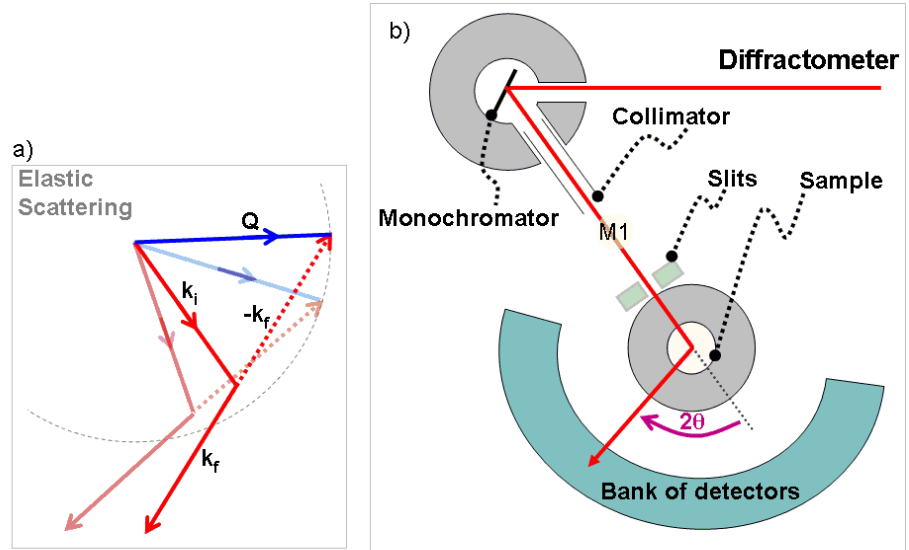


Figure 2.1: a) A diagram of the neutron scattering triangle for elastic scattering showing two configurations where the incident wavelength is constant but the wave vector transfer, Q , differs. b) A sketch of a diffractometer used to measure elastic scattering at a reactor source and described in the text.

cross-section is:

$$\frac{d^2\sigma}{dE_f d\Omega} = \frac{k_f}{k_i} \left(\frac{m}{2\pi\hbar^2} \right)^2 \sum_{\lambda_i, s_i} p_{\lambda_i} p_{s_i} \sum_{\lambda_f, s_f} |\langle \mathbf{k}_f s_f \lambda_f | \hat{V} | \mathbf{k}_i s_i \lambda_i \rangle|^2 \delta(E_{\lambda_i} - E_{\lambda_f} + \hbar\omega) \quad (2.2)$$

where \mathbf{k}_i is the incident wave vector, s_i is the incident neutron spin state, λ_i is the state of the sample before scattering, E_{λ_i} is the energy of state λ_i , p_{λ_i} is the probability of moving to state λ_i , and $\hbar\omega$ is the energy transferred to the sample from the neutron. \hat{V} is the operator corresponding to the scattering potential V . The subscript f indicates the properties of the scattered neutron and final state of the sample. In Chapter 5 polarized neutron diffraction measurements will be presented and the contributions to the intensity for various polarizations will be discussed. However, all the remaining equations in this chapter consider unpolarized neutrons since the majority of the measurements made in this thesis were unpolarized neutron scattering experiments.

Nuclear Scattering

In the case of nuclear scattering, which is the main component of the partial differential cross-section, the scattering potential has a short range and is dependent on the position, \mathbf{r}_l , of the nuclei l . It can be approximated by the Fermi pseudopotential:

$$V(\mathbf{r}) = \frac{2\pi\hbar^2}{m} \sum_l b_l \delta(\mathbf{r} - \mathbf{r}_l), \quad (2.3)$$

where b_l is the scattering length of the atomic nucleus l and it is dependent on the type of nucleus, the isotope and the orientation of the nuclear and neutron spins relative to each other.

The nuclear scattering is comprised of coherent scattering and incoherent scattering:

$$\frac{d^2\sigma}{dE_f d\Omega} = \left(\frac{d^2\sigma}{dE_f d\Omega} \right)_{\text{coherent}} + \left(\frac{d^2\sigma}{dE_f d\Omega} \right)_{\text{incoherent}}.$$

The coherent scattering is a result of coherent interference from the nuclei in the sample whereas the incoherent scattering is due to the variance in scattering lengths and creates an isotropic background. The incoherent cross section is $\sigma_{\text{inc}} = 4\pi(\bar{b}^2 - \bar{b}^2)$.

The partial differential cross-section for nuclear scattering, using Eqns. 2.2 and 2.3, is :

$$\left(\frac{d^2\sigma}{dE_f d\Omega} \right)_{\text{coherent}} = \frac{k_f}{k_i} S(\mathbf{Q}, \omega) \quad (2.4)$$

$$\left(\frac{d^2\sigma}{dE_f d\Omega} \right)_{\text{incoherent}} = \frac{k_f}{k_i} S_{\text{inc}}(\mathbf{Q}, \omega) \quad (2.5)$$

where the *correlation functions*, $S(Q, \omega)$ and $S_{\text{inc}}(Q, \omega)$, are,

$$S(\mathbf{Q}, \omega) = \frac{1}{2\pi\hbar} \sum_{l,l'} b_l b_{l'} \int_{-\infty}^{\infty} \langle \exp(-i\mathbf{Q} \cdot \mathbf{r}_{l'}(0)) \exp(i\mathbf{Q} \cdot \mathbf{r}_l(t)) \rangle \exp(-i\omega t) dt \quad (2.6)$$

$$S_{\text{inc}}(\mathbf{Q}, \omega) = \frac{1}{2\pi\hbar} \sum_l \int_{-\infty}^{\infty} \frac{\sigma_{\text{inc}}}{4\pi} \langle \exp(-i\mathbf{Q} \cdot \mathbf{r}_l(0)) \exp(i\mathbf{Q} \cdot \mathbf{r}_l(t)) \rangle \exp(-i\omega t) dt \quad (2.7)$$

It is now more obvious how the scattering is separated. The coherent nuclear scattering is the interference pattern between positions of the same nucleus at different times and the interference between the positions of different nuclei at different times. The incoherent scattering is the interference of the same nucleus at different times.

In general, the samples studied in this thesis have a large coherent scattering cross-section and therefore information can be gained about the crystalline structure and excitations within the sample. An example of a largely incoherent scatterer is Vanadium, which has a well characterized large isotropic incoherent cross-section and is therefore useful in calibrating the efficiency of detectors at a variety of scattering angles.

The coherent scattering provides information about the sample excitations and sample structure. The major contribution to coherent nuclear scattering from a crystalline sample is the elastic contribution and this is caused by the periodic atomic planes, which produce Bragg peaks in the scattering pattern. Intense peaks in scattering are seen at scattered wave vectors that satisfy the Bragg condition: they are equal to a reciprocal lattice vector and are perpendicular to the crystal planes. The partial differential cross-section under the Bragg condition for coherent nuclear scattering is:

$$\left(\frac{d^2\sigma}{d\hbar\omega d\Omega} \right)_{\substack{\text{Nuclear} \\ \text{coherent} \\ \text{elastic}}} = \left(\frac{(2\pi)^3 N}{V_0} \right) |F_N(\mathbf{Q})|^2 \delta(\mathbf{Q} - \boldsymbol{\tau}) \delta(\hbar\omega). \quad (2.8)$$

Here, the crystal reciprocal lattice vectors are $\boldsymbol{\tau}$ and the nuclear structure factor is,

$$F_N(\mathbf{Q}) = \sum_l b_l \exp(i\mathbf{Q} \cdot \mathbf{r}_l) \exp(-W_l(Q, T)),$$

where the sum is over atoms, l , in the unit cell. The factor $\exp(-W_l(\mathbf{Q}, T))$ is the Debye-Waller factor at a temperature, T for a given \mathbf{Q} . It indicates the probability that an atom is at the position, \mathbf{r}_l , at temperature T as a result of thermal motion.

Magnetic Scattering

Magnetic scattering results from the interaction of the neutron with the electromagnetic field of the unpaired electrons and from the orbital momentum of the unpaired electrons of the ions in the sample. The magnetic dipole moment of the neutron, σ , interacts with this electromagnetic field. As a result, the scattering potential is more complicated than that for nuclear scattering:

$$\hat{V}_m(\mathbf{Q}) = r_0 \sigma \cdot \hat{\mathbf{M}}_{\perp}, \quad (2.9)$$

where

$$\hat{\mathbf{M}}_{\perp} = \tilde{\mathbf{Q}} \times \left(-\frac{1}{2\mu_B} \hat{\mathbf{M}}(\mathbf{Q}) \times \tilde{\mathbf{Q}} \right).$$

$\hat{\mathbf{M}}(\mathbf{Q})$ is the Fourier transform of the magnetic field distribution in the sample and $\tilde{\mathbf{Q}}$ is the unit vector along the direction of the scattering vector \mathbf{Q} , and r_0 is a constant. In Eqn. 2.9 it is evident that the scattering vector, \mathbf{Q} , must be perpendicular to the magnetic field distribution of the sample for magnetic scattering to occur. Substituting the potential defined in Eqn. 2.9 into Eqn. 2.2, the partial differential cross-section for a sample with one type of magnetic ion with quenched orbital angular momentum is:

$$\frac{d^2\sigma}{d\hbar\omega d\Omega} = \frac{k_f}{k_i} \left(\frac{\gamma r_0}{2} \right)^2 (gf(\mathbf{Q}))^2 \exp(-2W(\mathbf{Q}, T)) \sum_{\alpha\beta} \left(\delta_{\alpha\beta} - \tilde{Q}^{\alpha} \tilde{Q}^{\beta} \right) S^{\alpha\beta}(\mathbf{Q}, \omega), \quad (2.10)$$

where $f(\mathbf{Q})$ is the magnetic form factor and γ is the gyromagnetic ratio. It is the Fourier transform of the electromagnetic field distribution of the sample. This distribution imposes an intensity envelope on the observed scattering which usually causes the signal to diminish considerably for large Q . Here the correlation function is,

$$S^{\alpha\beta}(\mathbf{Q}, \omega) = \sum_{l'l''} \exp(-i\mathbf{Q} \cdot (\mathbf{r}_{l'} - \mathbf{r}_{l''})) \int_{-\infty}^{\infty} \langle S_l^{\alpha}(0) S_{l'}^{\beta}(t) \rangle \exp(-i\omega t) dt \quad (2.11)$$

where S_l^{α} is the time-dependent α component of the spin of atom l . $S^{\alpha\beta}(\mathbf{Q}, \omega)$ is the dynamical spin correlation function and is a Fourier transform in both the space, \mathbf{r}_l , and

time, t , of the spin-spin correlation function $\langle S_l^\alpha(0)S_l^\beta(t) \rangle$. Therefore it gives the response of the sample to the magnetic field created by the neutron.

If $M(\mathbf{Q})$ is a periodic function then, just as in the case of nuclear scattering, there will be magnetic Bragg scattering. Within the magnetically ordered phase, peaks in scattering will be seen at scattered wave vectors which are equal to a magnetic reciprocal lattice vector if there is a component perpendicular to the planes of co-aligned spins. The partial differential cross-section for this coherent elastic scattering is:

$$\left(\frac{d^2\sigma}{d\hbar\omega d\Omega} \right)_{\text{Magnetic coherent elastic}} = \left(\frac{(2\pi)^3 N_m}{V_0} \right) \left(\frac{\gamma r_0}{2} \right)^2 \sum_{\alpha\beta} \left(\delta_{\alpha\beta} - \hat{Q}^\alpha \hat{Q}^\beta \right) F_M^\alpha(\mathbf{Q}) F_M^\beta(\mathbf{Q}) \delta(\mathbf{Q} - \tau_M) \delta(\hbar\omega), \quad (2.12)$$

where N_m is the number of magnetic ions and the magnetic structure factor is, $F_M^\alpha(\mathbf{Q}) = f(\mathbf{Q}) \exp(-W(Q, T)) \sum_l \mu_l^\alpha \exp(i\mathbf{Q} \cdot \mathbf{r}_l)$. μ_l^α is the α component of the magnetic moment of atom l in the magnetic unit cell at position \mathbf{r}_l .

The Detailed Balance Factor

The sample can be probed by observing either neutron energy loss or neutron energy gain. In the case of neutron energy gain the temperature becomes an important factor in determining the occupation number of particular energy states. The difference between the probabilities of the neutron gaining or losing energy is accounted for through the detailed balance factor and so the correlation function for neutron energy loss becomes:

$$S(-\mathbf{Q}, -\omega) = \exp(-\hbar\omega/k_B T) S(\mathbf{Q}, \omega), \quad (2.13)$$

where T is the temperature and k_B is the Boltzmann constant. The term, $\exp(-\hbar\omega/k_B T)$, is known as the detailed balance factor. For measurements at very low temperatures the probability of neutron energy gain is greatly reduced and can often be ignored.

2.3 Neutron Scattering Experiments

The aim of the neutron scattering experiments was to measure the partial differential cross-section and to compare it to theoretical models. In this work a variety of neutron scattering experiments used different instruments to measure the elastic and inelastic neutron

cross-section from three different samples. The type of instrument that was used in each experiment depended upon the neutron source. Measurements were made at

- the reactor source at the Institute Laue Langevin
- the reactor source BENSC at the Hahn Meitner Institut
- and the spallation source ISIS at the Rutherford Appleton Laboratory.

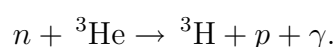
For the inelastic scattering measurements at the reactor sources it was possible to use triple axis-spectrometers effectively whereas at the spallation source the time-of-flight technique had to be used. Each of the main experimental techniques used in this study are briefly described next, beginning with an explanation of the difference between the energy distributions produced by the two types of neutron source.

Neutron Sources

At a reactor source a steady flux of neutrons is produced in a controlled fission process. The neutrons are thermalised to a particular temperature in a moderator and their energy has a Maxwell-Boltzmann distribution. A high intensity beam of monochromatic neutrons is extracted for use in experiments by illuminating a monochromator composed of a large array of single crystals.

A spallation source produces a relatively low flux of neutrons and with an extremely broad range of energy. The energy distribution of a spallation source has a higher intensity of neutrons at higher energies than does the Maxwellian distribution of the reactor source. A pulse of neutrons is produced when a pulse of high energy protons is fired into a heavy metal target. Again a moderator is used to slow neutrons to energies suitable for experiments. A chopper is normally used in the incident beam to gain a beam of constant energy or a range of energies. A chopper is constructed of curved sheets alternately made of neutron absorbing and neutron transparent materials. These slats and slits reject and accept neutrons within a pulse from the source. By varying the phase and frequency that the chopper spins, the desired incident energy is selected as the slats and slits pass through the beam at different times within the pulse.

Thermal neutrons are generally detected with ^3He detectors, through the reaction



The proton is detected because it ionizes the gas. The detectors are set up such that they

have a high efficiency for low-energy neutrons but a low efficiency for high-energy neutrons and γ -rays.

2.3.1 The Neutron Diffractometer

The neutron diffractometer was the most basic instrument used in this work and Fig. 2.1 b) is a sketch of it. The figure shows how a beam of neutrons is incident on the sample and how the neutrons are diffracted into an array of detectors which cover a large solid angle. At a reactor source a monochromatic beam is incident on the sample and the array of detectors counts the neutrons scattered in a particular direction, and generally no energy analysis is made. The figure shows that a monitor, marked M1, is placed in the incident beam. The counts from this monitor enable the observations to be normalised to the incident beam flux.

A diffractometer at a spallation source, such as the General Materials diffractometer (GEM), has a disk chopper which selects a range of wavelengths to be incident on the sample. At a spallation source the neutrons are produced in a pulse at a known time. By measuring the time taken for the neutrons to reach a particular detector in an array the wavelength of the neutron can be determined using the formula:

$$k = \frac{2\pi}{\lambda} = \frac{mL}{\hbar t}, \quad (2.14)$$

where t is the time of flight and L is the length of the flight path. Since the scattering angle for the detector is known the direction of the wave vector transfer is also known. Again, banks of multi-detectors, both within and below the horizontal scattering plane and at fixed distances around the sample collect neutrons over a large solid angle. Such an instrument at a spallation source is generally used for investigations of powder samples or liquids however in this study it was also used to look at a single crystal sample. A crystalline powder sample produces rings of scattering at constant wave vector magnitude, Q , whereas points of scattering at particular Q are seen in the case of single crystal samples. The sample can be placed a large distance from the pulse source to improve the resolution of the instrument. Eqn. 2.14 shows that increasing the time of flight of the neutrons improves the ability to differentiate neutrons of different wavelengths. High scattering angles further increase the resolution. The high resolution of the High Resolution Powder Diffractometer (HRPD) at ISIS is achieved by a long flight path of approximately 100 m and its array of

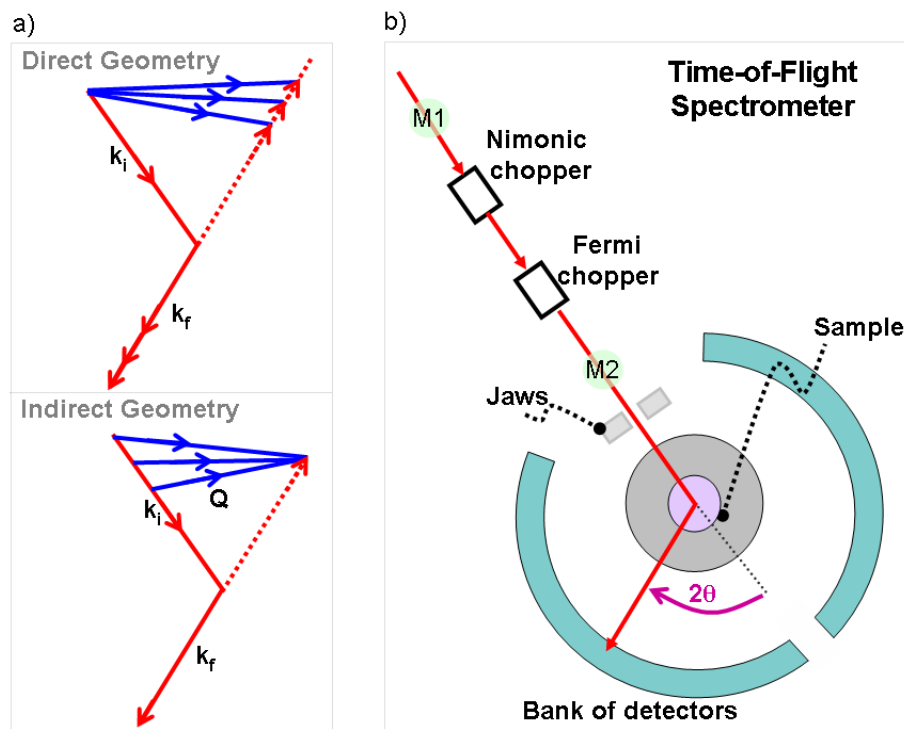


Figure 2.2: a) The two possible setups for a times-of-flight instrument. b) A diagram of a direct time-of-flight chopper spectrometer.

detector banks which are in the backscattering position where $2\theta \sim 180^\circ$. In the work that will be described in chapter 3 the high resolution available at HRPD was necessary to observe a very small crystal distortion. In such backscattering situations the detectors cover large Q values. Unfortunately, for magnetic scattering, it is not so advantageous because the magnetic form factor drops considerably therefore the intensity of magnetic Bragg peaks decreases rapidly with increasing Q .

2.3.2 The Neutron Time-of-Flight Spectrometer

The time-of-flight technique can also be used to measure inelastic scattering cross-sections with a pulsed source of neutrons. There are two possible instrumental setups which are illustrated in the scattering triangles shown in Fig. 2.2 a).

The direct geometry instrument, the incident beam of neutrons has a fixed energy selected by a chopper in the incident beam. The energy difference is measured from the the time-of-flight of the scattered beam.

The **indirect geometry** instrument is the second case where only scattered neutrons with a fixed energy are selected by means of analyzer crystals. The incident energy is calculated from the time of flight of the neutrons and so the energy difference can be calculated.

The scattering angles of the neutrons again gives the wave vector transfer, Q . In this thesis only the direct geometry configuration was used. A schematic diagram of a direct geometry spectrometer is given in Figure 2.2 b). The incident beam energy was selected by means of a combination of choppers. A nimonic chopper reduced background by blocking the beam tube at the time of the proton pulse and thereby reduced the number of fast neutrons scattered from the sample area. A Fermi chopper then selected an incident energy as described above. The ^3He detectors surrounded the lower section of the sample tank and covered a large solid angle of the scattered neutrons. The detector and sample area were normally enclosed and under vacuum to reduce air scattering. In this study, the time-of-flight spectrometer, IN6, was also used. It is placed on the main neutron guide at the ILL reactor source. In such a case a chopper is used to create the pulse of neutrons and a monochromator selects the incident neutron energy beam. The advantage of the time-of-flight instrument is that an overview of the scattering in (Q, ω) is possible in one measurement although it may take some time to collect statistically significant neutron intensity data. The resolution of the instrument is related to the pulse width of the neutrons and to the flight path length and density of detectors.

The program ‘Homer’ [23] was used to convert the intensity to $S(Q, \omega)$ for the experiments made on HET and MARI at ISIS. This is a standard program which calculates the energy transfer and wave vector transfer of the scattered neutrons and, by using the sample mass and a standard vanadium measurement, converts the data into absolute units of mbarns/meV/sr/atom. A monitor on the IN6 spectrometer was used to take into account the $1/k_f$ factor in the intensity and a vanadium measurement was made to convert the data into absolute units.

2.3.3 The Neutron Triple-Axis Spectrometer

Fig. 2.3 is a diagram of a triple-axis spectrometer used at a reactor source for inelastic scattering experiments. The incident neutron energy is chosen by use of a monochromator composed of an array of single crystals. The initial energy and corresponding wave vector are selected by a Bragg reflection. The final energy of the neutrons is also selected in the

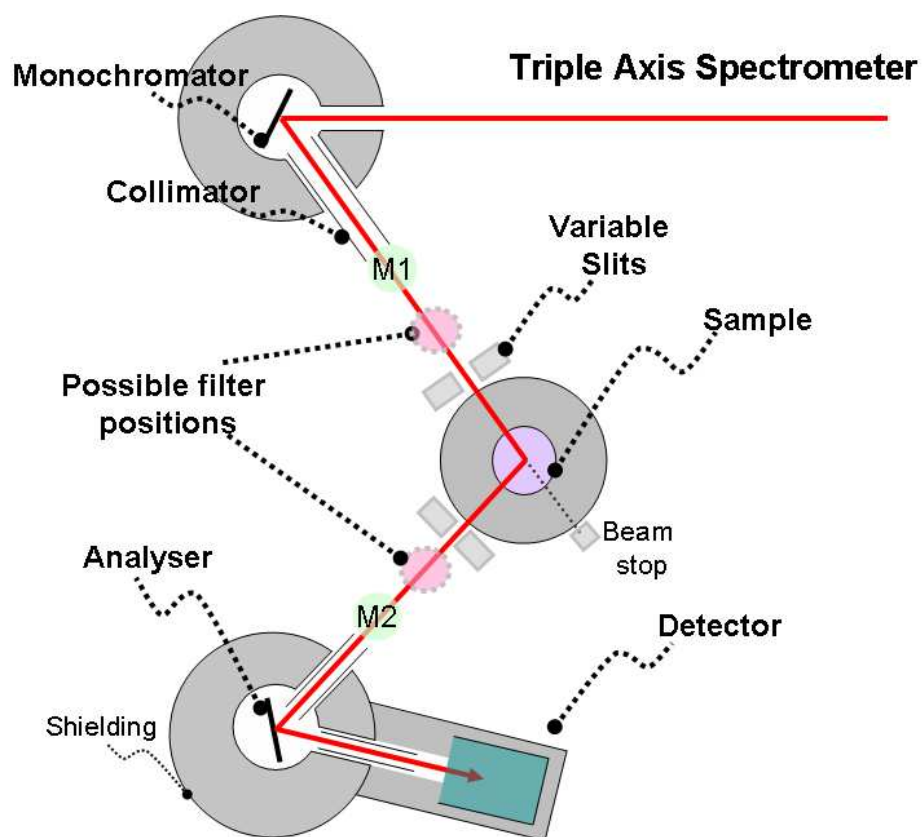


Figure 2.3: A diagram of a triple-axis spectrometer. The monochromator rotates and the analyser and sample tables move to achieve a desired energy transfer and wave vector transfer in a given measurement.

same way by use of an array of single crystals. The intensity of the scattered neutrons at the resulting energy and wave vector transfer can then be measured. Thus the instrument is extremely flexible. However, since only a single detector is used, a data set may take some time to collect. In general, the final energy of the neutrons is fixed by the analyser and scans are made by varying either the wave vector transfer (constant energy scans) or the energy (constant wave vector scans).

The resolution of the measurement is dependent on the angular divergence of the neutron beam and the mosaic spread of the monochromator and analyser crystals. Collimators can be used to reduce the angular divergence of the beam and the monochromator and the analyser curvature can be set to an optimum balancing intensity and resolution.

When making inelastic scattering measurements there is the danger of measuring second-order reflections from the monochromator and/or the analyser. To avoid this, two types of filters are commonly used: a nitrogen-cooled beryllium-filter and a pyrolytic graphite filter (PG). The cooled Be-filter acts to avoid transmission of neutrons above ~ 5.2 meV and the PG filter can be used with optimally chosen wavelengths where, for example, the transmission curve has a peak at one wavelength λ , such as $\lambda = 2.360$ Å, but troughs at 2λ and 3λ . In this case, when a PG filter is placed in the scattered beam and the fixed final wavelength is $\lambda = 2.360$ Å higher order neutrons are not scattered into the detector because they are filtered before the analyser.

Measurements are usually performed with a constant final energy E_f . A monitor, labelled M1 in Fig. 2.3, is placed in the incident beam with a characteristic efficiency proportional to the reciprocal of the incident wave vector. Hence an advantage of measurements made with a constant E_f is that when the intensity is normalized to the counts in monitor M1 it is simply proportional to the correlation function. Another advantage of this configuration is that a greater neutron energy loss range is available and this is generally necessary for low temperature measurements.

2.4 Susceptibility and Heat Capacity

Measurements of bulk properties, such as the magnetic susceptibility and heat capacity of a sample, can be useful in characterizing the presence of any phase transitions and may indicate the main exchange interactions. In this work, susceptibility and heat capacity measurements have been carried out to complement the neutron-scattering measurements. The two instruments used for these measurements are briefly described next.

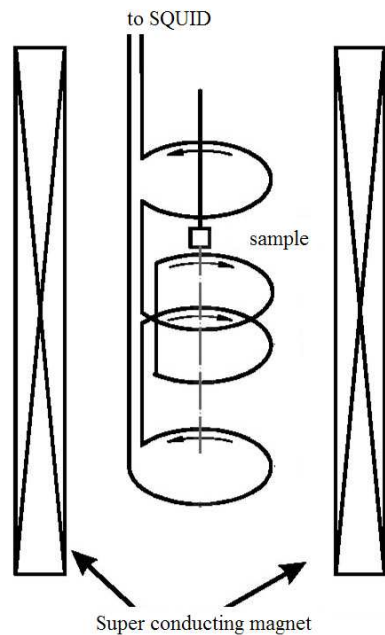


Figure 2.4: A diagram of the pick-up coil geometry used in an MPMS SQUID used to measure the susceptibility.

Susceptibility

Susceptibility measurements were made using a Superconducting Quantum Interference Device (SQUID) magnetometer. The sample was placed in a cryostat with a temperature variation from 2 K to 300 K. The superconducting magnet provided a magnetic field of up to 7 T.

A sketch of the main components of the instrument is given in Fig. 2.4. A small field was applied to the sample during measurements. The measurements in this study were taken using the Reciprocating Sample Option (RSO) technique by which the sample was oscillated about two superconducting detection coils. The current induced by the magnetization of the sample was proportional to the voltage output of the coils. The magnetization of the sample was given by the amplitude of the output voltage curve as a function of sample position.

Heat Capacity

The sample was mounted to the puck, which was a small microcalorimeter platform, using a standard cryogenic grease. The sample platform was suspended by eight thin wires that are the electrical leads for the heater and thermometer. The sample area was kept under a

high vacuum such that heat was not lost via exchange gas.

Measurements were made by stabilizing the sample at an initial temperature and then applying a fixed amount of heat to the sample for a set time interval. The sample temperature was monitored when the heat was removed as it decayed to the initial temperature. The heat capacity was obtained by modelling the decay time of the sample and puck [24].

Chapter 3

Investigation of the Frustrated Triangular Antiferromagnet AgNiO_2

This chapter describes neutron and X-ray diffraction measurements done to observe the crystal structure and magnetic order of AgNiO_2 over range of temperatures. Also, described are low-temperature inelastic neutron scattering measurements of the powder-averaged excitation spectrum. AgNiO_2 has been proposed to have a high symmetry structure in which Ni^{3+} ions have an unquenched e_g orbital moment and are in a spin-half state. The Ni^{3+} ions form an antiferromagnetic triangular lattice and so both the spin and orbital order are frustrated. Therefore it was of interest to investigate its magnetic and crystal structure. A high-temperature distortion of the crystal structure, which created inequivalent NiO_6 octahedra, was observed and suggested charge disproportionation within the Ni lattice. Magnetic order, observed below 20 K, could be described by the electron-rich $S = 1$ sites ordering into ferromagnetic rows of spins ordered antiferromagnetically. In the magnetically ordered phase, a band of excitations, extending to approximately 7.5 meV, was observed above an energy gap of about 1.8 meV. The shape of the lower boundary of the scattering suggested a small inter-layer dispersion, indicating strong two-dimensionality. A large antiferromagnetic in-plane dispersion explained the full bandwidth. However, a linear spin-wave model could not explain all the features of the dispersion and quantum fluctuations, beyond linear order, may have accounted for the dispersion renormalization.

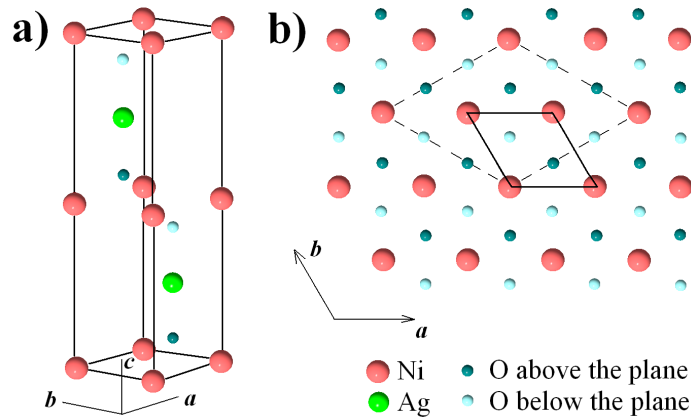


Figure 3.1: The idea crystal structure of 2H-AgNiO₂ deduced from X-ray measurements in [27] (space group $P6_3/mmc-D_{6h}^4$). a) There are two NiO₂ layers per unit cell related by a mirror plane reflection through the Ag⁺ layer at $z = 1/4$. b) A diagram of the basal plane showing the triangular network of Ni ions (large red balls) coordinated by oxygens (small blue balls). The thick solid line contour shows the unit cell and dashed line shows the unit cell tripling in the distorted structure.

3.1 Introduction

Spin and orbitally frustrated systems are predicted to stabilize a variety of unconventional ordered phases, [25] or orbital-liquid states [26]. This chapter describes investigations into such a system: AgNiO₂ is a two-dimensional low-spin triangular lattice antiferromagnet. The frustration generated by the triangular geometry of its lattice is relevant to both the spin and orbital order of the system. The two-dimensionality and frustration are all factors which increase the effect of quantum fluctuations.

Many delafossites, as in the case of AgNiO₂, occur in two structural polytypes which differ in the stacking pattern of the the NiO₂ layers along the c -axis. The transition metal ion, Ni, sits at the vertices of a triangular lattice in the basal plane, made up of a network of edge-shared NiO₆ octahedra. Work by Sörgel and Jansen [27, 28] investigated the two polytypes of AgNiO₂ which exist. The 3R polytype has a three-stage structure, where successive layers have the same orientation but have an in-plane offset with the nickel ions forming a three-stage staircase along the c -axis. This 3R polytype has a rhombohedral space group $R\bar{3}m$, [29, 30]. There is also the 2H polytype, which has a two-stage structure, where successive layers are stacked on top of each other but are rotated by 180°. The 2H polytype has the hexagonal space group, $P6_3/mmc$, [27] shown in Fig. 3.1. In both cases, the 3R and 2H polytypes, Ni ions spin and an orbital moments are frustrated.

AgNiO₂ is part of a group of materials of the form XNiO₂ which display spin and an orbital frustration if their nominal crystal structure is considered. One such material, LiNiO₂, has shown no long-range magnetic order but experiments have been hindered by the difficulty of attaining stoichiometric samples [31]. In contrast, with NaNiO₂ the degeneracy of the e_g orbital is lifted via a Jahn-Teller distortion which splits the e_g band and opens an energy gap that removes the orbital degeneracy [32, 33, 34, 35]. From elastic and inelastic neutron scattering measurements, NaNiO₂ is found to be a spin-half system with in-plane ferromagnetic interactions and weak antiferromagnetic inter-plane coupling.

The 2H-AgNiO₂ polytype is of particular interest and its properties were investigated in the present study. It had been recently synthesized using high-oxygen pressure techniques [27]. Susceptibility measurements on 2H-AgNiO₂ have indicated dominant antiferromagnetic order near 20 K [27]. Therefore the system is different to NaNiO₂ and the magnetism is potentially frustrated through the magnetic order. However, this had not yet been characterized before the current study. Metallic-like conductivity has been observed in this polytype from 300 K down to low temperatures. The high-temperature resistivity measurements have shown an anomaly at 365 K [28]. Finally, zero-field muon-spin relaxation measurements have observed six distinct muon precession frequencies within the magnetically ordered phase [36].

3.2 Structural and Magnetic Properties of AgNiO₂

In this section powder diffraction experiments are described which investigated the structural and magnetic properties of the 2H polytype of AgNiO₂. AgNiO₂ had been initially studied by Shin et al. [30] and has been furthered investigated by Sörgel and Jansen [27, 28]. Susceptibility measurements have been fitted to give an effective moment which is consistent with the Ni ions being in the low-spin configuration where the Ni³⁺ have a spin-half. The seven outer 3d electrons are then in the configuration $t_{2g}^6 e_g^1$. The high spin configuration would have been expected to give larger effective moment since $S=3/2$. Their susceptibility measurements have also suggested dominant antiferromagnetic interactions which are frustrated on a triangular lattice. They have proposed a high-symmetry crystal structure, deduced from X-ray measurements, which would leave an unquenched e_g orbital moment per Ni site. Therefore there is a tendency for each of the NiO₆ octahedra to distort locally and to change the Ni environment, lowering the orbital energy by the Jahn-Teller effect. Yet on a triangular lattice the cooperative order is frustrated because neighbouring Ni sites

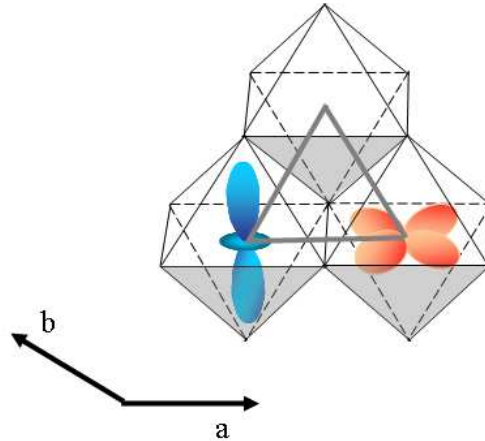


Figure 3.2: Sketch to show that the co-operative orbital ordering of the e_g orbital moment is frustrated on a triangular lattice since the neighbouring sites on a triangle cannot all be in different orbital states.

on a triangle cannot all be in different orbital states. Fig. 3.2 shows this. Such a situation of spin and orbital frustration has been predicted to result in non-trivial forms of orbital order or orbital liquid states, depending on the details of the interactions [25, 26]. Alternatively, the lattice may distort in a different way to lift the orbital degeneracy.

The related materials which have potential to show spin-orbital frustration are: NaTiO_2 , which undergoes a structural transition at low temperatures [37]; NaNiO_2 , which is a ferromagnetic and undergoes a distortion to ferro-orbital order [32, 33, 34, 35]; and LiNiO_2 , in which no long-range magnetic or orbital order has been observed [31].

The results of the diffraction measurements described in this section showed evidence for a weak structural modulation in 2H-AgNiO_2 which led to a tripling of the unit cell in the basal plane. It will be proposed that this structural modulation results in charge disproportionation on the Ni sites which occurs in order to avoid the strong orbital frustration of the undistorted structure. Magnetic ordering was observed at low temperatures and it will be proposed that this is due to ordering of the charge-depleted Ni sublattice into a collinear structure with spins aligned along the c -axis.

3.2.1 Experimental Details

Diffraction measurements were made on powder samples of the 2-stage AgNiO_2 which had less than one percent admixture of the 3-stage polytype. The sample was prepared from Ag_2O and Ni(OH)_2 using high oxygen pressures (130 MPa). The method has been

described elsewhere [27].

The crystal structure was probed by neutron powder diffraction measurements that used the high resolution time-of-flight diffractometers OSIRIS ($0.65 < Q < 6 \text{ \AA}^{-1}$) and HRPD ($2 < Q < 9 \text{ \AA}^{-1}$) at the ISIS Facility and the monochromatic D2B diffractometer at the Institute Laue-Langevin (ILL). Preliminary measurements were also made using the general materials diffractometer, GEM, at ISIS. In addition, X-ray powder diffraction measurements to investigate the crystal structure at room temperature were made using the Philips X'pert diffractometer at Bristol and Oxford University using the $\text{CuK}\alpha$ line, ($\lambda_{\text{CuK}\alpha} = 1.54 \text{ \AA}$).

The magnetic order was investigated by low-temperature neutron powder diffraction measurements with the high-resolution time-of-flight diffractometer OSIRIS ($0.65 < Q < 6 \text{ \AA}^{-1}$). Preliminary measurements were also made using the monochromatic neutron diffractometer D1B at the ILL using a wavelength, $\lambda = 2.52 \text{ \AA}$. The magnetic order parameter was obtained from elastic neutron scattering measurements using the direct-geometry time-of-flight spectrometer IN6 at the ILL, for which the details are given in the following section. Susceptibility measurements were made using a SQUID magnetometer (Quantum Design MPMS) and specific heat data were collected on a pressed powder pellet using a Quantum Design PPMS system.

3.2.2 Measurements and Results

Room-Temperature and High-Temperature Diffraction Measurements

The pattern observed in initial room-temperature measurements of the neutron powder diffraction of AgNiO_2 was in reasonable agreement with that reported previously by Sörgel *et al.* [27]. That work proposed that the room-temperature crystal structure of AgNiO_2 was within the hexagonal space group $\text{P6}_3/\text{mmc}$. The program FullProf [38] was used to analyse the data using a Rietveld refinement method. High resolution measurements revealed a series of additional low-intensity peaks which had approximately 1% the intensity of the of the main Bragg reflections. The powder diffraction pattern measured at 300 K is shown in Fig. 3.3, plot a, and a selection of the small additional peaks is shown in Fig. 3.4. The additional reflections could be indexed within the $\text{P6}_3/\text{mmc}$ space group with the *fractional* wave vectors of the type $(2/3, -1/3, 0)$ and $(2/3, -1/3, 1)$. These additional peaks were observed over the whole Q range that was measured. They were supercell peaks which moved in Q as the temperature was reduced because of the lattice contraction – as shown

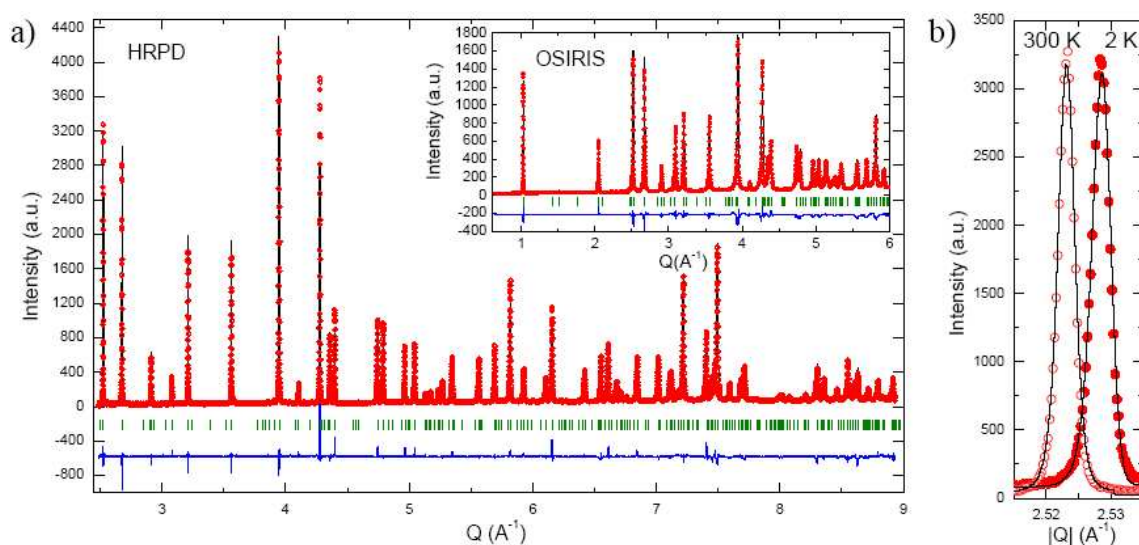


Figure 3.3: a) Room temperature (300 K) neutron diffraction pattern obtained using HRPD (resolution $\Delta Q/Q \sim 10^{-3}$, 15 hours counting on an 11 g powder sample). The solid curve through the data points was fitted to the distorted $P6_322$ space group. The vertical bars indicate calculated Bragg peak positions. The the bottom trace shows the difference between the fit and the data. The inset shows complementary OSIRIS measurements which extend the lower- Q coverage (resolution $\Delta Q/Q = 5 \times 10^{-3}$ at 3 \AA^{-1}). b) The (1, 1, 1) Bragg reflection, which would be expected to split in the case of a structural distortion to an orthorhombic or monoclinic structure, show no splitting. The lineshape at both 300 K (open circles) and 2 K (filled circles) could be well described by a resolution-convolved profile for the hexagonal $P6_322$ space group (solid lines) with lattice parameters adjusted for thermal contraction upon cooling.

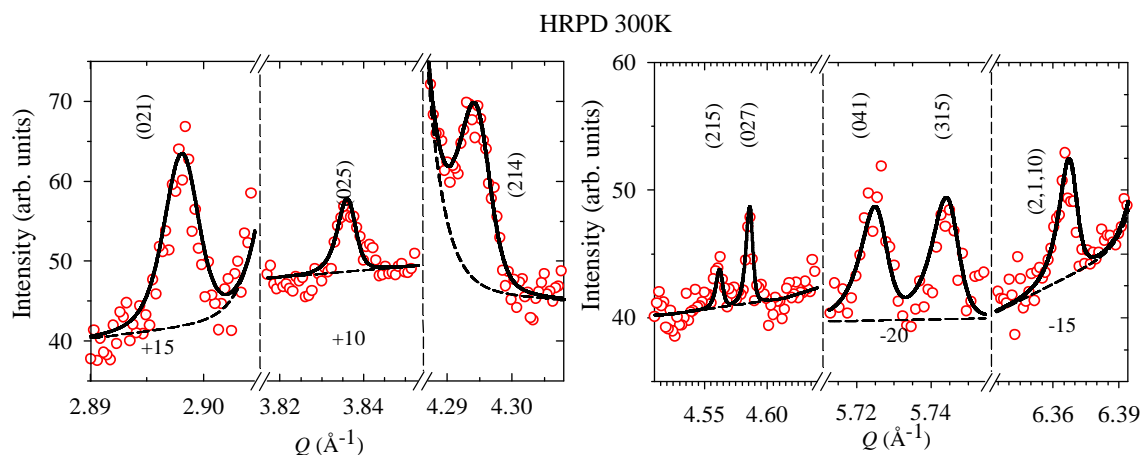


Figure 3.4: Regions of the 300 K neutron diffraction pattern showing a number of the weak supercell reflections disallowed in the ideal $P6_3/mmc$ structure and associated with tripling the unit cell in the ab plane. Solid lines are the calculated profile for the distorted $P6_322$ structure in Fig. 3.11 and dashed lines show the estimated local background including the resolution tails of nearby main structural peaks (data in some subpanels is shifted vertically by indicated amounts for clarity).

in the central panels of Fig 3.5. The wave vectors of the supercell peaks implied a structural modulation which was equivalent to tripling of the unit cell in the basal plane.

Fitting was attempted of the additional peaks to all the available structures of the form Ni_xO_y in the Inorganic Crystal Structure Database [39] in order to eliminate the possibility that the additional peaks were due to an impurity phase. Other structures of compounds of the type A_xB_y , $A_xB_yC_z$ (where $A, B, C = Ni, Ag, O$) were also considered. All were discounted as inconsistent with the measured data. Some small peaks were identified with the 3R polytype structure and these were estimated to be due to a small admixture of 1% by volume. The few weak peaks that were not indexed by any obvious commensurate fractional index of the main peaks were attributed to unidentified impurity phases below 1% of the sample volume and these would have been made during the chemical synthesis.

X-ray measurements were made in order to complement the neutron scattering measurements and to make use of the difference in scattering cross-section of X-rays and neutrons. The X-ray measurements are presented in Fig. 3.5. They did not show any statistically significant intensity at the supercell peak positions observed in the neutron diffraction measurements. Because lighter atoms have a smaller X-ray scattering cross-section, the lack of intensity in the X-ray pattern implied that the structural modulation would have involved displacements of the light oxygen ions predominantly and not of the heavier Ag or

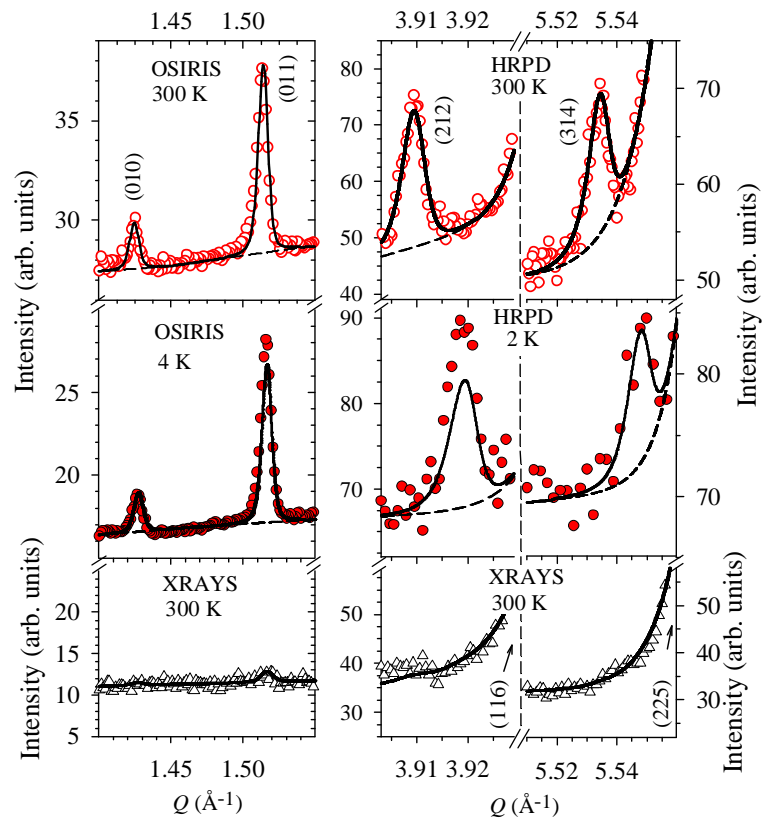


Figure 3.5: Comparison of the supercell diffraction pattern at 300 K to lower temperatures and to room temperature X-ray measurements. The comparison of the neutron diffraction data show that the peaks were displaced in Q following the lattice contraction upon cooling. The low temperature data has a higher overall background because it was collected in a cryostat. The supercell peaks were not observed in the X-ray data shown in bottom panels and is consistent with a structural modulation involving mainly displacements of the light oxygen ions.

Table 3.1: Lattice parameters and atomic positions in the unit cell in the ideal ($P6_3/mmc$) and the distorted ($P6_322$) structural space groups at 300 K. Oxygen positions are parameterized by an out-of-plane height $z_O = 0.08050(5)$ and an in-plane displacement $\epsilon = 0.0133(2)$. The distorted unit cell is tripled in the hexagonal plane with an unchanged extent along the c -axis, but the origin is shifted by $c/4$ such that the two NiO_2 layers appear now at $z = 1/4$ and $3/4$. The symbols a_0 and $a = \sqrt{3}a_0$, are used to denote the hexagonal lattice parameter of the high symmetry and distorted structures, respectively.

$P6_3/mmc$ (no. 194)			$P6_322$ (no. 182)		
$a_0 = 2.93919(5) \text{ \AA}$			$a = 5.0908(1) \text{ \AA}$		
$c = 12.2498(1) \text{ \AA}$			$c = 12.2498(1) \text{ \AA}$		
Atom	Site	(x, y, z)	Atom	Site	(x, y, z)
Ni	$2a$	$(0, 0, 0)$	Ni1	$2c$	$(\frac{1}{3}, \frac{2}{3}, \frac{1}{4})$
Ag	$2c$	$(\frac{2}{3}, \frac{1}{3}, \frac{1}{4})$	Ni2	$2b$	$(0, 0, \frac{1}{4})$
O	$4f$	$(\frac{2}{3}, \frac{1}{3}, z_O)$	Ni3	$2d$	$(\frac{1}{3}, \frac{2}{3}, \frac{3}{4})$
			Ag	$6g$	$(\frac{2}{3}, 0, 0)$
			O	$12i$	$(\frac{1}{3}, \epsilon, \frac{1}{4} + z_O)$

Ni ions. Therefore, the data was fitted to a model where only the oxygen positions varied from the structure of $2H\text{-AgNiO}_2$ published in [27].

The appropriate space group to describe the structural modulation was found by considering, in order of decreasing symmetry, those subgroups within the ideal structure space group, $P6_3/mmc$, which allowed for a tripling of the unit cell. Therefore the distorted structure had a unit cell of $\sqrt{3}a_0 \times \sqrt{3}a_0 \times c$, where a_0 is the high symmetry space group lattice constant within the basal plane. Space groups which were not compatible with the magnetic ordering observed in the low temperature diffraction measurements were also discounted. To accommodate the magnetic structure, the crystallographic Ni sites of the magnetically ordered and the magnetically unordered Ni ions were distinctly different. The best fit was achieved using the space group $P6_322$. The best-fit parameter was $R_F = 6.49\%^1$. The details of the fit are given in Table 3.1. Within this space group the twelve oxygen atoms are within one crystallographic site and so they are related by the symmetry elements of the group. The structural modulation can be described by a small displacement, ϵ , of the oxygen atoms from the ideal structure. It was found that adjacent layers had opposite displacements.

¹

$$R_F = 100 \frac{\sum_n [|G_{obs,n} - G_{calc,n}|]}{\sum_n G_{obs,n}}$$

where G is the structure factor and n runs over all observables.

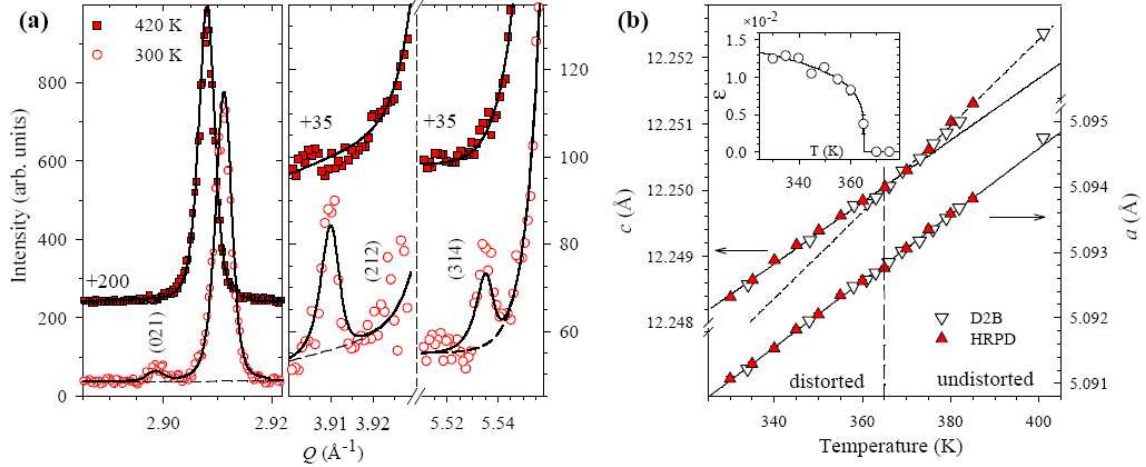


Figure 3.6: Plot a) A comparison between the 300 K (open symbols, lower trace) and 420 K data (filled symbols, upper trace) showing the absence of the triple-cell peaks (021), (212) and (314) at high temperature. Solid lines are fits to the distorted structure for the 300 K data and ideal structure for the 420 K data. The dashed lines show the estimated background level. The high-temperature data was shifted vertically by the indicated offsets for clarity. Plot b) The temperature dependence of the lattice parameters: c left axis, a right axis. Solid (dashed) lines for the c parameter are straight line fits to the data below (above) $T_S = 365$ K. The inset shows the temperature-dependence of the oxygen displacement parameter ϵ and the solid line is a guide to the eye.

A further test of the origin of the additional peaks was made by refinement of the lattice parameters and by fitting separately the main peaks or only the supercell peaks. The results gave similar lattice constants for both: $a = 5.09082(1)$ \AA and $c = 12.24984(4)$ \AA for the main peaks compared with $a = 5.0908(2)$ \AA and $c = 12.250(2)$ \AA for the supercell peaks. This was further evidence that supercell peaks were not due to an extra phase.

Measurements of the neutron diffraction pattern were made at temperatures down to 2 K. The main structural peaks observed at the base temperature of 2 K showed no splitting and were described by the same structure as that fitted to the 300 K data but with reduced lattice parameters of $a = \sqrt{3} \times 2.93360(1)$ \AA and $c = 12.24670(7)$ \AA . This was a reasonable fit with fit parameter value $R_F = 5.53\%$. Therefore the main Bragg peaks indicated that the lattice contracted at low temperature, as expected, and that no further structural transitions occurred upon cooling.

Measurements were also made at increasing temperatures above 300 K as shown in Fig. 3.6, plot a). As the temperature of the sample was increased the intensity of the supercell peaks decreased. Above $T_s = 365(3)$ K supercell peaks were not observed. The

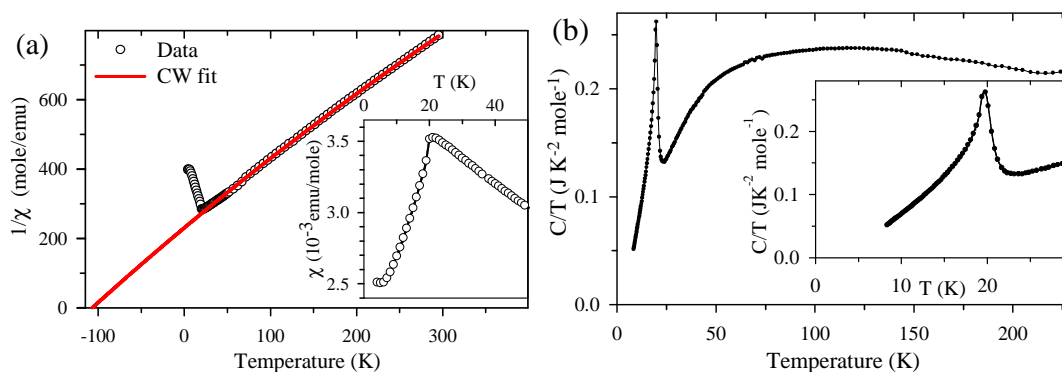


Figure 3.7: a) Inverse magnetic susceptibility ($1/\chi$) fitted to a Curie-Weiss law Eqn.3.1 (solid line) gives a large negative intercept indicating dominant antiferromagnetic interactions. The inset shows the suppression of the susceptibility below 20 K which was attributed to onset of antiferromagnetic order. b) Temperature dependence of the specific heat showing a sharp lambda-like peak near the magnetic transition temperature.

data was fitted to the distorted model found from the room temperature measurements but allowing the oxygen and lattice parameters to vary. The results are summarized in Fig. 3.6 b). The temperature dependence of the displacement of the oxygen atoms from the ideal structure, ϵ , showed a sharp decrease close to the temperature T_s . The lattice parameters increased smoothly as the temperature was increased. There was a small change in the c -lattice parameter which also occurred at T_s . The diffraction pattern at 420 K was fitted to the undistorted structure, $P6_3/mmc$ space group, with the lattice parameters $a = 2.94267(3) \text{ \AA}$, $c = 12.2554(2) \text{ \AA}$ and oxygen position $z_0 = 0.07991(6)$. The goodness-of-fit parameter was $R_f = 7.13\%$.

Susceptibility, Magnetisation and Specific Heat

Magnetic susceptibility measurements on a 66 mg powder sample were made using a SQUID magnetometer (Quantum Design MPMS). The results are shown, as the inverse susceptibility, in Fig. 3.7 a). There is a peak in the susceptibility at low temperatures near 20 K as shown in the inset. This peak is an indication of the onset of magnetic ordering. At higher temperatures the data can be well described by a Curie-Weiss functional form plus a small temperature-independent part, χ_0 , which may be from the sample holder straw and the packaging material around the sample. The high-temperature susceptibility above 70 K

was fitted to:

$$\chi = \frac{C}{T - \theta_{CW}} + \chi_0 \quad (3.1)$$

where $C = 0.445(5)$ emu K/mole, $\theta_{CW} = -107(2)$ K, and $\chi_0 = 1.7(1) \times 10^{-4}$ emu/mole. The negative Curie-Weiss temperature indicated dominant antiferromagnetic interactions. The Curie-Weiss constant was used to extract an effective magnetic moment $\mu_{eff} = 1.88 \mu_B$ per Ni ion. This value is in accordance with measurements by Sörgel and Jansen [27] who suggested that this implied that all the Ni sites were in the low-spin Ni^{3+} state ($t_{2g}^6 e_g^1$) with $S = 1/2$. For a spin-half system with g-factor, $g = 2$, the effective moment is $\mu_{eff} = 1.73 \mu_B$. However, when considering the charge disproportionation model, as suggested by the structural measurements, then the three Ni sublattices of Ni^{2+} and two $\text{Ni}^{3.5+}$ sites have spin states of $S = 1$ and $S = 0$ respectively. The $\text{Ni}^{3.5+}$ is close to the t_{2g}^6 which would have $S = 0$. Therefore the average effective moment would be $\mu_{eff} = 1.63 \mu_B$, for $g = 2$, which is also consistent with the measurements. It may be improved further with a better understanding of the level of charge disproportionation in this particular case.

The saturation field can be estimated by extrapolating magnetisation measurements made up to 7 T at 2 K. The magnetisation data formed a straight line with a gradient of $1.884 \times 10^{-2} \mu_B/T$ per Ni1 site ($6.28 \times 10^{-3} \mu_B/T$ per Ni site) which therefore gave a lower limit to the saturation field as $B_{sat} \sim 212$ T of a $S=1$, which can only be reached by pulsed fields. Assuming a Heisenberg model of spin S sites on a triangular lattice then $B_{sat} = \frac{9JS}{g\mu_B}$, and the average exchange constant, $J \approx 2.7$ meV for the nearest neighbour exchange assuming $g = 2$ and ordering on the Ni1 sites only.

Specific heat measurements were made on a pressed powder pellet of 0.023 g using a Quantum Design PPMS system. The results are shown in plot b of Fig. 3.7. A sharp lambda-like peak, identified with the magnetic transition, was observed near 20 K and this is similar to the temperature of the anomaly observed in the susceptibility data. No other anomalies were observed up to the highest temperature of 240 K, suggesting that no additional transitions occur within this temperature range.

Low-Temperature Neutron Diffraction Measurements

Low-temperature neutron diffraction measurements were made on the powder sample to investigate further the transition observed at low temperature in the susceptibility and heat capacity measurements. On cooling, additional reflections were observed below 20 K which coincided with the peak in the susceptibility. The data in Fig. 3.8 show a subtraction of

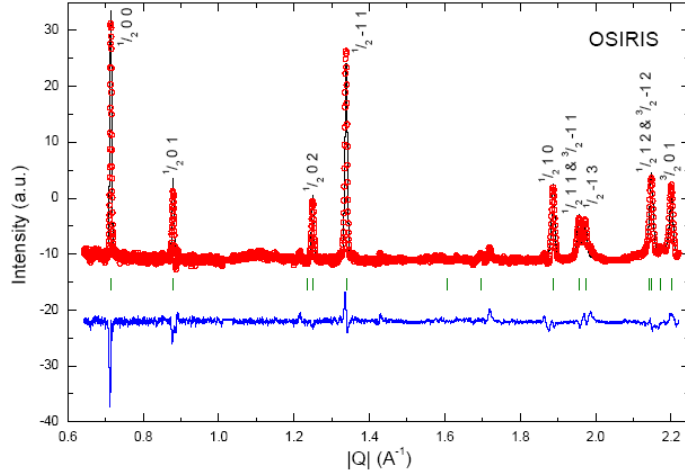


Figure 3.8: The difference pattern of 4 K – 300 K taken using OSIRIS. It shows the peaks of magnetic origin. They can be indexed by the propagation vector $\mathbf{k}=(1/2,0,0)$. The circles represent the observed intensities, the solid curve is a fit to the magnetic structure given in the text and vertical bars indicate the magnetic Bragg peak positions. The bottom curve shows the difference between the fit and the data.

Table 3.2: Irreducible representations for the six Ni ions in the unit cell, which form three independent sublattices, for a magnetic structure with propagation vector $\mathbf{k}=(1/2, 0, 0)$ for the $P6_322$ space group obtained using group theory package[40]. u, v, u', v', u'' and v'' are independent spin components.

site	Ni1 (2c)		Ni2 (2b)		Ni3 (2d)	
position	$(\frac{1}{3}, \frac{2}{3}, \frac{1}{4})$	$(\frac{2}{3}, \frac{1}{3}, \frac{3}{4})$	$(0, 0, \frac{1}{4})$	$(0, 0, \frac{3}{4})$	$(\frac{1}{3}, \frac{2}{3}, \frac{3}{4})$	$(\frac{2}{3}, \frac{1}{3}, \frac{1}{4})$
Γ_1	$(2u, u, 0)$	$(2u, u, 0)$	$(2u', u', 0)$	$(-2u', -u', 0)$	$(2u'', u'', 0)$	$(2u'', u'', 0)$
Γ_2	$(0, -u, v)$	$(0, -u, -v)$	$(0, -u', v')$	$(0, u', v')$	$(0, -u'', v'')$	$(0, -u'', -v'')$
Γ_3	$(0, -u, v)$	$(0, u, v)$	$(0, -u', v')$	$(0, -u', -v')$	$(0, -u'', v'')$	$(0, u'', v'')$
Γ_4	$(2u, u, 0)$	$(-2u, -u, 0)$	$(2u', u', 0)$	$(2u', u', 0)$	$(2u'', u'', 0)$	$(-2u'', -u'', 0)$

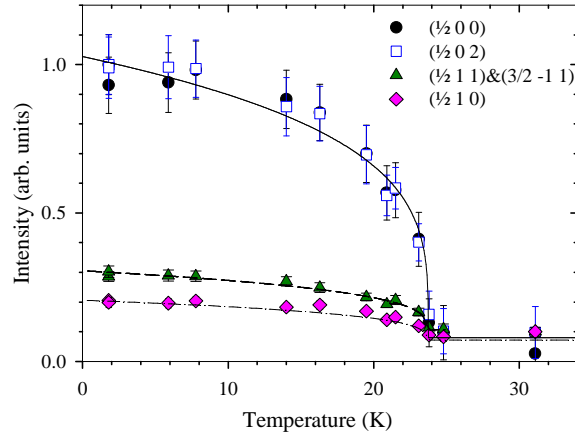


Figure 3.9: Temperature-dependence of the observed intensity at several magnetic Bragg peak positions (from elastic neutron powder scattering measurements using IN6). Lines are guides to the eye.

the neutron diffraction pattern at 300 K from the 4 K pattern, therefore the peaks present in the plot are the reflections which were observed only at low temperature. These peaks were observed only at low Q , indicating their magnetic origin, and were indexed by the commensurate propagation vector, $\mathbf{k} = (1/2, 0, 0)$. The intensity of the additional Bragg peaks increased as the temperature was reduced below 20 K, as shown in Fig 3.9.

To analyse the low temperature diffraction patterns, the possible magnetic structures within the $P6_322$ space group and with an ordering wave vector $(1/2, 0, 0)$ were considered. The four possibilities for the six Ni sites are given in Table 3.2. Table 3.2 shows that the symmetry restricts the moments on the same sublattice to be either parallel or antiparallel between the two layers in the unit cell. The spin direction and magnitude were independently varied on the three sublattices in the fitting process. The best fit to the observed diffraction pattern was obtained when only one of the three sublattices was ordered: either Ni1(2c) or Ni3(2d), with a moment of $\mu = 1.552(7) \mu_B$ along the c -axis and spins parallel between adjacent layers, $R_f = 13.9\%$. Therefore, the best-fit case corresponded to the irreducible representation Γ_3 in Table 3.2 with $v \neq 0(\text{Ni1})$ or $v'' \neq 0(\text{Ni2})$ and all the other spin components equal to zero.

The magnetic structure is illustrated in Fig. 3.10 a) and consists of ferromagnetic chains ordered antiferromagnetically in the triangular plane. Equivalent structures were obtained by a rotation $\pm 60^\circ$ around the c -axis, which all had the same powder averaged diffraction pattern. Those structures correspond to the symmetry-equivalent wave vectors, $\mathbf{k}' = (0, 1/2, 0)$

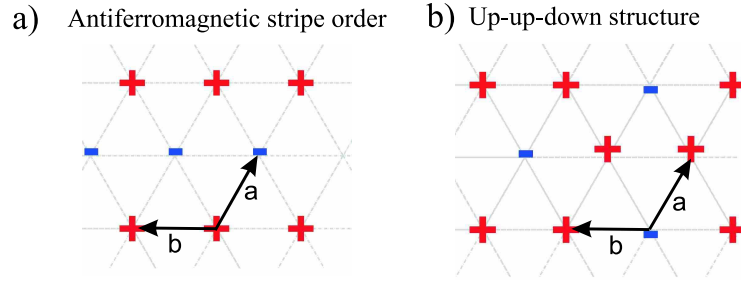


Figure 3.10: A single layer of Ni^{2+} ions form a triangular lattice. The projection of the spin moments along the c -axis is indicated by the \pm symbol for two magnetic structures. a) The antiferromagnetic stripe order structure found to be the magnetic ordering in AgNiO_2 and b) the honey comb Up-Up-Down structure which is the usual ground state of an easy axis triangular antiferromagnet.

and $\mathbf{k}''=(1/2, -1/2, 0)$. Three equally weighted domains of the three structures would be expected in a macroscopic sample.

3.2.3 Discussion

Crystal Structure

The high-resolution neutron powder diffraction measurements indicated a structural distortion occurred below $T_s = 365(3)$ K. The orbital order of AgNiO_2 is frustrated because of the triangular geometry. A related material to AgNiO_2 is NaNiO_2 which undergoes a strong ferro-distortive transition into a low-temperature monoclinic structure. It changes from the rhombohedral $R\bar{3}m$ to monoclinic $C2/m$ with a significant difference of 4% of the two in-plane lattice parameters [32, 33, 34, 35]. The orthorhombic $Cmcm$ space group was used to test for a similar distortion within the AgNiO_2 data, where the lattice parameters are $a \times b \times c$. Within the accuracy of the measurements, the fitted in-plane lattice parameters, a and b , had the same ratio as within the undistorted structure, $b/a = \sqrt{3}$. The hexagonal symmetry was preserved down to the lowest measured temperature of 2 K to less than 0.02% of the lattice constants. In the other related delafossite material, LiNiO_2 , measurements have shown that the triangular symmetry is preserved at low temperature [31]. Yet there has been evidence of lattice strain due to local Jahn-Teller distortions and the large broadening of the structural peaks of approximately 40% upon cooling from room temperature to 10 K [31]. In the present study some of the peak had increased widths at low

temperatures but the effect was much smaller than has been reported for LiNiO_2 . Therefore, a similar significant lattice strain did not appear to be present in AgNiO_2 .

The weak structural reflections, which were undetected in previous X-ray measurements by Sörgel and Jansen [27], indicated a small structural distortion with a tripling of the unit cell in the basal plane. The data suggested that this resulted from a periodic contraction and expansion of NiO_6 octahedra in a three-sublattice structure. The movements of the oxygen atoms is such that the three-fold rotation axis at each Ni site is preserved but the Ni sites are not equivalent. The Ni-O bonds are either contracted or expanded from the ideal $\text{P6}_3/\text{mmc}$ structure. In Fig. 3.11 the black circles, which are centred on the three independent Ni sites, correspond to average Ni-O distances. The three sites have average Ni-O bond lengths of 1.934 Å for Ni2 and Ni3 sites ($2b$ and $2d$) and 2.022 Å for Ni1 sites ($2c$). In Ni^{4+} oxides [41, 42] the typical Ni-O bond distances are about 1.92 Å, whereas in Ni^{2+} oxides [43, 44, 45] they increase to ~ 2.09 Å. Therefore, it may be the case that a charge disproportionation occurs among the Ni sites on the triangular layers in AgNiO_2 between charge-rich sites Ni2 and Ni3, which are at the centre of a contracted NiO_6 octahedron with valence close to Ni^{4+} , and the charge-depleted Ni1 sites, which are at the centre of an expanded octahedron with valence close to Ni^{2+} .

A phenomenological bond-valence model [46] is considered to relate the valence of the central ion to the bond-length:

$$\sigma = \sum_i \exp((r_0 - r_i)/B) \quad (3.2)$$

where r_i is the bond length of the central ion to oxygen bond, $B=0.37$ Å and $r_0 = 1.686$ Å for the $\text{Ni}^{3+}\text{-O}^{2-}$ pair. Using the bond lengths observed experimentally implies nominal valences in the ionic limit for the three sites: 2.42 for the Ni1 site and 3.07 for Ni2 and Ni3. This suggests significant, but most probably only partial, charge disproportionation within the sample in the distorted phase.

The bond lengths found for the Ni-O bond in AgNiO_2 are similar to those found in YNiO_3 . YNiO_3 is disposed to charge disproportionation by forming two Ni sublattices of valence $\text{Ni}^{3\pm\delta}$ where $\delta \simeq 0.35$. In that material the Ni-O distances are (Ni1-O)=1.923 Å and Ni2-O=1.994 Å, [47] and so results can be compared with AgNiO_2 .

A full symmetry analysis of the structural distortion in AgNiO_2 has been considered by Wawrzyńska *et al.* in [48] (section V and appendix). The charge order on the nickel sites and the displacement of the oxygens have been described as an order pattern with

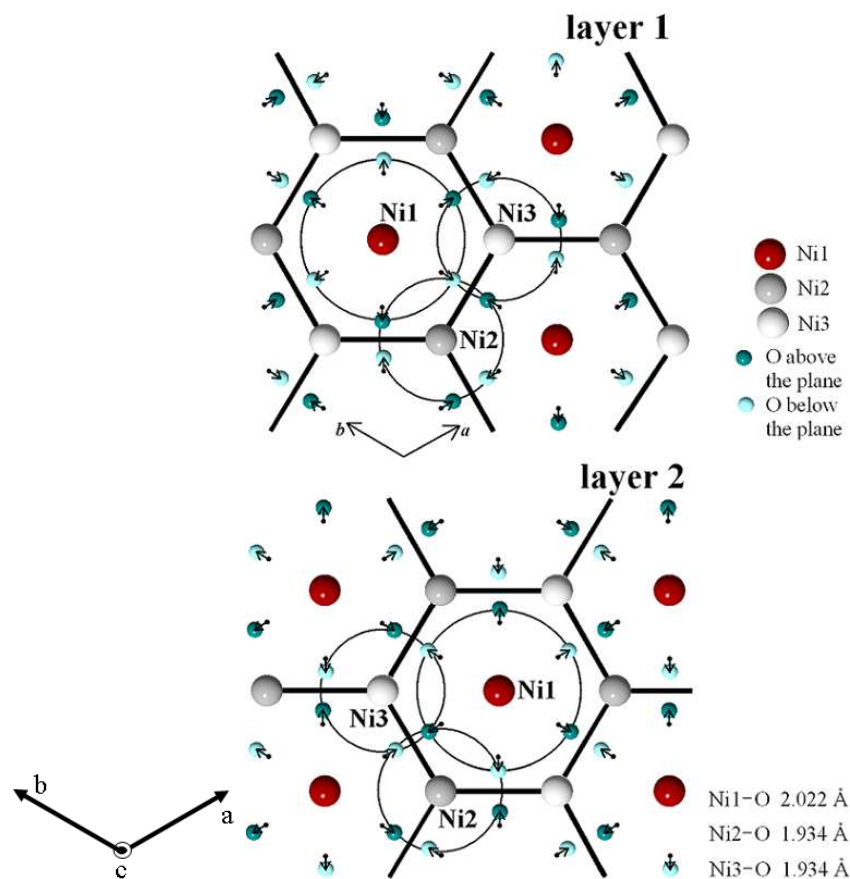


Figure 3.11: Upper figure is a schematic diagram of the NiO_2 layer at $z = 1/4$ showing how the displacements (small arrows) of the oxygen ions (small balls) lead to a periodic arrangement of expanded (large circle, Ni1) and contracted (small circles, Ni2, Ni3) NiO_6 octahedra. The thick hexagonal contour indicates the honeycomb network of contracted sites. The origin of the coordinate system is at the circled Ni2 site. The lower figure shows the expanded site Ni1 has a staggered zig-zag arrangement between even and odd layers stacked along the c -axis. Layer 2 in the unit cell ($z = 3/4$ and $-1/4$) is obtained from layer 1 by 180° rotation around the central $(1/2, 1/2, z)$ axis followed by a $c/2$ translation.

wave vector $\mathbf{q}_0 = (1/3, 1/3, 0)$ within the ideal structure space group $P6_3/mmc$. The co-representation analysis of the distortion has shown that the space group $P6_322$ is uniquely identified as the low symmetry space group describing AgNiO_2 below 365 K.

Magnetic Structure

The negative Currie-Weiss temperature indicated dominant antiferromagnetic interactions and the high Currie-Weiss temperature but low magnetic transition temperature pointed toward large fluctuations. These results may have arisen from the low dimensionality and frustration of the triangular lattice planes, which would have led to a suppression of the magnetic order in the triangular plane. The transition temperature that was observed from the magnetic order parameter curves, $T_N = 23.7(3)$ K, was slightly offset from the location of the specific heat anomaly near 19.7(3) K, and susceptibility maximum near 21(1) K. This was probably a result of a small temperature calibration offset in the neutron measurement, where the sensor was at some distance from the sample. The specific heat transition temperature was perhaps the most accurate value and it was consistent with the value found in recent μSR results [36].

The low-temperature diffraction pattern was fitted to a magnetic structure where only one sublattice was observed to order. The goodness-of-fit parameter was larger than in the case of the crystal structure because fewer Bragg peaks were observed: also there was difficulty in defining the OSIRIS profile pattern at low Q . The magnetic order pattern reinforced the structural analysis, where the Ni1 site carried a large moment in comparison to the other two sites. At complete charge disproportionation the Ni1 site would have been Ni^{2+} and therefore have $S = 1$. Although the data did not rule out the possibility of a small magnetic moment of order $0.1\mu_B$ along the c -axis on the Ni2 and Ni3 sites, including this possibility did not improve the fit to the data. Therefore, the simplest model was that where only the Ni1 site ordered. The fact that the magnetic moment was aligned along the c -axis indicated that there was a strong uniaxial anisotropy. Yet the proposed magnetic structure of ferromagnetic stripes arranged antiferromagnetically in the basal plane is unusual. That is because the up-up-down structure, shown in Fig. 3.10 b), is the ground state of the isotropic triangular lattice with nearest-neighbour antiferromagnetic exchange for the case of a strong uniaxial anisotropy [17]. The possible Hamiltonian that would stabilize the observed magnetic structure is discussed in the following section.

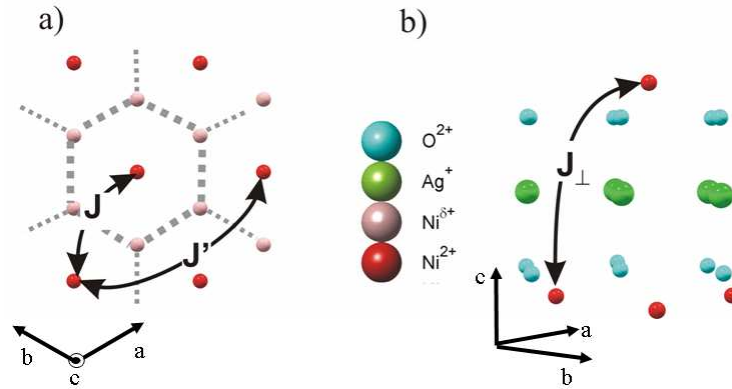


Figure 3.12: A sketch of a single Ni lattice within AgNiO_2 with the in-plane exchange interactions indicated in a) and inter-layer indicated in b). The Ni sites which order, the Ni1 sites, are plotted in red and they form an isotropic triangular lattice. The Ni2 and Ni3 sites form a honeycomb network around the Ni1 sites. Plot a) shows the nearest-neighbour and next-nearest-neighbour interactions and plot b) shows the inter-layer interactions for the Ni1 lattice including the oxygen and silver layers in the sketch.

3.3 Magnetic Excitations of AgNiO_2

Low-spin triangular-lattice magnets are systems suitable for investigating the interplay between quantum fluctuations and geometric frustration. The frustration generated by the geometry of the lattice and the quantum fluctuations, due to the low-spin state of the system, have been predicted to produce both unconventional ordered phases and unusual excitations [49].

The delafossite materials of the type X NiO_2 are generally thought of as possible two-dimensional frustrated magnets because a network of edge-sharing NiO_6 octahedra make up a triangular lattice of Ni ions in a plane spaced with layers of X^+ ions. If the Ni^{3+} is in the spin-half state then a low-spin triangular-lattice is formed. Two materials have been studied extensively of this type. In the first, LiNiO_2 , no long-range order has been observed in. In the second, NaNiO_2 , elastic and inelastic neutron scattering measurements have found that the Ni^{3+} is a spin-half system with in-plane ferromagnetic interactions and weak antiferromagnetic inter-plane coupling [33]. AgNiO_2 has been less well studied but it shows dominant antiferromagnetic in-plane interactions and thus promises to have an interesting excitation spectrum [29].

As discussed in the previous section, it has been proposed that, in the triangular lattice of Ni ions, charge disproportionation is a means of avoiding the orbital frustration effects

that have been inferred from the observed small distortion of the NiO_6 octahedra [48]. The expansion and contraction of the NiO_6 octahedra has indicated that the transition of the unpaired electron in the ideal structure, $3e_g^1 \rightarrow e_g^2 + e_g^{0.5} + e_g^{0.5}$, forms three independent Ni sites within one Ni layer. Below $T_N \sim 20$ K, a transition to a magnetically ordered state has been observed [48]. It has been suggested that the so-called Ni1 sites are ordered and form an isotropic triangular lattice, as shown in Fig 3.12. With a valence close to Ni^{2+} , the Ni1 sites have a spin state $S = 1$. The other two independent sites, Ni2 and Ni3, with a valence close to $\text{Ni}^{3.5+}$, have no sizeable magnetic moment. The spins on Ni1 sites order with moments aligned collinearly into ferromagnetic stripes arranged antiferromagnetically in the basal plane (see Fig. 3.10 a) as opposed to the more usual Up-Up-Down structure (UUD) (see Fig. 3.10 b). The UUD state is the ground state of the isotropic triangular lattice where there is nearest-neighbour antiferromagnetic exchange and a strong uniaxial anisotropy [17]. The striped ground state is quite unusual for the triangular antiferromagnet. The strong quantum fluctuations, due to the large frustration of the lattice, stabilize the antiferromagnetic stripes in this case. In fact, calculations of the two dimensional triangular lattice, with nearest (J) and next-nearest neighbour (J') antiferromagnetic coupling and a large easy-axis anisotropy, have shown that the antiferromagnetic stripes structure is stabilized when $J'/J > 1/8$ by an order-by-disorder mechanism [50]. The inter-layer coupling shown in Fig. 3.12 b) is thought to be weak because of the large distance between the layers. The easy-axis anisotropy is such that spins align along the c-axis and so they are perpendicular to the triangular lattice layers. Therefore, the magnetic structure balances the antiferromagnetic nearest and next-nearest-neighbour exchange couplings within the triangular lattice layer, and the ferromagnetic inter-layer interactions and an easy-axis anisotropy.

The remainder of this section describes inelastic neutron scattering measurements on a powder sample of hexagonal AgNiO_2 . It is shown that the observations are consistent with a generic sinusoidal dispersion and an antiferromagnetic structure factor. With this model, the observed powder-averaged spin spectrum could be parameterized and a quantitative measure of the bandwidth and main energy scales could be gained within the ordered phase. These results were compared with linear spin-wave theory calculations and with two models in particular. The nearest and next-nearest neighbour model calculated by Chubukov and Jolicoeur [50] and then an extended model Hamiltonian which included inter-plane couplings and a uniaxial anisotropy. While a set of parameters could be found to describe the gap and bandwidth, the intrinsic two-dimensional dispersion in this model

predicts large in-plane dispersion along the stripes and smaller in-plane dispersion between the stripes, but this is not captured by the linear spin-wave theory of the extended model Hamiltonian.

3.3.1 Experimental Details

The powder samples that were described in §3.2.1 were used for all the measurements. The space group, cell parameters and fractional co-ordinates of the three Ni sites are given in Table 3.1 for this polymorph.

Inelastic neutron scattering measurements up to 10 meV energy transfer gave an overview of the excitations. They were made using the direct geometry time-of-flight spectrometer, MARI at the ISIS Facility of the Rutherford Appleton Laboratory in the UK. MARI was also used to probe higher energy excitations. For the main measurements it was set up with an incident energy of 18 meV, achieving a resolution of 0.61(1) meV on the elastic line. Measurements were also made at higher incident energy settings. The low-energy part of the spectrum was investigated using the IN6 spectrometer at the ILL. It was operated at an incident energy of 3.86 meV and achieved an energy resolution of 0.142(1) meV on the elastic line. Measurements were taken between a base temperature of 1.8 K and 300 K. Both data sets were normalized to absolute units of $S(Q, E)$ of mbarns/meV/sr/Ni1, using the sample mass together with the results of the measurements of a vanadium standard. The low-energy IN6 data was also corrected for neutron absorption effects calculated for a flat-plate sample shape.

3.3.2 Measurements and Results

The powder averaged spectrum from both spectrometers is shown in Fig.3.13. Fig. 3.13 a) shows a band of scattering below the magnetic ordering transition temperature of $T_N \sim 20$ K. The band of intensity is seen to begin above an energy gap and extend to ~ 7.5 meV. The intensity is seen to reduce with increasing Q and so this confirms its magnetic origin. Fig. 3.15, left plot, shows a density of states over a wide Q range. Within the ordered phase a band of excitations is seen to extend above 1.8 meV and up to 7.5 meV, where the intensity decays to the background level.

The excitation band is seen to have further structure at its low-energy edge. Fig. 3.13 c) shows the high-resolution measurement in the lower energy transfer and low Q region. A clear modulation in the shape of the low edge of the excitation band can be observed.

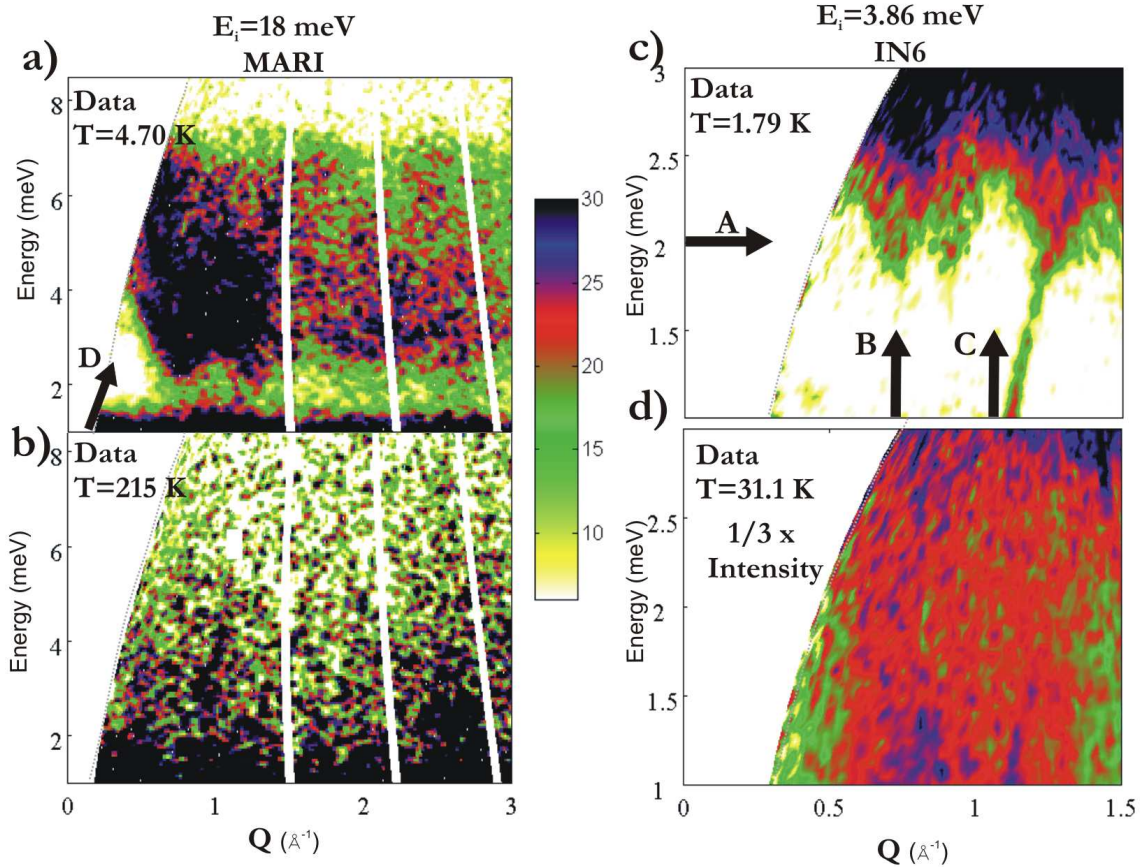


Figure 3.13: Powder-averaged magnetic excitation spectrum of AgNiO_2 measured with an incident energy, $E_i = 18\text{meV}$ (left column) and $E_i=3.86\text{meV}$ (right column) plotted as a function of wave vector, Q and energy transfer, E . Colour indicates the intensity in units of units of $S(Q, E)$ of mbarns/meV/sr/Ni1. The upper plots a) and c) give the measured spectra in the magnetically ordered phase showing a band of excited states above an energy gap of ~ 1.8 meV. The streak of intensity in plot c) near $Q=1.1\text{\AA}^{-1}$ is due to an acoustic phonon from the $(0, 0, 2)$ structural Bragg peak. At high temperature above the magnetic ordering transition in plots b) and d) a filling of the energy gap is observed and there appears to be little structure in the intensity pattern as a function of Q . The intensity shown in panel d) was rescaled by a factor of $\frac{1}{3}$ such that it is shown on the same scale as the rest of the figure. The grey dotted lines on all the plots indicate the edge of the measured region. The black arrows marked A-D indicate the Q value of the plots in Fig. 3.14.

There are minima in the intensity distribution at $Q \sim 0.7 \text{ \AA}^{-1}$ and $\sim 0.9 \text{ \AA}^{-1}$. These minima correspond to the positions of the two magnetic Bragg wave vectors, $(1/2, 0, 0)$ and $(1/2, 0, 1)$ respectively, as can be seen by comparing the plot in Fig. 3.14. The elastic line plot in Fig. 3.14 was measured made with the diffractometer GEM at ISIS, as described in § 3.2.1. The plot shows strong magnetic Bragg peaks that were observed below the magnetic transition temperature. The upper plot in Fig. 3.14 shows the data from the higher resolution IN6 measurements at an energy transfer of 2 meV, which is just above the energy gap. It shows that the minima in the dispersion are at the same Q as the magnetic Bragg peaks. The streak of intensity in Fig. 3.13 c) originates on at $Q = 1.1 \text{ \AA}^{-1}$ and arises from an acoustic phonon mode from the intense nuclear reflection $(0, 0, 2)$.

In Fig. 3.15 and other plots the estimated background level is shown as a green line for comparison. The background level was estimated by fitting a smooth function between the low energy and low Q data within the energy gap, and at high energy beyond the excitation band.

The low-energy edge of the band of intensity is seen to be shaped in Fig. 3.13 c) with a sharp onset edge at low Q that has a steep intensity gradient. The estimated lower boundary of the scattering is displayed as black crosses in the plots of Fig. 3.19. The crosses show where intensity was observed to be above a threshold for various values of Q . Cuts through planes in the directions B and C give the intensity in Fig. 3.14. The figure demonstrates the change in onset energy at different Q values. The different onset energy at the two wave vectors ($Q \sim 0.7 \text{ \AA}^{-1}$, associated with the wave vector $(1/2, 0, 0)$, Fig. 3.14 B and $Q \sim 1.1 \text{ \AA}^{-1}$ associated to the $(1/2, 0, 1)$ Fig. 3.14 C) indicates a dispersion of the lower boundary of approximately 0.5 meV. This will be shown below to be determined mostly by the inter-layer dispersion of the excitations.

Fig. 3.15 shows that upon heating above the magnetic ordering temperature the spin gap energy region increased in intensity and no energy gap could be observed at a temperature of 30 K. Deep into the paramagnetic phase at 300 K a broad over-damped signal is observed as shown in Fig. 3.13 b) and Fig. 3.15.

A search for high-energy excitations was made in order to measure crystal field excitations. The first excitation was observed at 366(1) meV. Fig. 3.16 shows that the intensity of the mode decreased with increasing Q and this showed that it had a magnetic origin due to a decreasing magnetic form factor. It was likely to be a crystal field excitation because this excitation was at a much higher energy compared to the exchange interactions in the material. It may have been due to the excitation of one electron from the filled t_{2g} level to

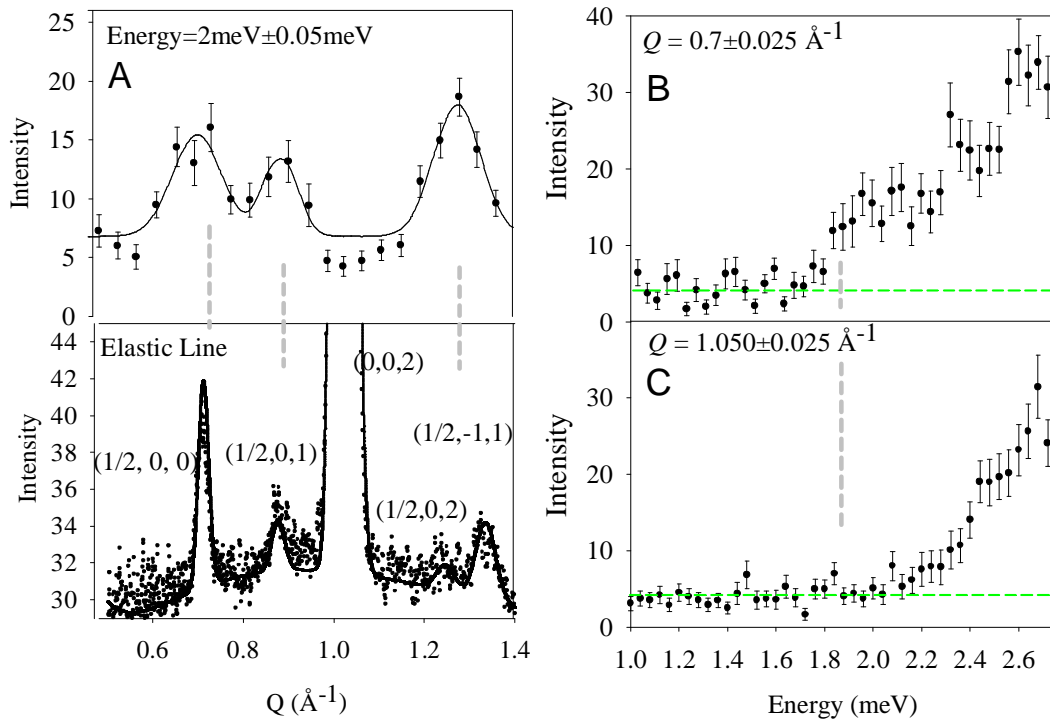


Figure 3.14: The lettering A-C of these plots refer to the markings in Fig. 3.13. Plot A: The upper plot shows the high resolution data just above the onset of the excitation band at a constant energy of 2 meV. The minima seen in the excitation edge are above the magnetic Bragg wave vectors seen in the elastic line data taken on the GEM diffractometer ISIS (lower plot). Plot B: The minimum of the energy gap where the onset of the scattering is at approximately 1.8 meV and $Q = 0.7 \text{ \AA}^{-1}$ associated with $(1/2, 0, 0)$. Plot C: The energy increases at $Q = 1.05 \text{ \AA}^{-1}$ between the two minima at $(1/2, 0, 1)$ and $(1/2, 0, 2)$.

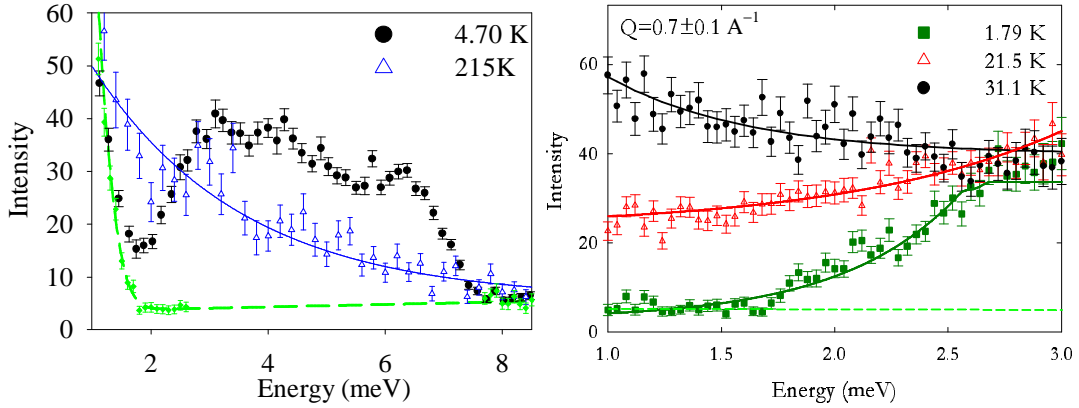


Figure 3.15: Left: A cut in energy over a broad Q range through the lower resolution data. This is a density of states type plot within the magnetically ordered phase and equivalent cut from the data set above the magnetic ordering temperature. A band of excitations is observed up to 7.5 meV at low temperature. It is seen that the energy gap to this band of excitations is filled with intensity as the temperature is increased. Right: A cut in energy through the high resolution data about the magnetic Bragg reflection $(1/2, 0, 0)$ which shows the variation of the energy gap with temperature and the increase in intensity at low energies on moving above the magnetic ordering temperature of 20 K. The lines are guides to the eye.

the e_g level. A schematic diagram for the strongly magnetic Ni1 ion is shown in the insert of Fig. 3.16. This transition may also occur for the other two Ni sites in the unit cell, which have been proposed to have an itinerant character [48].

3.3.3 Analysis

Parameterization Model

A simple model was constructed to understand the main energy scales in the system and in an attempt to parameterize the dispersion. A gapped sinusoidal three-dimensional dispersion was constructed to have minima at the magnetic Bragg peaks and included three independent dispersions along the three non-equivalent directions: firstly along the stripes of collinear spins; secondly perpendicular to the stripes within the plane; and thirdly an inter-planar dispersion. In detail the dispersion used was:

$$\begin{aligned}
 (\hbar\omega_{\mathbf{Q}})^2 &= \Delta^2 + (E_1^2 - \Delta^2) \sin^2(\pi k) \\
 &+ (E_2^2 - \Delta^2) \sin^2(\pi(2h + k)) + (E_3^2 - \Delta^2) \sin^2(\pi l)
 \end{aligned}
 \tag{3.3}$$

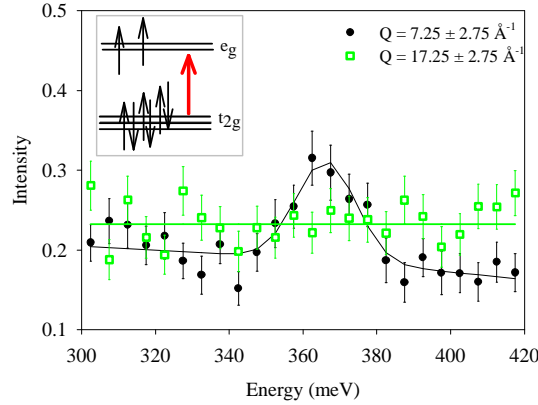


Figure 3.16: A high energy mode is seen in data taken using MARI with an incident energy $E_i=600$ meV. The cut at low Q (black closed points) shows a mode centered at $366(1)$ meV which is not present in the high Q cut (green open points). The large energy of this excitation suggests it could be a crystal field excitation from a t_{2g} level to the e_g level. The decrease in intensity of the mode at high Q values, open points in the plot, further indicates its magnetic character. The scenario for the strongly magnetic Ni1 site is indicated in the top left diagram, but it may also be due to the other Ni sites in the unit cell.

where the wave vector, $\mathbf{Q} = (h, k, l)$, is expressed in terms of the reciprocal lattice units of the hexagonal unit cell. The dispersion for two models is plotted in Fig. 3.17. Branches along key directions for the hexagonal space group are shown, which are labeled in the Brillouin zone and plotted in Fig. 3.17 left. The dispersion given by Equation 3.3 has a minimum energy gap, Δ , at the magnetic Bragg peaks and has a sinusoidal shape along the three non-equivalent directions, namely two in the plane and one between the planes. E_1 , E_2 and E_3 measure respectively the maximum energy of the dispersion: in-plane along the stripes of collinear spins; in-plane perpendicular to the stripes; and the inter-layer dispersion. An ordered magnet with collinear spins along the z -direction is expected to have spin-wave modes polarized in the xy -plane. Therefore, the functional form of the dynamic correlations is assumed to be:

$$S^{xx}(\mathbf{Q}, \omega) = S^{yy}(\mathbf{Q}, \omega) = C \frac{1 - \gamma_{\mathbf{Q}}}{2\omega} G(\omega - \omega_{\mathbf{Q}}) \quad (3.4)$$

where C is a normalization constant and $\gamma_{\mathbf{Q}} = \cos(\pi k) \cos(\pi(2h + k))$. For the best-fit model $C=700 \pm 10$. The factors $(1 - \gamma_{\mathbf{Q}})/2$ and $1/\omega$ are a geometric factor and an energy dependence factor respectively that concentrate intensity near the antiferromagnetic Bragg

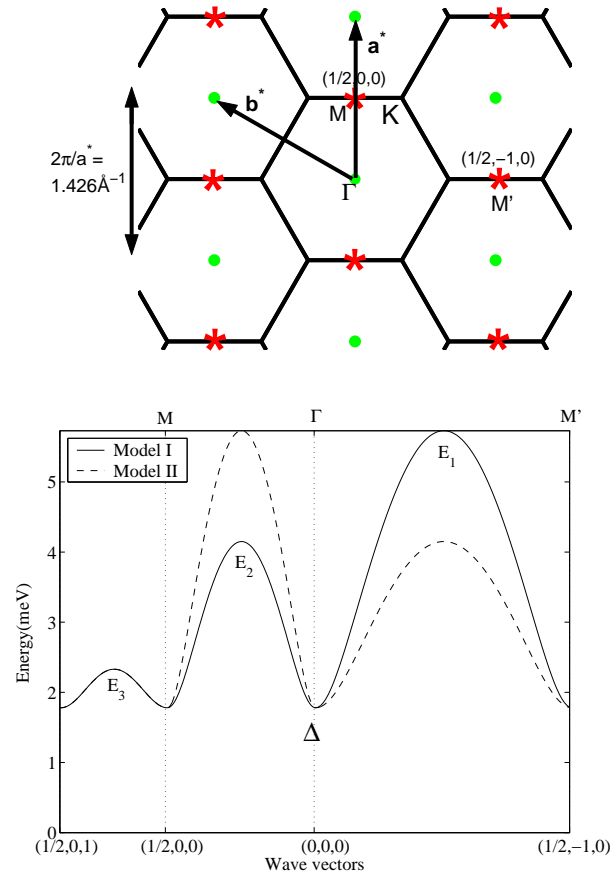


Figure 3.17: Upper: Brillouin zone for the triangular lattice of ordered Ni1 spins projected on the (a, b) -plane. The solid green points indicate nuclear Bragg reflections and the red stars indicate the locations of the magnetic Bragg reflections arising from the collinear stripe structure shown in Fig. 3.10 a). Labels, Γ , M, K, M' indicate key points of symmetry for the hexagonal space group and are indicated in the top labels in the right plot. Lower plot: Dispersion along the high symmetry directions in the three-dimensional Brillouin zone. Best fit to the data, model I (solid lines), gives largest dispersion along the in-plane stripe direction. In Model II (dashed lines) the largest dispersion is in-plane transverse to the stripe (this does not model the data successfully). The parameters for Model I are $E_1 = 5.73$ meV, $E_2 = 4.15$ meV and in Model II $E_1 = 4.15$ meV, $E_2 = 5.73$ meV with $E_3 = 2.33$ meV, $\Delta = 1.78$ meV.

peak wave vectors. These factors replicate the intensity distribution of many standard anti-ferromagnetic spin-wave models. $G(\omega - \omega_{\mathbf{Q}})$ is a gaussian function which models the resolution of the measurements. A powder average of the intensity distribution, which included the polarization factor and magnetic form factor for the Ni^{2+} ion, was taken for comparison with the experimental results. It is shown in the lower panels of Figs. 3.21 and 3.19. An estimate of the experimentally observed non-magnetic background scattering was added to the magnetic scattering calculated from the parameterization model. In particular, the incoherent quasi-elastic scattering was added to the calculation to make it directly comparable with the data.

The difference between lattice parameters was used to identify dispersion branches both within the plane and between planes and thereby to parameterize the model. In this way, it was possible to identify the dispersion branches along various directions in the Brillouin zone which shaped the lower edge of the excitation band, as shown in Fig 3.13 c). Having identified the relevant dispersion branches, the parameters were estimated and gave an indication of the main energy scales in the system.

As shown in Fig. 3.18 plot B, the minimum energy gap occurred at the Q values corresponding to the magnetic Bragg peaks. The energy scan above the Bragg point $(1/2, 0, 0)$ was fitted with the parameterization model to extract the size of the gap and this gave $\Delta = 1.78 \pm 0.04$ meV. The solid lines in Fig. 3.18 show the equivalent calculated intensity distribution for the best-fit model.

A steep sharp-edged boundary to the scattering at low Q was observed before the first magnetic Bragg peak $(1/2, 0, 0)$. The $(h, 0, 0)$ branch connecting $(0, 0, 0)$ to the $(1/2, 0, 0)$ shapes this edge as shown in Fig. 3.19 a). This branch is most sensitive to the dispersion transverse to the stripes, that is the E_2 energy scale, and a fit to the low energy section of Fig. 3.18 D gave a value of $E_2 = 4.15 \pm 0.04$ meV. Therefore the modelled dispersion between the stripes does not lead to the full bandwidth observed in the data. However, the bandwidth can be reproduced by fitting E_1 . With E_2 fixed by the sharp dispersion edge at low- Q , the overall bandwidth was fitted by varying the dispersion along the stripes which is associated with E_1 , since the inter-layer dispersion was presumed to be small. Thus the largest dispersion was assumed to be along the stripes of collinear spins. By fitting the parameterization model to the full experimental bandwidth in Fig. 3.18 D, gave a value $E_1 = 5.73 \pm 0.04$ meV.

Figure 3.18 C, shows a larger energy gap at $Q = 1.1 \text{ \AA}^{-1}$ than the value of 1.8 meV which

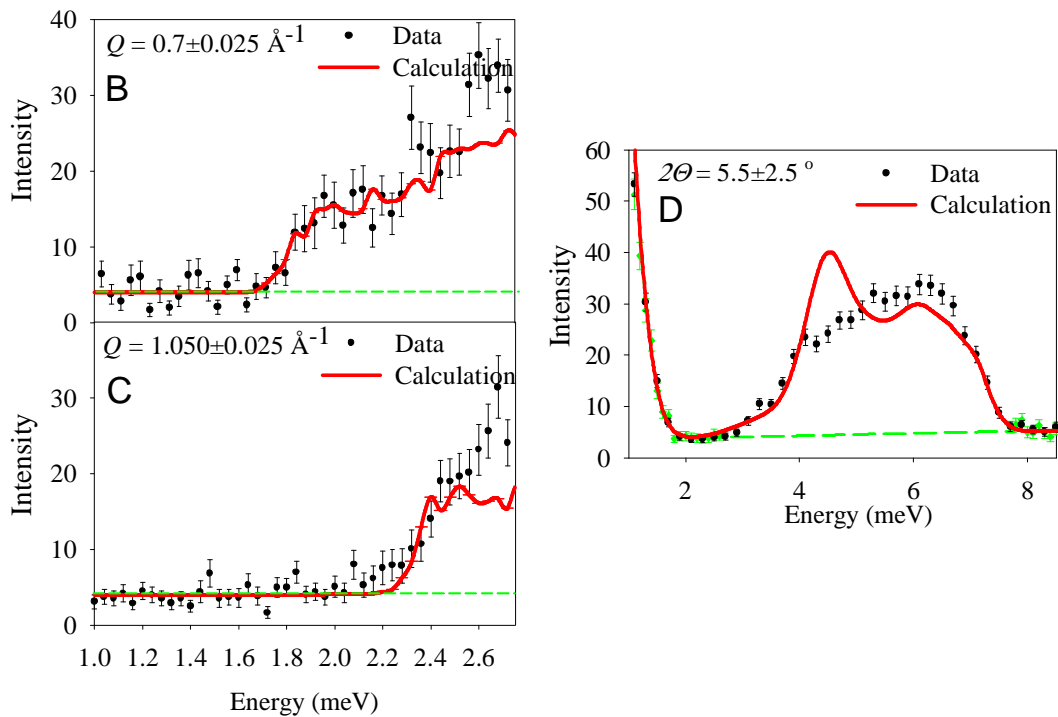


Figure 3.18: Plots comparing the best-fit of the model(see text) to the data for the scans B-D in Fig. 3.13. To quantitatively fit the lower energy edge of the band of excitations low Q scans were taken of the type B and C and the equivalent scans are shown for the parameterization calculation. Cut D shows the full bandwidth of the data. The bandwidth is reproduced by construction and this fit was used to determine the in-plane inter-stripe energy scale. The green dashed lines in the plots indicate a fit to the background points.

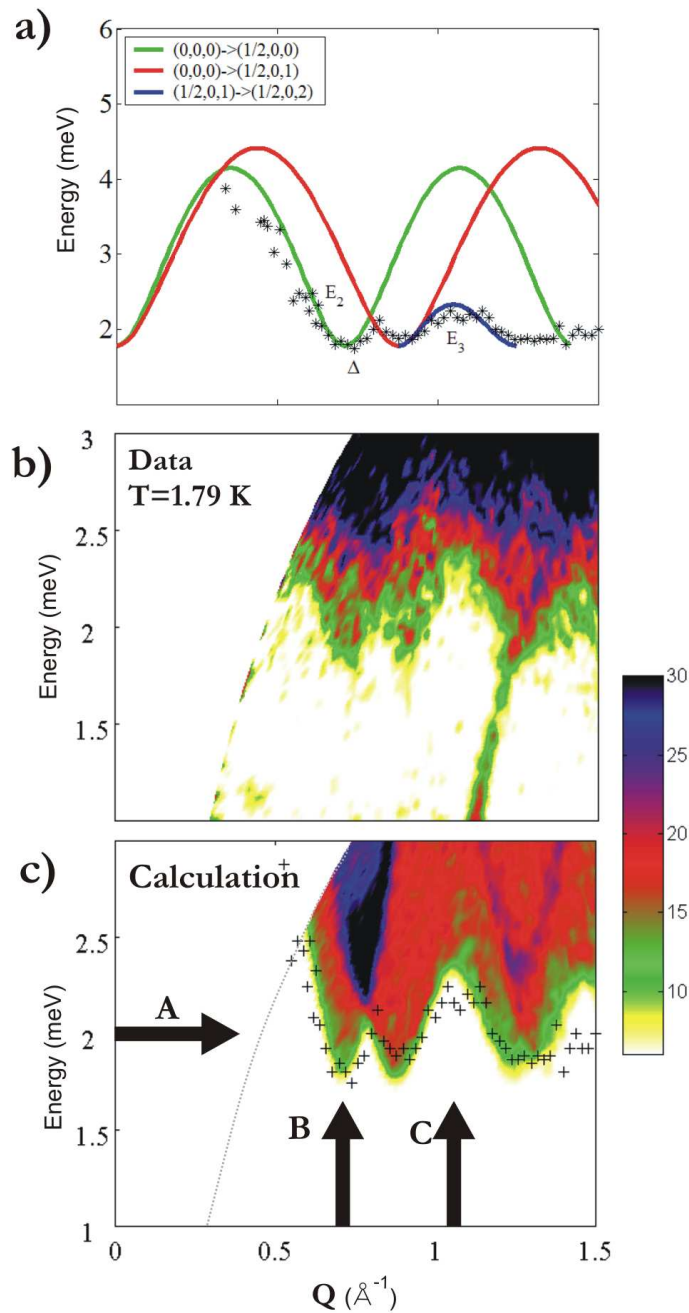


Figure 3.19: The parametrization of the data with the three energy scale E_1 , E_2 , E_3 model given in the text is plotted for the key branches which define the low-energy edge of the dispersion in plot a) and the powder average spectrum is given in plot b) for the best fit values. The black crosses on both plots indicate the onset of the intensity distribution from the data which are given for comparison and show there is a good fit to the data. The black arrows indicate the relevant cuts in the calculation given in plots A to C in Figs. 3.18 and 3.20.

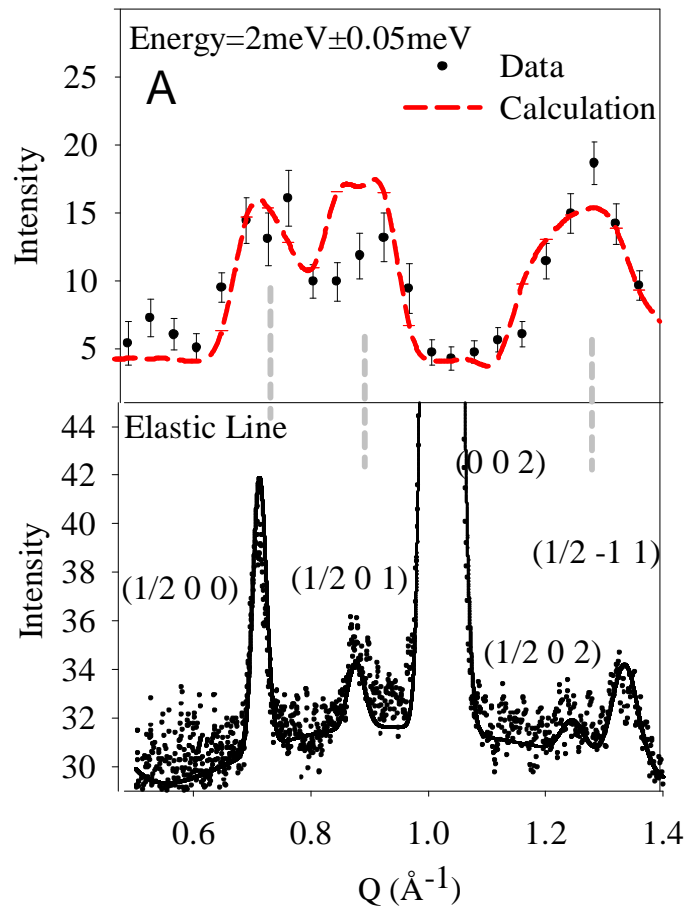


Figure 3.20: Plot A shows the intensity above the onset of the excitation band at a constant energy of 2 meV. The minima observed in the excitation edge in the data (black points) are also a feature of the parameterization model (red dashed line). The minima are at the same Q of the magnetic Bragg peaks show in the lower plot.

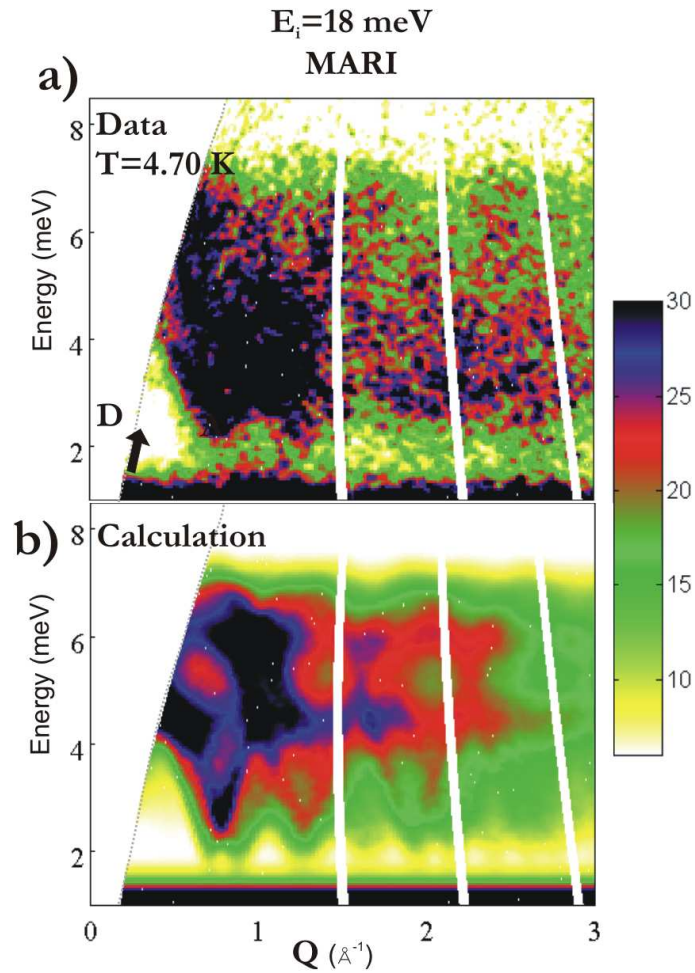


Figure 3.21: Comparison of the data from the power sample, plot a, and the parametrization model, plot b, discussed in the text. The calculations include an estimate of the experimentally observed non-magnetic background scattering. In particular, the incoherent quasi-elastic scattering was added to the calculation to make it comparable to the data. The bold arrow labeled D indicates the location of the scans plotted in Fig. 3.18 and the grey dotted lines on both plots indicate the edge of the measured region.

was observed at $Q=0.7 \text{ \AA}^{-1}$ (plot B). Because of the dissimilar lattice constants, it is possible to differentiate between dispersion branches within the triangular plane and between planes. The point $Q=1.1 \text{ \AA}^{-1}$ was identified as the mid-point between the two magnetic Bragg peaks, $(1/2, 0, 1)$ and $(1/2, 0, 2)$, which are along the inter-layer direction. Therefore the inter-layer energy scale, E_3 , determines the size of gap at this Q point from a branch such as $(1/2, 0, h)$, as shown in Fig. 3.19. E_3 was estimated as $E_3 = 2.33 \pm 0.04 \text{ meV}$ by fitting the energy gap in Fig. 3.18 C.

The lower panel in Fig. 3.19 shows the powder averaged spectrum for the best-fit model. The black points indicate the onset energy of the observed scattering. The black points do not take into consideration the resolution effects of the measurements and so the dispersion branches lie slightly away from the points. The model reproduced the shape of the lower edge of the intensity distribution at low- Q values and the overall features at low energy. Furthermore the model gave clear minima in the intensity distribution above the magnetic wave vectors and this is demonstrated in Fig. 3.20 A.

The model compared well to the data at low energy as shown in Fig. 3.20 A and Fig. 3.18 plots B and C. By construction, the bandwidth was reproduced as shown in Fig. 3.21. The form of the intensity distribution within the excitation band was not replicated in detail. This can be seen by comparing the observed with the modelled intensity in Fig. 3.18 D, which covers the full bandwidth. The calculation gave a more pronounced trough in intensity in the middle of the band; This was probably due to the over-simplified model. The model did identify two in-plane dispersion scales, an inter-plane interaction energy and an energy gap. The in-plane inter-stripe dispersion had a bandwidth of 60% that of the in-plane along the stripe dispersion bandwidth, whereas the inter-plane dispersion bandwidth was smaller, being 14% of the in-plane along-the-stripe bandwidth. This dispersion was above an energy gap of $1.78 \pm 0.04 \text{ meV}$.

The lower boundary of the intensity distribution greatly constrained the relative size of the energy scales of the model. In order to demonstrate the sensitivity of the model, the observed intensity distribution was compared with that predicted by the best-fit model and with a model where the two in-plane dispersion maxima are exchanged. The latter is referred to as model II and the dispersion is plotted as the dashed lines in Fig. 3.17. The dispersion of the modes in model II was largest transverse to the rows and within the triangular plane, i.e. $E_2 > E_1$. The shape of the sharp leading edge of the excitation band is defined by the dispersion branch between the wave vectors $(0, 0, 0)$ to $(1/2, 0, 0)$. In model II this dispersion branch is steeper than in model I. E_2 must be reduced in order to reduce

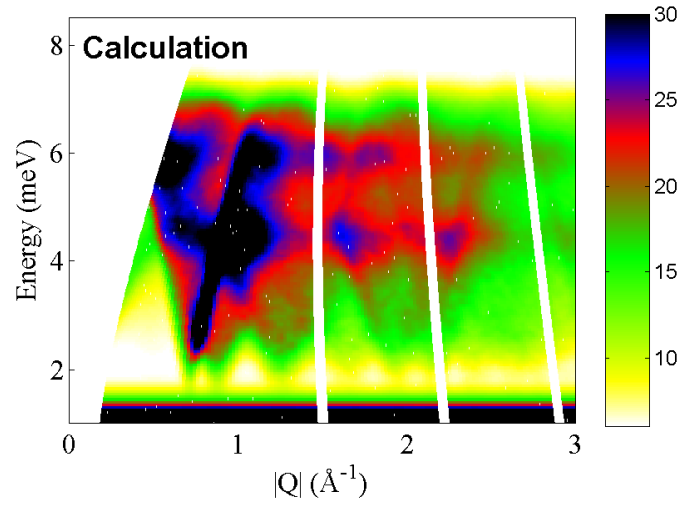


Figure 3.22: Powder averaged intensity distribution for Model II where the in-plane dispersion between the stripes is larger than along the stripe direction. The parameters are given in Fig. 3.17. This model should be compared directly to the data given in Fig. 3.13 a). It is seen that the sharp edge to the excitation band at low energy and low Q is steeper than that observed in the data indicating the sensitivity of the model to the in-plane inter-stripe band width which is too large in this model.

the gradient of the dispersion about the wave vector $(1/2, 0, 0)$. Since this is the largest energy scale in model II the full bandwidth would be become smaller than that observed in the data. The powder average intensity distribution of model II, shown in Fig. 3.22, is inconsistent with the distribution observed. The figure demonstrates clearly that the edge produced at low Q and low energy transfer is too steep and it demonstrates the sensitivity of the model to the inter-stripe energy scale. Therefore model II, where the in-plane dispersion transverse to the stripes is larger, is eliminated because it is an inappropriate model.

Linear Spin-Wave Analysis

The linear spin-wave excitation spectrum from the magnetically ordered state provides insight into the exchange mechanisms within the lattice. The Hamiltonian that was considered was based on the crystal structure. It modelled layers of $S = 1$ Heisenberg spins on an isotropic two-dimensional triangular lattice coupled antiferromagnetically within the

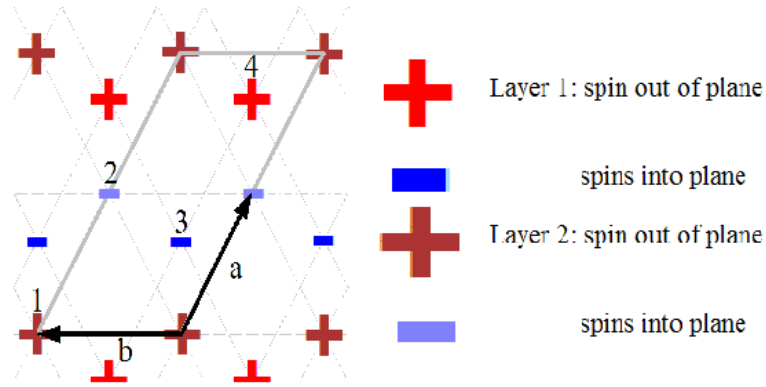


Figure 3.23: A sketch of the four sublattices used in the spin-wave calculation of the Ni1 sites. The crystallographic a and b lattice vectors are shown, and the magnetic unit cell is enclosed in the thick grey lines. The numbers innumerate the sublattices and the symbols indicate Ni1 spins collinear with the c -axis and within a layer at $z=1/4$ and $z=3/4$ for layer 1 and layer 2.

planes and ferromagnetically between the planes. The Hamiltonian was:

$$\mathcal{H} = \sum_{\substack{NN \\ \langle ij \rangle}} JS_i \cdot S_j + \sum_{\substack{NNN \\ \langle il \rangle}} J'S_i \cdot S_l + \sum_{\substack{\text{Inter} \\ \text{-layer} \\ \langle ik \rangle}} J_{\perp} S_i \cdot S_k - \mathcal{D} \sum_i (S_i^z)^2. \quad (3.5)$$

Here J , is an in-plane nearest-neighbour exchange, J' is an in-plane second-neighbour exchange, and J_{\perp} a ferromagnetic inter-layer coupling. The final term in Eqn 3.5 is an easy-axis anisotropy which could possibly originate from crystal field effects. It was introduced to reflect the spin ordering direction along the c -axis and the energy gap in the excitation spectrum. The couplings are indicated in the diagram of the lattice in Fig. 3.12.

The proposed magnetic structure is unusual for a triangular lattice of spins with nearest-neighbour coupling. Therefore, the possible ground states of the system will be considered in order to illustrate this choice of the model Hamiltonian. Firstly, the reduced model of a triangular Heisenberg lattice with nearest-neighbour and next-nearest-neighbour interactions ($J' = 0, J_{\perp} = 0, \mathcal{D} = 0$) is a highly frustrated model. The classical ground state for that model is a 120° spiral magnetic structure. It has Bragg peaks at the corners of the triangular lattice Brillouin zone, which are points equivalent to the point K in Brillouin zone plot in Fig. 3.17.

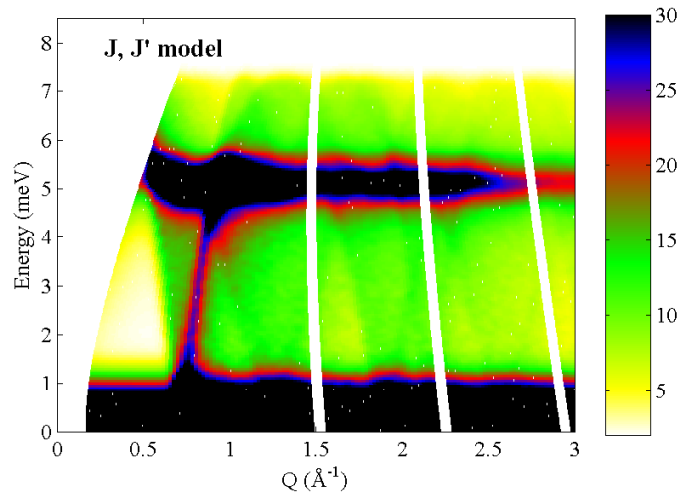


Figure 3.24: The powder average intensity distribution of the J, J' model including the quantum corrections as calculated by Chubukov *et al.* [51, 50], calculated for $J=4.8$ meV and $J'/J=1/8$. It demonstrates the failure of model to replicate the distribution observed in the data particularly the energy gap.

Spin-wave theory of the J, J' model

Secondly, if the next-nearest neighbour interaction, J' , is increased there are many possible degenerate ground states. Jolicoeur *et al.* have shown by spin-wave analysis that spins align into ferromagnetic stripes ordered antiferromagnetically from the ‘order by disorder’ mechanism if $J' \geq J/8$ [51, 50]. The magnetic structure is shown in Fig. 3.10 a). Such a magnetic structure gives the Bragg peaks at the mid-faces of the Brillouin zone hexagon and these are points equivalent to M in Fig. 3.17. The dispersion found from the linear spin-wave calculation has gapless modes at points such as K in the Brillouin zone and yet these are not Bragg peaks in this structure [50]. These modes become gapped when the first quantum corrections are included within the calculation because they renormalize the spin-wave result. Therefore the quantum fluctuations have a large effect on the main features in the linear spin-wave spectrum because the model is highly frustrated. A powder averaged intensity distribution of the spin-wave results, which includes the first quantum corrections, is shown in Fig. 3.24. To calculate the intensity distribution, the transverse dynamic correlation functions were assumed to follow the general formalism for a two

sublattice antiferromagnet:

$$\begin{aligned} S^{yy}(\mathbf{Q}, \omega) &= S^{xx}(\mathbf{Q}, \omega) \\ &= \frac{(S - \Delta S)}{2} |u_{\mathbf{Q}} + v_{\mathbf{Q}}|^2 G(\omega - \omega_{\mathbf{Q}}), \end{aligned} \quad (3.6)$$

where $u_{\mathbf{Q}} = \cosh(\theta_{\mathbf{Q}})$, $v_{\mathbf{Q}} = \sinh(\theta_{\mathbf{Q}})$, $\tanh(2\theta_{\mathbf{Q}}) = \frac{B_{\mathbf{Q}}}{A_{\mathbf{Q}}}$. The values of $A_{\mathbf{Q}}$ and $\omega_{\mathbf{Q}}$ come from the linear spin-wave calculation including the first quantum corrections (see Eqns. 5 and 7 in [50]). $\Delta S = \sum_{\mathbf{p}} v_{\mathbf{p}}^2$ is the reduction in spin due to the quantum fluctuations. $G(\omega - \omega_{\mathbf{Q}})$ is a gaussian function which models the resolution of the measurements. A polarization factor and magnetic form factor for the Ni^{2+} ion is also included. The energy scale of nearest-neighbour coupling, J , was chosen to give a bandwidth similar to that observed in the data. The intensity distribution was calculated for the critical value of J' which is where $J' = J/8$. Fig. 3.24 demonstrates the failure of the J, J' model to describe the data. For example, one of the main features of the data, that of the energy gap to the band of excitations, is not present. There is no structure in the low-energy edge of the scattering and this is partially a result of the over-simplification of using one layer and not two coupled layers as is actually the case in AgNiO_2 . The energy gap that was observed indicated that an easy-axis anisotropy was present and so such a situation is now discussed.

Easy-axis anisotropy and inter-layer interaction

A uniaxial state, such as sketched in Fig. 3.10, is further stabilized on a triangular lattice if there is an easy-axis anisotropy. In the regime of a large anisotropy, \mathcal{D} , and considering only nearest-neighbour interactions in the triangular plane, $J' = 0$, the ground state changes from the 120° spiral structure to a uniaxial structure when $\mathcal{D} \geq 3J/2$. In the uniaxial structure the three sublattice spins of the 120° spiral structure move to an up-up-down arrangement (UUD) as sketched in Fig. 3.10 [17].

In the limit where \mathcal{D} is large the physics of the Hamiltonian (Eqn. 3.5 where $J' = 0$ and $J_{\perp} = 0$) would be expected to approach that of an Ising triangular antiferromagnet where the ground state is infinitely degenerate for only nearest-neighbour interactions. However, the introduction of finite next-nearest-neighbour couplings, $J' > 0$, lifts the degeneracy and stabilizes the antiferromagnetic spin stripe order [52]. The degeneracy is also lifted if an inter-layer exchange is considered.

In the case of an inter-layer exchange, $J_{\perp} \neq 0$, the stacked antiferromagnetic stripe state is more favourable than the UUD state. This can be understood by considering the

energy per spin of the ground state. For a ferromagnetic inter-layer exchange ($J_{\perp} < 0$) and a magnetic structure of antiferromagnetic stripes in the plane, each spin has four favourable and two unfavourable inter-layer bonds. Whereas, in a stacked UUD structure, only two-thirds of the sites have two net favourable bonds and the remaining one third have two net unfavourable inter-layer bonds. Therefore, a ferromagnetic inter-layer coupling would give the energy per spin from the inter-layer exchange as $\text{Energy}_{\text{stripe}} = 2J_{\perp}$ compared with $\text{Energy}_{\text{UUD}} = J_{\perp}/3$. Hence, the antiferromagnetic stripes structure is the lower energy state of the two structures.

Linear-spin-wave calculation of full model Hamiltonian

In the discussion above, a simple J, J' model was shown to be insufficient to model the observed scattering distribution. There was evidence of an easy-axis anisotropy and a small ferromagnetic inter-layer interaction. A linear spin-wave calculation (LSWT) of the full model Hamiltonian was considered in an attempt to capture the main features of the excitations. A four sublattice model was used, in the linear spin-wave analysis, and this included the two lattices of up and down spins on the two Ni1 layers in the unit cell, as shown in Fig. 3.23. An easy-axis nearest-neighbour triangular antiferromagnet with additional weak in-plane next-nearest-neighbour antiferromagnetic exchange or weak ferromagnetic inter-layer couplings was considered. All these factors were incorporated into the model Hamiltonian in Equation 3.5.

Initially the minimal model, where $J' = 0$, is considered. In such a situation a collinear model is stable classically only if $\mathcal{D} \geq 3J/2$. The antiferromagnetic stripe order of AgNiO_2 is stabilized as the ground state if there is a ferromagnetic inter-layer exchange, $J_{\perp} < 0$. An example of the powder averaged spin-wave calculation is plotted in Fig. 3.25 b). The best-fit value of \mathcal{D} was that which reproduced the observed energy gap in Fig. 3.18 B.

The best-fit value of the inter-layer coupling, J_{\perp} , was that which best modelled the onset of scattering at $Q \sim 1.1 \text{ \AA}^{-1}$, in Fig. 3.18 C. The best-fit value of J was that which reproduced the observed bandwidth. Therefore, the model captured the overall bandwidth, the energy gap and the inter-layer coupling. Yet, the LSWT calculation does not fit the observed intensity distribution, demonstrated by taking a broad cut in Q though the intensity as shown in Fig. 3.25 a). The intensity distribution predicted by the LSWT calculation peaks at the onset energy within a slope to the end of the band of intensity. By contrast the data gave a more uniform block of intensity across this broad Q range. The shape of the low-energy band is not reproduced and the clear minima are not apparent in the

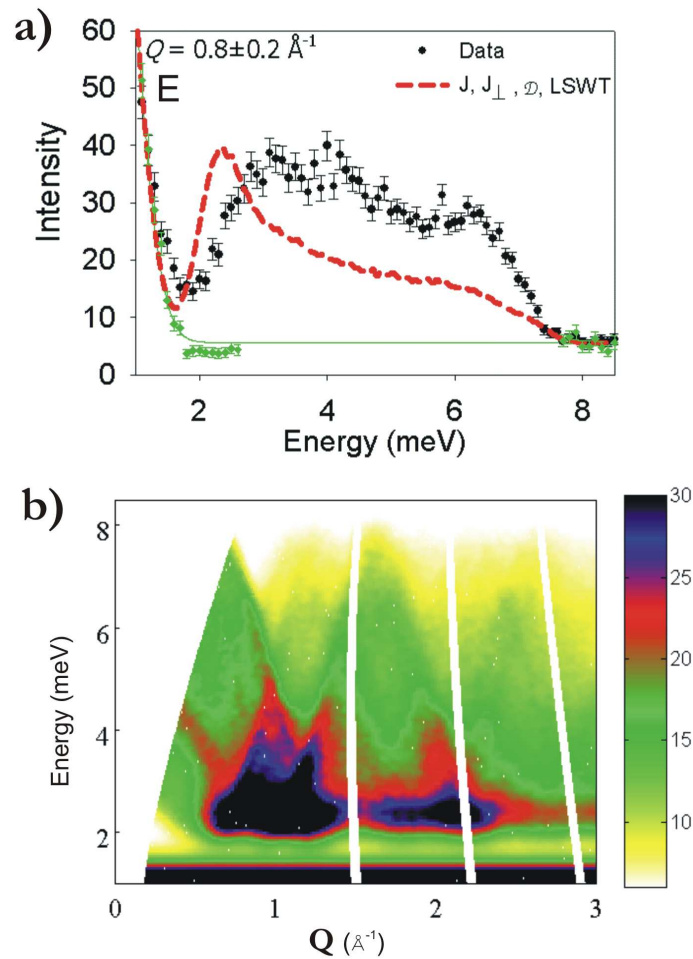


Figure 3.25: Spin-wave calculation results for the model parameters $J=0.97$ meV, $J'=0$, $J_{\perp}=-0.54$ meV, $\mathcal{D}=1.40$ meV. a) A broad plot of the intensity averaged over a broad range in Q . It shows the intensity distribution is not captured properly. b) The powder averaged simulation of the low resolution data for the spin-wave calculation shows the large intensity at low energies. The model captures the overall bandwidth observed in the data but not the intensity distribution.

energy gap at the Q points of the magnetic Bragg peaks. It was found that introducing next-nearest-neighbour couplings had the effect of making higher energy modes more intense and produced a more uniform intensity distribution in the broad Q cut. Although this fitted better to the data, the overall intensity distribution did not match the data because the low Q and low-energy edge of the excitation band was too shallow. This result was due to minima in the LSWT dispersion at Q points which are not Bragg peaks.

Chubukov and Jolicoeur [50], have found, by investigating the J, J' model within a single triangular layer, that the gapless modes at points such as K in Fig. 3.17 become gapped when quantum corrections are considered. Therefore it may be expected that if quantum corrections were to be considered the dispersion at low energies could change considerably and greatly improve the agreement between the LSWT calculation and the data. The dispersion may then approach something similar to that of the parametrization model.

3.4 Conclusions on AgNiO_2

These experiments have shown that AgNiO_2 displays a very different structural distortion and magnetic order from the current theoretical models. The high resolution diffraction measurements indicated a periodic contraction and expansion of NiO_6 octahedra in a three-sublattice structure. This was due to charge disproportionation on the Ni sites. The low-temperature magnetic diffraction pattern was explained by a collinear antiferromagnetic order of ferromagnetic chains with ordered moments present only on the electron-rich Ni sites. Both the magnetic order and structural distortion reported here are very different from theoretical models by Mostovoy and Khomskii [25] for Jahn-Teller transition metal ions coupled in a triangular lattice arrangement by near 90° metal-oxygen-metal bonds. That model predicted ferro-distortive orbital order and dominant ferromagnetic in-plane interactions, and this has been observed in NaNiO_2 [32, 33, 34, 35].

The observed low temperature dispersion was parameterized with a simple model that indicated the major dispersions were within the triangular plane. A smaller inter-layer dispersion was also probable. The data was compared to the results of two models. Firstly, the previous spin-wave calculation of Chubukov and Jolicoeur in which a single triangular layer was considered which had both J and J' coupling and which included quantum corrections. Secondly, the model Hamiltonian which included further terms from which a linear-spin-wave calculation was made. Although a ferromagnetic inter-layer exchange and an easy-axis anisotropy was added to the Hamiltonian, the data was not modeled fully.

The main features of the energy gap and band of excitations were replicated but the intensity distribution did not match that observed. The ordered magnetic moment of the NI1 sites, $1.552(7) \mu_B$, was reduced, ($\mu = 2\mu_B$ for a $S = 1$ system and $g = 2$) implying some quantum fluctuations. Although within the measured powder-average excitation spectrum no clear evidence for the effects of quantum fluctuation were found, it was realized that inclusion of quantum corrections could have a considerable impact on the key features in the spin-wave distribution because of the level of frustration. That has been highlighted by the work of Chubukov and Jolicoeur when considering the J, J' model. Therefore, it would be interesting to include these quantum corrections into the LSWT result for our model Hamiltonian to investigate whether a better agreement with the observations could be obtained.

Chapter 4

Quantum Phase Transition in the Quasi One-Dimensional Ising Ferromagnet CoNb_2O_6 in a Transverse Field

This chapter presents the magnetic phase diagram and the spin excitations as a function of applied field, for the quasi one-dimensional Ising ferromagnet, CoNb_2O_6 where the magnetic field was applied transverse to the Ising direction of the spins. The magnetic order of CoNb_2O_6 is suppressed at sufficiently large fields such that a transition occurs to a paramagnetic phase. Therefore the aim of these experiments was to observe how the magnetic order and excitations would evolve through the field-driven quantum critical point. The chapter firstly presents single-crystal neutron diffraction measurements of the magnetic order at low temperatures as a field was applied perpendicular to the Ising axis. Secondly, it presents inelastic neutron scattering measurements of the excitation spectrum close to the critical field. The phase diagram observed for the magnetic structure had three ordered phases and a paramagnetic phase. In the ordered phase gapless modes were observed together with the expected higher energy modes and in the high-field paramagnetic phase sharp magnon modes were observed.

4.1 Introduction

CoNb_2O_6 has been characterized as a quasi one-dimensional Ising-like ferromagnet with a relatively low exchange energy and this makes it an ideal system in which to study a quantum phase transition in an applied field. The Ising magnet in a transverse field is a simple system to explore the physics of quantum phase transitions. By applying a transverse field perpendicular to the Ising direction, the system undergoes a quantum phase transition at a field comparable to the intra-chain exchange energy. At low temperature quantum fluctuations largely drive the phase transition and the quantum fluctuations are increased by increasing the applied field. As the quantum fluctuations increase, the system moves from an ordered ferromagnet, with an ordered moment along the Ising direction, to a paramagnetic state where, on each site, the spins fluctuate between the two possible states, up or down.

The three-dimensional dipolar coupled Ising ferromagnet LiHoF_4 has been studied in a transverse field and inelastic neutron scattering has been used to study the behaviour of the energy gap [53]. The excitations that have been observed in the case of LiHoF_4 are magnons on both sides of the phase transition because the couplings are three-dimensional and long-range. Therefore the behaviour is well described by a mean-field approximation where spin-waves are excited on both sides of the transition. In addition, the hyperfine coupling to the nuclear spin is large and becomes relevant very close to the critical field when the gap is small. In that case the combined electron and nuclear spin had to be considered in order to understand the mechanism of the transition and so this was a departure from the simple model of Ising spins in a transverse field.

CoNb_2O_6 has been characterized as an Ising-like chain system with strong ferromagnetic couplings along the chains. The columbite crystal structure of CoNb_2O_6 is shown in Fig. 4.1 and it has the orthorhombic space group Pbcn . It has similar b and c lattice parameters ($b = 5.7019(2) \text{ \AA}$, $c = 5.0382(1) \text{ \AA}$) and the a lattice parameter is nearly three times their length, $a = 14.1337(2) \text{ \AA}$ at 2.5 K [54]. It forms layers of slightly distorted oxygen octahedra which are perpendicular to the a -axis. Within each layer, the edge sharing oxygen octahedra form chains along the c -axis. The main interaction is expected to be between neighbouring Co ions along the c -axis through a near 90° Co-O-Co bond. This bond is expected to be ferromagnetic due to the overlap of the outer d electron orbitals of the Co with orthogonal p-orbitals of the oxygen. In Fig. 4.1 b) the area marked in grey demonstrates the anisotropic triangular lattice in the (a, b) plane and the Co chains which run along the

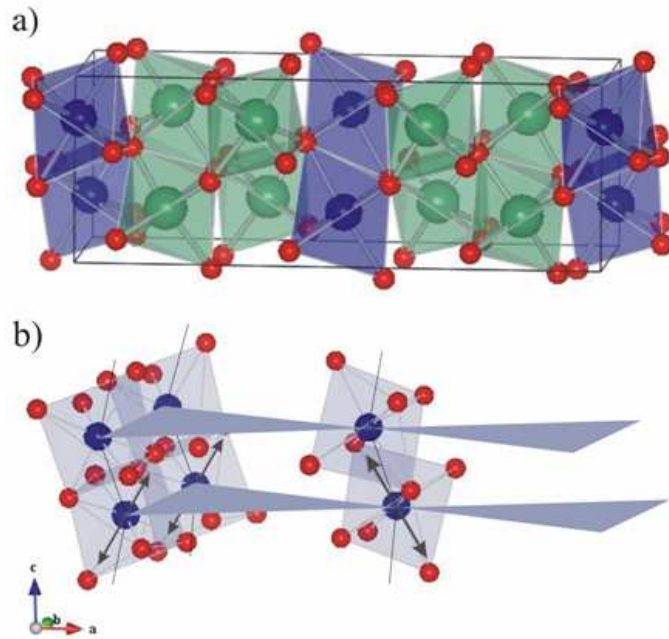


Figure 4.1: a) Unit cell of the crystal structure of CoNb₂O₆ the CoO₆ octahedra are coloured blue and the NbO₆ octahedra are coloured green. b) A quasi 1-D Ising like ferromagnet with magnetic chains running along the *c*-axis and the Ising direction is indicated by the double headed arrow [57].

c-axis. The canting angle of the moment of the Co²⁺ is 32° to the *c*-axis and it lies in the (*a*, *c*) plane [55].

Neutron diffraction measurements have revealed long-range magnetic order below 3 K where the spins in the chains order ferromagnetically. The order between the chains is more complex because the chains form an anisotropic antiferromagnetic triangular lattice in the (*a*, *c*)-plane. The chains order in an incommensurate magnetic structure below 3 K. Below 1.97 K a commensurate antiferromagnetic ordered state has been observed with a moment $\mu = 3.05(3)\mu_B$ and ordering wave vector (0, 0.5, 0) [56]. A series of neutron diffraction experiments have been carried out in zero magnetic field [56, 58] and with applied magnetic fields at a series of angles within the (*a*, *c*)-plane [57, 60, 61] and have mapped out the magnetic phase diagram at low fields. In further neutron scattering measurements the quasi one-dimensional character of the system has been confirmed by the observation of a diffuse sheet-like scattering in the (*a*^{*}, *b*^{*})-plane indicating chains of spins along the *c*-axis [62, 63].

Single crystal susceptibility measurements have shown that the susceptibility is significantly smaller along the *b*-axis than along the other crystallographic directions which

implies that the easy-axis direction must be perpendicular to the b -axis [56].

Specific heat measurements have shown a peak in the heat capacity at 3 K and a further anomaly at approximately 1.9 K which is indicative of a spin gap [64, 65]. Hanawa *et al.* have modelled the peak shape in the heat capacity by a two-dimensional spin-half Ising model and have found an effective ferromagnetic exchange $J=6$ K (0.52 meV) and inter-chain couplings $J'=0.062$ K (5.3 μ eV) [64]. However these values should be taken as qualitative since the geometry of the interactions should have been modelled as one-dimensional.

Magnetization measurements have been made for magnetic fields applied within a series of directions in the (a, c)-plane [65]. The measurements have been fitted to a Hamiltonian including crystal field levels, exchange couplings and dipolar interactions and have indicated that there is an intra-chain coupling between the true spins $J= 3.5$ K (0.30 meV) and antiferromagnetic inter-chain couplings of approximately $J'=-0.09$ K (7.7 μ eV). That analysis has been fitted to a crystal field model where the lowest energy state of the Co^{2+} ion is the Kramer's doublet of the $S=3/2$ state and therefore the high-spin state. The octahedral field around the Co^{2+} of CoNb_2O_6 splits the ^4F state and produces the orbital triplet $^4\text{T}_1$ ground state. The local C_2 distortion of the CoO_6 octahedra lifts the threefold degeneracy of the octahedral field. These levels are further split by the spin-orbit coupling and exchange interaction into six Kramer's doublets, the lowest of which is the $S=3/2$ state.

ESR measurements have been made with a field applied along the a -axis, which is 59° from the two Ising axes [66]. The results have been fitted to an anisotropic Heisenberg type spin model where, for the intra-chain coupling, the ratio of the coupling for spins aligned along the Ising axis to spins aligned perpendicular is $J/J_\perp = 0.11$. Ising-type behaviour is common in Co^{2+} compounds and has been seen in other cobalt compounds such as CsCoCl_3 [67] or CoF_2 [68].

Pfeuty has calculated that the critical field for an Ising chain in a transverse field is $B_C=J/(2g\mu_B)$, below which there is magnetic order at zero temperature. Given the estimated intra-chain coupling of 0.52 meV [64] and $g = 2.72$, the critical field has been estimated to be less than 10 T. Therefore the critical field of the Ising chain should be accessible with the magnets currently available for use in neutron scattering experiments.

Inelastic neutron scattering measurements in zero field have confirmed dominant one-dimensional interactions along the c -axis [69]. Those measurements have shown that there is a ferromagnetic Ising exchange, $J\sim 1.5$ meV, and other anisotropic terms have been estimated to be of order 0.5 meV. Fig. 4.2 shows how the excitation energy gap decreases

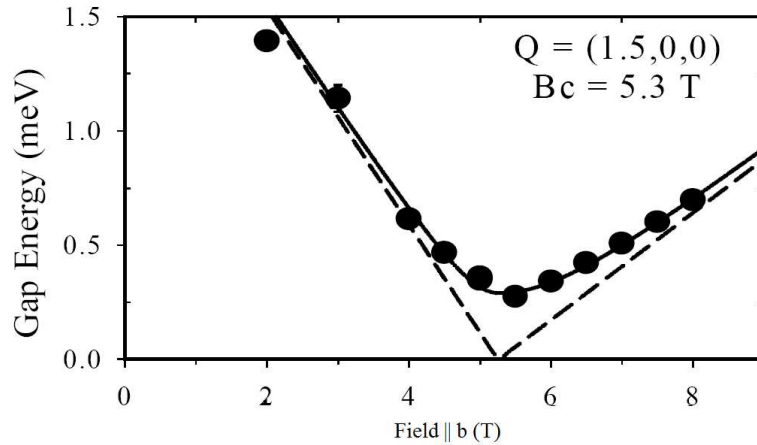


Figure 4.2: The energy gap to the first excitation measured at the $(1.5, 0, 0)$ as a field is applied perpendicular to the Ising direction of the chains [69]. The transition field is estimated to be 5.3 T. Since $(1.5, 0, 0)$ is not at a magnetic Bragg position the energy gap is not expected to close completely at this wave vector.

with an applied transverse field and then increases again which indicates a critical field at the energy gap minimum at $B_C \sim 5.3$ T.

In summary, neutron scattering measurements, susceptibility, specific heat and ESR measurements have shown that CoNb_2O_6 is a quasi one-dimensional Ising-like ferromagnet. The transition from the ferromagnetically ordered state to the high-field paramagnetic state occurs at an accessible magnetic field. This makes CoNb_2O_6 an ideal system to study the phenomena of quantum phase transitions and explore the change in energy gap of an Ising magnet and the excitations on either side of the transition.

4.2 Phase Diagram of CoNb_2O_6 in a Transverse Magnetic Field

The aim of the experiments described in this section was to explore the phase diagram of CoNb_2O_6 in an applied magnetic field that was transverse to the Ising direction. CoNb_2O_6 has been identified as a quasi one-dimensional Ising-like magnet in a series of studies [60, 64, 65, 66]. By applying a field transverse to the Ising direction, quantum fluctuations are expected to suppress the magnetic order and to drive a transition to a paramagnetic phase at a field comparable to the intra-chain exchange energy. Also, since large single-crystal samples can be grown, neutron scattering experiments are feasible and the intensity of the

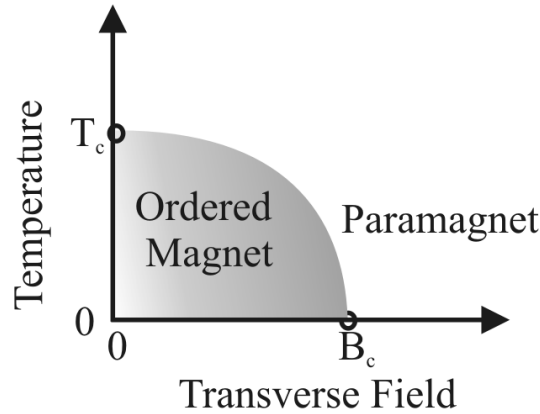


Figure 4.3: Predicted phase diagram of Ising chains with dominant intra chain coupling and much weak inter-chain couplings in a transverse field [71].

inelastic magnetic scattering is measurable [70]. Therefore CoNb_2O_6 is a good compound to study the Ising chain in a transverse field model because its small exchange couplings should lead to an experimentally accessible phase transition.

In contrast, as stated earlier in § 4.1, LiHoF_4 is a three-dimensional Ising magnet and magnon modes have been seen on both sides of the phase transition whereas in a one dimensional Ising magnet the excitations are solitons in the low field phase and magnons in the high field phase. The fact that there are two distinctly different excitations on either side of the transition leads to the interest in investigating the nature of this transition.

There are two properties of CoNb_2O_6 that are relevant to its magnetic structure. First the overriding feature is that it has chains of Ising-like spins. Second, its weak antiferromagnetic inter-chain couplings are geometrically frustrated. CoNb_2O_6 is quasi one-dimensional because it is composed of Ising chains with relatively stronger intra-chain coupling compared with its weaker inter-chain couplings. A system of weakly coupled Ising chains is predicted to show predominantly one-dimensional Ising physics in the ordered phase and far from the transition field [71]. Fig. 4.3 sketches the predicted phase diagram for an Ising chain in the case of weak inter-chain couplings. The effect of the inter-chain coupling is to increase the critical field of the transition and also stabilize long-range order at a finite temperature.

The weaker inter-chain couplings are frustrated. The reason is that the Ising chains are arranged in the (a, b) -plane in a triangular lattice which frustrates the weak antiferromagnetic inter-chain couplings. The effect of the frustration in this arrangement is also

relevant to the phase diagram of this material and is seen to affect the development of the zero-field magnetic structure. The zero-field magnetic order has been investigated in a series of studies [54, 56, 60]. The long-range magnetic order which has been observed in those studies can be understood from the physics of the classical Ising model on the antiferromagnetic triangular lattice with spatially anisotropic couplings. The system in zero field and at temperatures above $T_{N1}=2.96$ K is a paramagnet. Below T_{N1} , the spins order in an incommensurate spin-density wave along the b -axis, which is the strongest coupling direction of the triangular lattice. The magnetic Bragg peaks that have been measured in this phase have been indexed with an ordering wave vector $(0, q_y, 0)$ where $q_y = 0.37$ at T_{N1} [56]. As the temperature of the system is reduced to $T_{N2}=1.97$ K the ordering wave vector varies smoothly from $q_y = 0.37$ to $q_y = 0.5$. At T_{N2} a first-order transition occurs to a commensurate antiferromagnetic state where $q_y = 0.5$. The commensurate antiferromagnetic phase is more stable at $T = 0$ because, compared with the incommensurate phase, it has a lower mean-field energy.

The present work investigated the change in the magnetic ordering of CoNb_2O_6 as a magnetic field was applied transverse to the Ising direction. A transverse field does not commute with the Ising exchange Hamiltonian whereas a field parallel to the Ising direction does commute. The quantum fluctuations introduced by a transverse magnetic field are expected to drive a quantum phase transition at a critical field and so this was the focus of this study. In CoNb_2O_6 the application of a magnetic field perpendicular to the Ising direction is made difficult because there are two Ising directions in the unit cell. The Ising chains in the unit cell are tilted from the c -axis by $\pm 32^\circ$ within the (a, c) -plane. Previous studies, have investigated the phase diagram with a field applied within the (a, c) -plane. They have always had a component of the field along the Ising direction and therefore along an easy axis of the system such that at low fields a series of phase transitions have been observed [57, 60, 61, 72]. For a field along the crystallographic c -axis, above 0.1 T, a ferrimagnetic phase, indexed by $(0, 1/3, 0)$, has been observed below 3 K. At higher fields and higher temperatures two phases with the ordering wave vectors $(0, 1/3, 0)$ and $(0, 1/2, 0)$ have been seen to co-exist. Similarly, a series of phases have been observed when a field is applied along the crystallographic a -axis. The phase diagram for a series of field directions in the (a, c) -plane has also been investigated by Weitzel *et al.* [65].

The aim of the present study was to observe the effect of a field which was purely transverse to the Ising direction and therefore the field had to be applied along the crystallographic b -axis because the two Ising directions lay in the (a, c) -plane. Therefore the

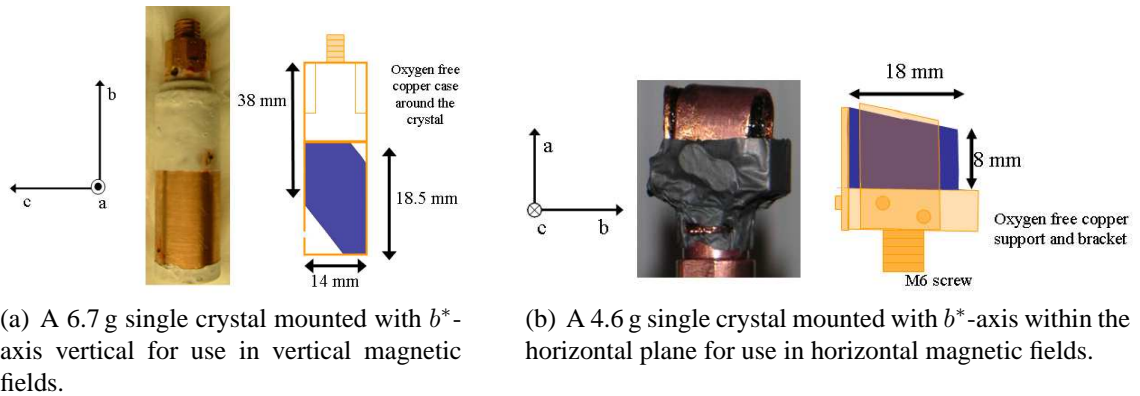


Figure 4.4: Photographs and sketches of the single crystal samples mounted onto an oxygen free copper support that ensured the crystal was kept firmly in place in an applied field. The white paint in a) on the oxygen free copper support is gadolinium paint and the grey foil in b) is gadolinium foil which masks most of the copper illuminated by the beam which reduces the background scattering.

phase diagram could be explored as the applied field smoothly varies the quantum fluctuations in the system.

4.2.1 Experimental Details

The neutron single-crystal diffraction experiments were performed in different scattering planes using both vertical and horizontal applied fields. In this way an overview of the phase diagram could be obtained together with an understanding of the sensitivity of the system to the alignment of the field with respect to the direction transverse to the Ising axis. The advantage of the vertical field magnet was that there were few restrictions on the available regions in the horizontal scattering plane and therefore by using an array of detectors a large area of reciprocal space could be observed in one measurement. However, in this setup the angle of the applied field with respect to the b^* -axis was fixed. Experiments with a horizontal field magnet allowed for measurements to be made where the field direction was tilted away from the b^* -axis and therefore the sensitivity of the measurements to the field direction could be tested.

The experiments were performed on single crystal samples. They had been cut from the same batch of crystals that have been described in [70]. The sample was mounted in an oxygen-free copper support as shown in the photographs and sketches in Fig. 4.4. Because the field was applied perpendicular to the large magnetic moment of the ferromagnetic

chains, a large torque was exerted on the sample. The sample mount ensured that the crystal did not rotate in the applied field and the oxygen-free copper ensured a good thermal contact with the sample stick at temperatures of tens of milli-kelvin.

Experiments Using Vertical Field Magnets

For these experiments the sample was mounted such that the crystallographic b -axis was vertical and the $(h, 0, l)$ reflections were accessible in the horizontal scattering plane. A 6.7 g single crystal was used. These experiments were technically challenging with the conventional vertical-field magnets that were used because it was necessary to have detectors that could measure the magnetic scattering out of the horizontal plane. This was in order to measure the magnetic Bragg reflections, which were at wave vectors of the type $(0, k, 0)$. Two methods were used to achieve this. At the reactor source at the HMI the Flat-Cone-Diffractometer E2 was used, which has a tilting multi-detector bank. At the spallation source ISIS the large detector array time-of-flight instruments, GEM and MAPS, were used.

Low field measurements using the E2 diffractometer

The initial experiment at low fields was performed using the Flat-Cone-Diffractometer E2 at the HMI. The sample was mounted on a dilution fridge insert in the cryomagnet VM-4 which had a large vertical opening angle. Therefore, a base temperature of 30 mK and a maximum vertical field of 4 T could be achieved. The crystal was mounted with the crystallographic b -axis vertical and the (a, c) -axes in the horizontal plane. The instrument, E2, had a tilting multi-detector bank, which could be tilted out of the horizontal plane, and it also had a tilting sample table that allowed the magnet to be tilted at the same angle. So measurements could be made of reflections (h, k, l) , where h and l were variable and k was fixed by the vertical angle of the detector. Fig 4.5 a) shows a sketch of the setup. The wavelength used was $\lambda = 5.19 \text{ \AA}$ ($k_f = 1.21 \text{ \AA}^{-1}$), which meant a 6.1° angular tilt of the sample and detector bank was necessary to reach $(h, 1/2, k)$ reflections. The angular width of the detector bank, $\pm 1.5^\circ$ from the nominal position, was such that the detectors integrated the intensity over a range of k values, $\delta k \pm 0.12$ at $k = 0.5$, as shown in Fig. 4.5 a).

Overview of phase diagram using the GEM and MAPS instruments

Further experiments were carried out using the diffractometer GEM and the chopper spectrometer MAPS at ISIS. The sample was mounted on either a dilution stick insert or a

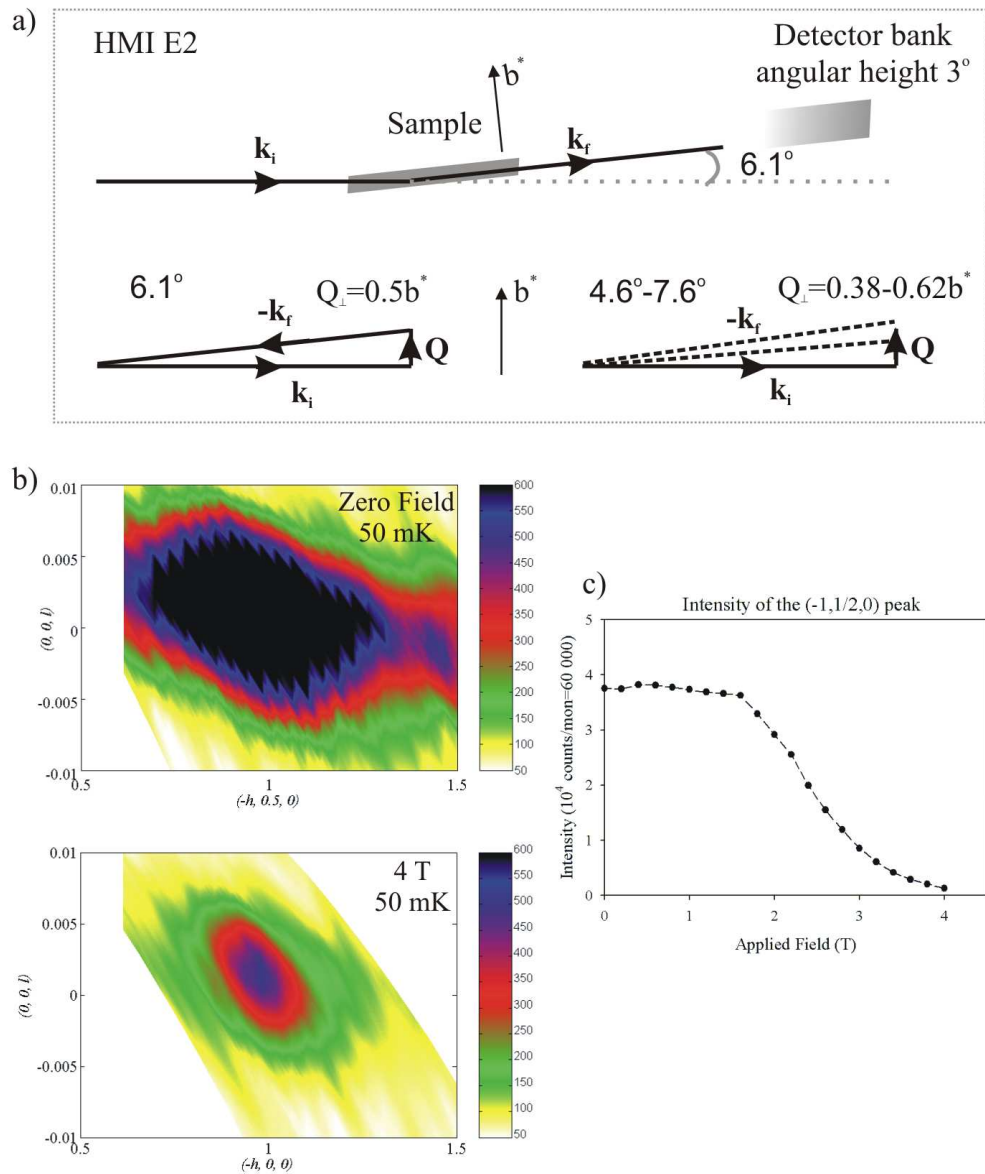


Figure 4.5: a) A sketch of the set up for accessing magnetic Bragg reflections using the lifting arm detector on the E2 instrument. Both the sample and the detector were tilted by 6.1° to access Bragg peaks $(h, 1/2, l)$, yet due to the finite height of the detector bank measurements integrated the intensity of scattering over a range of wave vectors $(h, 1/2 \pm \epsilon, l)$ as indicated in the lower sketch of the scattering triangles. Plot b) shows two measurements made at zero field and at 4 T at the nominal wave vector $(-1, 1/2, 0)$. The colour indicates the intensity in counts/(mon= 10000) approximately 30 s counting time. The change in the integrated area of the reflection with field is plotted in c) which shows a large decrease in intensity at approximately 2 T and there is a significant drop in the intensity by 4 T.

sorption insert, which reached base temperatures of 50 mK or 300 mK respectively. Again, a cryomagnet was used to apply fields of up to 8 T in the vertical direction, along the b^* axis of the crystal. Magnetic Bragg peaks were observed in the out-of-plane low-angle detectors, which were not masked by the vertical edges of the magnet window on the GEM diffractometer. The low-angle detectors, bank 1, were used such that certain magnetic Bragg reflections could be detected by rotating the sample. Fig. 4.6 a) shows the regions of the reciprocal lattice space covered by that bank of detectors for the position of the sample used for most measurements. The lines indicate the four sections of bank 1 and the hashed region shows the area of reciprocal space covered by the detectors.

The position-sensitive detectors of the MAPS spectrometer allowed better wave vector resolution measurements to be made. Fig 4.7 shows the large region of reciprocal space accessible with the MAPS large array of detectors and with the large vertical opening angle of the magnet. This angle was $\pm 7^\circ$. The lines show high resolution coverage of a large region of reciprocal space in which there is a series of Bragg peaks. This was a much larger area than that covered by the GEM diffractometer and the resolution of the measurements was better, which made it easier to identify and distinguish different reflections.

Experiments Using Horizontal Field Magnets

The horizontal field magnet experiments used the cold neutron triple axis spectrometer V2 at the Berlin Neutron Scattering Center (BENSCH), Germany. The sample was a 4.6 g single crystal of CoNb_2O_6 . It was mounted on a dilution stick insert in the horizontal field cryomagnet, HM1, which allowed for a base temperature of 30 mK and a maximum field of 6 T. The crystal was aligned with the crystallographic b - and c -axes in the scattering plane. Again, a sample mount was made such that the crystal would be held firmly in place during the experiment as shown in Fig. 4.4 b).

The spectrometer was set up with a vertically focused Pyrolytic Graphite (002) monochromator and a horizontally focused PG(002) analyser. Elastic measurements were made at a wavelength, $\lambda = 4.19 \text{ \AA}$ ($k_f = 1.5 \text{ \AA}^{-1}$) in order to align the crystal. The second-order scattered neutrons were used to observe nuclear Bragg peaks within the region of scattering angles allowed by the wedges of the magnet. The final neutron wavelength was fixed at $\lambda = 5.61 \text{ \AA}$ ($k_f = 1.12 \text{ \AA}^{-1}$) for the diffraction and inelastic measurements since it gave a narrow energy resolution. A liquid-nitrogen cooled beryllium filter was placed between the monochromator and the sample to eliminate the neutrons from higher-order scattering off

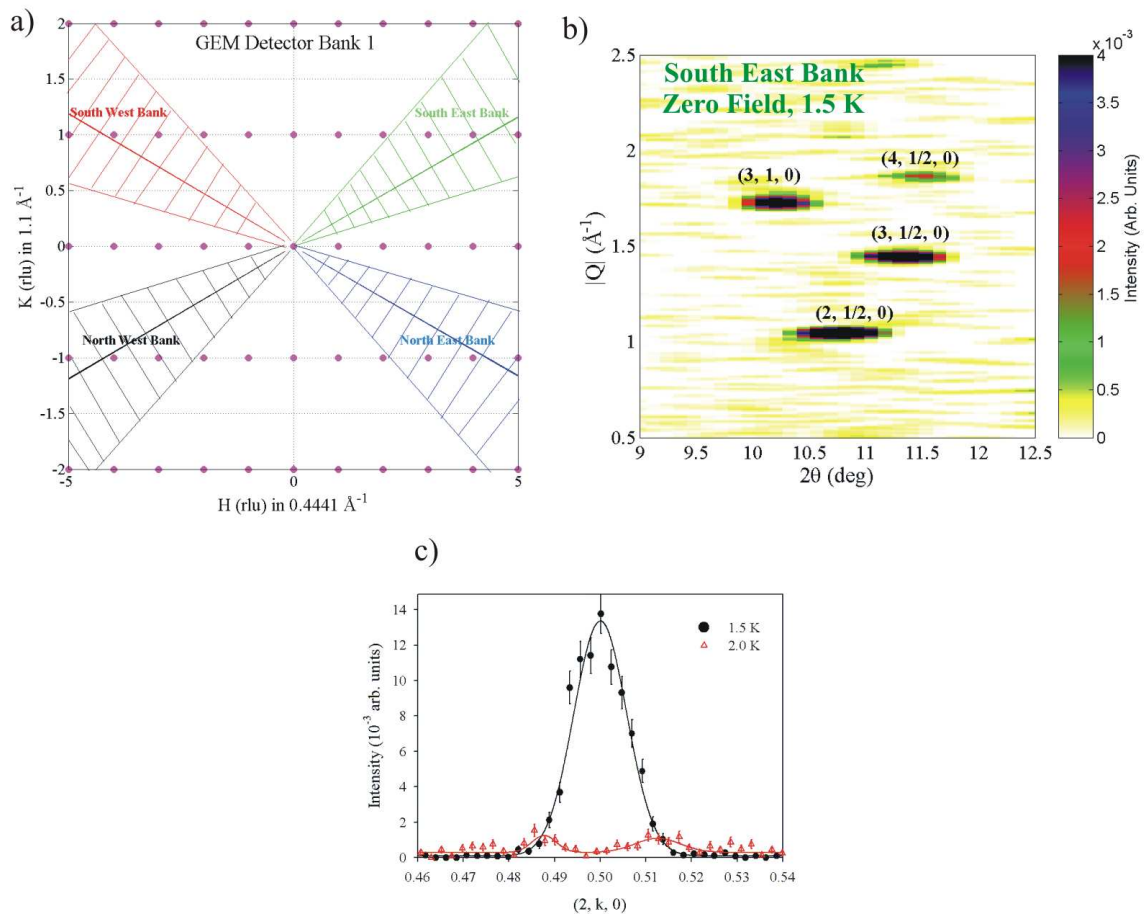


Figure 4.6: a) The detector coverage of the reciprocal space of CoNb_2O_6 by the low angle banks of the GEM diffractometer when the a^* -axis is 83° to the incident beam direction. This setup was used to observe changes in the magnetic structure. The hashed lines indicate the region of reciprocal space integrated over by the detectors which lie along Debye-Scherrer rings. b) A plot of a typical measurement indicating the Bragg reflections observed in the low angle banks of detectors at zero field. Counted for $10 \mu\text{A}$. c) A typical plot showing the commensurate phase and incommensurate phase observed in the measurements at higher temperatures.

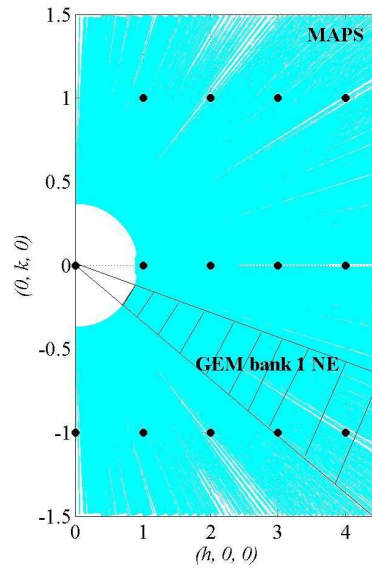


Figure 4.7: Detector coverage of the MAPS spectrometer. The region of reciprocal space covered by the MAPS detectors is coloured blue and the hashed section indicates the region of reciprocal space integrated over by a section of the GEM detector bank.

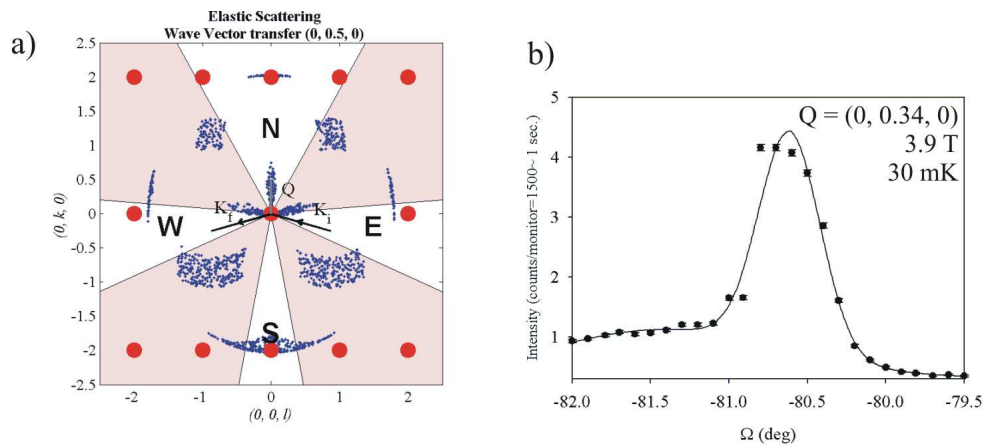


Figure 4.8: a) Diagram of the regions of reciprocal space masked by the horizontal magnet wedges. The sample was aligned such that the b -axis was parallel to the south(S)-north(N) direction in the magnet. The positions of the wedges are coloured pink. The red dots indicate the strong nuclear Bragg reflections. The black lines indicate the direction of the incident, K_i , and final, K_f , beam positions to achieve a wave vector transfer, Q , $Q=(0, 0.5, 0)$ for an initial and final energy of 2.6 meV ($K_f=1.12\text{\AA}^{-1}$). b) A plot of the intensity at the wave vector transfer $Q = (0, 0.34, 0)$ as the north-south magnetic field direction is rotated with respect to the sample while the b^* -axis with respect to the spectrometer is kept fixed. Therefore, this highlights the need for precise alignment of the sample since a small component of the field along the c -axis can considerably affect the magnetic order.

the monochromator. A 60' collimator was used between the monochromator and sample.

The setup used a horizontal magnet with four large wedges, which were present because of the coils of the magnet, and through which the beam could not pass. Figure 4.8 a) shows a diagram of the wedges in the horizontal plane and the necessary alignment of the sample to access the $(0, 0.5, 0)$ wave vector transfer. The wedges of the magnet caused restrictions on the wave vector positions that could be explored.

The sample was positioned such that the field was aligned along the b -axis for the measurements. This required initial alignment of the magnetic Bragg peaks with the central North-South regions of the magnet at zero field. It was necessary to adjust the angle of the sample to the applied field as shown in Figure 4.8 b).

4.2.2 Measurements and Results

The initial experiment using E2 explored the low field and low temperature phases of CoNb_2O_6 while the GEM and MAPS experiments investigated high fields and higher temperature regions. Finally, the horizontal field measurements allowed for detailed measurements of the behaviour close to the critical field at low temperatures. The results from each type of measurement will be discussed in turn.

Low Field Measurements

The sample was cooled at zero field and at low temperatures the field was increased in order to explore the phase diagram. Measurements were made at a series of temperatures and field values in order to map out the phase diagram.

The measurements from the E2 diffractometer mapped the intensity distribution for different rotation angles, ω , and scattering angles, 2θ . The intensity profiles were fitted with two-dimensional gaussians in $(\omega, 2\theta)$ space and corrected for the magnetic form factor and Lorentz factor. The Lorentz factor converts from $(\omega, 2\theta)$ to reciprocal space of the crystal. The Lorentz factor, L ,:

$$L^{-1} = \sin(\gamma) \cos(\mu),$$

where μ is tilt of the sample and detector with respect to the incident beam and γ is the projection of the scattering angle, 2θ , onto the horizontal plane [73]. Therefore γ can be derived as:

$$\cos(2\theta) = \cos(\gamma) \cos(\mu).$$

In this way the integrated intensities of the Bragg peaks were converted to magnetic structure factors. These integrated intensity values were then compared with the calculated intensity of the Bragg reflections for the nuclear structure and magnetic structure as given by Heid *et al.* [60]. The results were as follows.

At zero field the analysis agreed with the nuclear and magnetic structure suggested by Heid *et al.*. Magnetic Bragg peaks were observed, which could be indexed by the ordering wave vector $(0, 1/2, 0)$, where the chains of collinear spins were arranged antiferromagnetically along the b -axis. Therefore, the Ising chains were ordered in an up-down arrangement along the b -axis. The 4 T data showed no change in the magnetic structure but, as expected, the intensity of the peaks decreased considerably as shown in Fig. 4.5 for the $(-1, 0.5, 0)$ magnetic Bragg reflection. There was a significant drop in intensity above 2 T but Bragg peaks were still observed up to 4 T. Because of the larger vertical integration of the detector bank it was not clear if this drop in intensity was due to peaks at $(h, 0.5, l)$ reducing in intensity or due to peaks moving to another k position. The measurements taken above the ordering temperature, at the higher temperature of 5 K, showed no magnetic peaks above background intensity. Analysis of the $(h, 0, l)$ peaks showed no change in the crystal structure within the same range of temperature and field settings as were used for the magnetic Bragg measurements. The intensity of the magnetic Bragg peaks took some time to stabilize following a change in field and so this meant that the field was always changed slowly to avoid anomalous hysteresis effects. Further measurements would be needed to investigate the full field and temperature behaviour of this relaxation effect, though experiments into this relaxation have been reported at much weaker fields [57, 74].

High Field Measurements

High field experiments on the GEM diffractometer were made at a base temperature of 1.5 K with an applied field of up to 8 T. Again, measurements were made at a series of field and temperatures to form a phase diagram of the magnetic structure. Figure 4.6 shows the temperature dependence of the magnetic Bragg reflection $(2, 1/2, 0)$ which, upon heating, split into two incommensurate peaks at $(2, 1/2 \pm \varepsilon, 0)$. These measurements were in agreement with the zero-field measurements of Scharf *et al.* [56]. A similar transition to an incommensurate phase was seen when a magnetic field was applied.

Higher resolution measurements were made on the MAPS spectrometer at a base temperature of 300 mK. Since MAPS had a large array of position-sensitive detectors it was

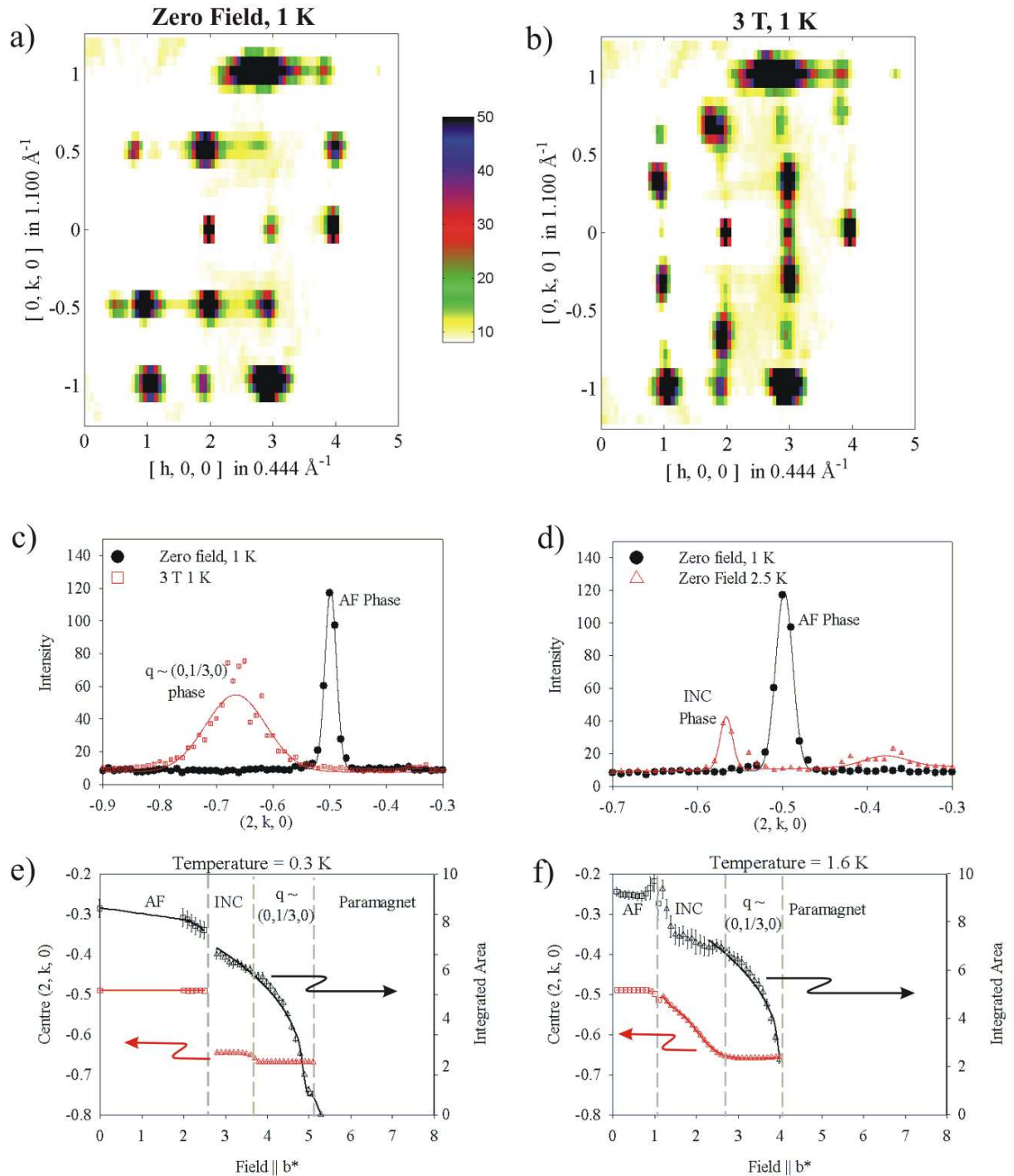


Figure 4.9: Plots a) and b) show a section through the MAPS white-beam diffraction data for a current of $10\mu\text{A}$. A series of magnetic Bragg peaks were observed in one measurement. The colour indicates the intensity and shows the change from a commensurate antiferromagnetic phase at zero field in plot a) to an incommensurate phase when a field is applied in plot b). Plots of integrating the intensity across one Bragg peak are given in c) and d) and they show the change in behaviour of the magnetic Bragg reflections at increased temperature, plot c, and in an applied field, plot d). Series of measurements were made in order to build the phase diagram in Fig. 4.10. Plots e) and f) show the change in the position (red) and integrated intensity (black) of the magnetic Bragg reflections at $(2, k, 0)$ as the field is varied at two temperatures, 0.3 K and 1.5 K.

possible to observe a large section of reciprocal space in one measurement and this is shown in Fig. 4.9 a) and b). The two figures show two measurements at zero field and 3 T where the colour indicates the intensity of the scattering. As a field was applied, the magnetic structure changed from a commensurate antiferromagnetic structure to an incommensurate magnetic structure. Plots of the intensity of one magnetic Bragg reflection are given in Fig. 4.9 c) where the magnetic Bragg peak is observed to move from $k = 1/2$ to $k \approx 2/3$. Measurements were also made at higher temperatures and Fig. 4.9 d) shows the Bragg peaks observed in an incommensurate phase at zero field which also had been observed in the GEM experiment. Three different ordered phases were identified by making a series of these measurements. They were the commensurate antiferromagnetic phase (AF), the incommensurate phase (INC), where the wave vector varied in field or temperature, and the phase where the ordering wave vector was approximately $(0, 0.34, 0)$ and where it 'locked in' to a stable structure over a range of fields and temperatures. The ordering wave vector of the phase near the critical field was $\mathbf{q} \sim (0, 0.34 \pm 0.01, 0)$, within the accuracy of the measurements, and this phase is indicated in Fig. 4.9 as $\mathbf{q} \sim (0, 1/3, 0)$ because an incommensurate wave vector close to $1/3$ was also consistent with the measurements. The majority of measurements were made as the applied field was increased at a fixed temperature. The results of two such measurements are shown in Fig. 4.9 e) and f). They show the variation in intensity and wave vector and the associated phases as the field was increased. The behaviour was different at low and high temperature. At low temperature the change from the antiferromagnetic phase persisted up to higher fields and the change to the incommensurate phase was sharper than at 1.6 K.

Fig. 4.10 shows the phase diagram which summarises the main results of the measurements in these high field experiments. At low temperature and low fields the commensurate $(0, 1/2, 0)$ phase was observed. Again at zero field the commensurate phase was seen to move into an incommensurate phase at higher temperatures, indexed with the ordering wave vector $(0, q_y, 0)$. A third phase was seen at higher fields. Above 2.8 T, at the base temperature of 300 mK, the magnetic Bragg peaks were indexed with an incommensurate wave vector. At 3.6 T the ordering wave vector was taken as $(0, \sim 1/3, 0)$ since the magnetic Bragg peaks were seen to be at $(0, \sim 1/3, 0)$ and $(0, \sim 2/3, 0)$. At 300 mK the transition to a paramagnetic phase occurred at 5 T.

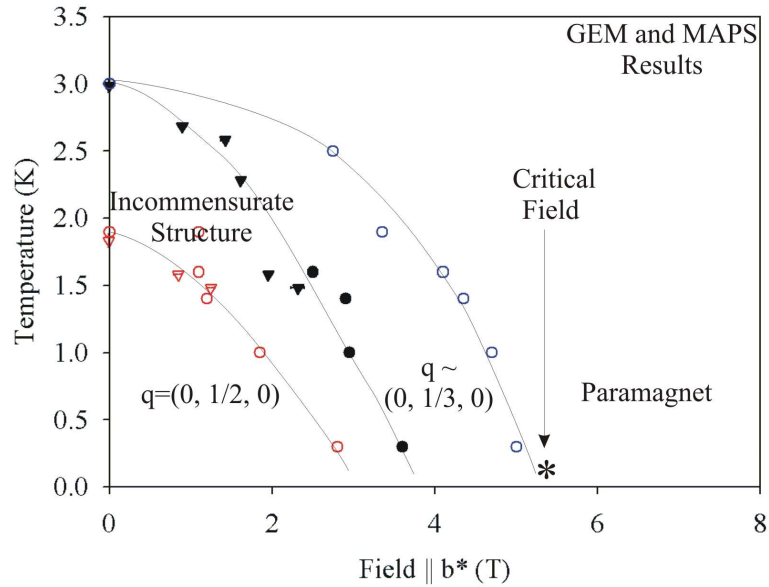


Figure 4.10: Phase diagram of the results extracted from the MAPS (circles) and GEM (triangles) experiments. Three phases were observed which were indexed with an ordering wave vector of $(0, 1/2, 0)$, an incommensurate wave vector which varied with field and temperature and a phase indexed with $(0, \sim 1/3, 0)$. The points indicate the measurements and the lines are guides to the eye.

Exploring the Sensitivity of the Phase Diagram to the Field Alignment

The experiments in a horizontal magnetic field allowed for an investigation of the stability of the $q \sim (0, 1/3, 0)$ phase as the field direction was rotated away from the b^* -axis. Therefore a small field component was applied along the c^* -axis also. In this experiment it was seen that close to the critical field in the $q \sim (0, 1/3, 0)$ phase the ordering wave vector was $(0, 0.34 \pm 0.01, 0)$. Figure 4.8 b) shows the result of measuring the intensity at the incommensurate wave vector $(0, 0.34, 0)$ Bragg peak as the North-South direction of the magnet was varied with respect to the b^* -axis of the crystal. This measurement indicated that the magnetic structure was extremely sensitive to the alignment of the magnetic field transverse to the Ising direction. Figure 4.8 b) shows that a variation of 0.5° from the optimum position would indicate no Bragg peak intensity at $(0, 0.34, 0)$ and this suppressed that phase and possibly stabilized order at other wave vectors in reciprocal space. At a field of 3.9 T a 0.5° rotation of the field from the b^* -axis would lead to a component of the field of 0.034 T along the c^* -axis.

All measurements in the horizontal field were made at the base temperature of 30 mK. Figure 4.11 a) shows two magnetic Bragg peaks observed at the base temperature and high

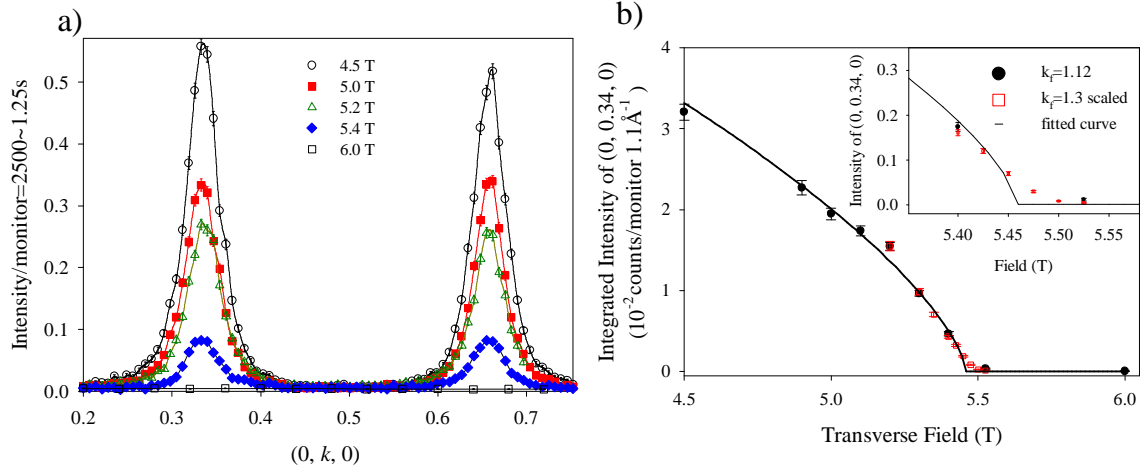


Figure 4.11: a) Measurements across the magnetic Bragg reflections $(0, k, 0)$ where $k = 0.34, 0.66$ at 30mK. The intensity of the magnetic Bragg reflections decreases in magnetic field. b) The change in intensity of the $(0, 0.34, 0)$ magnetic Bragg peak measured with $k_f = 1.12\text{\AA}^{-1}$ and 1.3\AA^{-1} . The line shows a fit with a power law form below a critical field of $5.45(5)$ T

field. The intensity of the magnetic Bragg peaks reduced to zero above $5.45(5)$ T. Above this field a search for Bragg peaks was made in the $(0, k, 0)$ region of reciprocal space and no reflections were measured. This signalled that either the order was suppressed completely or that the Bragg peaks moved to other points in reciprocal space. Inelastic experiments, to be described in the next section, showed that the excitation energy gap increased upon increasing the applied field above $B_C=5.45$ T, which is consistent with the behaviour expected for a paramagnet. It was therefore concluded that $B_C=5.45$ T was the critical field to the paramagnetic phase.

4.2.3 Analysis

It would seem that the low field measurements were not in agreement with the higher resolution measurements made on MAPS and GEM. Yet because the E2 multi-detector had a large vertical integration, it could have led to intensity from Bragg peaks at $(h, 1/2 - \epsilon, l)$ coming into the detector at the $(h, 1/2, l)$ position. Therefore the intensity at 4 T observed in the E2 experiment at the $(1, 1/2, 0)$ position may have been from the tail of the $(1, 0.34, 0)$ incommensurate Bragg peak, which was observed in the higher resolution experiments using MAPS and V2.

The phase diagram given in Fig. 4.10 shows the regions where three ordered phases

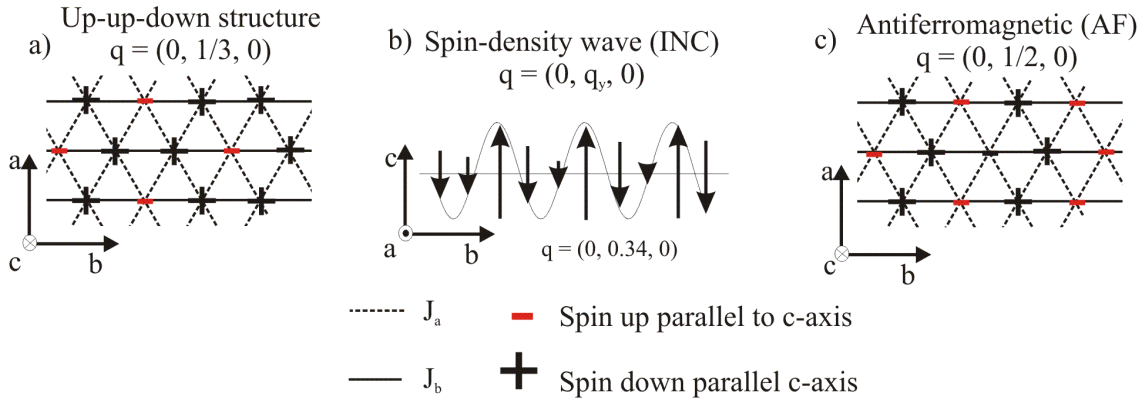


Figure 4.12: Sketches of the possible magnetic structures for three ordered phases observed: a) The Up-Up-Down structure (UUD), b) an incommensurate spin-density wave structure along the b -axis in the (a, b) -plane, c) antiferromagnetic structure (AF). The +/- symbols indicated chains of spins along the c -axis which align into or out of the (a, b) -plane

were observed. The three magnetic structures associated with those phases are given in the three sketches in Fig. 4.12. The long-range magnetic order is a result of the antiferromagnetic couplings of the spins in the (a, b) -plane which couple the Ising spins. The system is an anisotropic triangular lattice, where $J_a \neq J_b$, as indicated in the schematic diagram of Fig. 4.12.

The Ising model on the isotropic antiferromagnetic triangular lattice does not order down to $T = 0$ because there is a macroscopic number of degenerate ground states [17]. This degeneracy is lifted in the presence of a small longitudinal field and the system is then expected to develop a three sub-lattice order in a ferrimagnetic state. In this state the spins are aligned in a ‘up-up-down’ sequence (UUD) along each of the three equivalent directions of the lattice as shown in Fig. 4.12 a) [75]. In the case of an anisotropic coupling between the spins a spin-density wave structure is formed, where the ordering wave vector minimizes the energy of the system at that temperature. Therefore as the fluctuations in the system are reduced the ordering wave vector varies [76]. A sketch of the spin-density wave structure is given in Fig. 4.12 b) for $q = (0, 0.34, 0)$. Upon cooling to low temperatures the magnetic structure of CoNb_2O_6 is incommensurate as the ordering wave vector, $(0, k, 0)$, varies in the interval $0.37 \leq k \leq 1/2$. At a high magnetic field, the incommensurate region at low temperature is characterized by $1/3 < k \leq 1/2$. The anisotropic couplings lead to order along the strongest coupling direction, J_b . Analytical temperature dependence of the incommensurate wave vector, derived by considering the creation of domain walls due to

thermal fluctuations, has compared well with measurements on CoNb_2O_6 in zero field [65] where $J_a/J_b=0.63$. As the temperature is reduced the thermal fluctuations decrease and the ordering wave vector is dependent on the couplings and occurs at the value which minimizes the free energy of the system. In the mean-field approach, the energy of the system is minimized when the Fourier transform of the exchange couplings is minimized [76]. Therefore, the ratio of the inter-chain couplings is given by $J_a/J_b=2 \cos(\pi k) = 0.79$, $k = 0.37$, where the incommensurate ordering wave vector is $(0, k, 0)$ when the order first develops.

At low temperature and in low fields the fluctuations of the spins on each site were small and therefore a commensurate magnetic order was achieved whereby the spin on each site was maximized. The commensurate phase was characterized by the ordering wave vector $(0, 1/2, 0)$ and it had antiferromagnetic order along the b^* direction as shown in Fig. 4.12 c). The antiferromagnetic state becomes more favourable at zero temperature because the energy is minimized. The energy of the spin-density wave state at zero temperature to the antiferromagnetic state is:

$$E_{AF} = -J_b S^2 \quad E_{SDW} = -J_b S^2 \left(1 - \frac{3J_a^2}{2J_b^2}\right). \quad (4.1)$$

The strong hysteresis indicated that the transition from incommensurate order to antiferromagnetic order was probably a first-order phase transition. A first-order phase transition between the spin-density wave and antiferromagnetic order may be expected as the magnetic order ‘locks in’ to a commensurate wave vector and this is shown by the sharp change in the magnetic Bragg peak positions in Fig 4.9, plots e) and f). Heid *et al.* have concluded that the zero-field incommensurate-commensurate transition is a first-order transition due to the jump they have observed in the ordering wave vector [60].

When a small field is applied along the Ising direction it can stabilize the UUD state $\mathbf{q} = (0, 1/3, 0)$ as opposed to the antiferromagnetic state at $\mathbf{q} = (0, 1/2, 0)$. This can easily be seen by calculating the mean-field energies of the two states at $T = 0$. The energy per spin of the antiferromagnetic state is lower at zero field than the UUD state but the UUD state becomes more favourable as the field is applied, as shown below:

$$E_{AF} = -J_b S^2 \quad E_{UUD} = -\frac{J_b S^2}{3} - \frac{2J_a S^2}{3} - \frac{g\mu_B B S}{3}. \quad (4.2)$$

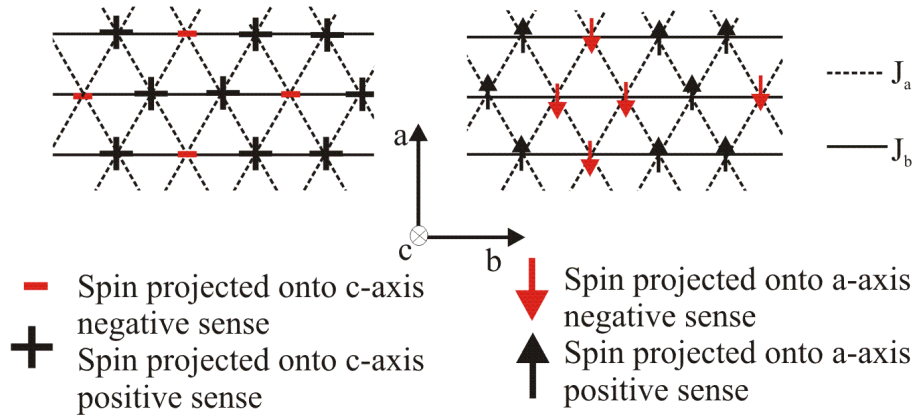


Figure 4.13: Sketches of the spins projected along the c - and a -axis for the UUD state in CoNb_2O_6 . Because the two different Ising chains in the unit cell are tilted in the (a, c) -plane differently, the spin structure when projected onto the a - or c - axes appears different. Left: A schematic diagram for the c component of the spins in the UUD structure which gives rise to magnetic Bragg reflections at $(h, k \pm 2/3, l)$. Right: The schematic diagram for the a component of the spins in the UUD structure which leads to magnetic Bragg reflections at $(h, k \pm 1/3, l)$. The selection rules are $h + k = 2n$ and $l = 2m$ where n and m are integers.

A transition to the UUD state is therefore expected above a field,

$$B \geq 2S(J_b - J_a)/g\mu_B.$$

At high fields the ordered phase in CoNb_2O_6 appears to be close to the commensurate UUD phase. Fig. 4.13 (left sketch) shows the magnetic structure for an UUD arrangement of the spins when projected onto the c -axis. The projection of the spin along the a -axis leads to a different structure because of the alternating tilt $\pm\gamma$, $\gamma = 32^\circ$, of the Ising axis away from the c -axis for the two chains in the unit cell. Fig. 4.13 shows that the magnetic structure of the a -component of the spins consists of a diamond arrangement of spins in the same sense. The arrangement is repeated every three b -lattice vectors and the surrounding spins are aligned in the opposite sense. The structure of the c -axis spin projection gives rise to magnetic Bragg reflections at $(h, k \pm 2/3, l)$ and the a -axis spin component leads to magnetic Bragg reflections at $(h, k \pm 1/3, l)$, where the selection rules are $h + k = 2n$ and $l = 2m$ where n and m are integers.

In the phase diagram of Fig. 4.10 the transition from the $(0, \sim 1/3, 0)$ phase to a paramagnetic phase is seen at 5 T at 300 mK. In the horizontal field measurements the $(0, 0.34, 0)$

magnetic Bragg reflection was observed to persist until 5.45 T at 30 mK and the phase diagram was also observed to be very sensitive to a slight change of the field direction from the crystallographic b -axis. In those experiments it was seen that, with a field of 0.034 T along the c -axis, the $(0, 0.34, 0)$ phase was suppressed well below the critical field of $B_{\parallel b^*} = 5.5$ T and may have been replaced by another phase with Bragg peaks not along the b^* -direction. Figure 4.11 indicates that the critical field was 5.45 T. Above 5.45 T a monotonic increase in the energy gap was seen from inelastic scattering measurements, described in the following section, and this was the behaviour expected for a paramagnetic phase. Therefore, the results above 5.45 T are consistent with a paramagnetic phase and not with another ordered phase with Bragg peaks at other points in reciprocal space. A misalignment could not be tested in the vertical field experiments because, in those diffraction measurements, the angle of the sample to field direction was fixed. Nevertheless, it is likely to have affected the phase diagram.

In summary, these measurements have investigated the phase diagram of the weakly coupled Ising ferromagnet as a function of a transverse field. The ordered antiferromagnetic structure was seen to undergo a first-order phase transition at zero field to an incommensurate phase before a transition to a paramagnetic phase. In transverse applied field, the quantum fluctuations were tuned and led to an incommensurate spin-density wave which was similar to an UUD state. At zero temperature, the transverse field drives a transition to a quantum paramagnetic state. At high fields, and therefore large quantum fluctuations, there was a transition to a paramagnetic phase at 30 mK when the critical field was 5.45(5) T. The nature and physics of this transition is further explored in the following inelastic scattering experiments.

4.3 Magnetic Excitations of CoNb_2O_6 in an Applied Magnetic Field Transverse to its Ising Axis

This section describes an inelastic neutron scattering experiment to investigate the interactions and excitation spectrum of CoNb_2O_6 in a magnetic field. As an Ising ferromagnet, the system can go through a phase transition when a transverse magnetic field is applied perpendicular to the Ising direction. The previous section showed that the application of the transverse field led to the suppression of long-range order and so to a paramagnetic state. Since CoNb_2O_6 is a quasi one-dimensional system, the two phases are expected to

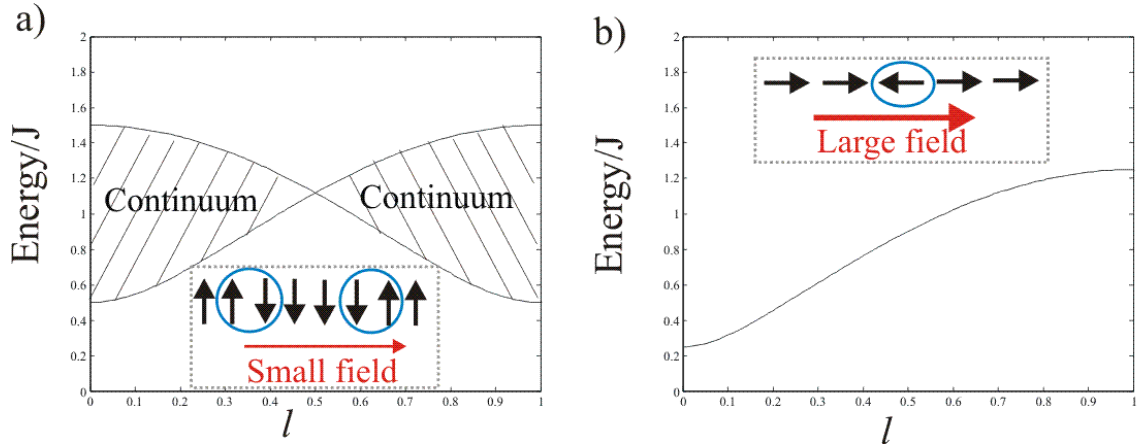


Figure 4.14: The excitation spectrum of a one-dimensional Ising ferromagnet: a) In the ordered phase, at low fields, two domain walls are excited creating a continuum of scattering between the plotted two lines. b) At high fields, in the paramagnetic phase, the excitations are single spin reversals opposite to the field direction which can propagate coherently leading to a single sharp mode.

have two distinctly different excitation spectra: at low fields pairs of solitons are excited in the ordered phase; spin flips are created at high fields in the paramagnetic phase. The aim of the experiment was to explore the change in the excitation spectrum in CoNb_2O_6 at transverse magnetic fields above and below this phase transition.

The Ising model in a transverse field was introduced in Chapter 1. At zero temperature the transverse field introduces quantum fluctuations that drive a quantum phase transition at a field comparable to the exchange energy. The Hamiltonian for the system is:

$$\mathcal{H} = -J \sum_i S_i^x S_{i+1}^x - g\mu_B B \sum_i S_i^z, \quad (4.3)$$

where J is a positive constant and is the magnitude of the ferromagnetic coupling. B is a field applied transverse to the Ising direction. The spectrum for the one-dimensional Ising chain in a transverse field is given in Fig. 4.14 for low and high fields. In the single Ising chain in the low-field case, there is a continuum of states between the two lines plotted in Fig. 4.14 a) which correspond to exciting two solitons by a scattered neutron. In the high-field phase one mode is observed as a spin is flipped opposite to the field direction and a magnon is created. The energy gap is lowest at the ferromagnetic Brillouin zone centre, $l = 0$, and is expected to decrease to zero as the magnetic field is increased from

the low-field phase. The critical field for the one-dimensional Ising chain is $B = J/2g\mu_B$. CoNb_2O_6 is predicted to have a sufficiently small ferromagnetic coupling that the critical field is experimentally accessible. In fact the previous section described how, at the critical field of 5.45(5) T at 30 mK, the system was observed to change from an ordered phase to a paramagnetic phase.

CoNb_2O_6 is a quasi one-dimensional system with inter-chain couplings that stabilize a long-range ordered phase at low temperatures. The spectrum considered for the one-dimensional Ising chain is also relevant to the quasi one-dimensional case. The inter-chain couplings are not expected to dominate the behaviour far from the transition field and so one-dimensional physics is relevant [71]. In the quasi one-dimensional system the dispersion of the excitations is expected to be three-dimensional around the critical field when the energy gap is small. In the paramagnetic phase the quasi-particles are spin flips from spins aligned along the field direction. Therefore the energy gap is increased again because of the Zeeman energy cost in reversing a spin opposite to the field axis.

The main coupling is along the Ising chains through a 90° Co-O-Co bond [56] because the exchange occurs via orthogonal oxygen orbitals and, according to the Goodenough-Kanamori rules, it is ferromagnetic. Analysis of heat capacity measurements and magnetisation measurements have shown that the main chain interaction is ferromagnetic and of the order of 1 meV. Also, the inter-chain interactions are weaker and in the (a, b) -plane where there is a series of exchange paths through a double Co-O-O-Co bond. Work by Heid *et al.* into the phase diagram of CoNb_2O_6 has identified some small antiferromagnetic inter-chain couplings within the triangular lattice of the order of $1 \mu\text{eV}$ [61].

The inelastic scattering measurements described next indicated the presence of strong magnon modes above the critical field. Below the critical field two components were seen in the inelastic scattering. There was low-energy scattering, which was possibly gapless, in addition to the scattering at higher energies, which would be expected from a soliton picture. The low-energy scattering was associated with the three-dimensional incommensurate magnetic order and so the inter-chain couplings appeared to have a significant effect.

4.3.1 Experimental Details

The experiment used the cold neutron triple-axis spectrometer, V2, at the HMI, which was described in § 4.2.2. The final neutron wavelength was fixed at $\lambda = 5.61 \text{ \AA}$ ($k_f = 1.12 \text{ \AA}^{-1}$). Again, the large wedges of the magnet restricted what measurements could

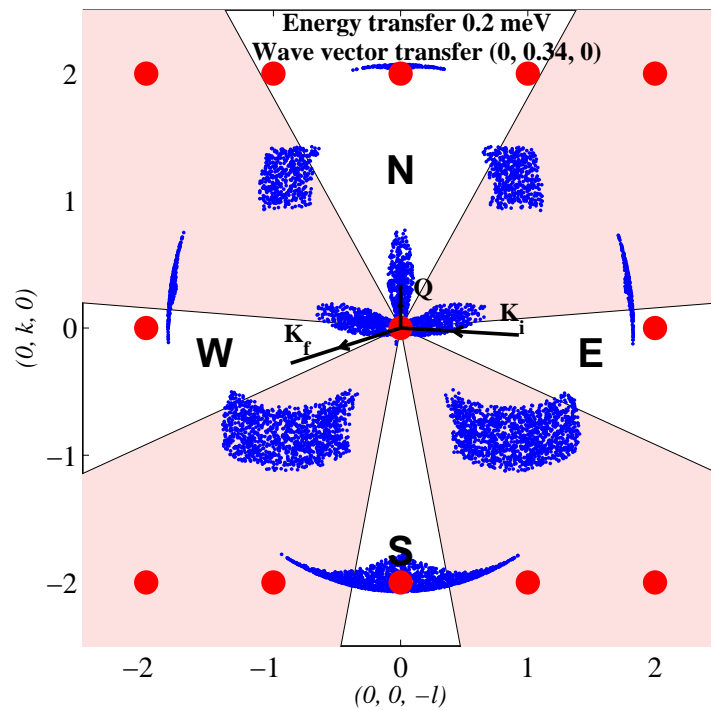


Figure 4.15: Diagram of the regions of accessible reciprocal space in the horizontal field magnet (blue dotted region). The sample was aligned such that the b -axis was parallel to the south(S)-north(N) direction in the magnet. The positions of the magnet wedges are coloured pink. The red dots indicate the strong nuclear Bragg reflections. The grey lines indicate the direction of the incident, K_i , and final, K_f , beam positions to achieve a 0.2 meV energy transfer and wave vector transfer, $Q=(0, 0.34, 0)$ for a final energy of 2.6 meV ($K_f=1.12\text{\AA}^{-1}$). The blue dots are the result of a Monte-Carlo simulation of the possible wave vector transfer positions accessible for the given energy transfer.

be made during the experiment. Figure 4.15 shows the necessary alignment of the spectrometer for a small energy transfer near the ordering wave vector $\mathbf{q} \sim (0, 0.34, 0)$. The available incident and exit angles for the neutron beam were very restricted and added to the difficulty of the experiment. The figure shows the extent of restrictions on the parts of reciprocal space that could be explored. The accessible regions are coloured in blue in the figure. It shows the limitations set by the small open sections of the magnet. There was a slight offset of the elastic line for which the data points are corrected. This setup gave a full-width half maximum of the elastic incoherent scattering of $0.062(2)$ meV and $0.053(3)$ meV.

4.3.2 Measurements and Results

The observations of the magnetic structure in the previous section indicated that at 30 mK the phase transition from the ordered structure to the paramagnetic phase occurred at a transverse field of $5.45(5)$ T. These inelastic measurements explored the excitation spectrum above and below the transition field. In the following, the measurements of the magnon dispersion in the paramagnetic phase are discussed first, followed by the measurements within the ordered phase.

Measurements within the Paramagnetic Phase

Fig. 4.16 a) shows that two sharp modes were observed at magnetic fields above the transition field. The two modes had a strong dispersion and a minimum energy gap of $0.168(3)$ meV at 6 T above the magnetic Bragg peak positions of the low-field ordered phase. Constant wave vector scans were made in order to probe the dispersion of these modes along the inter-chain direction, $(0, k, 0)$, and intra-chain direction, $(0, 0, l)$. Fig. 4.16 shows the measured dispersion of the modes at 6 T in the direction $(0, k, 0)$. In order to extract the energy of the modes from each constant wave vector scan, firstly the modes were fitted to gaussian profiles, as shown in Fig. 4.16 a), and secondly the centres of the gaussians were located. The results are plotted in the dispersion curve shown in Fig. 4.16 b). The inter-chain dispersion shows two modes dispersing through the Brillouin zone and one mode that was consistently lower in intensity than the other.

The intra-chain dispersion was probed by energy scans at constant wave vectors for various l values near the inter-chain dispersion minimum $(0, 0.34, 0)$ and near the crossing point of the two modes $(0, 0.5, 0)$. Fig 4.17 a) shows that two modes were observed in the

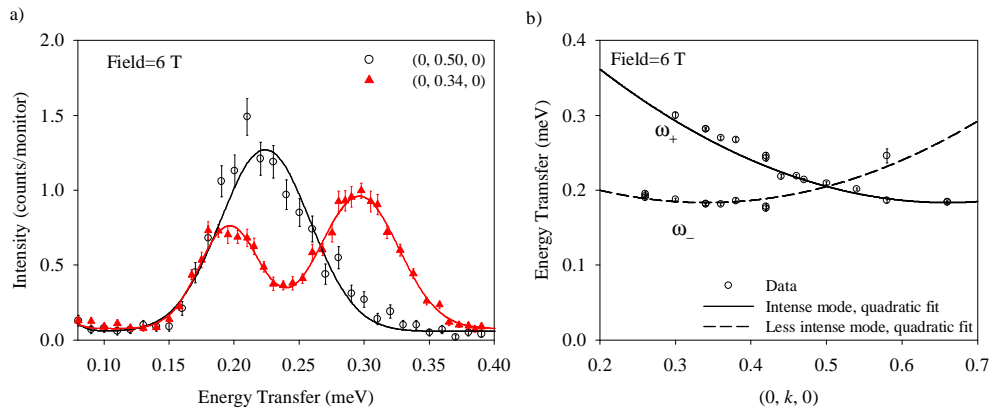


Figure 4.16: a) Two scans at constant wave vectors $(0, 0.34, 0)$ and $(0, 0.5, 0)$ showing two modes which disperse through the Brillouin zone. b) The extracted gaussian centres of fitting the constant wave vector scans at 6 T. Therefore, the inter-chain dispersion was mapped out along the $(0, k, 0)$ direction. The two lines are quadratic fits to the data with the parameterization model given in Eqn. 4.4 where the dashed line indicates the less intense mode.

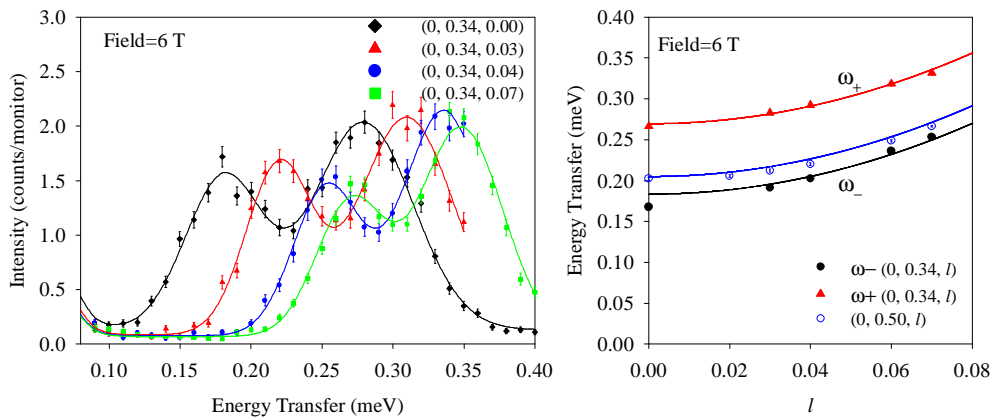


Figure 4.17: Left: Energy scans to probe the dispersion along the l direction at fixed $k = 0.34$. Right: Extracted dispersion of the two modes observed in the $(0, 0.34, l)$ scans and the single mode at $(0, 0.5, l)$. The lines are fits to the data with the parameterization model Eqn. 4.4.

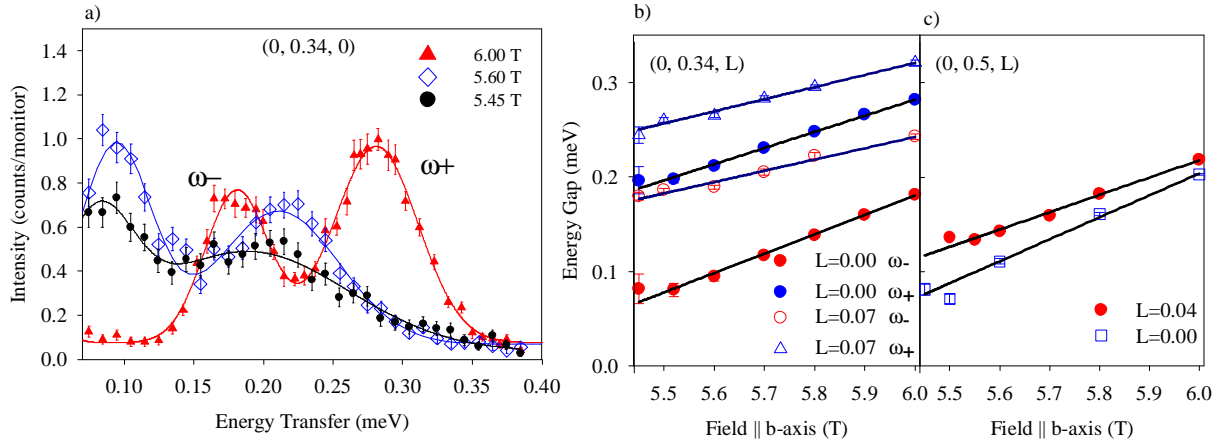


Figure 4.18: a) Constant wave vector scans at the dispersion minimum as the magnetic field strength was decreased showing that the two modes moved to lower energy. b) The extracted gaussian centres of the two modes observed at the dispersion minimum, $(0, 0.34, 0)$ and at the wave vector $(0, 0.34, 0.07)$ with a fitted straight line for both. c) The field dependence of the single mode at $(0, 0.5, 0)$ and $(0, 0.5, 0.04)$, also fitted with a straight line. The gradients of the straight line fits are different for differing values of L implying the dispersion changes as the field is decreased.

$(0, 0.34, l)$ measurements. One mode was observed at the crossing point of the two modes and this was $(0, 0.5, l)$. The line shape of that mode did not change with varying l . The same method was used to find the energy of the modes as that used for the $(0, k, 0)$ dispersion. The dispersion curve is plotted for both $k = 0.34$ and $k = 0.5$ in Fig 4.17 b). The figure shows that the dispersion was much steeper in the intra-chain direction in comparison with the inter-chain direction and this was expected for a quasi one-dimensional system where the chains run along the c -axis. The dispersion in the intra-chain direction was very similar for both the modes, at $k = 0.34$ and at $k = 0.5$.

When lowering the field below 6 T the two magnon modes moved to lower energies. Constant wave vector scans were made at a series of fields approaching the transition field to measure the field dependence of the energy gap. Fig. 4.18 a) shows the variation of the two modes that was observed at $(0, 0.34, 0)$, the wave vector of the dispersion minimum. As the magnetic field decreased, the two modes were observed to move to lower energies and therefore the energy gap to the excitations decreased. The change in the energy gap is shown in Fig. 4.18 b), where it is seen that the positions of the modes decreased linearly upon lowering the field. Around the transition field the gap remained level although, as can be seen in Fig. 4.18 a), the magnetic Bragg peaks of the incommensurate ordered phase

were at this wave vector and so the measurements of the energy gap became more difficult and inaccurate as soon as the incommensurate ordered phase was approached. Therefore scans at constant wave vector were made at various other wave vectors away from the Bragg point. Fig. 4.18 b) and c) show the results for scans at $(0, 0.34, L)$ and $(0, 0.5, L)$, respectively. They show that the dispersion does not have the same field dependence at all points in the Brillouin zone. The slope is greatest at $L = 0$. This indicates that the dispersion may have changed slightly as the critical field was approached. At $L \neq 0$ the dispersion appears not to move to lower energies as rapidly with field as the $L = 0$ modes. Therefore, from these results, it appears as though the dispersion is not simply shifted linearly down in energy, as the field is reduced to approach the critical field, but that the dispersion is slightly modified and the points near the energy gap minimum drop faster than higher energy points.

The energy gap varied linearly with the applied field at high fields such that the Zeeman energy reduced. The gradient of the line fitted to the data in Fig. 4.18 b) at the zone centre $(0, 0.34, 0)$ is $0.205(8)$ meV/T. Assuming a simple Zeeman form the gradient is $g\mu_B$ where g is an effective g -factor of $g = 3.5(1)$. This is larger than the value of $g = 2.72$ that has been found in a low-field ESR study [66]. The difference may have been due to the mixing of higher energy crystal field levels into the ground state doublet in the large transverse field.

Parameterization of High Field Dispersion

A simplified parameterization model was used to understand the main exchange within the system. The dispersion that was assumed is given below:

$$\begin{aligned}\hbar\omega(\mathbf{Q})_- &= \Delta + v_b^2(k - 0.34)^2 + v_c^2l^2 \\ \hbar\omega(\mathbf{Q})_+ &= \Delta + v_b^2(k - 0.66)^2 + v_c^2l^2.\end{aligned}\tag{4.4}$$

This model is based on the assumption that the quasi-particle dispersion is quadratic near the minimum of the band and therefore, $\epsilon(q) \approx \Delta + q^2v^2$ at low q , where v is the velocity of the excitations. In the Eqns 4.4, $\mathbf{Q} = (h, k, l)$ is expressed in terms of the reciprocal lattice units of the CoNb_2O_6 unit cell; Δ is an energy gap to the dispersion; v_b and v_c are associated with the dispersion in the b and c directions respectively. The dispersion was set up to create minima at the Bragg peak positions at $(0, 0.34, 0)$ and $(0, 0.66, 0)$. The model was fitted to the 6 T data shown in Fig. 4.17 and Fig. 4.16. The fitted model corresponds

to the lines plotted in those figures and the fit parameters are $\Delta = 0.17(1)$ meV, where $v_b = 1.0(1)$ meV^{0.5} and $v_c = 3.8(1)$ meV^{0.5}. The parameterization model indicates that the largest dispersion was along the $(0, 0, l)$ direction, which was along the chain direction and was expected to have the largest coupling. It also indicated significant in-plane dispersion, suggesting that the inter-chain couplings were sizeable.

Measurements within the Ordered Phase

Measurements at fields within the long-range ordered phase were made in order to measure the excitation spectrum. Figure 4.19 provides a summary of the main results. Figure 4.19 a) shows a plot of the raw data whereas the other plots in the figure are shown with a background scan subtracted, such as the zero field scan at $(0, 0.34, 0)$. The scattering was much lower in intensity than at high field strength and the features were much broader. Figure 4.19 b) shows that there were two distinct parts to the inelastic scattering. At 4.50 T a low-energy section, which extends towards the elastic line, was present as well as some scattering at higher energies. At higher fields the low energy scattering intensity increased and the higher energy scattering moved to lower energies such that the two components merged to form a continuous band of scattering at 5.10 T. The field dependence of the scattering at low energies was studied further by measuring the intensity at fixed wave vector and at fixed energy transfer as the applied field was changed. Figure 4.19 c) shows the results for an energy transfer of 0.11 meV. The intensity at the elastic line is shown for comparison. Fig. 4.19 c) shows that the scattering at the inelastic position increased at an increasing rate as the transition field was approached. The scattering at low energies was still present well below the transition field, reinforcing the result shown in Fig. 4.19 b).

A series of scans was made at both the magnetic Bragg reflection wave vector, $(0, 0.34, 0)$, and at the Brillouin zone boundary, $(0, 0.5, 0)$. Fig. 4.19 d) demonstrates that at low fields, 4.5 T, at both wave vectors there were two separate parts to the scattering. At $(0, 0.5, 0)$ wave vector transfer, the low-energy scattering seemed not to extend down to the elastic line, as was seen at the magnetic Bragg peak position. This was expected if the excitations were dispersing along k . A comparison of two measurements at $(0, 0.34, L)$, $L = 0, 0.07$ is shown in Fig. 4.19 e). It indicates that the band of scattering at low energies dispersed to higher energies along the $(0, 0, l)$ direction, reinforcing its magnetic character.

When approaching the transition field of 5.45(5) T the intensity increased across the whole energy range probed. Fig. 4.20 a) and b) show measurements at fields close to the

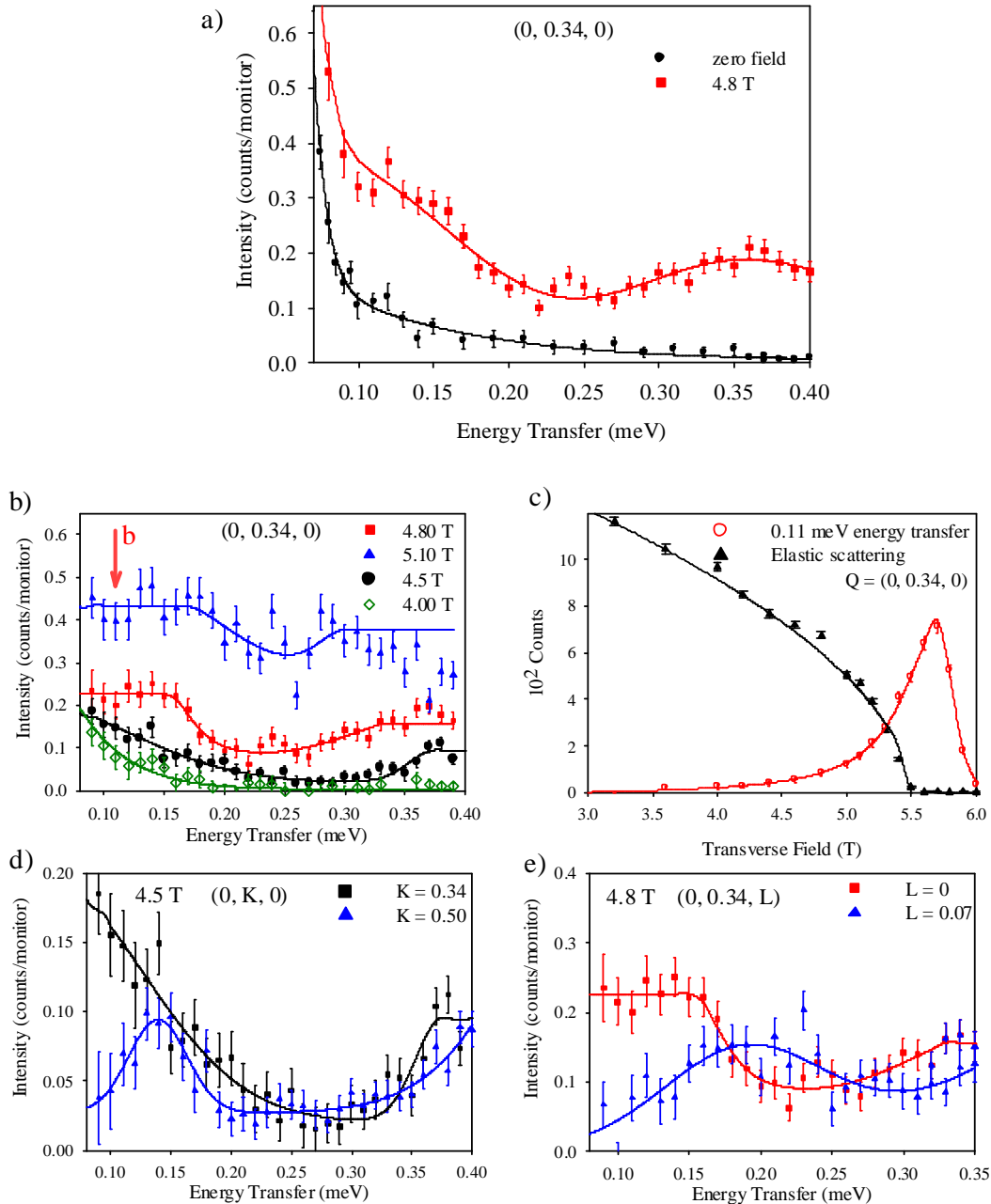


Figure 4.19: a) The raw data plot of the and the 4.8 T data and the background scan which has been subtracted from the data in plots b), d) and e). At $k = 0.34$ the background scan was the zero-field scan and at $k = 0.5$ it was the 3 T scan. The background scans do not have the Bragg peaks present that occur at these wave vectors. b) The development of the inelastic scattering as the field strength is increased at the wave vector transfer $(0, 0.34, 0)$ showing two components of the scattering developing. The arrow in plot a indicated the position of energy transfer of measurement in plot b. c) The signal measured as the field strength was increased at 0.11 meV for monitor= $4 \times 10^5 \approx 4.5$ mins and one third of the signal at the elastic line for monitor= $2 \times 10^3 \approx 1.5$ s. Far from the transition there was a small signal and the scattering increased rapidly approaching the critical field. Plots d) and e) show the wave vector dependence of the scattering within the ordered phase. d) Scans at wave vector transfer $(0, K, 0)$ where $K = 0.34, 0.5$ at 4.5 T. e) Scans at wave vector transfer $(0, 0.34, L)$ where $L = 0, 0.07$ at 4.8 T. In both plots the scattering at low energies moves to higher energies away from the magnetic Bragg peak position.

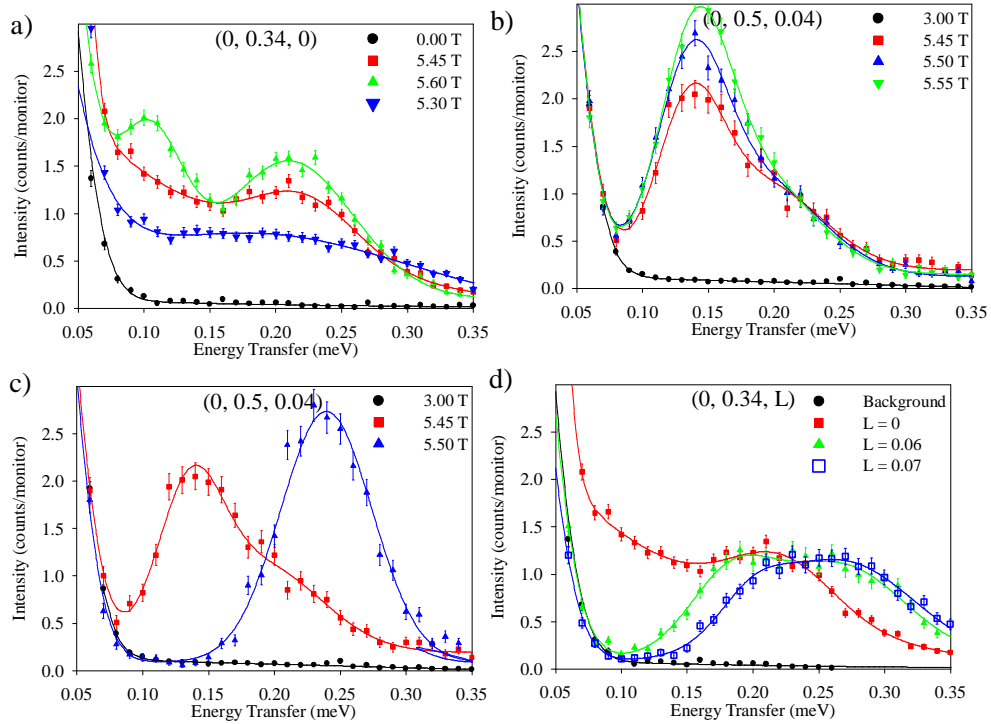


Figure 4.20: Constant wave vector scans at fields close to the transition. Plot a) A constant wave vector scan at $(0, 0.34, 0)$ showing the increase in intensity of the band of excitations and the two modes developing above the critical field. Plot b) constant wave vector scans at $(0, 0.5, 0.04)$ showing the increase in intensity of the main mode and a tail of scattering to higher energies. Plot c) shows the change in line shape of the scattering where at 6 T a single mode was observed which at 5.45 T was less intense and extends to higher energies. Plot d) shows the scattering at the critical field, at 5.45 T, at the wave vector of the magnetic Bragg peak, $(0, 0.34, 0)$, and at wave vectors $(0, 0.34, L)$, $L= 0.06, 0.07$.

transition field. The magnon modes observed at high fields were broad at fields just above the transition and the band of scattering observed below the transition field appeared to increase overall in intensity. The difference in line shape of the excitations is seen in Fig. 4.20 c). The measurements were at the crossing point of the two dispersions where at 6 T a single mode was observed. So at this wave vector the difference in line shape was that of a single excitation. At 5.45 T the measurement shows a strong mode with a tail of scattering extending to higher energies, in comparison with the single sharp mode at 6 T. The change in the scattering along the $(0, 0l)$ direction at the transition field was also measured. In Fig. 4.20 c), measurements along the $(0, 0.34, L)$ direction showed that the broad band of scattering observed at 5.45 T at the magnetic Bragg peak position moved to higher energies at larger L .

4.3.3 Analysis

Two sharp modes were observed above the critical field at 6 T, with dispersions which crossed at the $(0, 0.5, 0)$ point. The minima occurred at the wave vector positions of the magnetic Bragg reflections associated with the ordered phase at low field, as would be expected since it was at these points where the energy gap was expected to soften at the transition field. There are two different chains in the unit cell and therefore these two magnon modes could be associated with couplings between magnon modes on these two chains. In order to analyse these observations the classical and quantum predictions for the one-dimensional Ising chain are now reviewed.

Mean Field Picture of the Ising Magnet in a Transverse Field

Single Ising chain in a transverse field

The energy gap in the high-field phase decreased linearly upon lowering the field strength. This behaviour would be expected from lowering of the Zeeman energy of a spin-flip excitation. The measurements of the high-field energy gap of the modes at $(0, 0.34, 0)$ was fitted with a straight line:

$$\text{Energy gap} = g\mu_B B - \Delta_0, \quad (4.5)$$

where B is the field and $g\mu_B = 0.205(8)$ meV/T and $\Delta_0 = 1.05(5)$ meV. This fit to the high field data implies that the effective g -value was $g = 3.55$ and the field at which the energy gap was closed was $\Delta_0/g\mu_B = 5.1(4)$ T.

In the case of a single Ising chain spin-half system in a transverse field the Hamiltonian is:

$$\mathcal{H} = - \sum_i J_c S_i^x S_{i+1}^x - \sum_i g\mu_B B S_i^z \quad (4.6)$$

In the classical picture at zero field the spins align along the Ising direction, S^x , whereas at high fields the spins align along the field direction S^z . Hence, the Hamiltonian has two phases separated by a transition at a critical field. Therefore, in order to understand the high field magnon modes that were observed, spin deviations from the high field phase were considered where spins aligned along the field direction. A spin-wave calculation using the Holstein-Primkoff transformation leads to the dispersion of the mode as:

$$(\hbar\omega_q)^2 = g\mu_B B (g\mu_B B - 2J(q)S), \quad (4.7)$$

where $J(q) = J_c \cos(\pi l)$ is the Fourier transform of the couplings assuming the spacing between the sites is $c/2$; g is the g -factor; μ_B is the Bohr magneton; and B the magnetic field. The energy gap as a function of field, at $l = 0$, is plotted in Fig. 4.21. At very high field, where $2J_c S / (g\mu_B B) \ll 1$,

$$\hbar\omega_q \approx g\mu_B B - J(q)S. \quad (4.8)$$

The energy gap is at the minimum of the dispersion and this occurs at $l = 0$. Therefore the energy gap, at high fields, as a function of field is expected to be:

$$\text{Energy gap} \approx g\mu_B B - J_c S. \quad (4.9)$$

By comparing Eqn. 4.9 and Eqn. 4.5 an estimate of intra-chain ferromagnetic couplings was found to be $J_c \approx 2 \text{ meV}$. This value was consistent with the relatively steep dispersion along the intra-chain direction. In the classical picture spins are classical vectors pointing along the Ising axis in zero field and tilting toward the field axis at finite field. The equilibrium position is found by calculating the optimal angle θ for the minimum energy per spin, E :

$$E(\theta) = -J_c S^2 \cos^2 \theta - g\mu_B B S \sin \theta \quad (4.10)$$

Therefore the angle

$$\begin{aligned}\theta &= \frac{\pi}{2} && \text{when } B \geq \frac{2SJ_c}{g\mu_B} \\ \sin \theta &= \frac{g\mu_B B}{2J_c S} && \text{when } B < \frac{2SJ_c}{g\mu_B}\end{aligned}$$

therefore the magnetisation is calculated as:

$$\begin{aligned}S^z &= S \sin \theta = S && \text{for } B \geq \frac{2SJ_c}{g\mu_B} \\ &= S \frac{g\mu_B B}{2J_c S} && \text{for } B < \frac{2SJ_c}{g\mu_B}\end{aligned}\quad (4.11)$$

The ordered moment along the Ising direction is:

$$\begin{aligned}S^x &= S \cos \theta = 0 && \text{for } B \geq \frac{2SJ_c}{g\mu_B} \\ &= S \sqrt{1 - \left(\frac{g\mu_B B}{2J_c S}\right)^2} && \text{for } B < \frac{2SJ_c}{g\mu_B}\end{aligned}\quad (4.12)$$

Therefore, within the classical picture, the critical field separating the two phases is $B_{cl} = 2J_c S / (g\mu_B B) = 10.2(8)$ T. This is twice the observed critical field. The change in energy gap expected from this classical picture is shown in Fig. 4.21. The high-field linear behaviour observed in Fig 4.18 expected from Eqn. 4.7 is not present close to the critical field.

Quantum Solution for the Ising Chain in a Transverse Field

The mean field approximation considered above neglects quantum fluctuations and this alters the physics significantly, in particular close to the critical field. A full quantum solution of the Ising model in a transverse field, Eqn. 4.6, can be obtained by a full Jordan-Wigner spin-fermion mapping which gives the order parameter, $\langle S^x \rangle$, as [9]:

$$\langle S^x \rangle = \frac{1}{2} \left(1 - \left(\frac{2g\mu_B B}{J_c} \right)^2 \right)^{\frac{1}{8}}. \quad (4.13)$$

The ordered moment and the magnetisation, $\langle S^z \rangle$, is plotted in Fig. 4.21 b). It shows that the ordered moment has a very different behaviour to the classical predictions. By comparing Eqn. 4.13 and Eqn. 4.12 it can be seen that the functional form of the two equations is different. In the classical description the order parameter has the critical exponent, $\beta = 1/2$ whereas in the quantum case $\beta = 1/8$. The magnetisation is also quite different in the quantum description. By comparing the two plots Fig. 4.21 a and b it can be seen that the magnetisation tends towards saturation only at infinite fields whereas in the classical case

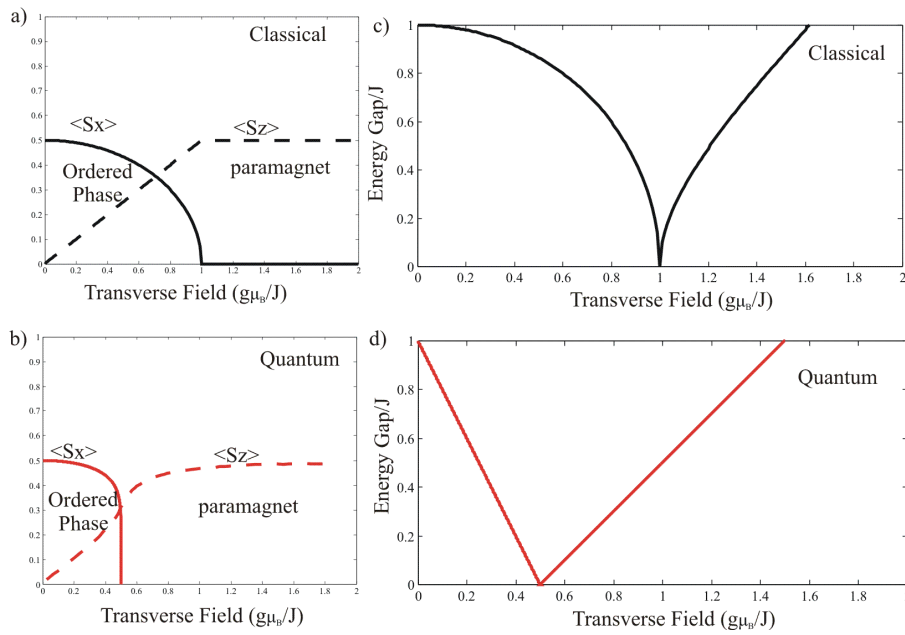


Figure 4.21: Plots a) and b) show the change in ordered moment, $\langle S^x \rangle$, and magnetisation, $\langle S^z \rangle$, as the transverse field is varied for the classical and quantum Ising chain at $T = 0$. The quantum solutions results are taken from calculations by Pfeuty [9]. They show that the classical critical field is twice that of the quantum case. The critical exponent in the classical case is $\beta = 1/2$ and in the quantum case $\beta = 1/8$. Plots c) and d) the energy gap dependence is given for both cases. In the classical picture spin-waves are excited on both sides of the transition. In the quantum case two solitons are excited in the low field phase and in the paramagnetic phase the excitation is the spin-flip from the field direction.

saturation is reached at the critical field.

At zero temperature, the dispersion as calculated by Pfeuty is [9]:

$$(\hbar\omega_q)^2 = (g\mu_B B^2 - g\mu_B B J_c \cos(\pi l) + J_c^2/4). \quad (4.14)$$

Therefore the energy gap at the dispersion minimum, $l = 0$ is:

$$\text{Energy gap} = |g\mu_B B - J_c/2|. \quad (4.15)$$

The dependence of the energy gap with field is plotted in Fig. 4.21. The classical solution approaches the quantum solution in Eqn. 4.15 at high fields as seen in Eqn. 4.8. The critical field in the quantum case is $B_c = J_c/(2g\mu_B) = B_{cl}/2$ which is half the classical result for a spin-half system. The physical interpretation of this result is that the quantum fluctuations prevent the energy gap from closing at the classical critical field and therefore the gap closure occurs at lower fields.

Mean-Field Solution of Coupled Ising Chains in a Transverse Field

At sufficiently high fields above the critical field the mean-field dispersion, Eqn. 4.7, tends to the full quantum solution, Eqn. 4.14. This shows that as the field strength tends to infinity the quantum fluctuations become small and the semi-classical spin-wave calculation of the excitations is appropriate. Therefore a more complete spin-wave calculation was considered in order to analyse the magnon dispersion more thoroughly.

CoNb₂O₆ departs from a perfect one-dimensional Ising chain in two aspects. The first is that there are two types of Ising chain in the unit cell which have the Ising axis tilted with respect to each other. Therefore two modes are expected in the high-field phase. Secondly, the inter-chain couplings have a frustrated triangular geometry and stabilize order at a point in the three-dimensional Brillouin zone at $\mathbf{Q} = (0, Q_k, 0)$ where $Q_k \sim 1/3$. To understand the effect of the inter-chain couplings between the Ising chains a simpler model is considered of a triangular Ising lattice.

The single Ising chain Hamiltonian is extended to include inter-chain couplings and the two different Ising directions of the two chains in the unit cell. Again the ground state is assumed to be the classical high-field state, where the spins are assumed to be ordered along the field direction, which is perpendicular to the Ising direction. The Ising direction

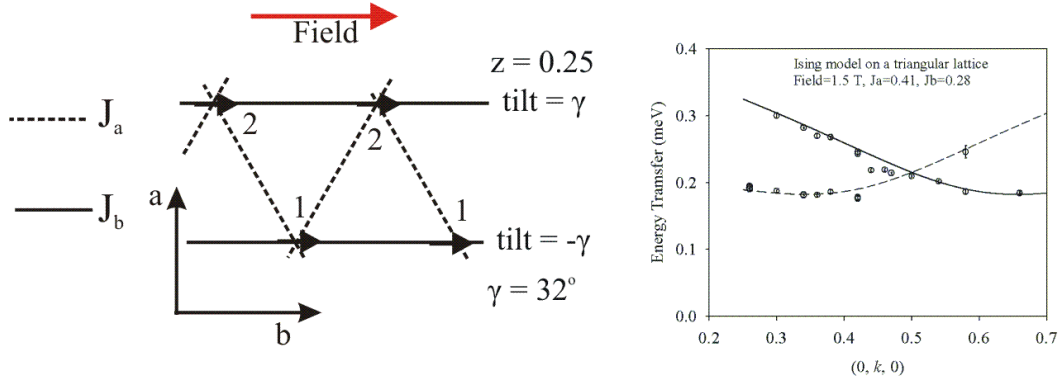


Figure 4.22: Left: The triangular lattice of spins in the (a, b) -plane, showing the couplings between the spins and the two sublattices used in the linear spin-wave derivation of the dispersion. The two lines of spins shown have Ising directions tilted from the c -axis by $\pm 32^\circ$. Right: A plot of the magnon dispersion branches derived from a linear the spin-wave calculation of the triangular lattice with coupled Ising spins and compared to the experimental data at $(0, k, 0)$.

alternates along the a -axis, as shown for sites 1 and 2 in Fig. 4.22 left. The Hamiltonian is:

$$\mathcal{H}_t = \sum_{il} J_b S_i^x S_l^x + \sum_{im} J_b S_i^{x'} S_m^{x'} + \sum_{ik} J_a S_i^x S_k^{x'} - \sum_i g\mu_B B S_i^z$$

where x and x' are the two local Ising directions in the unit cell, z is along the field direction and is perpendicular to both x and x' . J_a and J_b are the inter-chain couplings in the triangular lattice in the (a, b) -plane shown in Fig. 4.22 Left. It is important to note that only couplings between the components along the local Ising direction are included. The dispersion is derived using the Holstein-Primakoff transformations for the two sublattices and the result is:

$$\omega_{\pm}^2 = A(A - 2B') - 4C^2\Gamma \pm \sqrt{2(2A^2 - B'^2(1 + 12\Gamma))(1 - 4\Gamma)C^2} \quad (4.16)$$

where,

$$\begin{aligned} A &= g\mu_B B, \\ B' &= \frac{J_b}{2} \cos(2\pi k), \\ C &= \frac{J_a}{2} (\cos(\pi(h+k)) + \cos(\pi(h-k))), \\ \Gamma &= \cos^2 \gamma \sin^2 \gamma, \end{aligned}$$

where $Q = ha^* + kb^* + lc^*$ refers to the reciprocal lattice in the Pbcn space group.

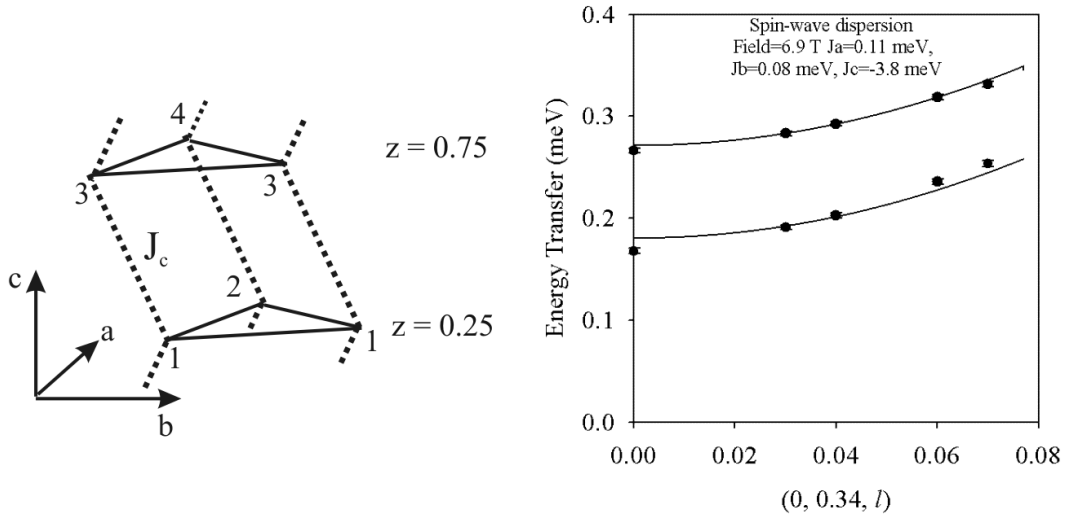


Figure 4.23: Left: The Ising chains are arranged in a triangular lattice. Along a chain the spins are in a zig-zag arrangement in the (b, c) -plane where each site is translated by $(0, \delta, 0.5)$, $\delta = 0.3686$ along a chain. J_c is the coupling along the chains and connects sublattice points with the Ising axis in the same direction: 1 to 3 and 2 to 4. Right: Plots of the two lower dispersion branches for a set of parameters which compares well with the measurements made in the $(0, 0.34, l)$ direction, yet this solution does not fit the $(0, k, 0)$ measurements.

The two-dimensional triangular Ising lattice has two modes in the high-field paramagnetic phase with incommensurate minima at wave vectors which depend on the ratio J_a/J_b . Two modes occur because of the two non-equivalent sublattices with rotated Ising axes. In order to approach the observed dispersion for the two modes in the $(0, k, 0)$ direction, the effective parameters, $B = 1.5$ T, $J_a = 0.42$ meV, $J_b = 0.28$ meV and $g = 3.5$ and $\gamma = 32^\circ$ were used as shown in Fig 4.22. These are ‘effective’ parameters because the effect of the main coupling along the c -axis was not considered in the model. This model gave minima at the positions of the magnetic Bragg reflections of the ordered phase but required a very small field in order to reach the energy scale of the observed excitations. Therefore, by using the the Ising model on an anisotropic triangular lattice, the magnitude of the small in-plane coupling between spins was determined which led to the small dispersion. These couplings were small in comparison with the main intra-chain coupling of 2 meV exchange which was calculated from the field dependence of the energy gap. Nevertheless the set of inter-chain dispersions were significantly larger than those found by Heid *et al.* when modelling the phase diagram in an applied field within the (a, c) -plane [61].

A more realistic model should include the main coupling, which is along the c -axis.

Therefore a model of Ising chains on each site in the triangular lattice was used such that the Hamiltonian was:

$$\mathcal{H} = \mathcal{H}_t + \sum_{ij} J_c S_i^x S_j^x + \sum_{ij} J_c S_i^{x'} S_j^{x'},$$

where J_c is the coupling along the Ising chain direction. Four sublattices were used to model the four Co^{2+} ions in the unit cell, two on each Ising chain forming two layers of Co^{2+} ions. The four sub-lattices are shown in the diagram in Fig. 4.23. The dispersion was derived to be:

$$\omega_{u\pm}^2 = \omega_{\pm}^2 + 2\sqrt{(\omega_{\pm}^2 - D^2 \sin^2(2\pi k\delta))D^2} \quad (4.17)$$

$$\omega_{l\pm}^2 = \omega_{\pm}^2 - 2\sqrt{(\omega_{\pm}^2 - D^2 \sin^2(2\pi k\delta))D^2} \quad (4.18)$$

$$(4.19)$$

where $D = \frac{S}{2}J_c \cos(\pi l)$ and $\delta = 0.3686$ and it results from the zig-zag of the chains in the (b, c) -plane. Again, the wave vector $\mathbf{Q} = h\mathbf{a}^* + k\mathbf{b}^* + l\mathbf{c}^*$ refers to the reciprocal lattice in the Pbcn space group. Attempts were made to fit the modes given by Eqn. 4.17 to the data. No complete set of parameters was found that fitted both the dispersion along the direction $(0, k, 0)$ and $(0, 0, l)$. In the figure a plot of this spin-wave model is given for a set of parameters that fits the $(0, 0.34, l)$ data, $B = 6.9 \text{ T}$, $J_a = 0.11 \text{ meV}$, $J_b = 0.08 \text{ meV}$, $J_c = -3.8 \text{ meV}$, $\gamma = 32^\circ$. However the model did not fit the $(0, k, 0)$ dispersion. The main coupling is along the Ising chains and it dominates the dispersion along the $(0, k, 0)$ direction due to the small k dependence of the coupling along the the Ising chain. The adjustment of the field from 6 T is also a sign that the model does not properly describe the system.

The above model of Ising chains coupled in a triangular arrangement by frustrated inter-chain couplings captures general features of the excitations in the high field phase since two modes are predicted above an energy gap with minima at incommensurate wave vectors. Yet the dispersion calculated from the mean-field approximation does not describe the detailed functional form observed for the dispersion and this suggests that a renormalization is required. One of the reasons may be because the mean-field approximation neglects quantum fluctuations as they may renormalize the dispersion sufficiently close to the critical field. Similar behaviour is seen in the case of the one-dimensional Ising model.

Magnon Hopping Model

It is expected that the high-field phase is a paramagnetic phase and that the excitations are magnons which hop coherently through the lattice. Therefore, a more general model of magnon excitations hopping on a three-dimensional lattice of stacked triangular layers was considered in order to parameterize quantitatively the observed dispersion. If h_a , h_b , h_c are the magnon hopping terms along the main nearest-neighbour coupling directions the Hamiltonian takes the form:

$$\mathcal{H} = \sum_{ij} (h_b + h_c)(a_i^\dagger a_j + b_i^\dagger b_j) + h_a a_i^\dagger b_j + \Delta(a_i^\dagger a_i + b_i^\dagger b_i) \quad (4.20)$$

where a_i^\dagger , a_i create and annihilate magnons at site i and the dispersion is of the form:

$$\hbar\omega_- = \Delta - 2h_a \cos(\pi h) \cos(\pi k) + h_b \cos(2\pi k) + h_c \cos(\pi l) \quad (4.21)$$

$$\hbar\omega_+ = \Delta + 2h_a \cos(\pi h) \cos(\pi k) + h_b \cos(2\pi k) + h_c \cos(\pi l) \quad (4.22)$$

where Δ is the energy gap. Equations 4.21 and 4.22 model hopping on an anisotropic triangular lattice in the (a, b) -plane and a dispersion between the lattice along the c -axis. If this dispersion is to reproduce the dispersion minima at the magnetic Bragg peaks, the hopping terms must satisfy the condition:

$$\cos(\pi k_0) = \pm \frac{h_a}{2h_b} = \pm 0.4817 \quad \text{for} \quad k_0 = 0.34, 0.66.$$

The difference between the two inter-chain hopping terms is small since the ordering wave vector is close to $k_0 = 1/3$ when $h_a = h_b$. Modelling the data in the $(0, k, 0)$ direction gave a best-fit value for $h_b = 0.051(1)$ meV and $h_a = 0.049(1)$ meV. Modelling the data of the $(0, 0, l)$ dispersion gave $h_c = -2.5(1)$ meV. The model is shown in Fig. 4.24 and fits the data reasonably well. The hopping terms should be interpreted as effective values of the exchange parameters corresponding to the bonds and including a renormalisation factor. The hopping terms are similar to the values of the simple quadratic form given in Eqn. 4.4 and described the low energy dispersion. As expected the largest exchange is along the Ising chains which are along the c -axis.

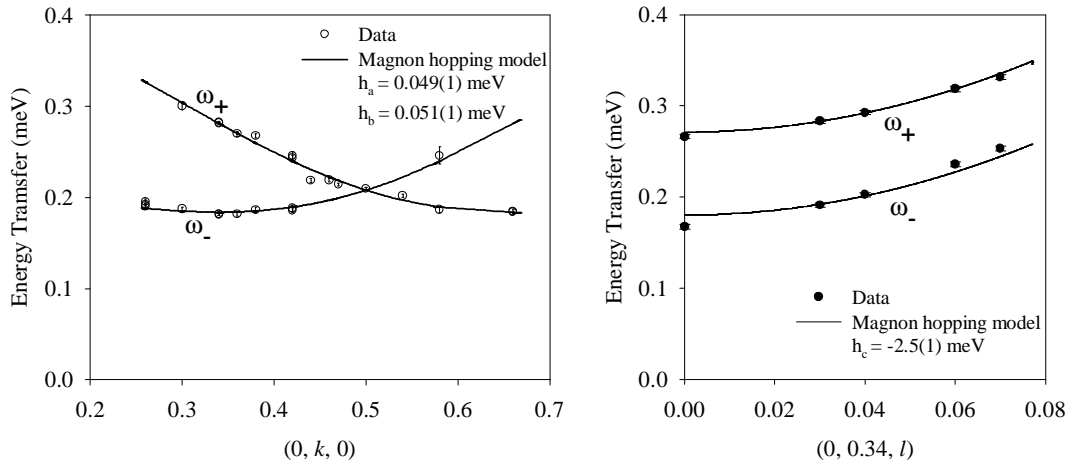


Figure 4.24: Plots of the fit to the data at $(0, k, 0)$ (left) and $(0, 0.34, l)$ (right) of the magnon hopping model as given in Eqn. 4.21.

Below the Transition Field

At fields within the ordered phase, below the critical field, the line shape of the excitations changed to broad line shapes from the sharp magnon modes observed above the critical field. The Ising chains ordered within the triangular lattice in the (a, b) -plane which resulted in magnetic Bragg peaks at the wave vectors near $(0, 0.34, 0)$ and $(0, 0.66, 0)$. As shown above, this suggested slightly anisotropic inter-chain couplings within the triangular lattice. Upon approaching the critical field from lower fields the zero point quantum fluctuations increased within the system and the ordered moment decreased, as observed in Fig. 4.19 c). As the ordered moment was reduced the scattering at low energies increased. This was to be expected because the energy gap to the two-soliton scattering is reduced as the critical field is approached. Therefore as the scattering moves to lower energies, the signal at a fixed energy transfer is expected to increase about the transition field. Fig. 4.19 c) shows such a measurement where the intensity at a finite energy transfer above the Bragg peak was seen to increase rapidly upon approaching the transition field. An unusual feature of the scattering at 0.11 meV was the existence of a signal far below the transition field. Energy scans at a series of fields indicated that there existed low energy scattering far below the critical field which was distinct from the high energy scattering. The possible origins of the two components are now discussed.

The high-energy scattering measured below the transition field within the ordering phase is expected to result from the creation of domain walls within the Ising chains, as

shown schematically in Fig. 4.14 a). A spin-flip caused by the scattered neutron creates two domain walls, solitons, which propagate creating a continuum (shown as the shaded area in Fig 4.14 a)). If inter-chain couplings exist then there is a small longitudinal mean field, along the Ising axis, predicted to split the states in the continuum and thereby cause a series of separate modes. The high-energy scattering is expected to be seen as series of sharp modes with a small energy separation. The individual excitations are not expected to be resolved within the resolution of the present measurements. Instead a band of intensity is expected to be observed which moves to lower energies as the field is increased, as expected for the field dependence of the solitons in an Ising chain given by Eqn. 4.14.

The presence of low-energy excitations is surprising and is not expected in the model of the one-dimensional Ising chain because the excitations are gapped across the whole Brillouin zone, see Fig 4.14 a), and the energy gap only closes near to the critical field. In addition any commensurate three-dimensional Ising order is also expected to be gapped at all fields apart from the the critical field. Therefore an UUD structure with an ordering wave vector $(0, 1/3, 0)$ is expected to be gapped at all fields apart from the critical field.

The presence of low-energy excitations well below the critical field can be explained if the order between the chains is not exactly commensurate but is an incommensurate spin-density wave. Incommensurate magnetic order was implied by the resulting Bragg reflection $(0, 0.34, 0)$. Such structures have been observed in the rare earth metals Er and Tm [77, 78]. In these systems longitudinal spin excitations, which are fluctuations along the ordered moment direction, are gapless modes caused by the translational invariance of the magnetic structure. Inelastic neutron scattering experiments on Er have shown that, in addition to the usual transverse excitations, broad longitudinal excitations with a linear gapless dispersion exist [77]. The modes have no energy gap and the linear dispersion relation has been predicted theoretically by Liu and Cooke [79]. In the present measurements on CoNb_2O_6 it was possible that the low energy scattering had no energy gap at the ordering wave vector $(0, 0.34, 0)$. Some evidence was found that the low-energy scattering dispersed in energy slightly upon moving away from the Bragg peak position both in the intra-chain direction and intra-chain direction. In Fig. 4.19 c) and d) the low energy scattering was observed to move to higher energies at wave vectors away from $(0, 0.34, 0)$. The overall intensity of the low-energy scattering increased as the critical field was approached. This was partly because the high-energy one-dimensional scattering moved to lower energy and combined with the scattering from the longitudinal fluctuations. The intensity of the longitudinal modes might have been expected to scale with the size of the ordered moment on

the Ising chains, yet as the ordered moment on the Ising chains decreased, the intensity of the low energy scattering increased. Future higher resolution measurements may help the understanding of the origins of the low-energy scattering so that better measurements of the field and wave vector dependence can be made.

The three-dimensional Ising ferromagnet LiHoF_4 [80] has been studied in a transverse field. Neutron scattering experiments have explored the behaviour of the energy gap in order to observe the energy gap closing [53]. Those measurements have shown that, when lowering the transverse field from the paramagnetic phase, the high field mode follows the predictions of the semi-classical spin-wave description [53]. When the gap was observed to become very small the coupling between the electronic spin component and nuclear spin moments due to the hyperfine interaction became important. This coupling prevents the closing of the gap for the spin-wave mode which results from the oscillations of the electron spin moment [81].

In the present measurements on the quasi one-dimensional system, CoNb_2O_6 , attempts also were made to follow the change in the energy gap as the field was reduced from the high field phase. The excitations in the three-dimensional ordered phase just below the critical field are most likely gapless and the lowest energy excitations are phason modes of the spin-density wave order of the chains. In the paramagnetic phase the dispersion did not appear to move down in energy at the same rate across the whole Brillouin zone, and this implied that the dispersion of the magnon modes changed as the field approached the critical field. Therefore, since measurements at the dispersion minimum are hindered due to the increased intensity at the elastic line as the transition field is approached, it is difficult to infer the energy gap from scans at wave vectors close to the dispersion minimum and only an upper bound can be estimated. If there is an energy gap at the critical field then it is below 0.08 meV and therefore less than 4% of the main exchange energy J .

The applied field direction was precisely applied in the (b, c) -plane to be along the b -axis. However it is still possible that the field was slightly inclined towards the a -axis by an angle of order 0.5° . This would have had the effect of creating a small longitudinal field along the Ising direction which may have prevented the total closure of the energy gap at the critical field. It is important to note that any small misalignment of the field from the perfect transverse direction will create a net longitudinal field along the Ising direction and in the case of a ferromagnet this will prevent the gap from closing because there is no longer a symmetry breaking.

The magnon modes also change in shape close to the transition field and so the gaussian

profile used to fit the modes becomes less appropriate. Therefore these do not show clearly the behaviour of the energy gap very close to the critical field but they do show that the energy gap in the ordered phase does not open away from the critical field as would be expected from the one-dimensional Ising system.

4.4 Conclusions on CoNb_2O_6

The aim of these measurements was to observe the phase transition which occurs when applying a field transverse to an Ising axis in an Ising-like system. CoNb_2O_6 is an Ising-like ferromagnet and the phase diagram for the system in a field purely transverse to the Ising direction has not been studied before. Inelastic neutron scattering experiments have not been made about a magnetic Bragg position and therefore the observation of the change in the minimum energy gap had not been observed before.

The main exchange interaction in CoNb_2O_6 couples the Ising-like spins into ferromagnetic Ising chains. Yet CoNb_2O_6 has demonstrated a more complex excitation spectrum than that expected from the isolated Ising chain in a transverse field.

Above the transition field a paramagnetic phase was observed in which sharp magnon modes dispersed along the Ising chains and slightly dispersed between the chains. The dispersion was described by a magnon hopping-model where the hopping along the chain was largest with a small hopping between the chains. The linear spin-wave calculation assumed completely Ising-type spins and was not successful in modelling the data. This may have been an over-simplification of the system since the spins may not be purely Ising-type and there may be corrections to the effective spin-half system. Also the classical ground state assumed in the linear spin-wave description is an approximation of the actual ground state of Ising chains in the paramagnetic phase. Therefore it may be expected that as quantum effects are considered, the parameters in the dispersion would be renormalized in the linear spin-wave model.

Three ordered phases were observed within the neutron diffraction measurements which explored the magnetic structure below the transition field. The observations imply that, close to the transition field, an incommensurate ordered phase was stabilized and this was further supported by the observation of gapless modes in the excitation spectrum away from the transition field. These are new results and indicate a transition between a gapless incommensurate ordered phase to gapped paramagnetic phase.

Chapter 5

Neutron Scattering Study of the Layered Spin-Half Antiferromagnet CuSb_2O_6

This chapter presents a neutron scattering study of the layered copper-oxide material $\beta\text{-CuSb}_2\text{O}_6$. The spin-half Cu^{2+} ions form a square lattice with a strong antiferromagnetic coupling across one diagonal of the square and the crystal structure consists of layers of Cu^{2+} ions. Firstly, single-crystal diffraction measurements were made to determine the low-temperature magnetic structure at zero field using both polarized and unpolarized neutrons. Further, unpolarized diffraction measurements investigated the development of the magnetic structure as a magnetic field was applied along the ordered moment direction. At low fields a spin-flop transition was observed and there are indications of a transition at high field. Secondly, inelastic neutron scattering measurements investigated the low-temperature magnetic excitation spectrum. An unusual intensity distribution was observed for the in-plane dispersions and a strong resonance feature was observed at 13 meV at the Brillouin zone boundary. This energy agreed with the predicted Brillouin zone boundary dispersion maximum for a one-dimensional spin-half Heisenberg chain with a coupling of 4.2 meV. An initial investigation of the low-energy phonon modes, using inelastic scattering at room temperature, showed that the energy of the resonance feature was close to that of a phonon mode associated with the bending of the bond through which the main super-exchange interaction occurs.

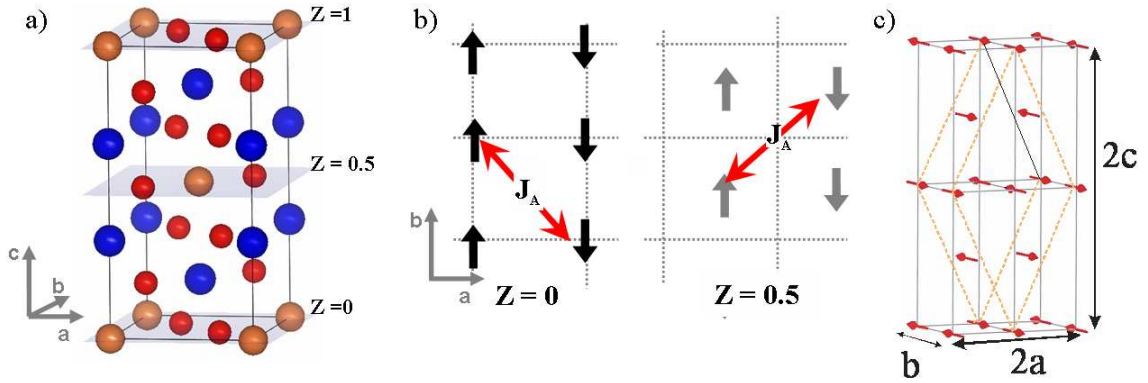


Figure 5.1: a) A sketch of unit cell of the crystal structure of CuSb_2O_6 . The black lines indicate the unit cell and the orange balls represent the copper ions, red the oxygen and blue the antimony. b) Schematic diagram of the Cu^{2+} lattice and the main exchange path for the two layers of Cu at $z = 0$ and $z = 0.5$. The arrows indicate the two Cu^{2+} sites. c) A sketch of the magnetic structure at zero field. The magnetic unit cell is indicated by the dotted lines and the arrows indicate the alignment of the Cu^{2+} spins at zero magnetic field.

5.1 Introduction

The following chapter presents a neutron scattering study of the layered copper-oxide material β - CuSb_2O_6 , whose unit cell is shown in Fig. 5.1. The spin-half Cu^{2+} ions form a square lattice in the basal plane with a strong antiferromagnetic coupling across one diagonal of the square. The crystal structure consists of layers of Cu^{2+} ions surrounded by oxygen octahedra. The outer nine electrons of the Cu^{2+} are in the 3d shell, such that there is one unpaired electron which lies either in the e_g or t_{2g} level. For both possibilities the orbital angular momentum is quenched and therefore the Cu^{2+} has a moment composed of the spin, $S = 1/2$. Susceptibility measurements on powder samples have confirmed that the Cu^{2+} ion is in a spin-half state [82] because fitting the observed high-temperature susceptibility to the Curie-Weiss law gives an effective moment $\mu_{eff} = 1.758 \mu_B$ close to that expected for a spin-half (for $S = 1/2$, $g = 2.21$ [83], $\mu_{eff} = 1.914 \mu_B$). The two Cu^{2+} ions in the unit cell form two square lattice layers of spin-half ions in the (a, b) -plane as shown by the shaded planes in Fig. 5.1 a). The two layers stack along the c -axis such that one Cu^{2+} ion is translated to the other by the fractional coordinates $(1/2, 1/2, 1/2)$.

The β polytype exists below 380 K where α - CuSb_2O_6 undergoes a slight monoclinic distortion from a tetragonal structure. Measurements have shown that the a and b lattice parameters, $a = 4.6349(1)$ and $b = 4.6370(1)$, are very similar and the c lattice parameter,

$c = 9.2931(1)$, is nearly twice their value with $\beta = 91.124(2)^\circ$ in the space group $P2_1$ [82]. The two copper atoms in the unit cell at positions $(0, 0, 0)$ and $(1/2, 1/2, 1/2)$ are connected by a screw axis parallel to the b -axis.

Koo and Whangbo [84] have investigated the coupling strengths in β - CuSb_2O_6 by calculating the spin correlation interaction energies of two adjacent spin sites. The strongest exchange interaction is predicted to be across the diagonal of the square between next-nearest neighbouring ions, as shown in Fig. 5.1 b). The exchange path is through the chemical Cu-O-O-Cu bond, where the bond angle is close to 180° , and is predicted to be antiferromagnetic. The nearest-neighbour interaction is relatively smaller since the Cu-O-Cu bond is closer to 90° . These couplings are predicted to be antiferromagnetic and of similar magnitude in both the a and b directions. The results of fitting the line widths of electron spin resonance measurements (ESR) have indicated that the exchange couplings are extremely anisotropic and that the sign of the couplings changes for spins aligned along the b -axis with respect to spins aligned along the a -axis [83].

Gibson *et al.* [85] have fitted their susceptibility measurements to a Bonner-Fisher curve [13] and have estimated the main quasi-one-dimensional exchange to be 4.2 meV. Therefore, the main exchange path is predicted to be antiferromagnetic, with a coupling strength of approximately 4.2 meV across one diagonal of the square lattice of spin-half sites, as in Fig. 5.1 b). Previously, in Chapter 1, the J_1 - J_2 spin-half square lattice model was discussed. In that model the two diagonal exchanges, J_2 , of the square lattice were large and equivalent. The calculated phase diagram was rich and showed that, for certain ratios of J_2/J_1 , non-classical behaviour was dominant. In CuSb_2O_6 only one diagonal on the square lattice is significant and antiferromagnetic but theoretical calculations of the phase diagram in such a scenario are currently not available. The system is frustrated if the predicted coupling scheme exists: the strong diagonal exchange and nearest-neighbour exchanges are all predicted to be antiferromagnetic and so cannot all be satisfied. The low spin of this system and its frustration would lead to quantum fluctuations and again to the possibility of non-classical behaviour.

Kato *et al.* [86] have observed three-dimensional long-range magnetic order below 8.9 K and indexed it with a propagation vector $(1/2, 0, 1/2)$. They have suggested that the spins align into ferromagnetic lines along the b -axis and into antiferromagnetic lines along the a -axis which are parallel to the neighbouring layers, as shown in Fig 5.1. Gibson *et al.* [85] have suggested that spins on neighbouring planes are canted away from the b -axis toward the a -axis. The canting has been found to be different for the two layers, at $z = 0$

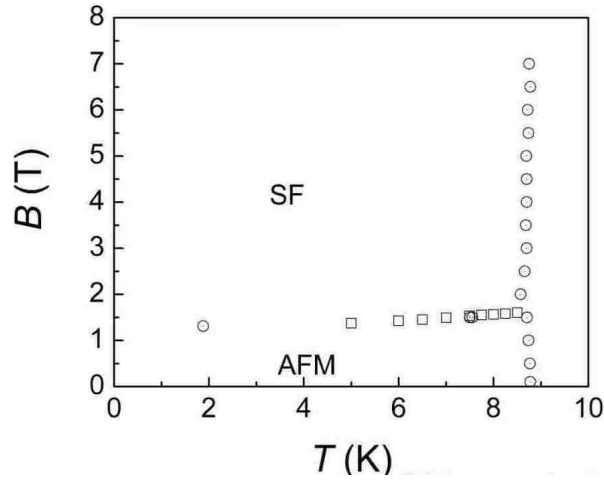


Figure 5.2: Phase diagram of CuSb_2O_6 for a field applied parallel to the crystallographic b -axis. These measurements show that the spin-flop field is nearly constant up to the ordering temperature [87].

and $z = 0.5$. The ordered moment has been found to be reduced to a value of $0.5\mu_B$ from the possible $1.12\mu_B$ ($S = 1/2$, $g = 2.23$ [83]) suggesting that substantial quantum fluctuations are present [85].

An abrupt change in the magnetization has been observed indicating that there is a spin-flop transition for an applied magnetic field of about 1.25 T along the b -direction [83]. The phase diagram for the spin-flop region is given in Fig. 5.2 and shows that it persists up to the ordering temperature of 8.9 K. Susceptibility measurements have suggested that the spin-flop transition will cause the spins to flop from the b -axis to the a -axis. At low temperatures there is a sharp drop in the susceptibility. Measurements on single crystals have shown that, at low temperature, the susceptibility is lowest for a small field along the b -axis and maximum for a field along the c -axis [85]. Therefore, since the susceptibility is considerably reduced along the b -axis it is expected that in zero field the ordered moment will be predominantly along this axis. The spins will then move to the a -axis as the critical field is applied along the b -axis.

The results of the ESR measurements [83] would suggest an unusual spin-flop transition. They predict that the couplings would change sign for spins aligned along the b -axis to those aligned along the a -axis. If the coupling scheme were to change dramatically before and after the spin-flop transition then the two phases would be expected to show two

different ordering wave vectors. The zero field structure has been indexed with the ordering wave vector $(1/2, 0, 1/2)$ therefore this may change as a completely different structure is stabilized.

The measurements discussed in this chapter investigated the magnetic structure present at zero field and in an applied magnetic field of 11.5 T. This field was much higher than the spin-flop field and so the development of the magnetic structure could be probed. Low-temperature inelastic scattering measurements of the excitation spectrum out to an energy transfer of 17 meV. These measurements were motivated by the possibility of exploring the frustrated couplings and the effect of quantum fluctuations in the system.

5.2 Low-Temperature Magnetic Structure of CuSb_2O_6

In this section, single crystal neutron diffraction measurements on CuSb_2O_6 are presented. The zero-field long-range magnetic order was investigated, using unpolarized and polarized neutrons. This study was motivated by the two different results given in the literature by Kato *et al.* [86] and Gibson *et al.* [85] for the zero-field magnetic structure. The spin-half Cu^{2+} ions form two square lattices at $z = 0$ and $z = 0.5$. Although both the Kato and the Gibson studies have indexed the Bragg reflections measured with the ordering wave vector $(1/2, 0, 1/2)$, Kato *et al.* have fitted a structure of collinear spins on the two lattices of Cu^{2+} sites, whereas Gibson *et al.* have fitted a canting of the spins between the two lattices.

In the experiments reported below, the magnetic order was observed continually as an increasing magnetic field was applied along the b -axis, up to a magnetic field strength of 11.5 T. Therefore, the magnetic structure could be investigated before and after the spin-flop transition and at high fields. The spin-flop transition was predicted to be an unusual transition, given the results of ESR measurements [83] and susceptibility measurements [85], because the couplings were predicted to be highly anisotropic such that the coupling scheme would change when going through the spin-flop phase.

5.2.1 Experimental Details

Sample Growth

The single crystal sample was grown by A. Prokofiev using the chemical vapour transport method [88]. Twinning occurred in the crystal because of the monoclinic to tetragonal structural distortion at 380 K. The sample used in the experiments was pressure treated

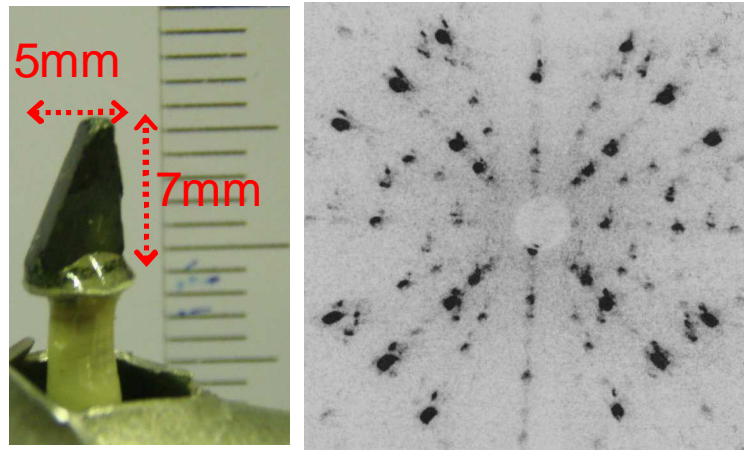


Figure 5.3: Right: The single crystal sample used in the measurements and mounted on an aluminium pin. Right: A Laue pattern taken of the sample which indicated that there was a large single crystal and small twinned crystallites present in the sample.

through this transition in order to de-twin the crystal of approximately 30 mm^3 . It was the same sample used in the experiments of Gibson *et al.* [85]. Figure 5.3 displays a neutron Laue pattern taken with the instrument Orient Express at the Institut Laue-Langevin (ILL). It shows an intense set of peaks with the addition of small peaks in the pattern. Although most of the sample was a single crystal, there were small crystallites and these produced weak Bragg peaks.

Unpolarized Diffraction

The instrument used for the unpolarized measurements was the two-axis neutron diffractometer, D23 at the ILL. The sample was mounted in the $(h, 0, l)$ horizontal plane in a cryomagnet with a base temperature of 2 K and maximum field of 12 T. The magnetic field was applied along the crystallographic b -axis and most measurements were made in the three-dimensional magnetically ordered phase, at the base temperature of 2 K. A neutron incident wavelength, $\lambda = 1.276 \text{ \AA}$ was used to check the nuclear structure and zero-field magnetic structure. Reflections out of the horizontal scattering plane were measured by making use of the lifting arm of the detector. A series of 87 integer (h, k, l) reflections at zero field were measured to fit the nuclear structure. A variety of other disallowed magnetic reflections were also measured including positions such as $(h, 0.5, l)$. Zero intensity was observed for these points in agreement with the published propagation vector $(0.5, 0, 0.5)$ [85]. In the measurements discussed below, a wavelength of $\lambda = 2.377 \text{ \AA}$ was used together with a graphite filter to filter out second-order scattering and to optimize the

measurements of the magnetic structure.

Measurements were made at zero field, 6 T and 11.5 T to observe changes in the magnetic structure with increasing field strength. A series of peaks with $(h \pm 0.5, 0, l \pm 0.5)$ and four nuclear peaks were measured to confirm that the crystal structure did not noticeably change. As a result it was possible to study the magnetic structure before and after the spin-flop and at high applied magnetic fields. Within the accuracy of the measurements, no change in the nuclear structure was seen in an applied field nor was any ferromagnetic component observed. All these peaks were measured again at 90 K with zero field to establish the background intensity and second-order feed through by the filter.

Polarized Diffraction

The polarized experiments were performed on the triple-axis spectrometer IN20 at the ILL. The single crystal of CuSb_2O_6 was mounted in a standard orange cryostat and aligned with $(h, 0, l)$ in the scattering plane. A Heusler monochromator and analyzer were used. Measurements were performed at a fixed wavelength of $\lambda = 2.360 \text{ \AA}$, with three polarization orientations of the incident beam on the sample: parallel to \mathbf{Q} ; perpendicular to \mathbf{Q} and in the scattering plane; and perpendicular to \mathbf{Q} and out of the scattering plane. These are summarized in Table 5.2. These measurements enabled a direct determination of components of the moments along the crystallographic axes.

5.2.2 Results

Zero Magnetic Field

The measurements permitted the reanalysis of the zero-field magnetic structure and, in particular, the effect of the twinned crystallites in the sample. The twinning produced small peaks in addition to the larger Bragg peaks from the main single crystal. These small side peaks increased the measured integrated intensity of the Bragg peaks as shown in Fig 5.4. The main Bragg intensity was extracted by fitting a series of gaussians to the observed spectra and extracting the integrated intensity of the main reflection. This method removed most of the effect of the small crystallites in the sample but it could not take account of small peaks which overlapped completely with the main Bragg reflection.

The extracted integrated intensity was corrected for the Lorentz factor and was fitted to the allowed magnetic structures using the program FullProf, which minimised a weighted

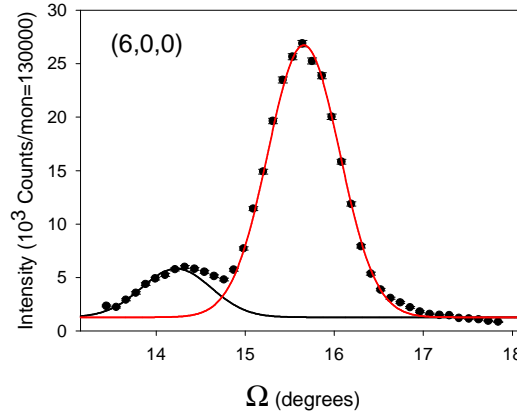


Figure 5.4: Plot demonstrating the effect of the small twinned crystallites on the sample which leads to side peaks. The method used to extract the main peak integrated intensity is shown by the red line.

Table 5.1: The possible magnetic moments for the two Cu^{2+} ions at the 2a site in the $\text{P2}_1/\text{n}$ space group with propagation wave vector $\mathbf{k}=(0.5,0,0.5)$.

(x,y,z)	Γ_1	Γ_2
(0, 0, 0)	(m_a, m_b, m_c)	(m_a, m_b, m_c)
(1/2, 1/2, 1/2)	$(-m_a, m_b, -m_c)$	$(m_a, -m_b, m_c)$

sum of squares. The fitted peaks had an ordering wave vector at $(0.5, 0, 0.5)$. Within the symmetry of the crystal this ordering wave vector allowed for two possible relative orientations of the spins on the two Cu^{2+} ions in the unit cell. The possible orientations of the spins are given in Table 5.1.

Γ_1 gave the best fit to the zero field measurements. The best fit had the moment aligned along the b -axis with an ordered moment component of $m_b = 0.389 \pm 0.011\mu_B$ giving $R_f = 9.6\%$ ¹. However after allowing for components of the moment along the a - or c -axes, in addition to the b -axis component, the resulting moments were not significantly different from zero ($m_a = 0.07 \pm 0.20\mu_B$, $m_c = 0.12 \pm 0.10\mu_B$).

It was possible to measure directly the three projections of the ordered moment along the crystallographic axes using polarized neutron diffraction. Table 5.2 shows the contributing components to the intensity for the spin-flip and non-spin-flip channels in the three polarization orientations. Each of the measurements in Table 5.2 were made for three

¹

$$R_f = 100 \frac{\sum_n [|G_{obs,n} - G_{calc,n}|]}{\sum_n G_{obs,n}}$$

where G is the structure factor and n runs over all observables.

Table 5.2: The contributing components to the intensity for the spin-flip and non-spin-flip channels in the three polarization orientations. μ_{\perp} is the component of the moment perpendicular to \mathbf{Q} , therefore $\mu_{\perp} = m_a \cos(\alpha) + m_c \sin(\alpha)$ and α is the angle of \mathbf{Q} to the a^* axis. μ_b is the component of the moment along the b -axis, out of the scattering plane. BG is the background in the spin-flip and non-spin-flip channel. N is the nuclear scattering and I is the nuclear spin scattering.

Polarization, \mathbf{P}	Spin-Flip	Non-Spin-Flip
$\mathbf{P} \parallel \mathbf{Q}$	$\frac{2}{3}\mathbf{I} + \text{BG}_{\text{SF}} + \mu_{\perp}^2 + \mu_b^2$	$\frac{1}{3}\mathbf{I} + \text{N} + \text{BG}_{\text{NSF}}$
$\mathbf{P} \perp \mathbf{Q}$ in scattering plane	$\frac{2}{3}\mathbf{I} + \text{BG}_{\text{SF}} + \mu_b^2$	$\frac{1}{3}\mathbf{I} + \text{N} + \text{BG}_{\text{NSF}} + \mu_{\perp}^2$
$\mathbf{P} \perp \mathbf{Q} \perp$ scattering plane	$\frac{2}{3}\mathbf{I} + \text{BG}_{\text{SF}} + \mu_{\perp}^2$	$\frac{1}{3}\mathbf{I} + \text{N} + \text{BG}_{\text{NSF}} + \mu_b^2$

Table 5.3: Calculated values for the tilt of the moment from the b -axis, β . These results are consistent with the unpolarized diffraction results that $\beta = 0$, within the error.

(h, k, l)	β	$\Delta\beta$
(1/2, 0, -1/2)	7.2	± 3.1
(1/2, 0, 3/2)	0	± 4.3
(-1/2, 0, 5/2)	0	± 12.5

different magnetic Bragg peaks. The six channels listed in Table 5.2 were measured on the peak maximum for three magnetic Bragg peaks. The tilt of the moment from the b -axis, β , was then calculated. Table 5.3 lists the results and shows that they are consistent with the unpolarized diffraction result, $\beta = 0$, within the error.

Applied Magnetic Field

The intensity of key magnetic Bragg reflections was measured as the magnetic field was increased, as shown in Fig. 5.5. The spin-flop transition was observed as the magnetic field was applied along the main moment direction, where spins moved from being predominantly along the b -axis to within the (a, c) -plane. The spin-flop field was measured to be 1.30(0.02) T, as shown in Fig. 5.5. Refinement of the magnetic structure at 6 T suggested that the moments flopped from being predominantly along the crystallographic b -axis to having a component along both the a - and c -axes. The fits of the high field magnetic Bragg reflections gave a structure in which the two spins in the unit cell were related by Γ_2 , where the moment lies such that at $(0, 0, 0)$:

$$(m_a, m_b, m_c) = (0.256 \pm 0.019, 0.054 \pm 0.032, 0.318 \pm 0.009) \mu_B$$

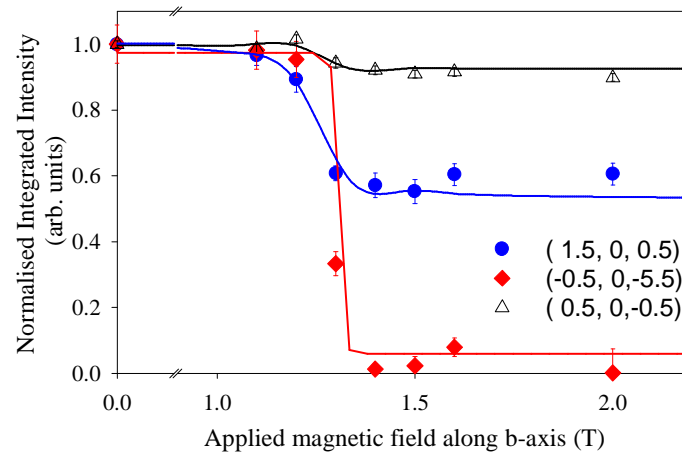


Figure 5.5: The change in the normalized integrated intensity of a series of peaks which indicates a change in the magnetic structure at the spin-flop transition.

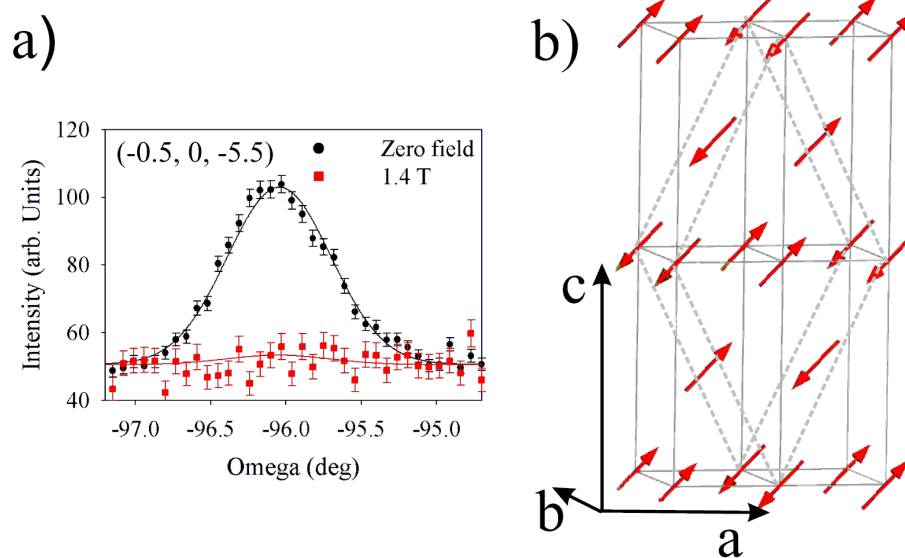


Figure 5.6: a) The intensity of the $(-0.5, 0, -5.5)$ reflection is reduced considerably on moving from zero field to 1.4 T. b) The fitted magnetic structure above the spin-flop transition field where spins are aligned within the (a, c) -plane.

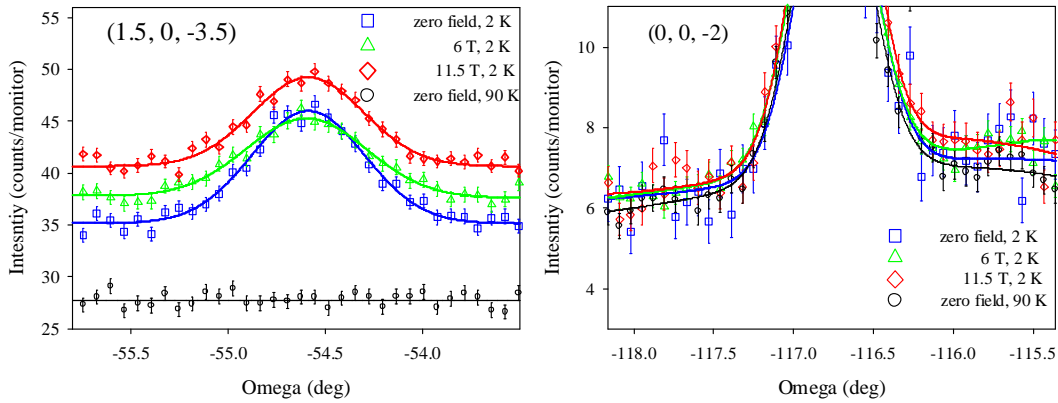


Figure 5.7: Omega scans over the magnetic Bragg reflection $(1.5, 0, -3.5)$ and nuclear Bragg reflection $(0, 0, -2)$ at increasing fields. The plots have not been displaced or normalized, but indicate that at high field the background around the magnetic Bragg reflections increased. The nuclear background around the nuclear Bragg reflection was constant. The high temperature scan of the $(1.5, 0, -3.5)$ shows a flat background considerably lower than all the scans in the ordered phase.

giving $R_f = 14.6\%$. Fig. 5.6 a) demonstrates this clearly by showing that the change in intensity of the $(-0.5, 0, -5.5)$ reflection drops considerably on moving above the spin-flop field. In contrast, the $(0.5, 0, -0.5)$ reflection shows little variation in intensity, as seen in Fig. 5.5. The spin-flopped magnetic structure is given in Fig. 5.6 b). In both the zero-field and the spin-flopped phase the magnetic moments were approximately perpendicular to the wave vector transfer at $(0.5, 0, -0.5)$. Therefore the intensity of the Bragg reflection was large and the change in intensity was small because the magnetic scattering is proportional to the size of moment perpendicular to the wave vector transfer. In contrast, the $(0.5, 0, -5.5)$ magnetic Bragg reflection was perpendicular to the magnetic moment in the zero field phase but in the spin-flopped phase was at an angle of 136° to the moment direction. Therefore the intensity changed considerably at the spin-flop transition.

The integrated intensity of a series of Bragg peaks measured at an applied field of 11.5 T revealed no change from the 6 T structure. At 11.5 T the best-fit values for the moment were

$$(m_a, m_b, m_c) = (0.253 \pm 0.018, 0.039 \pm 0.055, 0.320 \pm 0.0102) \mu_B$$

where the goodness of fit was $R_f = 10.2\%$. At high fields approaching 11.5 T the background around the measured magnetic Bragg reflections was seen to increase, as shown in Fig. 5.7 for the $(1.5, 0, 3.5)$ reflection. For comparison, the background around the nuclear

Bragg peak (0, 0 -2) is shown in Fig. 5.7 where it is clear that no increase was observed at high fields. The scan above the ordering temperature at 90 K shows a flat background and therefore there was no second-order scattering from the nuclear Bragg peaks present. The scan also shows that the intensity of the background was considerably higher at zero field and further increased at higher magnetic fields.

5.2.3 Discussion

In this study, the zero-field magnetic structure was found to be spins aligned into ferromagnetic lines along the b -axis and in antiferromagnetic line along the a -axis. Spins in two adjacent layers were collinear. The goodness of fit parameter, $R=9.6\%$, was reasonable for a single crystal study and was comparable to the value achieved by Gibson *et al.* of $R=7.4\%$. This zero-field magnetic structure agreed with the structure given by Kato *et al.* [89] to describe single crystal diffraction from a 1 mm^3 crystal. In contrast, the measurements of Gibson *et al.* [85], which were taken on the sample used in the present experiment, suggested that there was a small component of the ordered moment off the b -axis. They fitted a model in which the magnetic moment of $\mu = 0.51(2)\mu_B$ lay in the (a, b)-plane. Their model had a canted spin structure, where the spins were $103(6)^\circ$ at the (0, 0, 0) site and $70(5)^\circ$ at the $(1/2, 1/2, 1/2)$ site away from the a -axis. This implied a mixture of different irreducible representations but this was not expected in connection with a second-order phase transition.

In this study the long-range magnetic order resulted from spins aligned along the b -axis within the Cu^{2+} planes with both Cu^{2+} spins aligned along the b -direction. The unpolarized neutron diffraction indicated no canting of the spins from the b -axis and, therefore, no canting between Cu^{2+} in the unit cell, assuming a second-order phase transition. A small canting of the spins along from the b -axis on both Cu^{2+} sites would have been within the error of the measurements. Even so, the results did not overlap with the size of the angle proposed by Gibson *et al.*.

The observed low magnetic moment of $\mu = 0.39(1)\mu_B$ is not unusual for a spin-half low-dimensional system where quantum fluctuations and frustration reduce the ordered magnetic moment. For example, the one-dimensional spin-half antiferromagnet Sr_2CuO_3 has a moment of $0.06\mu_B$ [90]. Covalency could have led to further reductions from the full ordered moment of $1.12\mu_B$ (using $g = 2.23$ [83]). The ordered moment calculated from the present study was lower than the result given by Gibson *et al.* and this may be the

result of the inclusion of the intensity from the Bragg reflections originating from the small twinned crystallites within in the sample. If this were the case the ratio of the intensity of the nuclear Bragg reflections and magnetic Bragg reflections would be effected. The discrepancy may have arisen between this study and the Gibson magnetic moment result because the twinning had been accounted for to some extent within the analysis in this study.

The observed spin-flop field of 1.30(0.02) T, was in agreement with magnetisation measurements, where a small jump in the magnetisation has been seen at about 1.25 T [83]. This small spin-flop field implied a small anisotropy, which stabilised the spin ordering along the crystallographic b -axis. The magnetic structure measured above the spin-flop transition at 6 T had the same ordering wave vector as at zero field. This implies that the zero field coupling scheme did not change as dramatically as predicted by the results of ESR measurements. Yet the magnetic structure observed was unusual. It did not agree with predictions made from the susceptibility measurements, where the susceptibility was lower for the a -axis than the c -axis. Therefore it was expected that the spins would align along the a -axis. Instead the moment was nearly equally along both the a - and c -axes.

The anisotropy may in fact be complex, such that the local anisotropy is different at the $z = 0$ and $z = 1/2$ Cu^{2+} site. Therefore the effective anisotropy may change when going through the spin-flop transition. For such a case an inter-layer coupling between the two Cu^{2+} sites must exist. The symmetry of the crystal allows for two inter-layer couplings, J_γ and J_δ . J_γ links spins in the same sense on adjacent layers in the $(1/2, \pm 1/2, 1/2)$ direction. J_δ links spins in the opposite sense J_δ on adjacent layers in the $(-1/2, \pm 1/2, 1/2)$. Classically, the magnetic structure is stabilized if J_γ is ferromagnetic and J_δ antiferromagnetic.

If $J_\delta = J_\gamma$, a structure of collinear lattices is also expected. In such a case the mean field produced by one lattice on the other is zero and it may be assumed that the two lattices are independent of each other. Shender [91] has found that, when considering quantum fluctuations, the lattices are coupled and the quantum fluctuations select a collinear arrangement of the spin direction of the two sublattices.

At high field the increased background that was observed around magnetic Bragg reflections may have resulted from critical scattering due to the onset of a phase transition at higher magnetic fields. There was a large difference between the spin-flop field, an indication of a small anisotropy in the system and the high field caused the increased background. This difference is further developed in the next section.

5.3 Inelastic Neutron Scattering Study of the Excitation Spectrum of CuSb_2O_6 at Zero Field

5.3.1 Introduction

The experiments described in this section investigated the spin dynamics of CuSb_2O_6 . The main exchange paths of CuSb_2O_6 are in the basal (a , b)-plane where Cu^{2+} ions form a square lattice. The next-nearest neighbour exchange path is along the diagonal of the square of Cu^{2+} ions, where the angles of the Cu-O-O-Cu bond are close to 180° . This exchange path is expected to be the dominant strong antiferromagnetic interaction [84]. It is across only one diagonal of the square lattice and the coupling is frustrated by weaker nearest-neighbour interactions predicted to be antiferromagnetic. Previously, susceptibility measurements of CuSb_2O_6 have indicated quasi-one-dimensional Heisenberg behaviour with a Bonner-Fisher exchange of 49 K (4.2 meV) [85]. Within the spin-half one-dimensional Heisenberg model the excitations are expected to extend up to πJ [13]. Therefore, given the Bonner-Fisher exchange, $J \approx 4.2$ meV, the excitations are predicted to extend to $\pi J \approx 13$ meV.

A phase transition into a 3D phase has been observed at 8.6 K [86]. As shown in the previous section, spins are aligned along the b -axis in an antiferromagnetic arrangement with ordering vector $(1/2, 0, 1/2)$. In that section, diffraction measurements with a magnetic field applied along the b -axis, revealed that after the spin-flop transition, spins moved from the b -axis to within the (a , c)-plane. ESR measurements had suggested highly anisotropic couplings, where the coupling between spins would change sign as the alignment changed from the b - to the a -axis. The diffraction results suggested that those predictions of highly anisotropic coupling may not be present since the same ordering wave vector described both magnetic structures before and after the spin-flop transition. Although no change in the magnetic ordering was observed at high fields, increase in the background around the magnetic Bragg peaks suggested critical scattering, which could have indicated a transition at higher fields.

Before the present study, no inelastic neutron scattering studies had been performed on this system. Raman measurements on polycrystalline β - CuSb_2O_6 samples have shown phonon modes are present at approximately 15 meV [92, 93]. The experiments performed in this study were technically challenging due to the small volume of the crystal. Neutron

inelastic scattering experiments at low and high energy were performed at low temperatures, within the magnetically ordered phase, and at higher temperatures. The experiments investigated both the spin and lattice dynamics of the system.

The experiments showed that the layers of Cu^{2+} ions were weakly coupled with dominant in-plane interactions. The room temperature inelastic scattering experiments indicated a phonon mode in which the oxygen atoms of the the Cu-O-O-Cu bond oscillate; this led to the modulation of the main exchange path. Therefore an unusual intensity distribution of the excitations was observed and this was different to the one-dimensional spin chain intensity distribution predicted by the Bonner-Fisher model.

5.3.2 Experimental Details

A single crystal of CuSb_2O_6 of approximately 10 mm^3 was used as described in §5.2.1. It was mounted in a cryostat with the a- and c-axes in the scattering plane, thereby giving access to scattered wave vectors $(h, 0, l)$. The measured signal was small because the crystal was small and so the setup needed to have high flux and good background conditions. These conditions were achieved with a focussing analyser and boron carbide shielding to reduce background scattering. All the inelastic scattering measurements were carried out using triple-axis spectrometers. There were four experimental setups, two at low and two at higher energy, as briefly described below.

Low Energy Setups

The cold neutron triple-axis spectrometers IN12 and IN14 at the Institut Laue-Langevin (ILL) were used for low energy measurements. Each of them was set up with a pyrolytic graphite (PG) monochromator and analyser. The monochromators were vertically focussed and, in addition to the collimation provided by the neutron guide, a 60' collimator was placed after the monochromator. The analyser used on IN12 had a fixed vertical curvature and a variable horizontal curvature. IN14 was set up with a double-focussing analyser, which helped to improve the measurement of intensity from the small crystal. In addition, to increase signal, the distances were considerably reduced of the sample to the analyser in both setups. On IN12 the sample to monochromator distance was also varied.

The final wavelength was fixed at $\lambda = 4.188\text{ \AA}$ ($k_f = 1.5\text{ \AA}^{-1}$) and a Be-filter was placed between the sample and analyser to filter any higher-order neutrons scattered from the sample. The majority of measurements were taken at the base temperature of 1.5 K, which

was well below the magnetic ordering temperature of 8.6 K. A few measurements were taken at 12 K, which was above the ordering temperature but below the Bonner-Fisher temperature of 50 K.

Higher Energy Setups

Investigations at higher energy used the thermal triple-axis spectrometer IN20 at the ILL. For these measurements, a double-focussing silicon monochromator and a double-focussing PG analyser were used with a fixed final wavelength, $\lambda = 2.360 \text{ \AA}$ ($k_f = 2.662 \text{ \AA}^{-1}$), and a PG filter placed between the sample and analyser. Two different scattering senses were used when making the measurements. One scattering sense (SM=-, SS=+, SA=-) was found to put the detector in line with the direct beam such that certain energy and wave vector transfer positions were contaminated with higher background counts. Therefore, another scattering sense was used for most of the results presented, and this was SM=, SS=+, SA=+. The measurements were as follows:

- i) the majority were taken at 1.5 K, within the long-range ordered phase;
- ii) at 50 K, above the phase transition temperature and close to the Bonner-Fisher temperature;
- iii) at 130 K, a temperature above the Bonner-Fisher temperature.

Finally, the thermal triple-axis spectrometer IN3 at the ILL was used in a first search for phonon excitations. Even though the crystal was in an evacuated cryostat, the measurements were made at room temperature. The sample was mounted in an evacuated cryostat to reduce air scattering, which would otherwise have increased the background scattering. A copper monochromator was used with a PG analyser, which had a fixed vertical and a variable horizontal curvature. Measurements were made at a fixed final wavelength, $\lambda = 1.532 \text{ \AA}$ ($k_f = 4.1 \text{ \AA}^{-1}$), and once again, a PG filter was placed between the sample and analyser.

5.3.3 Measurements and Results

High-Energy Measurements

The main exchange was predicted to be across the diagonal of the Cu^{2+} square lattice within the (a, b) -plane. Constant wave vector scans of the type $(h, 0, 0.5)$ were made to

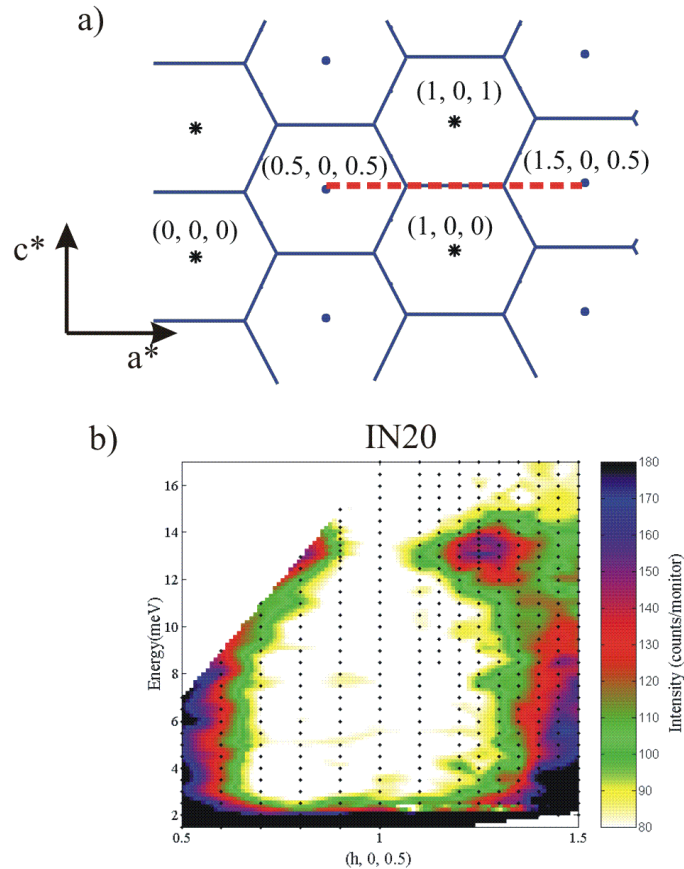


Figure 5.8: a) Plot of the reciprocal lattice of CuSb_2O_6 . The black stars represent the locations of possible nuclear Bragg reflections and the blue points represent the locations of magnetic Bragg reflections. The blue lines indicate the magnetic Brillouin zone. The red line indicates the line of constant Q scans plotted in b). b) An overview of constant Q scans made at high energy in the $(h, 0, 0.5)$ plane. A steep intense mode can be seen originating from the $(0.5, 0, 0.5)$ position and the central section has low intensity. These high energy measurements indicate a maximum to the dispersion at approximately 13 meV. The colour indicates the interpolated intensity between the measurements which are shown as black dots. Selected scans are given in Fig. 5.9

probe the in-plane interaction because the magnetic moments were aligned along the b -axis. The set of constant wave vector positions is indicated by the red line in the reciprocal lattice plot in Fig. 5.8 a) and an overview of the main measurements made is plotted in Figure 5.8 b). These measurements showed a strong dispersion of a mode that emerged from both the $(0.5, 0, 0.5)$ weak and the $(1.5, 0, 0.5)$ strong magnetic Bragg reflections. The dispersion was very steep and levelled off at 13 meV. There was an intense maximum at 13 meV at the Brillouin zone boundary corner $(1.25, 0, 0.5)$. The intensity was high close to the magnetic Bragg reflections and decreased at wave vectors close to $(1, 0, 0.5)$. The drop in intensity in the high energy measurements occurred along the zone boundary between two nuclear Bragg peaks. In Fig. 5.9 four constant wave vector scans are plotted which show that the 13 meV resonance appeared to be present across the Brillouin zone even at the magnetic zone centre. A gaussian profile with a mode at 12.5(4) meV fits the scan $\mathbf{Q} = (1.2, 0, 0.5)$. Figure 5.9 shows that the overall intensity increased greatly on approaching the $(1.5, 0, 0.5)$ magnetic Bragg reflection and the 12.5(4) meV mode was still present. In addition another mode was seen in the $(1.35, 0, 0.5)$ scan at approximately 6 meV which may have moved to higher energies at $(1.5, 0, 0.5)$. The four constant energy scans show that the main dispersion was steep and broad. The low-energy scans show that there was high intensity about the wave vector transfer position $(1.5, 0, 0.5)$ and the intensity decreased slightly at higher energy. At 12 meV the mode moved to lower Q and the dispersion appeared to bend towards the zone boundary. At 13 meV an intense mode was measured which was centred at $(1.2, 0, 0.5)$. These scans highlight the lack of clarity in the measurements due to: the broad Q resolution of the setup, which was needed to achieve a larger degree of focussing; and the thermal incident energies making the steep dispersion observed difficult to resolve.

Investigations into the nature of the 13 meV feature were made by taking constant \mathbf{Q} scans over the 13 meV resonance, where \mathbf{Q} was largely along either the a^* - or the c^* -direction. Two points within the Brillouin zone were measured and these are marked as points A and B in the sketch of the reciprocal lattice in Fig. 5.11. For each point two wave vectors were chosen which extended to an equivalent position in the Brillouin zone but which were approximately aligned with either the a^* or the c^* reciprocal lattice vector. The constant wave vector scans for points A and B are shown in Fig. 5.12 as plots a) and c) respectively. The intensity of magnetic scattering is proportional to the square of the wave vector transfer perpendicular the magnetic moment. In zero field the magnetic moment

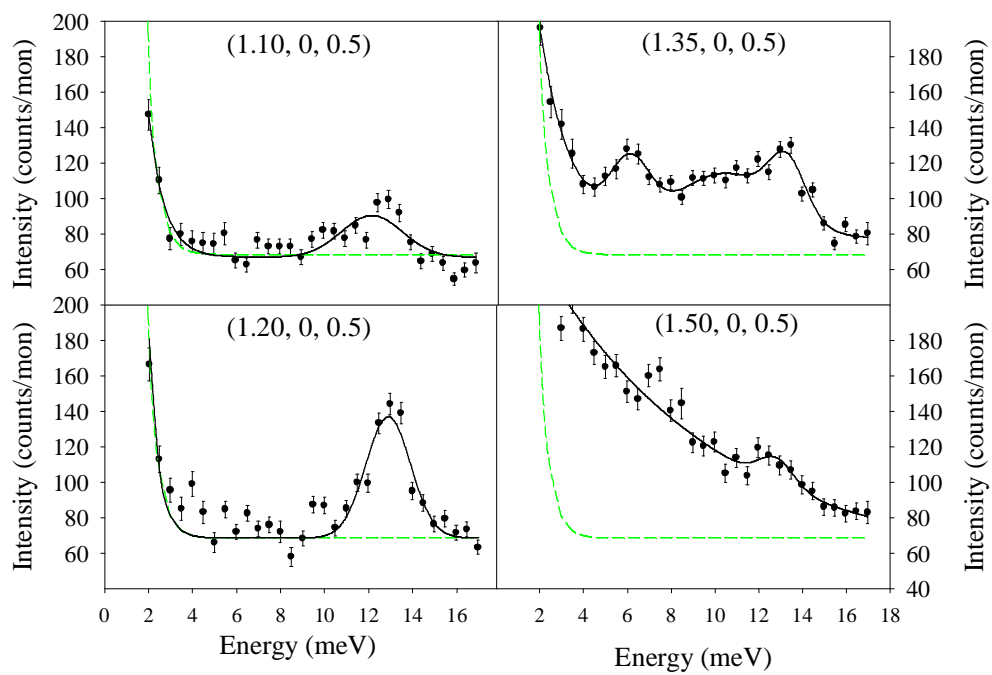


Figure 5.9: High energy constant Q scans showing the 13 meV resonance and a mode which moves from from high energy to low energy. The black lines are guides to the eye and the green line gives an indication of the non-magnetic background which is taken from fitting the (1, 0, 0.5) scan. An overview of all the measurements is given in Fig.5.8.

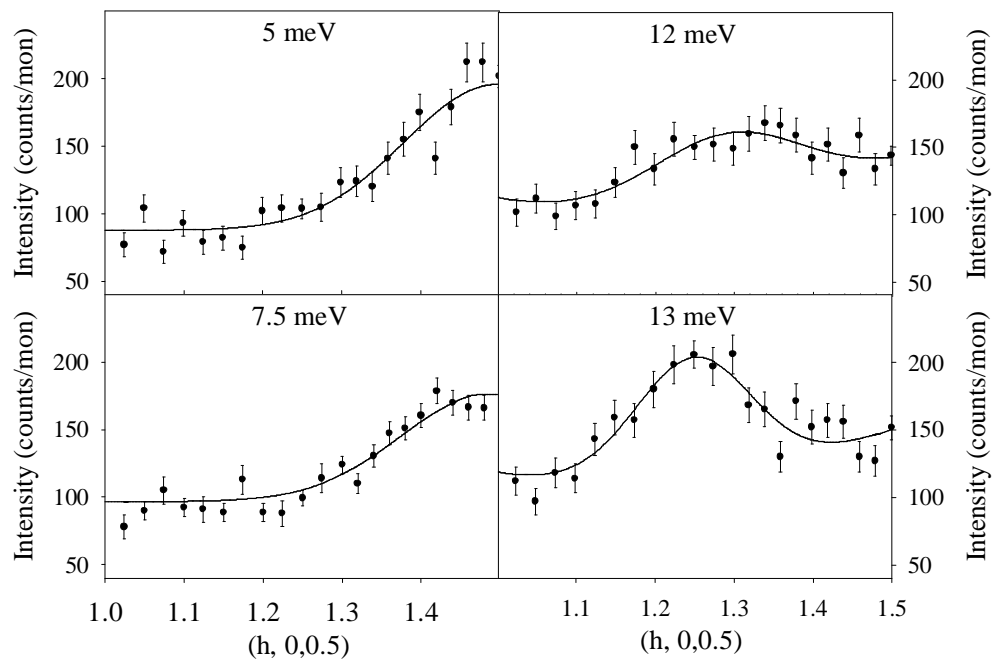


Figure 5.10: Constant energy scans at increasing energy showing a steep broad mode from the $(1.5, 0, 0.5)$ position which split into two modes at 12 meV. The feature is most intense at 13 meV. The black lines are guides to the eye. These measurements were made with the spectrometer in a different scattering sense to the measurements shown in Fig. 5.8 and Fig. 5.9. Therefore although shown with the same monitor value the counts are different due to a difference in resolution and background. However, the main features of the measured spectrum should remain the same.

in CuSb_2O_6 is perpendicular to both a^* - and c^* -directions and so no difference in intensity, due to the polarization factor, is expected for magnetic scattering. Therefore, since the wave vector transfer was of a similar magnitude, the magnetic form factor would be approximately the same for both points. The intensity of a phonon mode is dependent on its polarization and the wave vector transfer. If phonon modes are present then they may have a polarization factor which varies between the two orientations and so the intensity of phonon modes may differ. Plot a) shows that the intensity of the 13 meV resonance was the same for both wave vector transfers and this would be expected for a magnetic mode.

Constant wave vector scans were also made at equivalent positions in the Brillouin zone but at larger wave vector transfer values, Q . The intensity of phonon modes is proportional to Q^2 for a particular polarization. The results shown in Fig. 5.12 as plots b) and d) show large increases in intensity and therefore these indicate the presence of phonons within the measured energy range.

The intense excitation at 13 meV was measured at three temperatures as shown in Fig. 5.13. The figure shows that:

- i) above the ordering temperature the peak broadened but was still present;
- ii) at the Bonner-Fisher temperature the intensity of the peak fell considerably;
- iii) at 130 K, the intensity increased but there was no obvious peak about the 13 meV mode.

In order to probe the dispersion of the observed mode in other directions a series of constant wave vector scans were made of the type $(0.5, 0, l)$ and an overview is plotted in Fig. 5.14 a). The intensity in the colour plot is given as the natural logarithm to highlight the lack of any dispersion at high energy transfer. The two constant wave vector scans plotted in Fig. 5.14 b) show a significant change in the intensity at low energies approaching the zone boundary at $(0.5, 0, 3)$, indicating a small dispersion at low energies in the $(0.5, 0, l)$ direction.

Low-Energy Measurements

The high-energy measurements established that the dispersion within the $(0.5, 0, l)$ direction must have been small since no dispersion was observed at higher energy. Therefore, low-energy measurements were made in an attempt to observe this dispersion. An overview

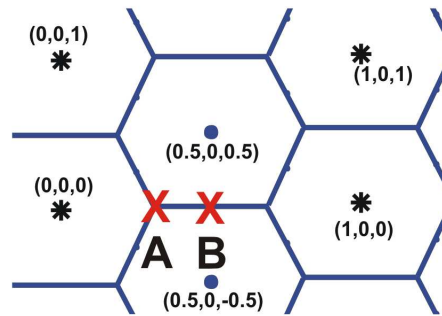


Figure 5.11: Sketch of the magnetic Brillouin zone for CuSb_2O_6 . The black stars represent the locations of possible nuclear Bragg reflections and the blue points represent the locations of magnetic Bragg reflections. The point A and B refer to the equivalent positions of the constant Q scans in Fig. 5.12.

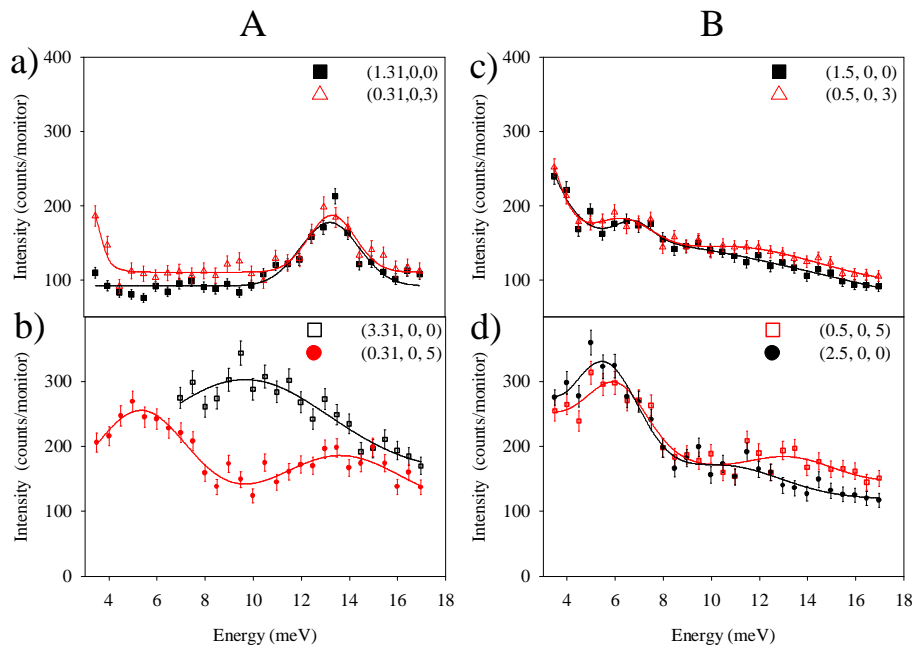


Figure 5.12: Plots of constant wave vector scans at low temperature. The left column and right column show constant wave vector scans at wave vectors equivalent to points A and B as plotted in the Brillouin zone given in Fig 5.11. Plot a) shows that the 13 meV feature was constant on moving from the orientation of Q nearly parallel to a^* and c^* . At large Q values modes were seen which do show a difference in intensity between the two orientations. The scan in plot c) shows little difference between the two orientations and plot d) shows that the equivalent points at larger Q values indicated the presence of phonon modes at low and high energy.

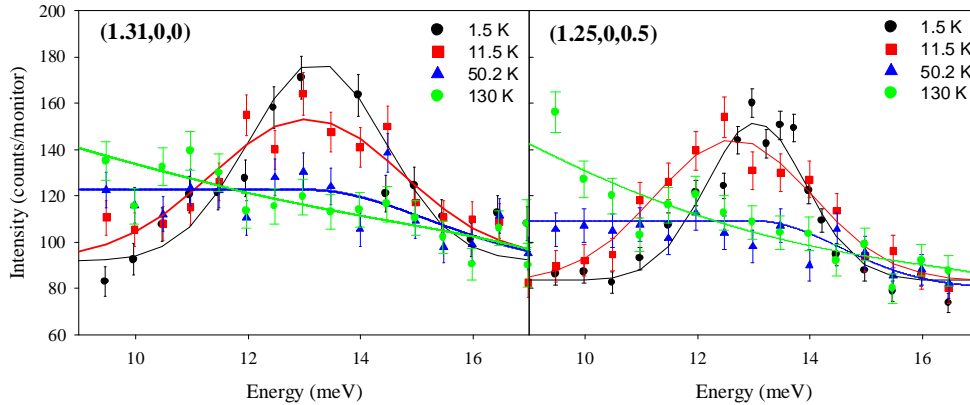


Figure 5.13: Intense peak of the 13meV mode at $(1.31, 0, 0)$ and $(1.25, 0, 0.5)$ in the ordered phase (black), which broadens above the transition temperature (red) and above the Bonner-Fisher temperature (green) is considerably reduced in intensity. The blue line indicates the low temperature background.

of the measurements made at $(0.5, 0, l)$ is plotted in Fig. 5.15. It should be noted that the majority of measurements in Fig. 5.15 do not have the same relative error bar as those in the colour figure at high energy, where the intensity distribution appeared smoother. The main features observed were two modes at approximately 2 meV and 3.25 meV which showed little dispersion. High intensity was observed about the strong magnetic Bragg peaks at $(0.5, 0, -0.5)$ and $(0.5, 0, 1.5)$. The intensity distribution in Fig. 5.15 suggests that the 2 meV mode dispersed from the $(0.5, 0, -0.5)$ and $(0.5, 0, 1.5)$ positions. Even if that were the case, however, some intensity measured at low energies may also have originated from the $(h, 0, 0.5)$ dispersion because the the resolution ellipsoid extended in energy and in all Q directions. Lower intensity was measured about the $(0.5, 0, 0.5)$ magnetic Bragg peak and this had also been observed to be weak in the diffraction measurements. The streak of intensity marked out by the white ellipse in Figure 5.15 was associated with a small crystallite, which produced a sharp peak on the elastic line at $(0.5, 0, 0.45)$.

A further set of scans that were counted for longer at selected constant wave vectors are shown in Fig. 5.16. The low-energy measurements at constant wave vector, shown in Fig. 5.16, were made in both the IN12 and the IN14 experiments. Key scans, for example at the Brillouin zone boundary, were repeated to compare results between the two experimental setups and the IN12 results were normalized to the IN14 measurements. Two modes were seen to disperse slightly in the direction $(0.5, 0, l)$ through the Brillouin zone within the ordered phase, and one mode at 3.25 meV was seen to be nearly flat. At the Brillouin

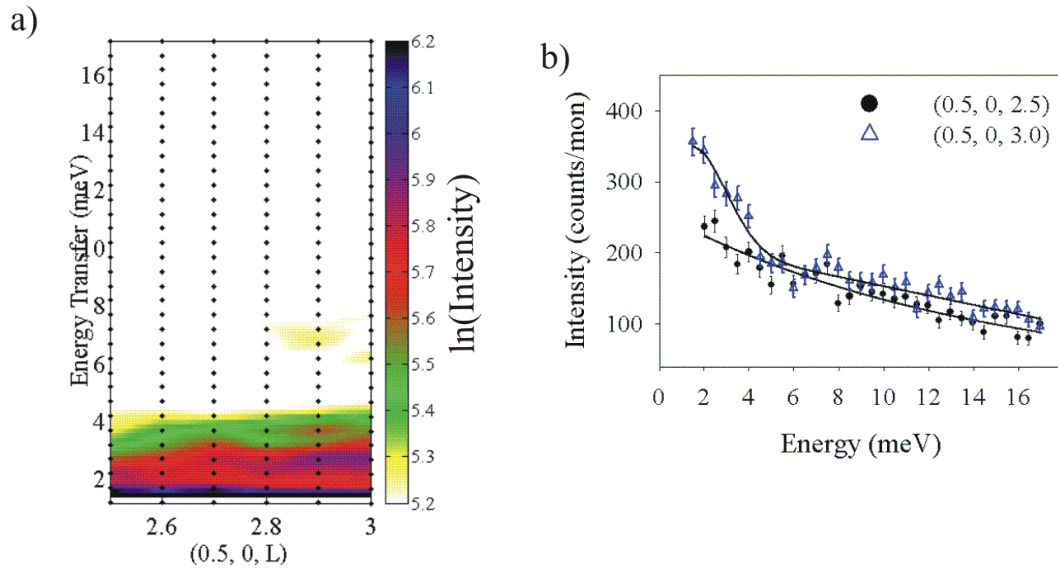


Figure 5.14: a) Overview of the high energy constant wave vector scans at $(0.5, 0, L)$ where no high energy modes were seen. The colour indicates the natural logarithm of the interpolated intensity. b) Two constant wave vector scans highlight that the intensity only changed at low energy.

zone boundary the energy gap to the three modes was maximized and had a value of approximately 2 meV. In Fig. 5.16, the constant wave vector scan at $(0.5, 0, -0.5)$, shows that there was an energy gap of approximately 1.25 meV at the Brillouin zone centre. Measurements of the gap were hindered at this wave vector since the Bragg reflection was strong yet at the weaker $(0.5, 0, 0.5)$ Bragg reflection the intensity from the crystallite at $(0.5, 0, 0.45)$ was observed.

Fig. 5.17 shows a constant wave vector scan at $(0.5, 0, 1)$ taken below and above the magnetic ordering temperature. The figure shows that the modes that were observed at low temperature were no longer measured above the long-range magnetic ordering temperature. Therefore no inter-layer dispersion of the modes was seen at temperatures higher than the ordering temperature.

Phonon Calculation and Preliminary Phonon Measurements

Phonon modes observed at low temperature should be more intense and therefore more easily observed at room temperature and so room temperature inelastic measurements were made to investigate low-energy phonon modes. A search was made to observe excitations in the region of the strong mode at 13 meV measured at low temperature. Fig. 5.18 shows

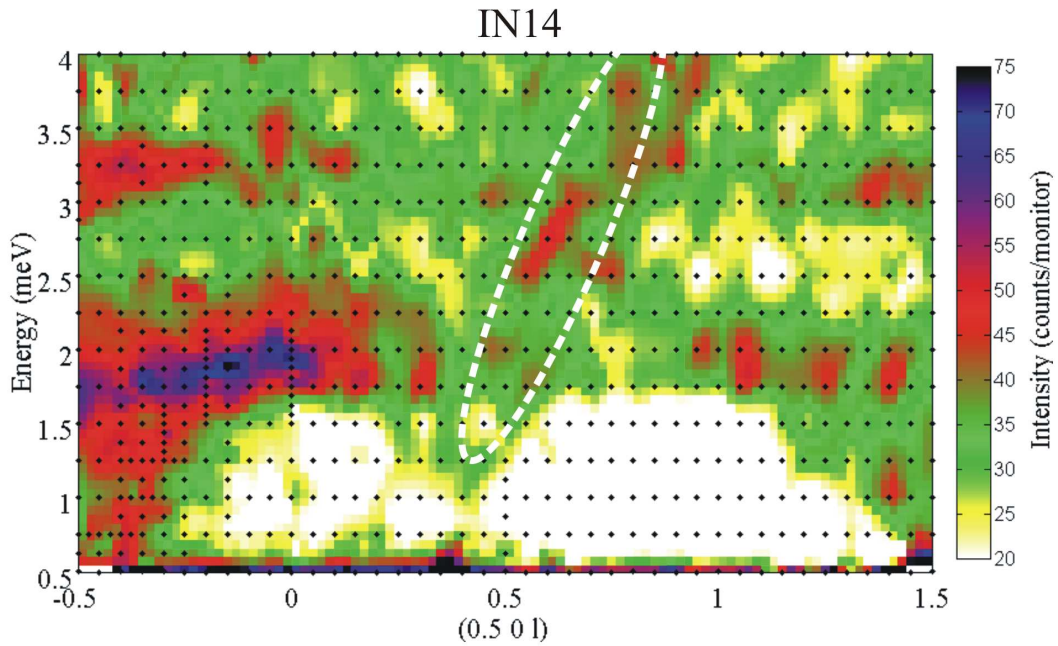


Figure 5.15: Overview plot of the measurements made on IN14. The black points indicate the measurements made. The white ellipse covers an region of intensity associated with a small crystallite producing a Bragg reflection on the elastic line at $(0.5, 0, 0.45)$.

a series of constant wave vector scans in which a phonon mode is visible at approximately 15 meV. The mode dispersed through the Brillouin zone in both the $(h, 0, 0.5)$ and $(0.5, 0, l)$ directions.

Initial theoretical calculations of the phonon modes, using the PHONON[94] and VASP software, were made based on the high temperature phase α -CuSb₂O₆ structure. VASP (The Vienna Ab-initio Software Package) was used to find the ground-state position of the atoms in the lattice and the forces on atoms displaced from the ground state due to the potential of the surrounding atoms. The resulting matrix of force constants was diagonalized using PHONON to give the energy of the levels and the eigenvectors which described the associated displacements. In this way a map of the dispersion of the phonons was made by diagonalizing the force matrix for a series of wave vectors. The results are shown in Fig. 5.18.

In order to compare the observations with the expected results from the theory, the intensity of the modes was first calculated using PHONON and then convolved with a gaussian to replicate the observed resolution. These plots were for comparison with the observations since the difference in symmetry of the two systems would have impacted on

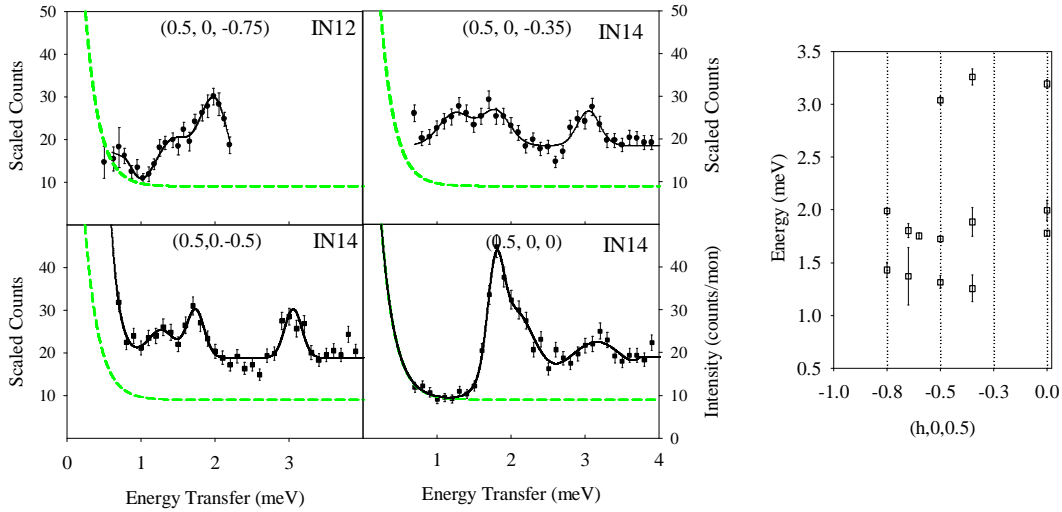


Figure 5.16: Left: Low-energy measurements of modes observed to disperse slightly along the $(0.5, 0, l)$ direction. IN12 measurements scaled with the data taken IN14 measurements. The black lines indicate a fit to the data using a gaussian profile. Right: The centres of the peaks are plotted for each constant wave vector scan.

the forces on the atoms and therefore on the energy and number of phonon modes. The calculation did give an indication of the position of the phonon modes and the associated movement of the lattice. These calculations guided the preliminary phonon measurements such that the phonon mode identified as potentially relevant to the magnetic excitations could be measured.

Figs. 5.12 b) and d) show the results of low temperature investigations of possible phonon modes in the region of the 13 meV feature. The figure shows that phonon modes were measured with large intensity at large wave vector transfer, Q . Constant wave vector scans at equivalent points in the Brillouin zone showed little variation at low Q , but a large difference at high Q . These observations indicated that the 13 meV feature had some magnetic contributions to the intensity but may have been influenced by phonon contributions. Fig 5.18 shows that at room temperature a phonon mode occurred at the nuclear Bragg peak $(4, 0, 0)$ at 15 meV.

The phonon mode measured at 15 meV was close to a mode calculated at 11 meV within the α - CuSb_2O_6 structure. This mode was associated with a displacement of the chemical Cu-O-O-Cu bond which links two Cu^{2+} ions across the diagonal of the square lattice. The vibration consisted of the oscillation of the oxygen atoms about the midpoint of the O-O bond.

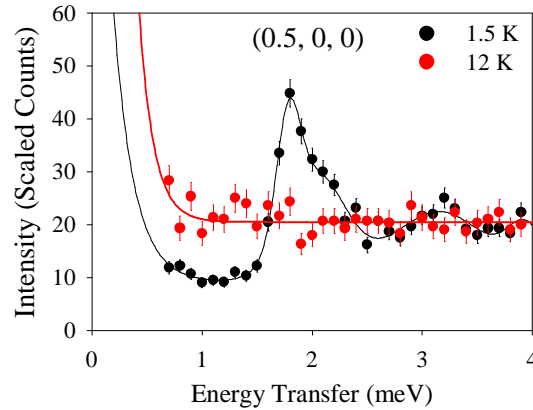


Figure 5.17: Low energy constant wave vector scan at $(0.5, 0, 0)$ shows a strong mode present in the ordered phase (black), which is not present on moving above the transition temperature (red) to 12 K.

5.3.4 Analysis

The inelastic scattering measurements in the $(h, 0, 0.5)$ direction showed a steep dispersion of a mode which has a maximum at approximately 13 meV. A Bonner-Fisher fit to the susceptibility measurements characterized the system as a one-dimensional spin-half chain, where the magnitude of the main interaction was $J = 4.2$ meV [85] and the zone boundary was therefore expected at $\pi J = 13.1$ meV. This was consistent with the strong 13 meV zone boundary energy measured that was actually measured. At the zone boundary point $(1.25, 0, 0.5)$ there was a resonance at 13 meV. The temperature dependence of the 13 meV feature indicated the contribution to its high intensity from magnetic interactions. The fact that at the Bonner-Fisher temperature the intensity of the peak fell considerably, demonstrated that there was a magnetic contribution to the intensity of the 13 meV resonance in Fig. 5.13.

The $(0.5, 0, l)$ dispersion was related to the inter-layer couplings and therefore the smaller dispersion indicated that the inter-plane couplings were weaker than the in-plane couplings. The modes were not observed above the transition temperature. The temperature dependence of the measurements suggested that the couplings were weak and that they brought about long-range order.

Three modes were measured in the $(0.5, 0, l)$ direction. A very small dispersion was observed within the ordered phase. The mode with the highest energy had a maximum of 3.25 meV. The bandwidth of the dispersion along the $(0.5, 0, l)$ direction gave an indication

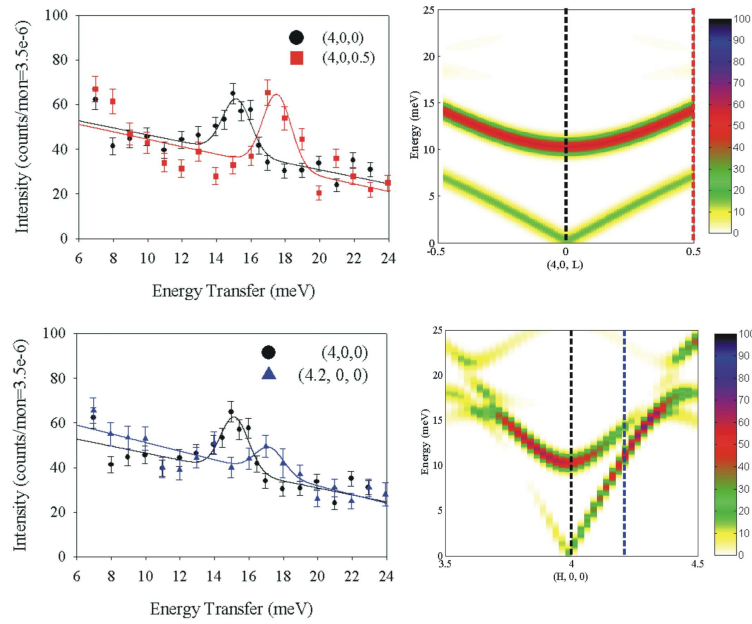


Figure 5.18: Room temperature inelastic scattering measurements. Left column: The 14.6 meV mode observed in Raman spectra was observed in constant wave vector scans about the $(4, 0, 0)$. The mode was seen to disperse through the Brillouin zone. In the right column an overview of the predicted intensities are given from the phonon calculations. These measurements are in reasonable agreement with the calculation of the dispersion of the phonon modes in the high temperature undistorted structure, α -CuSb₂O₆. This mode is predicted to bend the Cu-O-O-Cu bond, which is the main exchange path way. The coloured dotted lines on the calculation plots indicate the scans measured and plotted on the left.

of the inter-layer couplings between the Cu²⁺ planes. The measurements at low energy indicated that the inter-layer exchange was small in comparison to the in-plane exchange because the maximum of the dispersion in the $(0.5, 0, l)$ direction was 25% of the maximum dispersion in the $(h, 0, 0.5)$ direction. The measurements above the transition temperature at 12 K, shown in Fig. 5.17, indicated that the formation of long-range order in the crystal was due to the inter-layer coupling because no modes were observed. The crystal structure would suggest that these were the weaker couplings since the copper planes would have been separated by planes of antimony.

Spin-Wave Calculation

A spin-wave calculation was carried out to derive the dispersion relations to analyse the data further and to investigate the coupling scheme in this system. The initial Hamiltonian

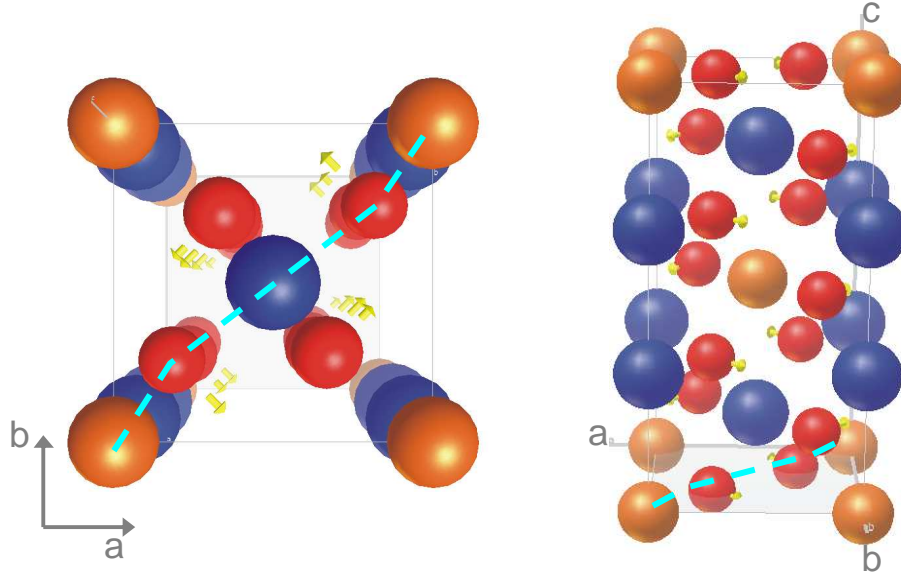


Figure 5.19: Sketch of the displacements of the oxygen atoms as calculated by phonon calculations for the phonon mode at 11 meV. The orange balls indicate the Cu ions, the red oxygen and blue antimony. The arrow indicate the the movement of the atoms and the dashed blue line indicates the main exchange path.

considered took the form:

$$\mathcal{H} = \sum_{in} J_n (S_{\mathbf{r}_i}^x S_{\mathbf{r}_i+\mathbf{r}_n}^x + S_{\mathbf{r}_i}^y S_{\mathbf{r}_i+\mathbf{r}_n}^y + (1 + \epsilon) S_{\mathbf{r}_i}^z S_{\mathbf{r}_i+\mathbf{r}_n}^z) \quad (5.1)$$

where ϵ modeled a symmetric coupling anisotropy within the system. It was introduced because of the observed spin-flop transition and the flat modes measured in the low energy spectrum. In this equation the exchange couplings are:

- J_A Exchange between next-nearest neighbours in the direction $(1,1,0)$ and $(-1,-1,0)$ in layer at $z = 0$, and $(1, -1, 0)$ and $(-1, 1, 0)$ at $z = 0.5$;
- J_a and J_b Exchange between nearest-neighbours along the a - and b -axes;
- J_γ Exchange between adjacent layers ie at $z = 0$ and $z = 0.5$. This exchange couples the two sets of sub-lattices along the $(1/2, \pm 1/2, 1/2)$ direction;
- J_δ Exchange between adjacent layers ie at $z = 0$ and $z = 0.5$. This exchange couples the two sets of sub-lattices along $(-1/2, \pm 1/2, 1/2)$.

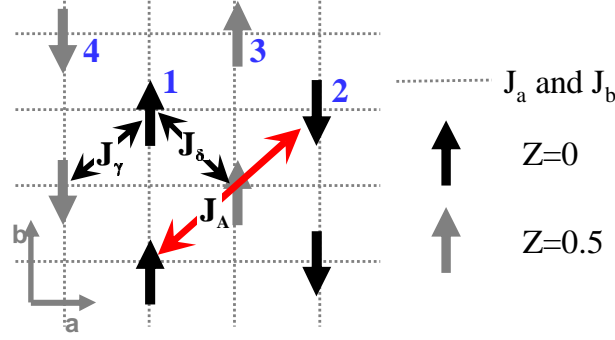


Figure 5.20: Sketch of the zero field magnetic structure indicating the four sublattices in the two Cu^{2+} ayers and considered in the spin-wave calculation and the couplings between the sublattices.

All the couplings are shown in Fig. 5.20. The couplings were introduced such that the crystal symmetry was respected, that is, bonds which were transformed into each other by a symmetry element were given the same label and kept the same strength. If no such symmetry requirement had existed, for example $J_a \neq J_b$, a new interaction would have been introduced.

The spin-wave calculation was made by taking the ground state as a structure of antiferromagnetically ordered collinear lines of spins within the plane and collinear to the neighbouring planes, as shown in Fig. 5.20. The calculation was set up by considering two types of spin site, which formed two sublattices in a plane, corresponding to the two senses parallel to the b -axis within the (a, b) -plane. Therefore there were four sublattices in the unit cell. The four sub-lattices are labeled in Fig. 5.20. The details of the calculation are given in Appendix F. For the assumed Hamiltonian there are two dispersion branches which are both two-fold degenerate. The dispersion relations for this model are:

$$\omega_+(\mathbf{Q}) = \sqrt{(A_{\mathbf{Q}} + B_{\mathbf{Q}} + C_{\mathbf{Q}} + D_{\mathbf{Q}})(A_{\mathbf{Q}} - B_{\mathbf{Q}} - C_{\mathbf{Q}} + D_{\mathbf{Q}})} \quad (5.2)$$

$$\omega_-(\mathbf{Q}) = \sqrt{(A_{\mathbf{Q}} + B_{\mathbf{Q}} - C_{\mathbf{Q}} - D_{\mathbf{Q}})(A_{\mathbf{Q}} - B_{\mathbf{Q}} + C_{\mathbf{Q}} - D_{\mathbf{Q}})} \quad (5.3)$$

where $\mathbf{Q} = (h, k, l)$ in reference to the reciprocal lattices of the monoclinic reciprocal lattice vectors. For $k = 0$:

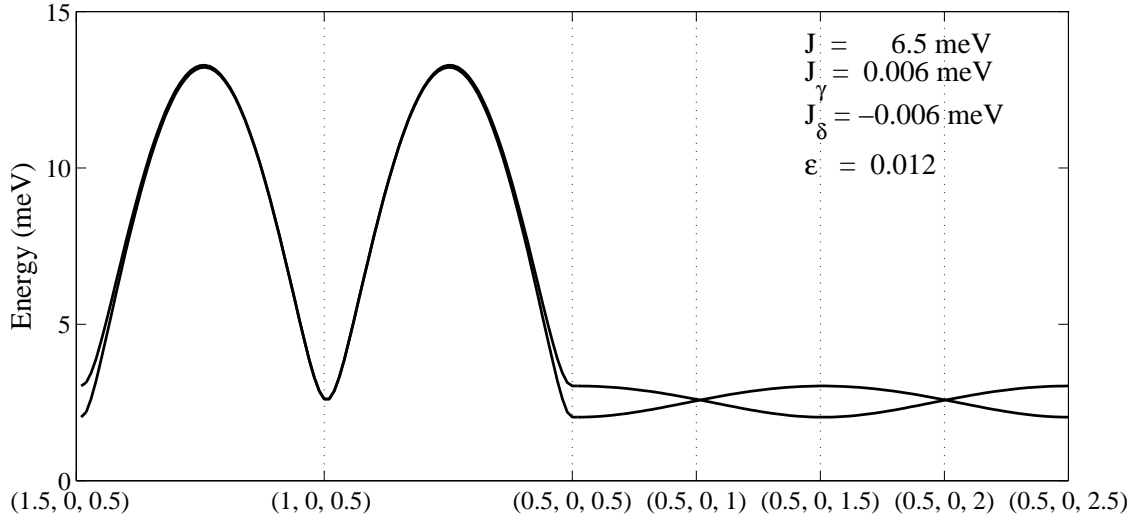


Figure 5.21: The spin-wave dispersion showing two modes which are both two fold degenerate. This model gave a small energy gap. In the $(h, 0, 0.5)$ direction the mode extends to 13 meV and in the $(0.5, 0, 1)$ direction the maximum is at approximately 2 meV.

$$\begin{aligned}
 A_{\mathbf{Q}} &= 2(J_A + J_a + 2J_\gamma - 2J_\delta)(1 + \epsilon) \\
 B_{\mathbf{Q}} &= 2J_A \cos(2\pi h) + 2J_a \cos(2\pi h) \\
 C_{\mathbf{Q}} &= -4J_\delta(\cos(\pi h) \cos(\pi l) + \sin(\pi h) \sin(\pi l)) \\
 D_{\mathbf{Q}} &= -4J_\gamma(\cos(\pi h) \cos(\pi l) - \sin(\pi h) \sin(\pi l))
 \end{aligned}$$

Equations 5.2 and 5.3 demonstrate that measurements at wave vector transfer $(h, 0, l)$ do not probe the nearest-neighbour coupling in the b-direction and that both couplings in the a-direction can be taken as an overall coupling, $J=J_A+J_a$.

Fig 5.21 shows a plot of the dispersion for a set of representative parameters. It shows that the in-plane coupling was the largest and produced a high energy mode with a maximum of 13 meV where the in-plane coupling was $J= 6.5$ meV. The energy of the branch at $(0.5, 0, 0)$ indicated the strength of the inter-layer couplings. The inter-layer couplings in this model are J_γ and J_δ and these couple adjacent layers of spins.

In the following discussion of the $(0.5, 0, l)$ dispersion, the range of possible J_γ , J_δ and ϵ are considered. In the spin-wave calculation J_δ and J_γ couple spins aligned in the same sense and opposite sense, respectively. Therefore, for a ferromagnetic J_δ , $J_\delta < 0$, and for an antiferromagnetic J_γ , $J_\gamma > 0$, reinforcing the stability of the ground state. Fig. 5.15 shows an overview of measurements in the $(0.5, 0, l)$ direction. A coarse interpretation of these measurements could be that a 2 meV energy gap was observed to a dispersion that extended

to 3 meV. Such a case would give a maximum value to the anisotropy factor ϵ . A 2 meV energy gap, Δ , is modeled by $\epsilon \approx \frac{\Delta^2}{8J^2} = 0.012$. If ϵ , J_γ and J_δ are small, as observed in the measurements, then

$$\omega_{\pm}^2 = 8J^2\epsilon + 16J(J_\gamma - J_\delta)(1 + \epsilon \pm \sin(\pi l)).$$

Therefore, the bandwidth of the $(0.5, 0, l)$ dispersion was of the order $16J(J_\gamma - J_\delta)$. For a band-width of approximately 1 meV above a 2 meV energy gap, $J_\gamma - J_\delta = 0.012$ meV. If instead the measurements are interpreted as flat modes then, to achieve a dispersionless mode in the $(0.5, 0, l)$ direction, $J_\gamma - J_\delta = 0$. The measurements would suggest that the maximum possible bandwidth of the excitations was 3 meV. Therefore considering no energy gap, then the couplings would be $J_\gamma - J_\delta = 0.022$ meV.

The spin-wave model captures the possibility of an energy gap as was observed in the data. The zero-field magnetic structure is stabilized when ϵ is positive, indicating an Ising-type Hamiltonian. The Ising-type anisotropy was further supported by the observation of the spin-flop transition and gapped excitations. The spin-flop field that had been measured from magnetisation measurements was $H_{SF} = 1.25$ T [83]. Using the spin-flop field and exchange interaction from the spin-wave model, $J = 6.5$ meV, an estimate of the magnitude of the anisotropy could be calculated using a mean field approach [95]. The H_{SF} , in terms of an anisotropy field, H_A , and exchange field, H_E , is:

$$H_{SF} = \sqrt{2H_E H_A - H_A^2},$$

where,

$$H_A = \frac{2JS}{g\mu_B}, \quad H_E = \frac{\epsilon 2JS}{g\mu_B}.$$

Using $g = 2.21$ as calculated from ESR measurements [83] and setting $S=1/2$ then, $\epsilon = 3 \times 10^{-4}$. This leads to an energy gap, Δ , of approximately 0.3 meV. This is a quarter of the size expected from the inelastic measurements which suggested a minimum energy gap of approximately 1.25 meV and therefore a deviation from the isotropic exchange of $\epsilon \approx 1 \times 10^{-3}$. The inelastic measurements could not discount a low energy mode with a small dispersion at 0.3 meV because of the steep increase in intensity about the $(0.5, 0, -0.5)$ scans at low energy which could have been due to the broad in-plane dispersion.

In the model used so far the gap arises as a result of the anisotropy of the main in-plane exchange. If this model were true the modes should have been present above the ordering

temperature. The initial model assumed that all the couplings, in-plane and inter-plane, were anisotropic to the same degree. Fig. 5.17 shows that the observed modes were no longer present above the ordering temperature. This suggests that if they were gapped because of an anisotropy they were not linked to the one-dimensional coupling. If the observed modes were associated with the in-plane coupling then they would be expected to be present above the ordering temperature but to be dispersion-less. That is, the gapped modes should be associated with the inter-chain couplings, responsible for the 3D-order. Therefore a second model was considered in which the Hamiltonian takes the form:

$$\mathcal{H} = \sum_{i,n=A,a,b} J_n (\mathbf{S}_{\mathbf{r}_i} \cdot \mathbf{S}_{\mathbf{r}_i+\mathbf{r}_n}) + \sum_{i,n=\gamma,\delta} J_n (S_{\mathbf{r}_i}^x S_{\mathbf{r}_i+\mathbf{r}_n}^x + S_{\mathbf{r}_i}^y S_{\mathbf{r}_i+\mathbf{r}_n}^y + (1 + \epsilon) S_{\mathbf{r}_i}^z S_{\mathbf{r}_i+\mathbf{r}_n}^z). \quad (5.4)$$

In this case the dispersion of the two modes can be described with equations 5.2 and 5.3 where $A_{\mathbf{Q}}$, $B_{\mathbf{Q}}$, $C_{\mathbf{Q}}$, $D_{\mathbf{Q}}$ are for $k = 0$:

$$\begin{aligned} A_{\mathbf{Q}} &= 2(J_A + J_a) + 4(J_\gamma - J_\delta)(1 + \epsilon), \\ B_{\mathbf{Q}} &= 2J_A \cos(2\pi h) + 2J_a \cos(2\pi h), \\ C_{\mathbf{Q}} &= -4J_\delta(\cos(\pi h) \cos(\pi l) + \sin(\pi h) \sin(\pi l)), \\ D_{\mathbf{Q}} &= -4J_\gamma(\cos(\pi h) \cos(\pi l) - \sin(\pi h) \sin(\pi l)). \end{aligned}$$

In this case again assuming small J_γ , J_δ and ϵ the dispersion can be approximated to:

$$\omega_{\pm}^2 \approx 16J(J_\gamma - J_\delta)(1 + \epsilon \pm \sin(\pi l))$$

In this model no energy gap, Δ , is present for any ϵ if $J_\gamma = J_\delta$ because $\Delta \approx \sqrt{16J(J_\gamma - J_\delta)\epsilon}$. Therefore, the model predicts that gapped modes due to an anisotropy of the couplings must also be associated with some dispersion of those modes. The bandwidth of the dispersion is approximately $\sqrt{16J(J_\gamma - J_\delta)}$. The observed modes are gapped with a small dispersion. Therefore for a large gap with respect to the dispersion bandwidth $\epsilon \gg 1$. This is the case for flat gapped modes as seen in the data.

The same equations as above hold for H_{SF} and H_E . Assuming small inter-layer coupling, and using the mean field approach to estimate the magnitude of the anisotropy constant from the spin-flop field, the anisotropy field is now:

$$H_A = \frac{4\epsilon(J_\gamma - J_\delta)S}{g\mu_B}.$$

At a spin-flop field of 1.25 T, $\epsilon(J_\gamma - J_\delta) = 0.001$ leads to an energy gap of the order of 0.3 meV and once again this does not explain an energy gap of approximately 1.25 meV. For such an energy gap $\epsilon(J_\gamma - J_\delta) = 0.015$.

The spin-wave calculation describes some key features of the observed dispersion but it does not give the correct number of modes or the full dispersion that was measured. The results of the spin-wave calculation would be consistent with the largely one-dimensional spin-half chain predicted by susceptibility measurements but the measured intensity distribution was not consistent with such a one-dimensional system. The three modes seen in the $(0.5, 0, l)$ direction cannot be explained by the calculation, in which two modes are predicted which are two-fold degenerate. A canting of the spins in one layer with respect to the next may cause a small splitting of the degenerate modes although this would not be expected to cause a splitting as great as 1 meV, which was actually observed between the 2 meV and 3 meV modes.

The energy gap that was observed of approximately 1.25 meV is inconsistent with the small spin-flop field of 1.25 T. The modes were not present above the ordering transition temperature and therefore the dispersion and associated anisotropy were linked to the onset of long-range order. A classical spin-wave calculation cannot explain the flat gapped modes that were observed using a simple anisotropy for the Cu^{2+} sites at $z = 0$ and $z = 1/2$.

The anisotropy may also have been less trivial. The elongation of the CuO_6 octahedra in the $\beta\text{-CuSb}_2\text{O}_6$ phase is known to lead to the unpaired spin on the Cu^{2+} in the $d_{x^2-y^2}$ orbital, which lies within the equatorial plane of the oxygen octahedra [84]. The plane is inclined in the same direction for all Cu^{2+} sites within a layer. This may mean that a local anisotropy symmetry axis would lie perpendicular to the plane. The tilt of the equatorial plane is different for the two Cu^{2+} sites in the unit cell and can be transformed into the other site by symmetry operations of the crystal space group. An inter-layer coupling of the two copper sites may lead to an overall effective Ising-type anisotropy while the local anisotropy in the plane may be quite different. The b -axis is unique and leads to the description of the overall effect of the anisotropy as Ising-type along the b -axis. Alternatively, a more complex anisotropy where the two Cu^{2+} sites have different local anisotropy axes (eg. planar-type within the octahedron equatorial plane) may be necessary to explain the observations. This may lead to a more complex relationship between the spin-flop field, the anisotropy gap and the inter-layer couplings.

Another consideration is that the quantum nature of the system may have led to gapped modes. In the spin-half quasi one-dimensional Heisenberg antiferromagnet, KCuF_3 , a

gapped mode has been observed which is present only below the ordering transition temperature. Measurements on KCuF_3 have shown the presence of a longitudinal bound state due to weak inter-chain coupling and the onset of three dimensional order [96]. Therefore the mode is only observed below the magnetic ordering temperature. The energy gap of the longitudinal mode is predicted to be proportional to m_0^2 , where m_0 is the ordered moment per spin site [97]. The ordered moment per spin in KCuF_3 is $0.54\mu_B$. The zone boundary energy is about 53.5 meV [98] and the longitudinal mode is predicted to be at 17.4 meV [97]. The mode is measured to be at 15.8(0.1) meV if localized and 14.9(0.1) meV if dispersive [96]. The elastic measurements, presented in the previous chapter, have indicated a highly reduced ordered moment in CuSb_2O_6 , suggesting quantum fluctuations. The ordered moment per spin was $0.39(0.01)\mu_B$ and the zone boundary energy was measured as 12.5(0.4) meV. The ratio of the zone boundary energies of the two materials is 0.234. Therefore, simply by naively scaling the energy gap of the longitudinal mode by this ratio and considering the ratio of m_0^2 the gapped longitudinal mode would be expected at approximately 1.7-1.2 meV. The reduced ordered moment implies large quantum fluctuations and is smaller in CuSb_2O_6 than in KCuF_3 . Therefore the probability of quantum effects is increased. Hence, it may be possible that similar bound states as have been observed in KCuF_3 also occur in CuSb_2O_6 .

The spin-wave calculation predicted a large in-plane interaction and susceptibility measurements indicate a spin-half antiferromagnetic chain, yet this seems inconsistent with the intensity distribution that was actually observed where the excitation spectrum had a resonance at the zone boundary. The intensity distribution of the excitations of a one-dimensional Heisenberg chain for the classical Néel ground state is calculated to be:

$$I_{\perp}(q) = A \tan(q\pi),$$

where A is a constant. For the spin-half quantum case the intensity decreases more rapidly with q [99]. Therefore the spin-half Heisenberg chain does not have a peak in the intensity at the Brillouin zone boundary. Instead the intensity drops rapidly from the Brillouin zone centre, $q = 1/2$, as has been observed in the material KCuF_3 [100]. The intensity distribution for CuSb_2O_6 does not follow that measured for the predicted spin-half square lattice either. An experimental realization of the square lattice antiferromagnet is CFTD (copper deuteroformate tetradeurate). The calculated quantum mechanical structure factor for the

spin-half square lattice is [101]:

$$S(q) = 1 - \cos^2(q_x\pi) \cos^2(q_y\pi),$$

which is a maximum at $q = (1/2, 1/2)$. Measurements on CFTD support a similar intensity distribution to that calculated[102]. Neither of these cases show a peak in the intensity at the zone boundary as observed in the present study of CuSb_2O_6 .

The unusual resonance at 13 meV led to a brief investigation of phonon modes about this energy transfer range using PHONON. From these preliminary calculations it appeared probable that the phonon mode, which was measured at 15 meV, was the one in which the Cu-O-O-Cu bond was bending, so it is probable that the bending mode was linked to the magnetic coupling.

The room temperature measurements indicated a phonon at 15 meV about the wave vector transfer, $Q = (4, 0, 0)$, which was close to the 11 meV mode predicted from the calculation at the same Q . The discrepancy between the calculation and measured energy may be resolved if the calculation were to be preformed by taking into consideration the unpaired spins at the Cu^{2+} site. The calculated movement of the lattice was such that the oxygen octahedron around the Cu^{2+} site rotates about the c -axis. The movement of the lattice and the structure factor of the phonon modes is believed to be more accurate than the calculated energies in the diagonalization calculation carried out with PHONON. The results of the phonon measurements agree with earlier Raman measurements on polycrystalline β - CuSb_2O_6 which have shown a mode at 118 cm^{-1} (14.6 meV) [92]. The same measurements have shown that the mode is also present in the α - CuSb_2O_6 phase. A later study on a ceramic sample has observed the lowest mode near 130 cm^{-1} (16.1 meV) and has found no further modes down to 100 cm^{-1} [93]. The association of the lowest frequency mode with this type of phonon is in accordance with other studies of the rutile-type structures.

Spin exchange coupling calculations have considered the overlap between adjacent magnetic orbitals [84]. In that work the strongest exchange was found to be the diagonal exchange over the chemical Cu-O-O-Cu bond running along the $(1, 1, 0)$ direction in the $z = 0$ layer. The $(1, -1, 0)$ direction is very weak within that calculation, weaker than the nearest neighbour interaction. Hence the chemical Cu-O-O-Cu bond was predicted to give the strongest coupling between the Cu^{2+} ions. This main exchange path was associated with J_A coupling in the spin-wave calculation above. The O-O bond in the measured

phonon mode is predicted to oscillate about the mid point therefore producing a change in the Cu-O-O-Cu bond angle. The present measurements have suggested that the phonon contribution to the low-temperature 13 meV mode was related to the bending of the main exchange interaction.

In the material CuGeO_3 the bond angles in the main exchange paths are also bent in a low-energy phonon mode. There the main exchange path is through a Cu-O-Cu bond, which has a bond angle close to 90° and is a ferromagnetic exchange. A low-energy phonon mode modulates the bond angle such that the main anti-ferromagnetic exchange is induced [103]. This has been predicted to be the case in a calculation of the overlap of the electronic orbitals of the oxygen and copper ions [104]. In $\beta\text{-CuSb}_2\text{O}_6$ the present work found that a low energy phonon mode was related to the bending of the two Cu-O-O-Cu bonds associated with the main antiferromagnetic exchange coupling. Therefore it is possible that, in a similar way to CuGeO_3 , the main exchange path is linked to the bond angles of the Cu-O-O-Cu bond which vary in the low energy phonon mode measured at 15 meV. It may be a weaker coupling than the case of a 90° Cu-O-Cu bond but since a series of superexchange mechanisms are possible [3], a change in bond angle may still be significant for the interaction strength.

5.4 Conclusions on CuSb_2O_6

The investigations of the low-temperature magnetic excitations have measured an unusual intensity distribution for the main interactions. Measurement of the in-plane interactions showed that there was a strong resonance feature at 13 meV at the Brillouin zone boundary. This energy was in accordance with the predicted Brillouin zone boundary dispersion maximum for a one-dimensional spin-half Heisenberg chain with a coupling of 4.2 meV but it would not be expected to be an intense mode. The resonance feature energy was close to a low energy phonon mode which may modulate the main exchange interaction, and this suggests a magnon-phonon coupling.

The reinvestigation of the zero field magnetic order has indicated that the spins align along the b -axis and the spins of the two Cu^{2+} ions in the unit are collinear forming a collinear structure of antiferromagnetic stripes of spins. The small spin-flop field implies a small anisotropy, which would stabilize this structure, although the excitation spectrum appears to show an energy gap to at least two modes which is larger than expected for that associated with the spin-flop field. The magnetic structure in the spin-flop phase is unusual

since the spins align along both the a - and c -axis although susceptibility measurements show the susceptibility is lower for the a -axis than the c -axis. Therefore, it appears that the anisotropy in the sample may be complex, since a symmetric Ising-type anisotropy was not able to describe the inelastic scattering results and the spin-flop field. The inter-layer couplings were seen to be weak and linked to the low temperature long-range order. The energy gap was only observed within the magnetically ordered phase and so if it were associated with the anisotropy of the exchange couplings it would be linked to the inter-layer couplings.

At high field the background around the magnetic Bragg peaks was seen to increase, suggesting the presence of critical scattering due to a phase transition at higher field and may be associated with the gapped modes observed in the inelastic scattering data. These observations indicated that the energy gap observed at zero field was decreased because of Zeeman splitting as a magnetic field was applied, and thus at about 12 T the gap would be expected to close.

The ordered magnetic moment was found to be considerably reduced and the couplings within the lattice are predicted to be frustrated. Therefore it is probable that some consideration of non-classical behaviour is necessary to fully understand the excitation spectrum and energy gap observed in these measurements.

Chapter 6

Conclusions and Perspectives

Three low-dimensional, low-spin, frustrated systems were studied in this thesis. It has been shown that the behaviour of these systems reflects the presence of strong quantum fluctuations and the behaviour could not be explained with classical descriptions. The experiments presented in this thesis explored the spin-one triangular antiferromagnet, AgNiO_2 , in Chapter 3, the spin-half Ising chain ferromagnet, CoNb_2O_6 , in Chapter 4 and the spin-half layered antiferromagnet, CuSb_2O_6 in Chapter 5.

The triangular lattice antiferromagnet, AgNiO_2 , is geometrically frustrated and this frustration was also true for the cooperative Jahn-Teller distortion of the NiO_6 octahedra. This system had not been studied extensively and in particular no neutron scattering measurements had been made before. The investigation of the crystal structure identified a structural distortion whereby the NiO_6 octahedra periodically contract and expand across the lattice to form a three-sublattice structure. It was proposed that charge disproportionation on the Ni sites was responsible for the distortion because it relieved the frustration. In addition the low-temperature magnetic diffraction pattern that was observed was explained by order on the electron-rich spin-one sites. The triangular lattice of spin-one sites ordered in a collinear antiferromagnetic order of ferromagnetic chains. Investigations of the magnetic excitations at low temperature indicated that the main dispersions were within the triangular plane. The data was compared to the previous spin-wave calculation of Chubukov and Jolicoeur [50]. Their calculation of the antiferromagnetic nearest-neighbour (J) and next nearest-neighbour (J') interactions on an isotropic triangular lattice included quantum corrections. However, it did not capture the main features of the dispersion. Therefore, a linear spin-wave calculation was made for a model Hamiltonian that included inter-layer

exchange and an easy-axis anisotropy. The main features of the energy gap and band of excitations were replicated by this calculation but the intensity distribution did not match that observed. Since quantum corrections had a significant effect on the single triangular layer in the calculation of Chubukov and Jolicoeur, it is probable that the inclusion of quantum corrections would be necessary in the model Hamiltonian for the system that was used in Chapter 3. Further work is necessary to determine the extent of the charge disproportionation predicted for the distorted structure of AgNiO_2 . Single crystal measurements would give clearer measurements of the crystal structure and magnetic structure. Single crystal inelastic scattering measurements would provide clearer information about the dispersion and would allow investigation of particular points in the Brillouin zone. Further work to investigate the phonon modes of the high temperature structure should help in understanding why there is this particular distortion at lower temperature. Also, investigation of the three-layered ploytype 3R-AgNiO_2 may also bring insight since the published crystal structure would also imply orbital frustration.

CoNb_2O_6 had been previously identified as a quasi one-dimensional Ising ferromagnet. It had not been studied within a field purely transverse to the Ising direction. Neutron single crystal diffraction was used to investigate the phase transition which occurs when applying an increasing field transverse to the Ising axis in an Ising-like system. Three ordered phases were observed in the phase diagram of CoNb_2O_6 as the field was increased. The Ising-like spins in CoNb_2O_6 are coupled into ferromagnetic chains which order at low temperatures due to weaker inter-chain couplings. The inter-chain couplings are frustrated because the Ising chains are arranged on an anisotropic antiferromagnetic triangular lattice. Therefore, a spin-density wave structure was stabilized along the largest coupling direction within the triangular lattice. A transition to a paramagnetic phase was observed at 5.45(5) T. The transition from an incommensurate ordered phase to a paramagnetic phase by the application of a transverse field was further investigated by inelastic neutron scattering. Interesting behaviour was observed when the system was in a field just below the transition field. There were low energy, probably gapless, modes which added further evidence to support the idea that there was an incommensurate ordered phase just below the transition field. In addition higher energy scattering was observed which moved to lower energies as the critical field was approached. The higher energy scattering was attributed to two-soliton scattering. At higher field, in the paramagnetic phase, no low-energy scattering was observed away from the critical field and at higher energies sharp magnon modes were observed. The dispersion of the magnon modes was mapped and an analysis of the magnon dispersion implied that

there was a need for renormalization of the classical dispersion. As expected, the dispersion along the chain direction was largest because this was where coupling was predicted to be strongest. The dispersion was weaker between the chains within the triangular plane. The energy gap was observed to decrease as the field approached the critical field from the paramagnetic phase and in the ordered phase gapless modes were observed. A question that remains to be investigated is whether there is a sharp change in the energy gap at the phase transition or if the gap closes smoothly. Further work is also required to understand the development of the energy gap close to the transition field by studying how the dispersion changes as the transition field is approached. More measurements need to be made close to the transition field and models beyond the linear-spin wave models need to be developed to explain the magnon dispersion observed at 6 T. The effective spin-half system may have sizeable terms in the Hamiltonian which are not Ising-like. High energy inelastic scattering measurements have been made to investigate the crystal field levels of the Co^{2+} ion and the analysis is in progress to develop the effective spin-half Hamiltonian. Therefore a more detailed model of the interactions could be eventually calculated.

The spin-half layered antiferromagnet CuSb_2O_6 has a square lattice of Cu^{2+} ions in which the main interaction is across one diagonal of the square. The two Cu^{2+} ions in the unit cell form two square lattices. The edge interactions frustrate the system. Inelastic scattering measurements had not been previously made on this material. Initial neutron diffraction measurements of the zero-field magnetic order reinvestigated measurements by Gibson *et al.*. The results suggested that, contrary to the Gibson result, the system was in a collinear antiferromagnetic state with a reduced ordered moment. The subsequent measurements went on to investigate the change in the magnetic structure as a field was applied along the moment direction. At a field of 1.35(5) T the spin-flop was observed where the spins flop to within the (a, c) -plane whereas susceptibility measurements would have indicated a flop to the a -axis. It was proposed that a more complicated anisotropy than a Ising-type anisotropy was needed to explain the results. At high field the background around the magnetic Bragg peaks was seen to increase, suggesting the presence of critical scattering due to a phase transition at higher fields. Also, the zero-field inelastic neutron scattering observations could not be described with a simple Ising-type anisotropy within the exchange couplings of the Hamiltonian. The inter-layer dispersion was much smaller than the in-plane dispersion, which had an intense maximum at 13 meV at the Brillouin zone boundary. The modes observed had an energy gap which was associated with the indication of a phase transition at high fields close to 12 T. The ordered magnetic moment

was found to be considerably reduced and the couplings within the lattice were predicted to be frustrated. The preliminary phonon measurements suggested that there were low energy phonon modes close to the 13 meV feature. Further work is now necessary to investigate this unusual magnetic excitation spectrum and to characterize fully these excitations. Clearly, a more complete analysis and experimental study of the phonon modes is necessary. For example, polarized inelastic scattering measurements would help to confirm the magnetic origin of the resonance feature but these will be difficult because of the small volume of the single crystal currently available. High magnetic field elastic and inelastic neutron scattering measurements are necessary to investigate the high field transition and to observe the change in the excitation spectrum to see if a transition is present at 12-15 T.

Appendix A

Low-Temperature and High-Temperature Structure Factors from Powder-Diffraction Measurements on AgNiO_2

This appendix refers to Chapter 3 §3.2 and presents the results from the powder diffraction experiments on AgNiO_2 . The observed intensities for a series of Bragg reflections is given and indexed within the distorted $P6_322$ group and the ideal structure $P6_3/mmc$ space group. A selection of nominal reflections of the ideal structure is given in Table A.1. Table A.2 lists the supercell peaks observed. The magnetic Bragg peaks are given in Table A.3. The structures were fitted using FULLPROF [38].

Table A.1: A list of the nominal peaks with the observed and calculated structure factors for the model of expanded and contracted Ni-O bonds shown in Fig. 3.11. The observed $|F|^2$ is the peak intensity, divided by the peak multiplicity and normalized per unit cell of the $P6_322$ group. In this table a selection of the nominal peaks of the ideal structure $P6_3/mmc$ space group.

Q (\AA^{-1})	(h, k, l) $P6_322$	(h, k, l) $P6_3/mmc$	$ F _{obs}$ (^{-14}m)	$ F _{calc}$ (^{-14}m)
1.026	002	002	6.24	6.36
2.052	004	004	7.19	6.76
2.469	110	100	1.14	0.94
2.523	111	101	5.89	5.98
2.675	112	102	5.86	6.12
2.911	113	103	2.79	2.90
3.080	006	006	4.49	4.30
3.212	114	104	5.83	5.92
3.562	115	105	6.40	6.52
3.947	116	106	11.36	11.40
4.105	008	008	5.69	5.43
4.278	300	110	18.07	16.55
4.359	117	107	5.34	5.40

Table A.2: List of supercell structural peaks associated with the tripling of the unit cell in the basal plane with the observed and calculated structure factors for the model of expanded and contracted Ni-O bonds shown in Fig. 3.11. The observed $|F|^2$ is the peak intensity, divided by the peak multiplicity and normalized per unit cell of the $P6_322$ group. The peak indices are given in both space groups.

Q (\AA^{-1})	(h, k, l) $P6_322$	(h, k, l) $P6_3/mmc$	$ F _{obs}$ (10^{-14} m)	$ F _{calc}$ (10^{-14} m)
1.425	010	2/3 -1/3 0	0.15	0.16
1.515	011	2/3 -1/3 1	0.24	0.24
1.756	012	2/3 -1/3 2	0.05	0.09
2.097	013	2/3 -1/3 3	0.02	0.02
2.851	020	4/3 -2/3 0	0.31	0.35
2.898	021	4/3 -2/3 1	0.57	0.53
2.936	015	2/3 -1/3 5	0.23	0.23
3.031	022	4/3 -2/3 2	0.14	0.19
3.393	016	2/3 -1/3 6	0.00	0.16
3.514	024	4/3 -2/3 4	0.00	0.15
3.807	211	4/3 1/3 1	0.35	0.22
3.836	025	4/3 -2/3 5	0.53	0.50
3.865	017	2/3 -1/3 7	0.46	0.26
3.910	212	4/3 1/3 2	0.60	0.62
4.074	213	4/3 1/3 3	0.37	0.42
4.105	026	4/3 -2/3 6	0.39	0.35
4.295	214	4/3 1/3 4	0.73	0.66
4.562	215	4/3 1/3 5	0.30	0.26
4.586	027	4/3 -2/3 7	0.49	0.56
4.998	028	4/3 -2/3 8	0.35	0.22
5.166	311	5/3 2/3 1	0.67	0.67
5.209	217	4/3 1/3 7	0.37	0.19
5.242	312	5/3 2/3 2	0.71	0.74
5.366	313	5/3 2/3 3	0.56	0.48
5.535	314	5/3 2/3 4	0.77	0.77
5.575	218	4/3 1/3 8	0.63	0.58
5.703	040	8/3 -4/3 0	0.54	0.60
5.726	041	8/3 -4/3 1	0.89	0.90
5.745	315	5/3 2/3 5	0.56	0.65
5.794	042	8/3 -4/3 2	0.41	0.32
5.821	0 1 11	2/3 -1/3 11	0.22	0.21
5.870	0 2 10	4/3 -2/3 10	0.17	0.12

Table A.3: List of magnetic Bragg peaks with the observed and calculated unit cell structure factors for the magnetic structure in Fig. 3.11. The observed $|F|^2$ is the peak intensity corrected for instrumental resolution effects, divided by the peak multiplicity and normalized per unit cell of the $P6_322$ group. The peak indices are given both in the distorted ($P6_322$) and the ideal ($P6_3/mmc$) crystal structures.

Q (\AA^{-1})	(h, k, l) $P6_322$	(h, k, l) $P6_3/mmc$	observed $ F $ (10^{-14} m)	calculated $ F $ (10^{-14} m)
0.714	1/2 0 0	1/6 1/6 0	0.61	0.71
0.879	1/2 0 1	1/6 1/6 1	0.28	0.33
1.236	1/2 -1 0	1/2 0 0	0.00	0.00
1.250	1/2 0 2	1/6 1/6 2	0.37	0.39
1.339	1/2 -1 1	1/2 0 1	0.74	0.72
1.607	1/2 -1 2	1/2 0 2	0.00	0.00
1.697	1/2 0 3	1/6 1/6 3	0.16	0.16
1.889	1/2 1 0	-1/6 5/6 0	0.58	0.63
1.957	1/2 1 1	1/6 5/6 1	0.34	0.35
1.957	3/2 -1 1	1/6 5/6 1	0.34	0.35
1.974	1/2 -1 3	1/2 0 3	0.48	0.45
2.142	3/2 0 0	1/2 -1 0	0.00	0.00
2.150	1/2 1 2	1/6 5/6 2	0.50	0.53
2.150	3/2 -1 2	1/6 5/6 2	0.50	0.53
2.173	1/2 0 4	1/6 1/6 4	0.15	0.20
2.202	3/2 0 1	1/2 -1 1	0.70	0.68

Appendix B

Linear Spin-wave Theory for Stacked Triangular Layers with Stripe Order in AgNiO₂

This appendix refers to Chapter 3 §3.3 and presents an outline of the derivation of the magnon dispersion relations for a system of stacked triangular layers as appropriate for AgNiO₂ within linear spin-wave theory. The spin-wave calculation was made taking the antiferromagnetic stripe order as the ground state. The calculation was setup by considering two types of spin sites (spin in and out of the triangular planes) forming two sublattices in the plane, giving four sublattices in the unit cell, as show in Fig. 3.23. The Hamiltonian resulting from the four sublattice description is given in Eqn. F.2, using the Holstein-Primakoff transformations and the model Hamiltonian in Eqn. 3.5:

$$\mathcal{H} = \sum_q X^\dagger H X + E_0 \quad (\text{B.1})$$

where E_0 is the energy of the ground state of the system and each bond J is counted once in the summation and given

$$X^\dagger = [\alpha_q^\dagger, \gamma_q^\dagger, \beta_{-q}, \epsilon_{-q}],$$

where the operators $\alpha_q^\dagger, \beta_q^\dagger$, etc. create magnon modes localized on each of the four sublattices and the g matrix is the commutator matrix for the operator basis, hence

$$g = X(X^*)^T - (X^* X^T)^T = \begin{pmatrix} 1 & 0 & 0 & 0 \\ 0 & 1 & 0 & 0 \\ 0 & 0 & -1 & 0 \\ 0 & 0 & 0 & -1 \end{pmatrix},$$

then

$$H = \begin{pmatrix} A & B\delta & C & D\delta^{2*} \\ B\delta^* & A & D\delta^2 & C \\ C & D\delta^{2*} & A & B\delta \\ D\delta^2 & C & B\delta^* & A \end{pmatrix} \quad (\text{B.2})$$

taking

$$\begin{aligned} A &= 2(SJ(\cos(2\pi k) - 1) + SJ'(\cos(2\pi(2h + k)) - 1) \\ &\quad + 2SJ + 2SJ' - SJ_\perp) + S\mathcal{D} \\ B &= 4SJ_\perp \cos(\pi k) \cos(\pi l) \\ C &= 4SJ \cos(\pi k) \cos(\pi(2h + k)) \\ &\quad + 4SJ' \cos(3\pi k) \cos(\pi(2h + k)) \\ D &= 2SJ_\perp \cos(\pi l) \\ \delta &= e^{-(2h+k)\pi i/3}, \end{aligned}$$

where $\mathbf{Q} = ha^* + kb^* + lc^*$ refers to the reciprocal lattice in the $P6_322$ space group. Diagonalising this Hamiltonian gives the magnon dispersion relations:

$$\begin{aligned} (\hbar\omega_\pm)^2 &= A^2 + B^2 - C^2 - D^2 \pm \\ &\quad \sqrt{4|AB\delta - CD\delta^{-2}|^2 - 2B^2D^2|\delta^{-3} - \delta^3|^2} \end{aligned} \quad (\text{B.3})$$

where \pm indicates the two two-fold degenerate dispersion branches present. The intensity distribution is proportional to the correlation functions which are:

$$\begin{aligned} S^{xx}(\mathbf{Q}, \Omega) &= \frac{S}{2} \left(\frac{|(W(-\omega_+) + X(-\omega_+) + Y(-\omega_+) + Z(\omega_+))|^2}{N(-\omega_+)} + \right. \\ &\quad \left. \frac{|(W(\omega_+) + X(\omega_+) + Y(\omega_+) + Z(\omega_+))|^2}{N(\omega_+)} \right) G(\Omega - \omega_+) \\ &\quad + \frac{S}{2} \left(\frac{|(W(-\omega_-) + X(-\omega_-) - Y(-\omega_-) + Z(\omega_-))|^2}{N(-\omega_-)} + \right. \\ &\quad \left. \frac{|(W(\omega_-) + X(\omega_-) - Y(\omega_-) + Z(\omega_-))|^2}{N(\omega_-)} \right) G(\Omega - \omega_-) \end{aligned} \quad (\text{B.4})$$

where,

$$W(\omega) = -(A + \omega)(A^2 + B^2 - C^2 - D^2 - \omega^2) + B(2AB - CD(\delta^{-3} + \delta^3))$$

$$X(\omega) = C(A^2 + B^2 - C^2 + D^2 - \omega^2) - ABD(\delta^{-3} + \delta^3) - \omega BD(\delta^{-3} - \delta^3)$$

$$Y(\omega) = \delta^5(\delta^{-6}B((A + \omega)^2 - B^2 + C^2) - 2C(A + \omega)D\delta^{-3} + BD^2)$$

$$Z(\omega) = \delta^2(D(A^2 + C^2 - D^2 - \omega^2) + B^2D\delta^{-6} - 2ABC\delta^{-3})$$

$$N(\omega) = |-WW^* + XX^* - YY^* + ZZ^*|.$$

$G(\Omega - \omega)$ are gaussian functions with a FWHM which models the resolution broadening of the modes. For comparison with the data the dynamical correlation functions need to be multiplied by the pre-factor

$$\left(1 + \frac{Q_z^2}{Q}\right) \left(\frac{g\gamma f(Q)}{2}\right)^2 \frac{(2\pi)^3}{v_0}$$

where $f(Q)$ is the magnetic form factor, the g -factor is taken to be $g = 2$, v_0 is the magnetic unit cell and $\gamma = 5.39 fm$. Q_z is the component of Q parallel to the c -axis. A powder average of this intensity was taken to simulate the experimental sample conditions.

Appendix C

Measured Magnetic Bragg Intensities in the Single-Crystal Diffraction Measurements on CoNb_2O_6

This appendix refers to Chapter 4 §4.2 and presents the results from the measured magnetic Bragg intensities for the zero field (Table C.1(a)) and 4 T (Table C.1(b)) measurement which have been scaled for comparison to the calculated intensities based on the structure the study by Heid *et al.* [60].

Table C.1: Observed intensities and calculated intensities of the peaks measured at zero field and 4 T. The calculated intensities are for the magnetic structure as given by the Heid study.[60]

(a) Zero Field		
(h, k, l)	Scaled Experimental Intensity	Calculated Intensity
-1, 1/2, 0	18(1)	17.5
-2, 1/2, 0	14(3)	15.0
-3, 1/2, 0	13(1)	12.8
-4, 1, 2, 0	11(1)	10.9
-5, 1/2, 0	8.5(1)	8.9
-6, 1/2, 0	7.5(1)	7.1
-7, 1/2, 0	5(1)	5.5
0, 1/2, 1	2(0.5)	2.0
0, 1/2, 2	3(0.5)	2.9
-2, 1/2, 1	3(0.5)	2.4

(b) 4 T		
(h, k, l)	Scaled Experimental Intensity	Scaled Calculated Intensity
-1, 1/2, 0	17 (2)	17.5
-2, 1/2, 0	14(2.5)	15.0
-3, 1/2, 0	15(3)	12.8
-4, 1, 2, 0	7(3)	10.9
-5, 1/2, 0	12(2.5)	8.9
0, 1/2, 1	8(2)	2.0
0, 1/2, 2	5(2)	2.9

Appendix D

Linear Spin-Wave Calculations of the Magnon Dispersion Relations of the Ising Chains in CoNb_2O_6

This appendix refers to Chapter 4 §4.3 and presents the main elements of the linear spin-wave calculation of the magnon dispersion relations for a system of Ising spins on a triangular lattice and then extended to coupled Ising chains on a triangular lattice as appropriate for CoNb_2O_6 . In both cases the ground state was assumed to be made up of spins aligned along the field direction. Initially the calculation was setup by considering two types of spin sites corresponding to the two Ising directions to the chain, see Fig. 4.22. The initial Hamiltonian considered was:

$$\mathcal{H}_t = \sum_{il} J_b S_i^x S_l^x + \sum_{im} J_b S_i^{x'} S_m^{x'} + \sum_{ik} J_a S_i^x S_k^{x'} - \sum_i g \mu_B B S_i^z$$

Using the Holstein-Primakoff transformations the Hamiltonian in terms of the basis states:

$$X^\dagger = [a_q^\dagger, b_q^\dagger, a_{-q}, b_{-q}],$$

and the commutator matrix for this operator basis is a diagonal matrix:

$$g = \text{diag}\{1, 1, -1, -1\}$$

which create magnon modes localized on each sublattices becomes

$$\mathcal{H} = \sum_q X^\dagger H X + E_0 \quad (\text{D.1})$$

where E_0 is the energy of the ground state of the system and H was:

$$H = \begin{pmatrix} A & B & C & D \\ B & A & D & C^* \\ C^* & D & A & B \\ D & C & B & A \end{pmatrix}, \quad (\text{D.2})$$

where,

$$\begin{aligned} A &= \frac{S}{2} J_b \cos(2\pi k) + g\mu_B B, \\ B &= \frac{S}{2} J_a (\cos(\pi(h+k)) + \cos(\pi(h-k))) (\cos^2 \gamma - \sin^2 \gamma), \\ C &= \frac{S}{2} J_b \cos(2\pi k) (\cos^2 \gamma - \sin^2 \gamma + 2i \cos \gamma \sin \gamma), \\ D &= \frac{S}{2} J_a (\cos(\pi(h+k)) + \cos(\pi(h-k))). \end{aligned}$$

The dispersion relations were derived by diagonalizing the Hamiltonian. The Hamiltonian was then adapted to include the intra-chain interaction J_c . This coupled the spins into Ising chains within a triangular lattice see Fig. 4.23. The Hamiltonian considered was:

$$\mathcal{H} = \mathcal{H}_t + \sum_{ij} J_c S_i^x S_j^x + \sum_{ij} J_c S_i^{x'} S_l^{x'},$$

The intra-chain coupling coupled spins with the same Ising axis, therefore, using the basis states:

$$X^\dagger = [a_q^\dagger, \alpha_q^\dagger, a_{-q}, \alpha_{-q}],$$

and the commutator matrix:

$$g = \text{diag}\{1, 1, -1, -1\}.$$

the Hamiltonian was as in D.1 with

$$H = \begin{pmatrix} E & G & 0 & F \\ G & E & F & 0 \\ 0 & F & E & G \\ F & 0 & G & E \end{pmatrix}, \quad (\text{D.3})$$

where,

$$A = \omega_{\pm}$$

$$E = \frac{S}{2} J_c \cos(\pi l) \exp(2\pi i k \delta) (\cos^2 \gamma - \sin^2 \gamma - 2i \cos \gamma \sin \gamma),$$

$$F = \frac{S}{2} J_c \cos(\pi l) \exp(2\pi i k \delta),$$

and ω_{\pm} is defined in Eqn. 4.16 and the diagonalized solutions are given in Eqn. 4.17.

Appendix E

Integrated Magnetic Bragg Intensities for the Single-Crystal Diffraction Measurements on CuSb_2O_6

This appendix refers to Chapter 5 §5.2. Using the integrated intensities of the Bragg peaks the best-fit magnetic structure was using FULLPROF [38]. The fitted magnetic moment are given in Table E.1 and the observed and calculated integrated intensities for the fits at 0, 6 T and 11.5 T are given in Tables E.2(a), E.2(b) and E.2(c).

Table E.1:

Field (T)	m_a (μ_B)	m_b (μ_B)	m_c (μ_B)
0	0	0.389 ± 0.011	0
6	0.256 ± 0.019	0.054 ± 0.032	0.318 ± 0.009
11.5	0.253 ± 0.018	0.039 ± 0.055	0.320 ± 0.010

Table E.2: Observed intensities and calculated intensities of the peaks measured at zero field, 6 T and 11.5 T. The calculated intensities are for the Cu magnetic moment as given in Table E.1.

(a) Zero Field			(b) 6 T		
(h, k, l)	I_{obs}	I_{calc}	(h, k, l)	I_{obs}	I_{calc}
1/2 0 -1/2	136.65	123.17	1/2 0 -1/2	126.68	125.92
-1/2 0 1/2	137.45	123.17	-1/2 0 1/2	126.52	125.92
3/2 0 -3/2	102.46	81.27	3/2 0 -3/2	97.54	83.10
-1/2 0 -7/2	101.64	73.95	5/2 0 -5/2	61.46	39.13
1/2 0 -5/2	99.21	95.89	3/2 0 -6/2	55.19	57.49
3/2 0 -7/2	74.54	55.46	1/2 0 -5/2	49.37	77.29
1/2 0 -9/2	64.17	54.99	5/2 0 -9/2	42.34	25.69
5/2 0 -5/2	63.49	38.26	5/2 0 -1/2	40.79	34.78
3/2 0 1/2	62.57	87.06	3/2 0 1/2	35.55	40.75
3/2 0 5/2	53.56	67.51	5/2 0 -11/2	22.13	26.61
5/2 0 -1/2	51.05	46.73	1/2 0 -9/2	20.60	35.24
-1/2 0 -11/2	44.99	37.34	5/2 0 3/2	18.97	14.43
5/2 0 3/2	44.51	42.62	5/2 0 7/2	10.79	2.47
3/2 0 -11/2	39.73	29.26	3/2 0 3/2	8.45	0.00
5/2 0 7/2	32.91	29.39	-1/2 0 -7/2	6.65	11.18
1/2 0 1/2	3.67	0.00	-1/2 0 -11/2	3.93	8.62
1/2 0 -11/2	1.71	0.00	1/2 0 1/2	1.54	0.00
			5/2 0 1/2	0.64	0.00

(c) 11.5 T		
(h, k, l)	I_{obs}	I_{calc}
1/2 0 -1/2	129.14	126.51
-1/2 0 1/2	127.15	126.51
3/2 0 -3/2	97.81	83.50
5/2 0 -5/2	58.97	39.31
3/2 0 -7/2	57.97	57.33
1/2 0 -5/2	54.38	76.52
5/2 0 -1/2	33.13	35.23
3/2 0 1/2	32.19	41.63
1/2 0 -9/2	27.24	34.74
3/2 0 -11/2	25.42	26.42
5/2 0 3/2	18.44	14.83
5/2 0 7/2	8.04	2.63
-1/2 0 -7/2	6.55	10.69
3/2 0 5/2	6.39	3.187
-1/2 0 -11/2	6.04	8.33
1/2 0 1/2	1.26	1.26
5/2 0 1/2	0.04	0.47

Appendix F

Linear Spin-Wave Calculations of the Magnon Dispersion Relations of Heisenberg Spins in a Square Lattice in CuSb_2O_6

This appendix refers to Chapter 5 §5.2 and outlines the linear-spin wave derivation of the magnon dispersion relations for a system of square lattices which are stacked along the c -axis. The ground state was assumed to be the observed zero-field magnetic structure shown in Fig. 5.20. The calculation was set up by considering two types of spin sites in the two senses along the b -axis forming two sublattices in the plane, giving four sublattices in the unit cell, as show in Fig. 5.20. The initial Hamiltonian that was considered is given in Eqn.F.1.

$$\mathcal{H} = \sum_{in} J_n (S_{\mathbf{r}_i}^x S_{\mathbf{r}_i+\mathbf{r}_n}^x + S_{\mathbf{r}_i}^y S_{\mathbf{r}_i+\mathbf{r}_n}^y + (1 + \epsilon) S_{\mathbf{r}_i}^z S_{\mathbf{r}_i+\mathbf{r}_n}^z) \quad (\text{F.1})$$

By using the four sublattice description and the Holstein-Primakoff transformations and the basis of states:

$$X^\dagger = [\alpha_q^\dagger, \gamma_q^\dagger, \beta_{-q}, \eta_{-q}],$$

where the operators $\alpha_q^\dagger, \beta_q^\dagger$, etc. create magnon modes localized on each of the four sublattices and the g matrix is the commutator matrix for the operator basis, where

$$g = \text{diag}\{1, 1, -1, -1\}.$$

the Hamiltonian can be written as

$$\mathcal{H} = \sum_q X^\dagger H X + E_0 \quad (\text{F.2})$$

where E_0 is the energy of the ground state of the system and each bond J is counted once in the summation. The matrix H is then:

$$H = \begin{pmatrix} A & B & C & D \\ B & A & D & C \\ C & D & A & B \\ D & C & B & A \end{pmatrix} \quad (\text{F.3})$$

where

$$\begin{aligned} A_{\mathbf{Q}} &= 2(J_A + J_a + J_b(\cos(2\pi k) - 1) + 2J_\gamma - 2J_\delta)(1 + \epsilon) \\ B_{\mathbf{Q}} &= 2J_A \cos(2\pi(h + k)) + 2J_a \cos(2\pi h) \\ C_{\mathbf{Q}} &= -2J_\delta(\cos(\pi(-h + k + l)) + \cos(\pi(h + k - l))) \\ D_{\mathbf{Q}} &= -2J_\gamma(\cos(\pi(h + k + l)) + \cos(\pi(h - k + l))). \end{aligned}$$

where $\mathbf{Q} = h\mathbf{a}^* + k\mathbf{b}^* + l\mathbf{c}^*$ refers to the reciprocal lattice in the $P2_1/n$ space group. The Hamiltonian was then diagonalized to give the dispersion relations of Eqn. 5.2 and 5.3.

The second Hamiltonian considered was:

$$\mathcal{H} = \sum_{i, n=A, a, b} J_n (\mathbf{S}_{\mathbf{r}_i} \cdot \mathbf{S}_{\mathbf{r}_i + \mathbf{r}_n}) + \sum_{i, n=\gamma, \delta} J_n (S_{\mathbf{r}_i}^x S_{\mathbf{r}_i + \mathbf{r}_n}^x + S_{\mathbf{r}_i}^y S_{\mathbf{r}_i + \mathbf{r}_n}^y + (1 + \epsilon) S_{\mathbf{r}_i}^z S_{\mathbf{r}_i + \mathbf{r}_n}^z). \quad (\text{F.4})$$

The same basis states were used and the Hamiltonian can be described with Eqn.F.3 where $A_{\mathbf{Q}}, B_{\mathbf{Q}}, C_{\mathbf{Q}}, D_{\mathbf{Q}}$ are defined as:

$$\begin{aligned} A_{\mathbf{Q}} &= 2(J_A + J_a + J_b(\cos(2\pi k) - 1)) + 4(J_\gamma - J_\delta)(1 + \epsilon), \\ B_{\mathbf{Q}} &= 2J_A \cos(2\pi(h + k)) + 2J_a \cos(2\pi h) \\ C_{\mathbf{Q}} &= -2J_\delta(\cos(\pi(-h + k + l)) + \cos(\pi(h + k - l))) \\ D_{\mathbf{Q}} &= -2J_\gamma(\cos(\pi(h + k + l)) + \cos(\pi(h - k + l))). \end{aligned}$$

Bibliography

- [1] P. W. Anderson, *Mater. Res. Bull.***8** 153 (1973).
- [2] A. Auerbach, *Interacting Electrons and Quantum Magnetism* Chapter 2 Springer Verlag, New York (1988).
- [3] J. B. Goodenough *Magnetism and the chemical bond* Wiley, New York (1963).
- [4] J. Kanamori, *J. Phys. Chem. Solids***10**, 87 (1959).
- [5] F. Bloch, *Z. Physik***61** 206 (1930).
- [6] T. Holstein and H. Primakoff, *Phys. Rev.***58**, 1098 (1940).
- [7] R.M. White, M. Sparks and I. Ortenburger, *Phys. Rev.***139** A450 (1965).
- [8] S. Sachdev *Quantum Phase Transitions* (Cambridge University Press) (1999).
- [9] P. Pfeuty, *Ann. Phys.***57**, 79 (1970).
- [10] A.H. Bougourzi, M. Couture, and M. Kacir, *Phys. Rev. B* **54**, R12669 (1996).
- [11] D. A. Tennant, R. A. Cowley, S. E. Nagler, A. M. Tsvelik, *Phys. Rev. B* **52**, 13368 (1995).
- [12] M. Karbach, G. Muller, A. H. Bougourzi, A. Fledderjohann, and K. H. Mutter *Phys. Rev. B***55**, 12510 (1997).
- [13] J. C. Bonner, and M. E. Fisher, *Phys. Rev. A***135**, (3A), A640 (1964).
- [14] N. D. Mermin and H. Wagner, *Phys. Rev. Lett.***17**, 1133 (1966).
- [15] H. M. Ronnow, D. F. McMorrow, R. Coldea, A. Harrison, I. D. Youngson, T. G. Perring, G. Aeppli, O. Syljuasen, K. Lefmann, and C. Rischel, *Phys. Rev. Lett.***87**, 0372021 (2001).

- [16] N. Shannon, B. Schmidt, K. Penc, and P. Thalmeier, *Eur. Phys. J. B***38** (4),599, (2004).
- [17] G. H. Wannier, *Phys. Rev.* **79** 357 (1950).
- [18] R. M. F. Houtappel, *Physica***16** 425 (1950).
- [19] P. Fazekas, and P. W. Anderson, *Philos. Mag.***30**, 423 (1974).
- [20] G. L. Squires *Introduction to the theory of thermal neutron scattering* Cambridge University Press, Cambridge (1978).
- [21] *Oxford Neutron Scattering Course Notes* (2005).
- [22] A.-J. Dianoux and G. Lander (editors) *Neutron Data Booklet* Insitut Laue-Langevin (2002).
- [23] For information on Homer can be found at <http://www.isis.rl.ac.uk/excitations>
- [24] J. Shang Hwang, K. Lin, C. Tien , *Rev. Sci. Instrum.* **68** 94 (1997).
- [25] M. V. Mostovoy and D. I. Khomskii, *Phys. Rev. Lett.* **89**, 227203 (2002).
- [26] F. Vernay, K. Penk, P. Fazekas, F. Mila, *Phys. Rev. B* **70**, 014428 (2004).
- [27] T. Sörgel and M. Jansen, *Z. Anorg. Allg. Chem.* **631**, 2970 (2005).
- [28] T. Sörgel and M. Jansen, *J. Solid State Chem.*, **180** 8 (2007).
- [29] A. Wichainchai, P. Dordor, J. P. Doumerc, E. Marquestaut, Mi. Pouchard, P. Hagenmuller, A. Ammar, *J. Solid State Chem.* **74**, 126 (1988).
- [30] Y.J. Shin, J.P. Doumerc, P. Dordor, C. Delmas, M. Pouchard, P. Hagenmuller, *J. Solid State Chem.* **107**, 303 (1993).
- [31] J.-H Chung, Th. Proffen, S. Shamoto, A.M. Ghorayeb, L. Croguennec, W. Tian, B.C. Sales, R. Jin, D. Mandrus, T. Egami, *Phys. Rev. B* **71**, 064410 (2005) and references therein.
- [32] E. Chappel, M. D. Núñez-Regueiro, G. Chouteau, O. Isnard, and C. Darie, *Eur. Phys. J. B* **17**, 615 (2000)

- [33] M.J. Lewis, B.D. Gaulin, L. filion, C. Kallin, A.J. Berlinsky, H.A. Dabkowska, Y. Qiu, J.R.D. Copley *Phys. Rev. B*, **72**, 014408 (2005).
- [34] C. Darie, P. Bordet, S. de Brion, M. Holzappel, O. Isnard, A. Lecchi, J.E. Lorenzo, and E. Suard, *Eur. Phys. J. B* **43**, 159 (2005).
- [35] M. Sofin, and M. Jansen, *Z. Naturforsch. B* **60**, 701 (2005).
- [36] T. Lancaster, S.J. Blundell, P.J. Baker, M.L. Brooks, W. Hayes, F.L. Pratt, R. Coldea, T. Soergel, M. Jansen *ArXiv.condmat 0708.0344*, (2007).
- [37] S. J. Clarke, A. J. Fowkes, A. Harrison, R. M. Ibberson, and M. J. Rosseinsky *Chem. Mater.* **10**, 372 (1998).
- [38] J. Rodriguez-Carvajal, *Physica B* **192**, 55 (1993). Further information is also available at <http://wwwold.ill.fr/dif/Soft/fp/index.html> (last visited Dec 2007)
- [39] ICSD database, Fachinformationszentrum (FIZ) Karlsruhe, <http://icsdweb.fiz-karlsruhe.de/> (last visited Dec 2007)
- [40] W. Sikora, F. Białas, and L. Pytlik, *J. Appl. Cryst.* **37**, 1015 (2004).
- [41] J.M. Tarascon, G. Vaughan, Y. Chabre, L. Seguin, M. Anne, P. Strobel, G. Amatucci, *J. Solid State Chem.* **147**, 410 (1999).
- [42] A. Hirano, R. Kanno, Y. Kawamoto, Y. Takeda, K. Yamaura, M. Takano, K. Ohyama, M. Ohashi, Y. Yamaguchi, *Solid State Ionics* **78**, 123 (1995).
- [43] K. Nakahigashi, Y. Shimomura, N. Fukuoka, *Acta Crystallographica A* **28**, 234 (1972)
- [44] D. Rodic, V. Spasojevic, V. Kusigerski, R. Tellgren, H. Rundlof, *Physica Status Solidi B* **218**, 527 (2000).
- [45] D. Taylor, *Phase Transition* **38**, 127 (1992).
- [46] N. E. Brese and M. O'Keefe, *Acta Crystallogr. Sect. B* **47**, 192 (1991).
- [47] J.A. Alonso, J.L. García-Muñoz, M.T. Fernández-Díaz, M.A.G. Aranda, M.J. Martínez-Lopez, M.T. Casais, **82**, 3871 (1999).

- [48] E. Wawrzyńska, R. Coldea, E.M. Wheeler, T. Sörgel, M. Jansen, R.M. Ibberson, P.G. Radaelli, M. Koza *ArXiv.condmat 0710.2811*, (2007) to appear in *Phys. Rev. B*.
- [49] Misguich, G. and Lhuillier, C. In *Frustrated spin systems*, Diep, H. T., editor. World Scientific, Singapore (2005).
- [50] A.V. Chubukov and Th. Jolicoeur, *Phys. Rev. B* **46**, 11137 (1992).
- [51] Th. Jolicoeur, E. Dagotto, E. Gagliano, and S. Bacci, *Phys. Rev. B* **42**, 4800 (1990).
- [52] P.A. Slotte and P.C. Hemmer, *J. Phys. C.* **17**, 4645 (1984).
- [53] H.M. Ronnow, R. Parthasarathy, J. Jensen, G. Aeppli, T.F. Rosenbaum, D.F. McMorrow, *Science***15**, 389 (2005).
- [54] H. Weitzel *Z. Kristallogr.***144** 238 (1976)
- [55] I. Maartense, I. Yaeger, B. M. Wanklyn *Solid State Comm.* **21** 93 (1977).
- [56] W. Scharf, H. Weitzel, I. Yaeger, I. Maartense, B. M. Wanklyn *J. Magn. Magn. Mater.* **13** 121 (1979).
- [57] , S. Kobayashi, S. Mitsuda, K. Prokes, *Phys. Rev. B* **6302** 2 (2001).
- [58] S. Mitsuda, K. Hosoya, T. Wada, H. Yoshizawa, T. Kanawa, M. Ishikawa, K. Miyatani, K. Saito, K. Kohn, *J. Phys. Soc. Japan***63** 3568 (1994).
- [59] S. Mitsuda, H. Okano, S. Kobayashi, K. Prokes *J. Magn. Magn. Mater.* **272** 121 (2004).
- [60] C. Heid, H. Weitzel, P. Burlet, M. Bonnet, W. Gonschorek, T. Vogt, J. Norwig, H. Fuess, *J. Magn. Magn. Mater.***151** 123 (1995).
- [61] C. Heid, H. Weitzel, P. Burlet, M. Winkelmann, H. Ehrenberg, H. Fuess, *Physica B* **2234** 574 (1997).
- [62] S. Kobayashi, S. Mitsuda, M. Ishikawa, K. Miyatani, K. Kohn, *Phys. Rev. B* **60** 3331 (1999).
- [63] S. Kobayashi, H. Okano, T. Jogetsu, J. Miyamoto, S. Mitsuda, *Phys. Rev. B* **60** R9908 (1999).

- [64] T. Hanawa, Shinkawa K., Ishikawa M., Miyatani K., Saito K., Kohn K., *J. Phys. Soc. Jpn.* **63** 2706 (1994).
- [65] H. Weitzel, H. Ehrenberg, C. Heid, H. Fuess, P. Burlet *Phys. Rev.* **B62** 12146 (2000).
- [66] Kunimoto T., Nagasaka K., Nojiri H., Luther S., Motokawa M., Ohta H., Goto T., Okubo S., Kohn S. *J. Phys. Soc. Jpn.* **68** 1703 (1999).
- [67] U. Tellenbach, *J. Phys. C*, **11**, 2287 (1978).
- [68] S. J. Allen Jr., H. J. Guggenheim *Phys. Rev. B* **4** 950 (1971).
- [69] R. Coldea, D.A. Tennant, *ISIS experimental report* RB12650 (2002).
- [70] D. Prabhakaran, F. R. Wondre, A. T. Boothroyd, *J. Cryst. Growth* **250** 72 (2003).
- [71] S. T. Carr and A. M. Tselik, *Phys. Rev. Lett.* **90** 177206 (2003).
- [72] S. Kobayashi, S. Mitsuda, K. Hosoya, H. Yoshizawa, T. Hanawa, M. Ishikawa, K. Miyatani, K. Saito, K. Kohn, *Physica B* **213** 176 (1995).
- [73] G. J. McIntyre and R. F. D. Standfield *Acta Cryst.*, **A44** 257 (1988).
- [74] S. Mitsuda, Y. Inomoto, *BENSC experimental report* PHY-01-1128 (2001).
- [75] H. Takayama, K. Matsumoto, H. Kawahara, K. Wada *J. Phys. Soc. Jpn.*, **52** 2888 (1983).
- [76] P. Bak and J. Boehm *Phys. Rev. B*, **21** 5297 (1980).
- [77] R. M. Nicklow and N. Wakabayashi. *Phys. Rev. B*, **26** 3994 (1982).
- [78] K. A. McEwan, U. Steigenberger, J. Jensen *Phys. Rev. B*, **43** 3298 (1991).
- [79] S.H. Liu and J. F. Cooke *Phys. Rev. B*, **53** 14996 (1996).
- [80] D. Bitko, T. F. Rosenbaum, and G. Aeppli, *Phys. Rev. Lett.*, **77**, 940 (1996).
- [81] H. M. Rønnow, J. Jensen, R. Parthasarathy, G. Aeppli, T. F. Rosenbaum, D. F. McMorrow, and C. Kraemer *Phys. Rev. B.*, **75**, 054426 (2007).
- [82] A. Nakua, H. Yun, J.N. Reimers, J.E. Greenan, C.V. Stager *J. Solid State Chem.* **91**, 105 (1991).

- [83] M. Heinrich, A. K. von Nidda, A. Krimmel, A. Loidl, R. M. Eremina, A. D. Ineev, B. I. Kochelaev, A. V. Prokofiev, W. Assmus, *Phys. Rev.* **B67**(22) 224418 (2003).
- [84] H.-J. Koo and M.-H. Whangbo *J. Solid State Chem.* **156**, 110 (2001).
- [85] Gibson, B., Kremer, R. K., Prokofiev, A., Assmus, W., and Ouladdiaf, B. *J. Magn. Mater.* **272**, 927 (2004).
- [86] Kato, M., Hatazaki, A., Yoshimura, K., and Kosuge, K. *Physica B* **281**, 663 (2000).
- [87] R. K. Kremer, *private communication* Max Plank Institut, Stuttgart. (2007).
- [88] Prokofiev, A. V., Ritter, F., Assmus, W., Gibson, B. J. and Kremer, R. K. *J. Cryst. Growth*, **247** 457, (2003).
- [89] M. Kato, K. Kajimoto, K. Yoshimura, K. Kosuge, M. Nishi, K. Kakurai, *J. Phys. Soc. Jpn.* **71**, 187 (2002).
- [90] K. M. Kojima, Y. Fudamoto, M. Larkin, G. M. Luke, J. Merrin, B. Nachumi, Y. J. Uemura, N. Motoyama, H. Eisaki, S. Uchida, K. Yamada, Y. Endoh, S. Hosoya, B. J. Sternlieb, G. Shirane *Phys. Rev. Lett.* **78**, 1787 (1997).
- [91] E.F. Shender, *Sov. Phys. JETP* , **56** 178, (1982).
- [92] E.-O. Gieré, A. Brahimí, H.J. Deiseroth, D. Reinen *J. Solid State Chem.* **131**, 263 (1997).
- [93] V. I. Torgashev, V.B. Shirokov, A. S. Prokhorov, B. Gorshunov, P. Haas, M. Dressel, B.J. Gibson, R. K. Kremer, A. V. Prokofiev, W. Assmus *Phys. Rev. B* **67**, 134433 (2003).
- [94] Krzysztof PARLINSKI *PHONON Software* For which information can be found at <http://wolf.ifj.edu.pl/phonon/> (last visited Dec 2007).
- [95] H. Rohrer and H. Thomas *J. Appl. Phys.* **40** 1025 (1969).
- [96] B. Lake, D.A. Tennant, and S.E. Nagler *Phys Rev. Lett.* **85** 832 (2000).
- [97] F. H. L. Eessler, A. M. Tsvellik and G. Delfino *Phys Rev. B* **56** 11001 (1997).
- [98] S. K. Satija, J. D. Axe, G. Shirane, H. Yoshizawa K. Hirakawa *Phys. Rev. B* **21** 2001 (1980).

- [99] G. Müller, H. Thomas, H. Beck, J.C. Bonner *Phys. Rev. B* **24**, 1429 (1981).
- [100] D.A. Tennant, R.A. Cowley and S.E. Nagler *Phys Rev. Lett.* **70** 4003 (1993).
- [101] J. T. Haraldsen, T. Barnes, J.L. Musfeldt *Phys Rev. B* **71** 064403 (2005).
- [102] N. B. Christensen, H. M. Rønnow, D. F. McMorrow, A. Harrison, T. G. Perring, M. Enderle, R. Coldea, L. P. Regnault, G. Aeppli *Proc. Natl. Acad. Sci. U.S.A.* **104** 15264 (2007).
- [103] M. Braden, B. Hennion, W. Reichardt, G. Dhalenne, A. Revcolevschi *Phys. Rev. B* **80** 3634 (1998).
- [104] M. Braden, G. Wilkendorf, J. Lorenzana, M. Aïn, G.J. Mc Intyre, M. Behruzi, G. Heger, G. Dhalenne, A. Revcolevschi *Phys. Rev. B* **54** 1105 (1996).